



---

**POLITECHNIKA POZNAŃSKA**

---

FACULTY OF CIVIL AND TRANSPORT ENGINEERING

**INSTITUTE OF STRUCTURAL ANALYSIS**

DOCTORAL DISSERTATION

# **STRUCTURAL BEHAVIOR OF SANDWICH PANELS UNDER FIRE CONDITIONS**

Zachowanie się paneli warstwowych w warunkach pożaru

**MGR INŻ. EL MEHDI ABLAOU**

Supervisor: **dr hab. inż. ZBIGNIEW POZORSKI, prof. PP**

Auxiliary supervisor: **dr inż. MICHAŁ MALENDOWSKI**

Poznań, 2025



## Acknowledgement

*I would like to express my sincere gratitude to all those who have supported and guided me throughout the course of this research and dissertation.*

*Firstly, I am deeply thankful to my supervisor, dr hab. inż. Zbigniew Pozorski, professor at the Poznań University of Technology, whose expertise, encouragement, and patience have been invaluable. Your guidance has been essential in shaping this research. As well, I would like to express my sincere thanks to my auxiliary supervisor, dr inż. Michał Malendowski, for his care and ensuring the precise direction of the work.*

*My appreciation extends to the technical staff and laboratory assistants of civil engineering laboratory at Poznan University of Technology (Politechnika Poznańska), as well as to the personnel of the Fire Research Department of the Instytut Techniki Budowlanej in Warsaw, for the valuable support and assistance provided on the experimental phases of this research. Their dedication and expertise were instrumental in the successful completion of the laboratory test.*

*On a personal note, I am forever grateful to my family and close friends for their unwavering support and encouragement throughout my academic journey. Your love and understanding have been my greatest source of strength. Your contributions have been essential, and I am deeply appreciative of your support.*

*Thank you all for being part of this journey.*

*El Mehdi ABLAOU*



## Abstract

The thermal and structural behavior of sandwich panels under fire conditions was rigorously investigated through a systematic methodology combining experimental testing and numerical modelling. The aim of the research was to determine the influence of the properties of core materials, adhesive layers, geometric configurations and boundary conditions on the fire resistance of sandwich panels. A comprehensive literature review was conducted to identify existing research gaps and to establish the framework for experimental and numerical approaches. Experiments, included both small-scale and large-scale tests, provided valuable data on thermal diffusivity, anisotropic behavior, and structural performance of sandwich panels with mineral wool cores.

The findings from small scale tests highlighted the significant influence of temperature on material properties of the mineral wool. The anisotropic thermal diffusivity of the mineral wool was identified as a critical parameter for ensuring both insulation and structural integrity during fire exposure, which is highly dependent on the development of the thermal gradient between surfaces of the sandwich panel. Large-scale fire tests demonstrated the effects of geometric configurations, joint design, and boundary conditions on overall fire resistance and structural stability. These experiments provided essential benchmarks for validating numerical simulations.

Finite element models were developed using ABAQUS software, incorporating material properties, complex thermomechanical interactions, and advanced interface modelling to simulate fire conditions. The numerical simulations captured heat transfer behavior, displacement trends, and thermomechanical responses observed during laboratory tests, underscoring their robustness and applicability for real fire scenarios. The integration of experimental and numerical approaches provided a reliable framework for understanding the fire performance of sandwich panels and enabled the extrapolation of results to a wide range of fire scenarios.

The outcomes of this research have primarily contributed to a general understanding of the complex thermal and mechanical behavior of sandwich panels under the influence of fire actions. By analysing the influence of material properties, wall dimensions, as well as the effects of boundary conditions on the structural behavior, significant insights into fire-induced deformations and material interactions have been

gained. Furthermore, the study highlights the importance of cohesive behavior in thermomechanical analysis, particularly in capturing delamination and material separation under thermal stress.

By bridging theoretical knowledge with practical applications, this investigation advances the understanding of fire behavior in sandwich panels and provides actionable insights for improving their resilience under fire conditions. The findings have far-reaching implications for fire safety engineering, structural design, and regulatory frameworks, offering a robust foundation for future innovations in materials science and construction technology.

## Streszczenie

Rozwój temperatury i zachowanie paneli warstwowych w warunkach pożaru zostało szczegółowo przeanalizowane przy zastosowaniu metodologii łączącej badania eksperymentalne z modelowaniem numerycznym. Celem przeprowadzonych badań było określenie wpływu właściwości wełny mineralnej stanowiącej wypełnienie rdzenia, warstw adhezyjnych, geometrii oraz warunków brzegowych na odporność ogniową paneli warstwowych. Przeprowadzono kompleksowy przegląd literatury w celu identyfikacji istniejących luk badawczych oraz opracowania podstaw metodyki eksperymentalnej i numerycznej. Badania eksperymentalne objęły zarówno scenariusze pożarowe w małej, jak i dużej skali, dostarczając cennych danych dotyczących dyfuzyjności cieplnej, anizotropii termicznej oraz właściwości mechanicznych rdzeni z wełny mineralnej.

Wyniki testów w małej skali wykazały istotny wpływ właściwości wełny mineralnej na odporność ogniową paneli warstwowych. Anizotropowa dyfuzyjność cieplna wełny mineralnej została zidentyfikowana jako kluczowy parametr warunkujący zarówno izolacyjność, jak i integralność strukturalną zależną od gradientu temperatury pomiędzy okładzinami płyt. Badania w dużej skali ukazały wpływ konfiguracji geometrycznych, konstrukcji złączy oraz warunków brzegowych na ogólną odporność ogniową i trwałość konstrukcji. Eksperymenty te stanowiły istotne punkty odniesienia do walidacji symulacji numerycznych.

Modele elementów skończonych zostały opracowane z wykorzystaniem oprogramowania ABAQUS, uwzględniając właściwości materiałowe, złożone interakcje termomechaniczne oraz zaawansowane modelowanie interfejsów celem symulacji warunków pożarowych. Symulacje numeryczne odzwierciedlały zachowanie w zakresie przewodzenia ciepła, trendy przemieszczeń oraz reakcje termomechaniczne obserwowane w trakcie testów laboratoryjnych, podkreślając ich wiarygodność oraz przydatność w rzeczywistych scenariuszach pożarowych. Integracja podejścia eksperymentalnego i numerycznego umożliwiła stworzenie rzetelnego modelu służącego do analizy zachowania paneli warstwowych w warunkach pożaru oraz ekstrapolację wyników na szerszy zakres sytuacji pożarowych.

Wyniki przeprowadzonych badań przyczyniły się w głównej mierze do pogłębienia ogólnego zrozumienia złożonego zachowania termicznego

---

i mechanicznego paneli warstwowych pod wpływem działania temperatur pożarowych. Poprzez analizę wpływu właściwości materiałowych, wymiarów ścian oraz efektów warunków brzegowych na zachowanie przemieszczeń uzyskano istotne informacje dotyczące deformacji będących skutkiem rozwoju pola temperatury wewnątrz struktury oraz interakcji materiałowych. Ponadto wykazano znaczenie konieczności stosowania kompleksowego podejścia w analizie termomechanicznej, w szczególności w odniesieniu do odwzorowania zjawisk delaminacji oraz separacji materiałów pod wpływem naprężeń termicznych.

Poprzez połączenie teorii z zastosowaniami praktycznymi, przeprowadzone badania przyczyniły się do rozwoju wiedzy na temat zachowania ogniowego paneli warstwowych oraz dostarczyły praktycznych wniosków służących zwiększeniu ich odporności ogniowej. Uzyskane rezultaty mają szerokie implikacje dla inżynierii bezpieczeństwa pożarowego i projektowania konstrukcji, stanowiąc solidną podstawę dla przyszłych innowacji w dziedzinie nauki o materiałach oraz technologii budowlanych.



## Table of contents

<b>Nomenclature.....</b>	<b>11</b>
<b>Chapter 1. Introduction .....</b>	<b>12</b>
1.1 Background .....	12
1.2 Gap of knowledge and hypotheses .....	14
1.3 Research objectives .....	16
1.4 Motivation .....	17
1.5 Layout of the research .....	17
<b>Chapter 2. Literature review .....</b>	<b>19</b>
2.1 Sandwich panels .....	19
2.2 Fire behavior of sandwich panels .....	22
2.3 Fire testing methods and evaluation .....	29
2.4 Material behavior at elevated temperature .....	31
2.4.1 Thermal properties of mineral wool at elevated temperatures .....	38
2.4.2 Thermal diffusivity of porous materials .....	42
2.5 Thermomechanical modelling of sandwich panels .....	46
2.6 Summary of literature review .....	49
<b>Chapter 3. Experimental and numerical investigation on the thermal properties of mineral wool.....</b>	<b>50</b>
3.1 Introduction .....	50
3.2 Experimental setup on mineral wool at elevated temperature .....	50
3.3 Calculation method for thermal diffusivity .....	51
3.4 Experimental procedure .....	52
3.5 Results .....	53
3.5.1 Experimental results .....	53
3.5.2 Thermal diffusivity results.....	54
3.6 Validation Procedure.....	60
3.7 Summary and conclusion .....	62
<b>Chapter 4. Experimental and numerical investigation on thermal behavior .....</b>	<b>64</b>
4.1 Introduction .....	64

---

4.2 Experimental setup for fire resistance testing .....	64
4.3 Experiments of large-scale fire resistance tests.....	72
4.4 Numerical modelling of thermal behavior .....	75
4.5 Thermal analysis results .....	77
4.5.1 Experimental results .....	77
4.5.2 Numerical results.....	83
4.6 Summary and conclusions.....	88
<b>Chapter 5. Thermomechanical evaluation and finite element analysis.....</b>	<b>90</b>
5.1 Introduction .....	90
5.2 Deformation of sandwich panels.....	90
5.3 Parameters considered for thermomechanical analysis.....	97
5.4 Numerical modelling of thermomechanical problem.....	102
5.4.1 Analysis of panels displacement under thermal and boundary effects .	104
5.4.2 Modelling methodology and numerical simulation framework.....	110
5.4.3 Model configuration and graphical representations .....	120
5.5 Numerical and experimental displacement results .....	126
5.6 Summary and conclusions.....	139
<b>Chapter 6. Conclusions .....</b>	<b>141</b>
<b>Literature .....</b>	<b>145</b>
<b>List of figures .....</b>	<b>154</b>
<b>List of tables .....</b>	<b>159</b>
<b>Appendix A. Thermal response of mineral wool.....</b>	<b>160</b>
<b>Appendix B. Thermal response of large-scale sandwich panels .....</b>	<b>171</b>
<b>Appendix C. Large-scale fire resistance experiments.....</b>	<b>174</b>

## Nomenclature

### Latin symbols:

$C_p$	specific heat capacity,
$q$	the internal heat generation per unit volume,
$t$	time,
$x, y, z$	spatial coordinates,
$K_{nn}$	the normal stiffness,
$K_{ss}$	the first tangential stiffness,
$K_{tt}$	the second tangential stiffness,
$D$	damage variable.

### Greek symbols:

$\lambda$	thermal conductivity (as a function of spatial coordinates $(x, y, z)$ ),
$\theta$	temperature,
$\alpha$	thermal diffusivity,
$\rho$	density,
$\rho/\rho_{20}$	relative density,
$\delta_{nn}$	normal separation,
$\delta_{ss}$	first tangential separation,
$\delta_{tt}$	second tangential separation,
$\delta_0$	separation threshold being a criterion for damage initiation,
$\delta_{eff}$	effective separation,
$\delta_f$	final effective separation,
$T_{nn}$	normal traction,
$T_{ss}$	first tangential traction,
$T_{tt}$	second tangential traction.

### Generally used superscripts:

$t+1, t-1$	time indices representing future or past time steps, respectively,
$i+1, i-1$	spatial indices representing neighbouring nodes, respectively.

## **Chapter 1. Introduction**

### **1.1 Background**

One of the definitions of a sandwich panel is found in the European standard EN-14509 [1]. According to this standard, a sandwich panel typically consists of two thin "face sheets" made from strong, stiff materials such as metal or fibre composite, bonded to a thick, lightweight insulating material called the "core". The faces are adhesively bonded to the core to facilitate load transfer between the components.

Sandwich panels began to be used in aeronautical applications during World War II, particularly in small planes. In the 1930s, England and the United States pioneered the use of bonded sandwich composites, leading to a revolutionary production process. By the late 1940s, theoretical advancements in sandwich panel construction had progressed significantly. Today, sandwich panels are widely used due to their numerous advantages. In recent years, they have been employed as structural components in industrial and office buildings across Europe, Africa, and the USA. Their application has now extended to residential building construction due to their ability to enhance thermal performance and occupant comfort.

In many cases, sandwich panels can be self-supporting, meaning they can bear loads through their structural composition. They are fixed to spaced structural supports, transmitting all applied loads (e.g., snow, wind, internal air pressure) to these supports. The utilization of sandwich panels in construction could as well, require consideration of thermal actions, include uniform temperature changes, causing predictable expansion or contraction, temperature gradients, leading to uneven expansion and internal forces and stresses, and cyclic temperature changes, which can result in material fatigue over time. These actions arise from environmental factors like solar radiation and seasonal changes, operational factors such as machinery-induced heating or cooling, and accidental events as fires, explosions, or thermal shocks. In this work, fire actions are the main factors considered.

As mentioned earlier, sandwich panels consist of two thin metal sheets with an inner core of insulation, which can be either combustible or non-combustible. The metal can delay ignition but still transfer heat to the core. Common core materials used in sandwich panels include EPS (Expanded Polystyrene), XPS (Extruded Polystyrene), PUR

(Polyurethane), PIR (Polyisocyanurate), and PF (Phenolic Foam). The fire behavior of these materials involves characteristics such as ignition, flame spread, heat release rate, toxicity, and the occurrence of building debris. Therefore, nowadays sandwich panels with the mineral wool core gain popularity, as non-combustible material. Using this type sandwich panels results in the lower fire risk of the whole building assembly.

Fire development can be divided into three global phases: growth, fully developed, and decay, as shown in Figure 1. Understanding these phases is crucial for assessing the behavior of sandwich panels under fire conditions. While a brief overview is provided below, a more explanations can be found in the review section.

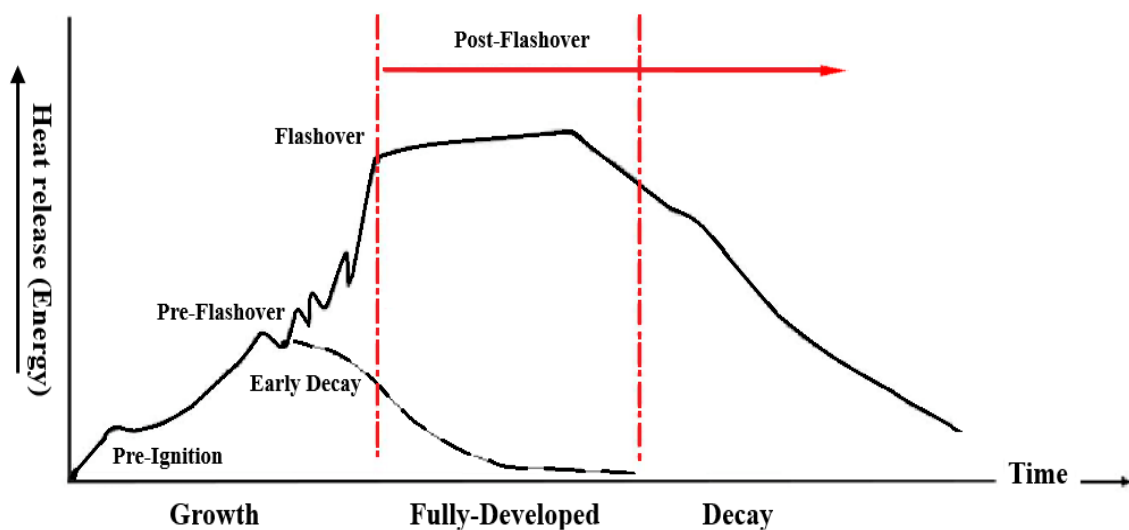


Figure 1. Development of fire.

There is a significant risk to life safety in both pre- and post-flashover phases of building fires. On average, approximately 44,300 fire deaths occurred annually between 1993 and 2015 [2]. The first phase of fire development includes pre-ignition (smouldering), where the stage of ignition is small, and the heat is relatively low. This phase ends when volatile combustion products ignite. The second phase, the fully developed phase, begins with flashover, where all combustible materials suddenly become involved in the fire. The final decay phase is characterized by a lowering of combustion gas temperature while the remaining small amount of fire load is consumed.

The property of fire resistance becomes particularly important after flashover occurs. In this case, fire resistance tests measure the panel's ability to isolate the fire to the area of ignition when exposed to a fully developed fire for a specific time. Fire resistance is defined by the ability of a construction element to resist collapse, prevent the

penetration of flames and hot gases while maintaining structural integrity, and keep unexposed faces sufficiently cool [3]. In other words, the fire resistance is defined as the ability of the materials, product, assembly, or structure to fulfil the required stability, integrity, thermal insulation, and/or other requirements from the standards of fire resistance tests for a specific period.

In Europe, there are numerous fire test methods for sandwich panels, such as ISO 13784-2:2020 [4] (Reaction-to-fire tests for sandwich panel building systems), EN 1364-1 [5] (non-loadbearing walls), EN 1364-2 [6] (non-loadbearing ceilings), and prEN 13381-1 [7] (horizontal membranes). These standards aim to provide a comparative evaluation of products under conditions related to reality rather than predict actual performance in practice.

Using sandwich panels involves classifying them based on their fire resistance performance as specified by 'European Recommendations for Sandwich Panels,' considering mechanical action, smoke production, and heat control. Numerous studies have investigated the fire behavior of sandwich constructions and developed rational design procedures. However, not all aspects of fire design are well understood, indicating the need for further research to examine the fire behavior of these panels, evaluate current design procedures, and develop new rules to address challenges faced by designers and manufacturers.

## **1.2 Gap of knowledge and hypotheses**

Sandwich panels are extensively used in the construction of walls, roofs, enclosures of industrial equipment, and more. Their application scope is broad due to their excellent strength-to-weight ratio and insulation properties. When investors utilize sandwich panels for construction, the passive and active fire protection measures are often more stringent than general life safety regulations. These fire precautions aim to reduce damage to the building, and it is contents, not only during the evacuation period (the primary concern of life safety regulations) but also afterward, when additional fire damage may occur. One of the critical and challenging issues regarding sandwich panels is modeling their structural behavior under fire conditions.

Recent scientific studies have explored various aspects of sandwich panel behavior at elevated temperatures. Despite these efforts, several key issues remain inadequately addressed. The following points outline the gap of knowledge.

---

- Lack of Comprehensive Standards

The European Recommendations for Sandwich Panels is currently the only widely recognized document available for their design and testing, primarily addressing panels with metal face sheets and standard core materials. However, the tests required to evaluate fire behavior vary significantly between countries in terms of fire safety standards and how they approach fire performance testing. While many standards aim to achieve the same goal, evaluating the fire safety of materials and systems—their methodologies, testing conditions, and classification systems often differ. These variations arise from differences in regional building codes, safety philosophies, and historical development of standards. For instance, Europe relies on the EN 13501-1 [8], while the United States employs standards as ASTM E84 [9] and NFPA 286 [10], leading to non-comparable outcomes. Consequently, these disparities hinder the global certification of products and limit their applicability in international markets. A harmonized framework that accommodates diverse materials and innovative configurations is essential to address these inconsistencies and ensure the safe and efficient use of sandwich panels worldwide.

- Insufficient Understanding of Core Material Behavior in Fire Conditions

There is limited knowledge about the thermal response and diffusivity of core materials used in sandwich panels when exposed to elevated temperatures. This gap necessitates experimental investigations to measure these properties and their impact on overall fire performance.

- Lack of Comprehensive Data on Large-Scale Fire Behavior

Existing studies often rely on small-scale tests, simplified conditions, or different core material, which may not fully represent the behavior of sandwich panels in large fire scenarios. A need exists for large-scale fire tests with the same composite material, but with different panel wall assemblies to assess horizontal displacement, thermal behavior, and overall fire resistance under realistic conditions.

- Research Gaps

Many critical aspects of sandwich panel behavior under fire conditions, such as the early-stage delamination between the core and facing material during the

initial heating phase in fire testing scenarios, remain insufficiently explored, which provides significant gaps in understanding the structural integrity and thermal performance of these panels under fire exposure. Additionally, when it comes to modeling of sandwich panel in fire, the definition of interaction properties in finite element modelling (FEM) is rarely explained. Addressing these gaps is crucial for developing reliable design for sandwich panel.

The proposed research aims to thoroughly investigate the structural behavior of sandwich panels under fire conditions. This research will help achieve design recommendations, which may a significant contribution to the construction industry. In the context of above observation, the following hypotheses were formulated:

- **Prediction of Fire Resistance**

Based on material tests, known geometrical properties, and technological solutions, it is possible to predict the fire resistance of sandwich panels and to extrapolate the fire test with varying the boundary condition.

- **Influential Parameters**

It is possible to specify a group of parameters that significantly affect the fire resistance of sandwich panels.

By addressing these hypotheses, the research will contribute to a deeper understanding of the fire resistance of sandwich panels and provide practical insights for improving their design and safety in construction applications.

### **1.3 Research objectives**

The aim of the research is to explain and predict the behavior of sandwich panels subjected to fire temperatures and to determine the influence of material properties, geometric properties and boundary conditions on this behavior. This will be accomplished by employing a systematic approach that includes a literature review, laboratory tests to measure thermal performance at elevated temperatures and to assess material behavior. Numerical models using finite element analysis will be developed and compared with experimental data. Large-scale fire tests will be examined to evaluate the overall fire resistance of the panels. The literature review will involve an examination of existing



research to identify current trends, knowledge gaps, and critical issues related to the fire behavior of each of the composite materials, with a focus on their response at elevated temperatures and their fire resistance. Experimental investigations will include the performance core material – the mineral wool (MW). Small-scale tests will be conducted to evaluate the changes due to the temperature of the thermal diffusivity, its load-bearing capacity, and the bonding strength to the metal sheets. Large-scale fire tests with different boundary conditions will be analyzed to assess the overall fire behavior, structural integrity, and insulation performance of sandwich panel walls under realistic fire scenarios, and the results of these tests will be compared with numerical simulations to confirm the applicability of the models in practical situations. Numerical investigations will involve the development of several models using the finite element analysis software ABAQUS to simulate the thermal and mechanical behavior of sandwich panels under fire conditions. The comparison of the numerical models with experimental data will be carried out to ensure the influence of parameters and the reliability of the simulations.

#### **1.4 Motivation**

The importance and motivation of this research lies in its potential to influence fire safety regulations and contribute to advancements in the construction industry. The growing demand for safer, energy-efficient, and sustainable construction materials has highlighted the importance of sandwich panels due to their lightweight, insulating, and cost-effective properties. Despite these advantages, their behavior under fire conditions remains a significant concern, especially given the serious consequences of structural failures during fire incidents. Understanding the response of core materials, such as mineral wool, to elevated temperatures is critical for advancing fire safety standards and enhancing the reliability of these materials in practical applications. Addressing these challenges emphasizes the value of exploring this topic further and highlights its significance in both scientific and practical contexts.

#### **1.5 Layout of the research**

The behavior of sandwich panels under fire conditions is presented in this research across six chapters. The contents of each chapter are described as follows. Chapter 1 introduces sandwich panels, including their areas of application, various fire behaviors,

and design aspects. It defines the problem addressed in this research, outlines the hypotheses, and states the overall and specific objectives of the study.

Chapter 2 presents a general overview of fire behavior, and a summary of the current literature related to the behavior of sandwich panels at elevated temperatures. The structure and composition of sandwich panels, their thermal and mechanical responses to fire, and testing methods are explored. Additionally, the review addresses material behavior at elevated temperatures, particularly the thermal properties and diffusivity of core materials such as mineral wool as a porous medium, alongside thermomechanical modelling approaches used for predicting performance under fire exposure. The results of the literature review clarify the aims, assumptions, and directions of this research.

Chapter 3 focuses on the thermal properties core material of sandwich panels, specifically those made with mineral wool. The experimental setup used to determine thermal diffusivity and heat transfer behavior of mineral wool is described, including the reduction of a three-dimensional problem to a one-dimensional heat analysis. The chapter presents the results of the experiments, including the calculated diffusivity of the core material, and discusses the findings through a validation procedure.

Chapter 4 outlines the fire tests conducted to evaluate the thermal response of sandwich panel walls made with a mineral wool. Laboratory test methods and the thermal response of each specimen evaluated are explained, along with numerical studies performed to simulate the thermal behavior. The results and findings from these tests are discussed in detail, providing insights into the fire resistance capabilities of the panels with different geometries and solutions.

Chapter 5 investigates the thermomechanical behavior of mineral wool sandwich panels under fire actions using a finite element model. The model captures displacement trends and the effects of thermal gradients and mechanical load transfer, providing relevant findings on the structural response of sandwich panels under fire configurations. The chapter concludes with findings and offering a foundation for advancing predictive capabilities and enhancing structural resilience in future studies.

Chapter 6 summarizes the main conclusions drawn from the research. The fire behavior of sandwich panels, the thermal properties of the composite materials, and the validation of the finite element method simulations are reviewed. Recommendations for further research and improvements to the fire resistance of mineral wool panels are also provided.

## Chapter 2. Literature review

### 2.1 Sandwich panels

Sandwich panels have been used since ancient times in construction operations, but they have developed greatly in recent years and have received great and growing interest from individuals, companies, government agencies and factories as cladding for buildings and a great deal of the research and development of this product. Therefore, there are many types of these panels that have many uses. They offer advantages as it leads to structures that are: lightweight, cost effectiveness and durability.

The sandwich panel, as described previously, is a composite structure of layered materials (Figure 2) which comprises outer facings of rigid material (usually sheet metal) and an adhesively bonded lightweight core material(s) which provides the insulation and other mechanical properties. In general, cores fall into two groups: the homogeneous and the structured cores. As it is illustrated in Figure 3 and described below.

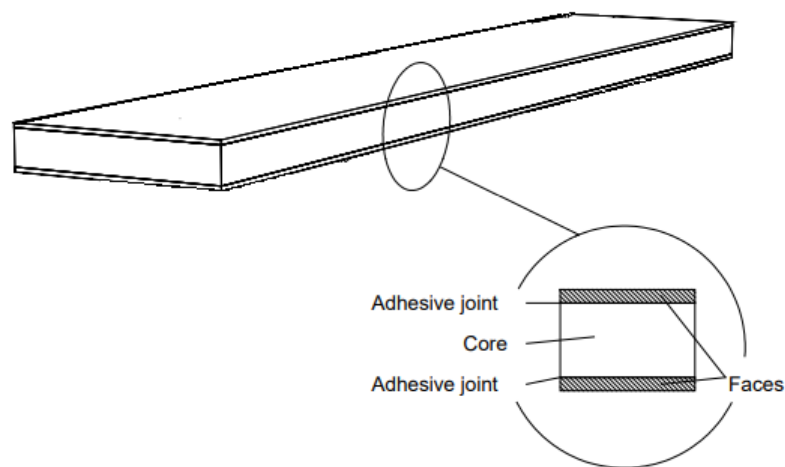


Figure 2. Graphical decomposition of structural sandwich panel.

- Face Sheets

Metal face sheets, such as steel or aluminum, offer integrity and can delay the ignition in the case of combustible core material. They provide a barrier to heat and flames, contributing to the overall fire resistance of the panel.

- Core material

A lightweight material providing insulation and other mechanical properties, either homogeneous (e.g., foam cores) or structured, can be either combustible or

non-combustible regarding fire behavior. Combustible cores, such as Expanded Polystyrene (EPS), Extruded Polystyrene (XPS), Polyurethane (PUR), and Polyisocyanurate (PIR), can contribute to the fire load. However, their fire performance can be enhanced using fire retardants and proper encapsulation. Non-combustible cores, such as mineral wool (MW) and other non-combustible materials as glass wool, calcium silicate, and foamed glass. Such material provides superior fire resistance, as they do not contribute to the fire load and can withstand elevated temperatures without significant degradation.

- Adhesive Layer

The adhesive used to bond the face sheets to the core must maintain strength at elevated temperatures to prevent delamination and ensure the panel's structural integrity during a fire.

The production of sandwich panels involves several key steps. First step, materials are selected: face sheets and core materials. Foam cores are created using a chemical reaction, while mineral wool is made by melting and spinning raw materials into fibers. The process moves on to preparation and assembly, where each component is readied and brought together. Facings are precisely cut and shaped, sometimes through roll forming, to achieve the desired dimensions and profiles that enhance performance. Core materials are also processed to meet exact thickness and density specifications, ensuring uniformity. During assembly, the core is carefully positioned between the facings, and specialized adhesives are applied to bond the layers. The type of adhesive and its application is critical, as they directly affect the panel's strength and durability, depending on the intended use. This step is conducted with great precision to ensure the layers are aligned and securely bonded [11]. Finally, the pressing and finishing stages bring the panels to completion. The assembled components are subjected to heat and pressure to cure the adhesive, creating a uniform, durable bond. After curing, the panels are trimmed to exact dimensions and may receive additional treatments like sanding, painting, or protective coatings to enhance their appearance and resistance to wear. Rigorous quality control checks are conducted to confirm that each panel meets industry standards before being packaged and distributed. This thorough process ensures sandwich panels deliver a combination of strength, insulation, and lightweight properties, making them indispensable in various applications [11].

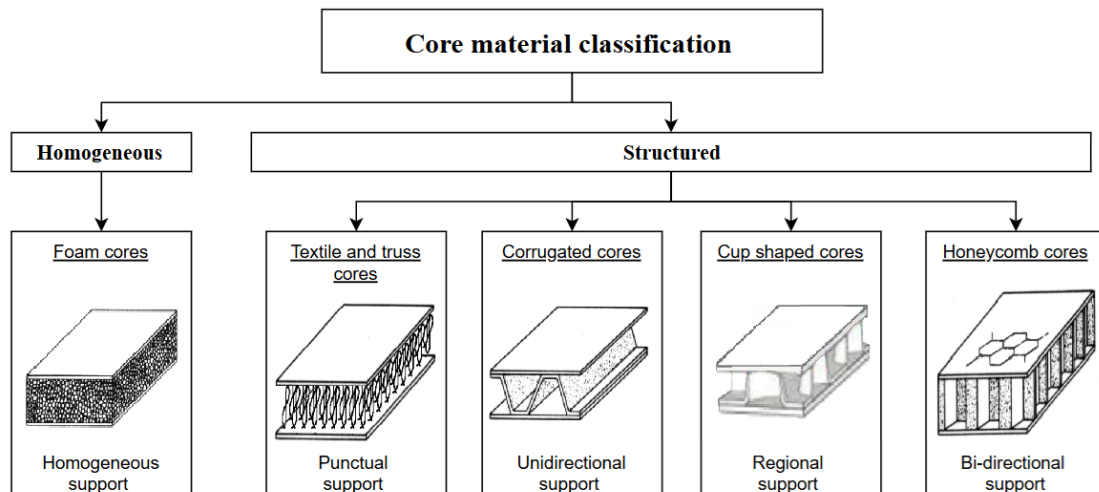


Figure 3. Core material classification of homogeneous and structured sandwich panels.

Providing good fire resistance is a key performance requirement for sandwich panels, especially when buildings require mitigation of the fire risk. Recent advancements in homogeneous core materials used in sandwich panels have significantly improved their fire performance. Figure 4 presents an example of how sandwich panels are used for industrial construction.



Figure 4. Example of homogeneous sandwich panel used for industrial construction.

Ensuring the fire resistance of sandwich panels involves addressing several challenges and considerations, particularly focusing on their thermal properties. Structurally, it is essential that these panels maintain their load-bearing capacity during a fire, which requires a deep understanding of how materials behave at elevated

temperatures and a careful design of the panel's structural configuration. The thermal properties of insulation materials are crucial as they directly influence the effectiveness of the panels in fire conditions. Effective thermal insulation helps in slowing down heat transfer, which is vital for maintaining structural integrity during a fire.

## **2.2 Fire behavior of sandwich panels**

Reviewing sandwich panels in fire conditions is essential to understand fire behavior. Different fire phases require specific considerations for material properties such as ignitability, combustibility, and heat release rate. Nominal fire curves as the ISO 834 standard fire curve [12], hydrocarbon fire curve, and parametric fire curves model the temperature-time relationship during fire exposure. The ISO 834 curve serves as a benchmark for structural fire resistance, while the hydrocarbon fire curve represents more severe conditions typical in petrochemical fires. Parametric fire curves offer tailored assessments based on variables such as ventilation and fuel load.

Fire is a chemical reaction that produces energy in the form of heat light inflamed and rapid and self-sustaining. It requires combustible fuel, a source of heat and oxygen. Fires behave differently that concludes some burn slowly and steadily; others are extremely hot and burn extremely hard. Different lights have different flames, some fires start easily, others do not, and some fires could produce a deadly toxic gas. The major of fire deaths arise because of inhalation of smoke produced by burned material. The behavior of the fire also depends on the combustible substance that provides energy [3].

The structural designer during the modulization of the fire protection system has required an understanding of fire behavior as relates to the fire hazard present. The fire hazard is the hazard load, and it is affected by several things such as occupancy and use conditions, materials present within the building, products...etc. and [13] defined fire hazard as a fuel complex, defined by volume, type, condition, arrangement, and location that determines the degree of ease of ignition and the resistance to control. Fire hazard expresses the potential fire behavior for a fuel type, regardless of the fuel type's weather-influenced fuel moisture content.

When attempting to assess the behavior of sandwich panels in the fire, it is helpful to understand firstly how the fire behaves and the way how the fire develops. The fire developed and evolved through a series of specific stages or phases as shown in Figure 5. The first stage is the incipient stage or the growth phase when still the heat production

small, in this stage it is very important to take into consideration all proprieties such as ignitability, combustibility, the rate of heat release, smoke, the flame spread of any material, because are quantified during fire test for a small scale. The second stage of fire development is the free burning stage or fully developed phase after ignition fire survives by consuming air and material which become suddenly involved in the fire. This leads to an increase in the combustion gas temperatures to above  $650^{\circ}\text{C}$  and a sudden increase in the radiation emitted by the fire. A comprehensive discussion on fire development and its characterization can be found elsewhere in the literature [14]. The temperatures in the fully developed phase can exceed  $1000^{\circ}\text{C}$ . During this stage, fire can cause significant degradation in strength and stiffness properties of structural materials (concrete, steel, and wood, etc.) [15]. Here the fire resistance and non-combustibility of the sandwich panels are especially important after flashover occurs. The final stage is the decay or smouldering phase, which is characterized by a lowering of combustion gas temperature with a small amount of fire load. This phase occurs when the available fuel is exhausted, or the oxygen level drops below 16%.

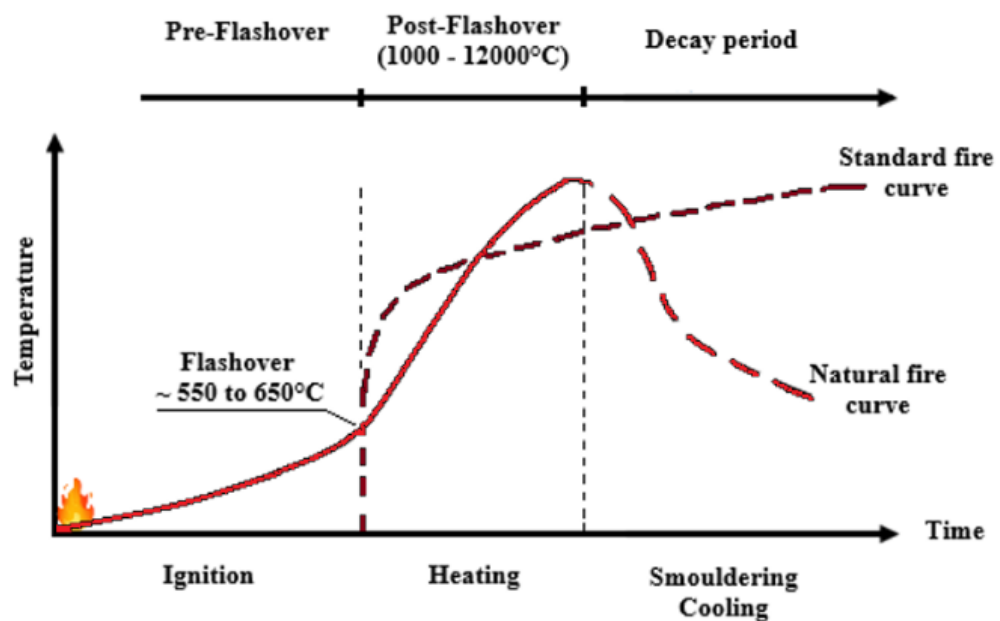


Figure 5. Evolution curve of fire behavior.

For modelling fire, the simplest approach is to use nominal fire curves (ISO 834, hydrocarbon, parametric), which represent the evolution of gas temperature as a function of time:

- ISO 834 standard fire

Conventional fire is characterized by an ambient temperature which increases continuously over time but with a growth rate. A logarithmic curve is used in the laboratories to model fire. The fire resistance duration value does not indicate the actual length of time a component resists in a building fire. It constitutes a comparison indicating the severity of a fire which the component can withstand. The temperature evolution as a function of time in accordance with the ISO 834 standard is presented in Table 1, which illustrates the corresponding temperature values at specific time intervals under standard fire exposure conditions.

Table 1. Time-temperature values for the ISO 834 curve.

Time [min]	Temperature [C°]
0	20
5	576
10	678
15	739
30	842
60	945
90	1006
120	1049
180	1110
240	1153
300	1186
360	1214

The equation governing this time-temperature relationship, commonly referred to as the cellulosic fire curve, is defined by the ISO 834 standard and is given by Equation 2.1:

$$\theta_f = \theta_{\text{initial}} + 345 \log_{10} (8t + 1). \quad (2.1)$$

This logarithmic function captures the rapid initial rise in temperature followed by a progressively slower increase, characteristic of compartment fires under controlled test conditions. To visually represent this time-temperature relationship, Figure 6 illustrates the curve as defined by Equation 2.1, corresponding to the data presented in Table 1.



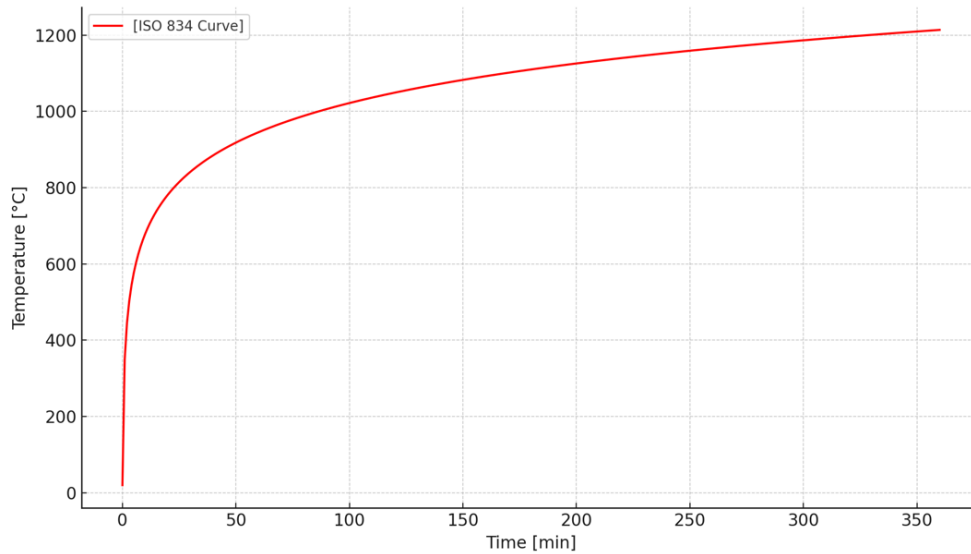


Figure 6. Time-temperature curve of the ISO 834 standard.

#### ■ Hydrocarbon fire

The hydrocarbon fire, or pool fire, is a fire fuelled by compounds of hydrocarbons such as oil and gas. In the 1970s, the oil company Mobil developed a standardized procedure to evaluate the fire performance of materials exposed to hydrocarbon-based fires. This procedure characterizes a rapid temperature rise, with temperatures reaching approximately 900°C within the first 5 minutes, eventually stabilizing around 1000°C. The time-temperature relationship for hydrocarbon fires is defined by Equation (2.2):

$$\theta_h = 20 + 1080 (1 - 0,325 \times e^{-0,167t} - 0,675 \times e^{-2,5t}). \quad (2.2)$$

The temperature-time curve corresponding to Equation (2.2) is illustrated in Figure 7. As observed, the curve rises sharply and reaches near-maximum temperatures within a few minutes, reflecting the severe thermal conditions typical of hydrocarbon fires.

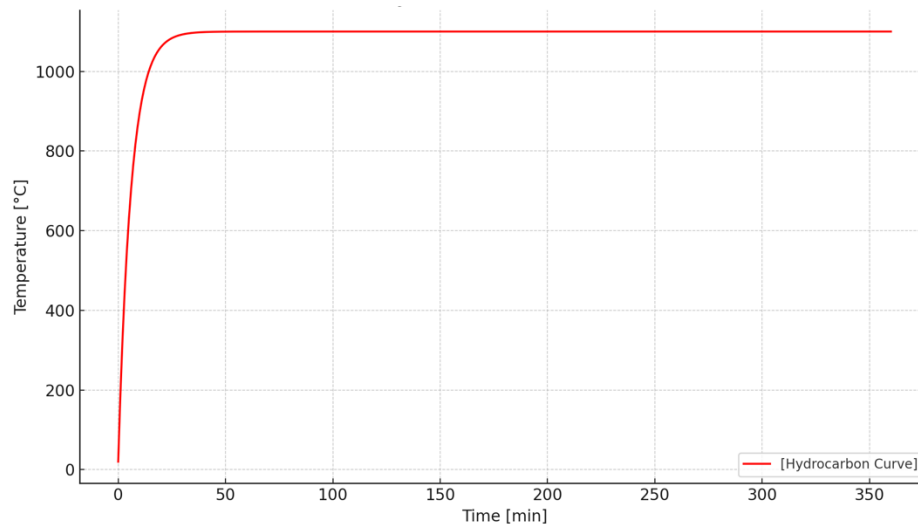


Figure 7. Time-temperature of hydrocarbon curve.

#### ■ Parametric fire

Parametric fires provide a straightforward method to incorporate key physical phenomena that can influence fire development in specific elements. Like the above nominal fires, they involve determining a time-temperature curve. However, parametric fire curves consider certain parameters to idealize aspects of reality [3]. These fires assume uniform temperature distribution within the compartment, which limits their applicability to "flashover" conditions in moderately sized compartments.

From the behaviors described above, reactions to fire properties are important and desirable, wherever possible, to reduce the number of combustibles involved in fire with specific materials. In metal-faced sandwich panels, the core can be either combustible or non-combustible, significantly influencing the panel's reaction and protective capabilities. The facing of these panels serves critical fire and heat protection functions, depending on their insulation and integrity performance. Using a combustible core as polymers (e.g. polyurethane, polystyrene), it is possible to obtain a useful period using sandwich panels up of 30 minutes as an adequate time for people to escape, on another hand when using a non-combustible material as rock wool or mineral wool cores, panels can exceed 2 hours as time of resistance against fire [16]. It has been demonstrated that walls constructed using sandwich panels with expanded polystyrene (EPS) cores exhibit significantly lower thermal insulation performance when compared to those utilizing mineral wool (MW) or polyisocyanurate (PIR) cores [17]. By careful selection of

materials and installation of whole panels system will result in good resistance when the panel is exposed to fire.

The fire resistance of sandwich panels may be defined as the ability of whole element to fulfil, for a stated period of time, the required stability, and/or other expected duties specified in the standard of fire tests.

When testing the fire resistance of sandwich panels according to European standards as EN 1364-1 [5], the panels are exposed to a standard fire curve and their performance is evaluated against specific criteria, including thermal insulation, integrity, and load-bearing capacity (cf. Figures 8 and 9). These parameters are critical for assessing the ability of sandwich panels to act as effective fire separating elements in walls, ceilings, or roofs.

The fire resistance or reactions of the building component is measured by testing in a laboratory furnace. The designs of furnaces change but the time-temperature curve of the combustion gas is standardized and most countries using it, which is described in ISO-834 standard [4], and it is related to equation (2.2).

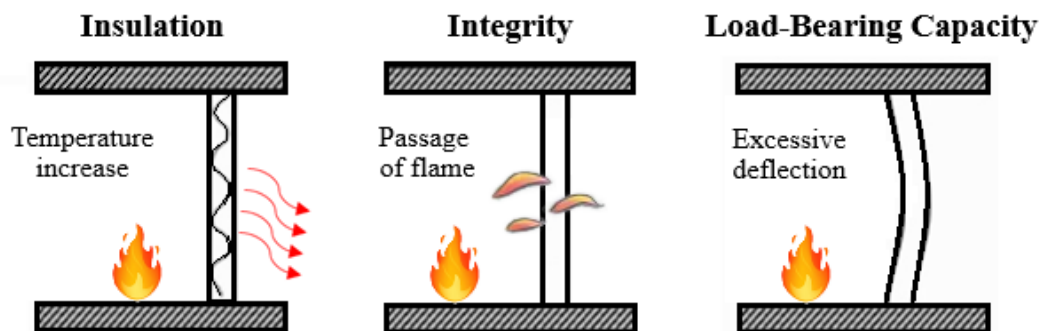


Figure 8. The concept of fire resistance test on wall specimens.

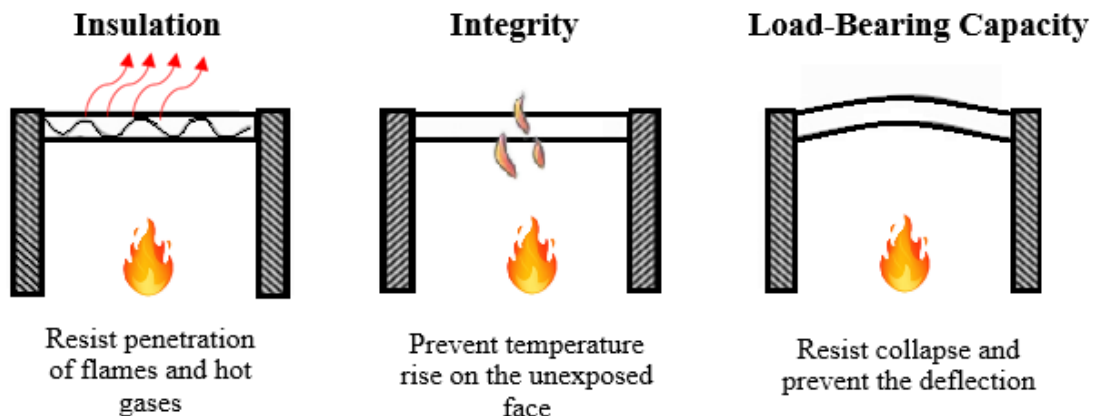


Figure 9. The concept of fire resistance test on roof and ceiling specimens.

In general, as illustrated in Figure 10, the progressive structural behavior of sandwich panels exposed to one-sided fire is presented, as outlined in EN 15254-5 [18]. This includes the early occurrence of delamination (typically occurring within the first five minutes), which significantly compromises structural integrity. The standard describes this behavior, emphasizing that there is a risk that these panels may become unable to support even their own weight over time.

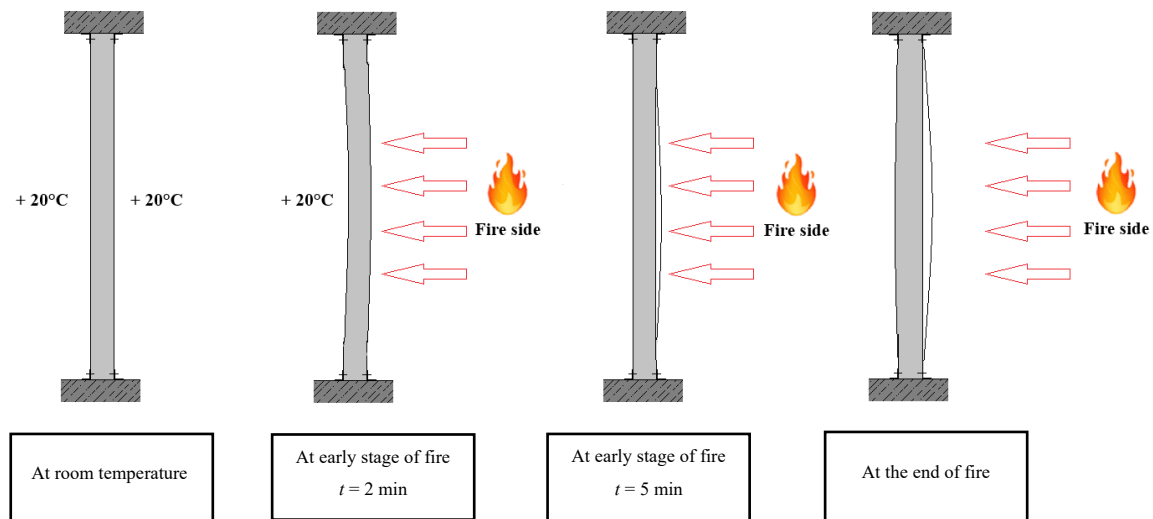


Figure 10. General aspects of sandwich panels exposed to fire according to [18].

In a fire scenario, the facing materials on a sandwich panel could potentially detach from the core material in the first minutes of heating for several reasons. One of the reasons is that the facing material, the core material, and the adhesive itself may change in their physical properties due to exposure to elevated temperatures. If we are talking about material properties, facing materials and core material may have different conductivity and different coefficients of thermal expansion. As it is known, the rapid heating of materials can lead to thermal expansion, potentially causing delamination or detachment. Another reason for the phenomenon of detachment is if the adhesive used is not fire-resistant or if temperatures exceed the specified limits to maintain effective adhesion. In that case, adhesive automatically loses its strength at elevated temperatures, leading to detachment.

For instance, the study of [19] emphasizes that delamination and related face instabilities are critical factors influencing the structural response of sandwich panels in fire scenarios. Additionally, [20] discusses the complex behavior of sandwich panels under fire conditions, noting that delamination can lead to significant reductions in load-bearing capacity and overall structural performance.

The detachment of facing materials from core material (e.g., mineral wool) insulation in a fire scenario can have a significantly influence on the thermal and mechanical behavior of a structure. This influence becomes particularly significant when gaps occur or if the elements are no longer in place to absorb, reflect, or block heat. Such occurrences can lead to several impacts. Firstly, there is an increase in thermal resistance as the gap introduces an obstacle to heat transfer between facing and core materials, resulting in reduced overall thermal conductivity and a higher temperature gradient across the panels. In the context of heat transfer studies, the occurrence of a gap between the face material and the core material rises to several consequences as was mentioned above. It becomes evident that the results of heat transfer calculations can be significantly impacted by the existence or absence of detachment in this case. It emphasizes how crucial it is to make sure that these materials are connected to getting precise and reliable findings from heat transfer analyses.

### **2.3 Fire testing methods and evaluation**

Different standards for evaluating the fire behavior of walls share common parameters such as fire exposure scenario, specimen geometry and shape, type of fire load, fire flux, and testing period. However, these parameters vary across standards, making the test results difficult to compare [21]. Fire resistance of sandwich panels is defined as the ability to maintain stability and fulfil required duties for a specified period under fire test standards. In other hand, fire resistance testing and evaluation play a crucial role in ensuring the safety and performance of building materials and structures, including sandwich panels. However, fire resistance of sandwich panels needs rigorous testing to ensure they meet safety standards. The following references offer detailed insights into fire resistance testing standards and evaluation methods for sandwich panels.

- ASTM E119-20 [22]

The standard [22] provides a detailed methodology for evaluating the fire resistance of building components, including sandwich panels. This standard involves exposing test specimens to controlled fire conditions following a standardized time-temperature curve and assessing their performance in terms of load-bearing capacity, integrity, and insulation. The performance criteria include structural stability (ability to bear loads during fire exposure), integrity (preventing

the passage of flames and hot gases), and insulation (limiting the temperature rise on the unexposed side).

- ISO 834-1:2014 [12]

The general requirements for fire resistance tests of structural elements are described in [12], as was mentioned in previous section 2.2. The mentioned standard [12] is similar to ASTM E119 [22], it uses a standard time-temperature curve to expose materials to fire and evaluates structural stability, integrity, and insulation, ensuring global applicability.

- EN 1363-1:2020 [23]

The standard [23] describes methods for assessing the fire resistance of building elements under specified conditions. It focuses on load-bearing capacity, integrity, and insulation, with specific criteria for each element evaluated.

- EN 1364-1:2015 [5]

The standard [5] provides a standardized methodology to assess the fire resistance of non-loadbearing wall assemblies. The test evaluates the wall's integrity and insulation performance under controlled fire exposure, measuring its ability to function as a thermal barrier and maintain structural separation over a specified time. This standard ensures consistent assessment criteria in fire safety engineering, supporting scientific analysis of material behavior under fire conditions.

- EN 14509:2013 [24]

The standard [24], indeed, includes testing protocols that simulate realistic fire conditions to evaluate integrity, insulation, and structural stability under fire exposure. As was mentioned, these assessments are crucial for ensuring that sandwich panels fulfil stringent fire safety criteria in construction contexts.

Standard fire resistance tests as [5, 12, 22, 23] provide essential frameworks, but there are significant limitations and challenges. One primary challenge is the realistic representation of fire scenarios. Standard tests often use idealized fire scenarios that may not accurately reflect real fire conditions, such as variability in fire dynamics, ventilation, and fuel load. This can lead to results that may not fully predict actual performance during a fire event. The studies as [25] highlight the need for advanced computational models

that can simulate fire behavior and material response more accurately. These models provide a cost-effective alternative to physical testing and can oversee a wide range of scenarios and material properties. [14] present performance-based fire safety engineering, where designs were evaluated based on their ability to achieve specific safety objectives under realistic conditions. This method allows for more flexible and innovative building designs while ensuring fire safety. In [26] hybrid testing methods that combine small-scale physical tests with advanced simulations to improve accuracy while reducing cost and complexity. Integrating data from actual fire incidents into testing and evaluation processes can enhance the reliability of tests by grounding them in practical fire dynamics and outcomes.

To address the limitations of current fire resistance testing methods, several improvements are essential. Advanced numerical simulations, such as Finite Element Analysis (FEA), can complement physical testing by modelling various fire scenarios and material behaviors, providing valuable insights into fire dynamics and structural responses. Hybrid testing approaches, which combine small-scale tests with advanced simulations, can enhance understanding of fire performance while reducing costs, bridging the gap between laboratory conditions and real test scenarios. A shift from prescriptive to performance-based standards would allow for more flexibility in evaluating fire resistance, focusing on achieving specific safety outcomes rather than strictly adhering to predefined protocols. Additionally, improved material characterization methods at elevated temperatures are crucial for better predictive modelling, as accurate data as function of temperature of thermal conductivity, specific heat, and mechanical properties are needed. Incorporating realistic fire scenarios, as varying fire loads and ventilation conditions, into testing protocols can also improve the relevance and applicability of results.

## **2.4 Material behavior at elevated temperature**

The previous sections clearly explained how the fire reaction of the substances influences the fire growth phase until ignition. In the context of sandwich panels, when subjected to an external heat source, each component material responds uniquely due to its inherent properties. These responses can profoundly impact the overall fire performance of the panel. Below, the behavior of each material at elevated temperatures is described.

- Surface coating at elevated temperature

The fire behavior of surface coating in sandwich panels are usually investigated by surface spread of flame and may be affected by adhesive layer. Surface coatings are combustible, and the small thickness which are usually used in the element means that the contribution of the coating to the fire load of a melting faces is negligible. The most important aspect of the behavior of the surface coating exposed to fire is the reaction to fire.

Commonly used coatings include Polyvinyl Fluoride (PVF), Polyvinylidene Fluoride (PVDF), and Polyester (SP), all of which are classified as non-combustible. A key fire-resistance characteristic of these coatings is the emissivity on the unexposed side, typically ranging from 0.8 to 0.95 for coated steel sheets according to EN15254-5:2018 [18]. PVDF further demonstrates high thermal endurance, characterized by a molecular weight greater than 100,000 g/mol, a melting range of 171 to 180 °C, a crystallization interval between 141 and 151 °C, and a glass transition point near -40 °C, which collectively contribute to its suitability for high-temperature applications [27].

- Face material at elevated temperature

Steel sheets, Aluminum and Aluminum alloy sheets, according to European standards, EN 13501-1 [8] and EN 1993-1-2 [28] highlight the robustness of steel sheets in fire resistance, making steel a top choice in applications requiring high fire safety. Stainless steel offers even greater fire resilience due to its alloy composition and high resistance to oxidation at elevated temperatures. Ordinary steel sheets expand at a rate of about  $14 \times 10^{-6} \text{ }^{\circ}\text{C}$  between 0 and 600°C, while stainless steel, depending on its alloying elements, expands at approximately  $19,5 \times 10^{-6} \text{ }^{\circ}\text{C}$  over a broader temperature range from 0 to 1200°C. Steel's melting point, around 1550°C, further supports its suitability in high-temperature environments as detailed in [28].

Another material sometimes used as a facing for sandwich panels is aluminum or aluminum alloy sheets, although this is uncommon. Aluminum facings are typically only selected when the core material provides excellent fire insulation, combined with high density and inherent structural strength. Pure aluminum has a melting point of approximately 660°C, while certain aluminum



alloys may have slightly lower melting points, around 600°C. In contrast, the mechanical properties of commonly used low-carbon and structural steel sheets, which are more frequently employed as facing materials, are presented in Table 2.

Table 2. Properties of common steel sheet and metallic coatings use in sandwich panel [3].

Low-carbon steel sheet EN 10142			Structural steel sheet EN 10147		
Steel grade	Yield strength <sup>a</sup> max. (N/mm <sup>2</sup> )	Tensile strength <sup>b</sup> max. (N/mm <sup>2</sup> )	Steel grade	Yield strength min. (N/mm <sup>2</sup> )	Tensile strength min. (N/mm <sup>2</sup> )
DX51D	—	500	S220GD	220	300
DX52D	300	420	S250GD	250	330
			S280GD	280	360
			S320GD	320	390
			S350GD	350	420
			S550GD	550	560
<sup>a</sup> A minimum value of 140 N/mm <sup>2</sup> may be expected					
<sup>b</sup> A minimum value of 270 N/mm <sup>2</sup> may be expected					
Available zinc coatings (EN 10142, EN 10147)					
Hot-dipped zinc	Total amount of zinc on both surfaces (g/m <sup>2</sup> )	Thickness of coating on one surface (μm)	Alloyed zinc	Total amount of zinc on both surfaces (g/m <sup>2</sup> )	Thickness of coating on one surface (μm)
Z100	100	7	ZF100	100	7
Z140	140	10	ZF140	140	10
Z200	200	14			
Z225	225	16			
Z275	275	19.5			
Z350	350	25			
Other available metallic coatings (EN 10214, EN 10215)					
Hot-dipped zinc–aluminium <sup>c</sup> EN 10214 (95% Zn/5% Al)			Hot-dipped aluminium–zinc <sup>d</sup> En 10215 (55% Al/1.5% Si/rest Zn)		
	Total amount of coating on both surfaces (g/m <sup>2</sup> )	Thickness of coating on one surface		Total amount of coating on both surfaces (g/m <sup>2</sup> )	Thickness of coating on one surface (μm)
ZA200	200	15	AZ150	150	20
ZA255	255	20	AZ185	185	25
ZA300	300	23			
<sup>c</sup> tradename <i>Galfan</i> <sup>d</sup> tradenames <i>Aluzink</i> , <i>Galvalume</i> , <i>Aluzinc</i> , <i>Zalutite</i> , <i>Algafort</i>					

The research [29] provides a detailed examination of how thermomechanical properties of S280GD+Z steel (yield strength, modulus of elasticity, thermal conductivity, thermal elongation, and specific heat) vary as functions of temperature. Recognizing the need for temperature-specific data, the researchers derived formulas that predict these properties more accurately at elevated

temperatures, ensuring more reliable structural assessments in fire scenarios. By using experimental data to develop temperature-dependent models, [29] addresses limitations in existing standards, which often overlook the nuanced effects of temperature on these properties. This approach not only enhances predictive accuracy but also aligns the analysis with real tests conditions, contributing to safer and more effective fire-resistant design in cold-formed steel structures.

- Adhesives at elevated temperature

The temperature at which an adhesive used to bond the face sheets to the core softens should ideally be as high as possible to maintain the flexural strength of the sandwich panel and prevent delamination in the event of fire. This means that the sheet on the exposed side should not detach from the core at the very beginning of the fire (ignition). In [20] was noted that the polyurethane adhesive layer in a mineral wool panel effectively “melts” around 60 °C, with a sharp drop in stiffness and strength beyond this point.

- Core material

- **Expanded and extruded polystyrene (EPS and XPS).** These are thermoplastic materials, the behavior in the fire for those materials is dominated by their unfavourable tendency to melt at a temperature less or equal to 100°C, which means that they melt before ignite and they tend to form a burning droplet. These are thermoplastic materials. Both are expanded and extruded polystyrene withdraw rapidly from flames due to melting and shrinking. Specifically, EPS begins to shrink between 70°C and 100°C, with melting occurring around 100°C [30]. Both thermoplastic materials start to decompose at 300°C and ignite at 360°C.
- **Phenolic foam (PF).** The PF is also thermosetting materials the same as Polyurethane and Polyisocyanurate, it starts to decompose between 350 and 500°C, and ignites between 530 and 580°C. During burning a stable char is formed releasing hydrocarbons and carbon monoxide.
- **Polyurethane (PUR) and Polyisocyanurate (PIR).** These are thermosetting materials, which do not melt when exposed to fire but rather from a

carbonaceous char. With good and correct chemical formula, on heating are solid typically remain solid up to a point when they melt and change to discontinues liquids. In general, when the polymer is exposed to a substantial heat flux radiated from a fire, it begins to decompose chemically to yield volatile gases, solid carbonaceous char and smoke. This process occurs by a series of chemical reactions that break down the polymer chains into low molecular weight fuel vapours that then diffuse into the flame. PUR starts to decompose at 150-200 °C and become flammable at 300°C and release toxic smoke at temperature above 600°C, and for PIR start to decompose at 150-200 °C and become flammable at 400°C and release toxic smoke at temperature above 500°C.

It is especially important to present the knowledges of thermal decomposition, and rigidity of material as PIR or PUR. [12] defined thermal decomposition as a “process whereby the action of heat or elevated temperature on an item causes changes to the chemical composition”.

Figure 11 highlights the progression of damage through the thickness of a laminate when exposed to heat. Starting at the unheated surface, the matrix remains intact, though minor damage such as delamination and cracking can occur. Closer to the heat source, in the decomposition zone, the polymer matrix begins to degrade, forming char, gas, and cracks. At higher temperatures, the matrix fully decomposes, leaving behind a fiber-char state. Depending on the fiber type, the char may either oxidize or volatilize, with thermally stable fibers remaining intact longer, while reactive fibers, such as carbon or organic types, decompose at elevated temperatures.

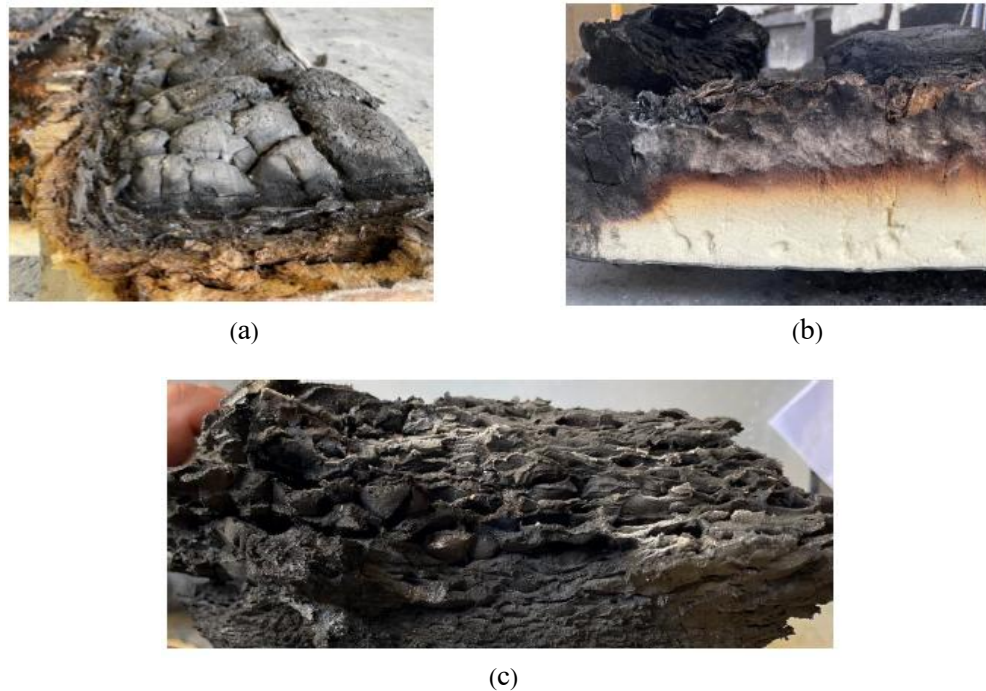


Figure 11. View of the fire-damaged PIR core material after fire laboratory test. (a) charred foam, (b) cross-section view, (c) full damage of PIR.

- **Mineral wool (MW).** The general term of mineral wool includes different type as glass wool slag wool and stone wool; The glass wool has a melting point approximately 600-650°C and usually classified as combustible. The slag wool a usually a mixture of metal oxides and silicon oxides. It can remain stable up to about 900°C, but unsuitable for using it as core material in structural sandwich panels as it is often acidic in nature, and it can cause corrosion problems in the structure. Stone wool is more usually used in the construction industry as thermal insulation and for sandwich panels as a core, the melting point approximately 1400°C with density range 50kg/m<sup>3</sup> to 150kg/m<sup>3</sup>[3].

Figure 13 below shows a series of mineral wool samples that have been subjected to different firing temperatures, ranging from 20°C to 700°C, with each row representing a specific temperature.

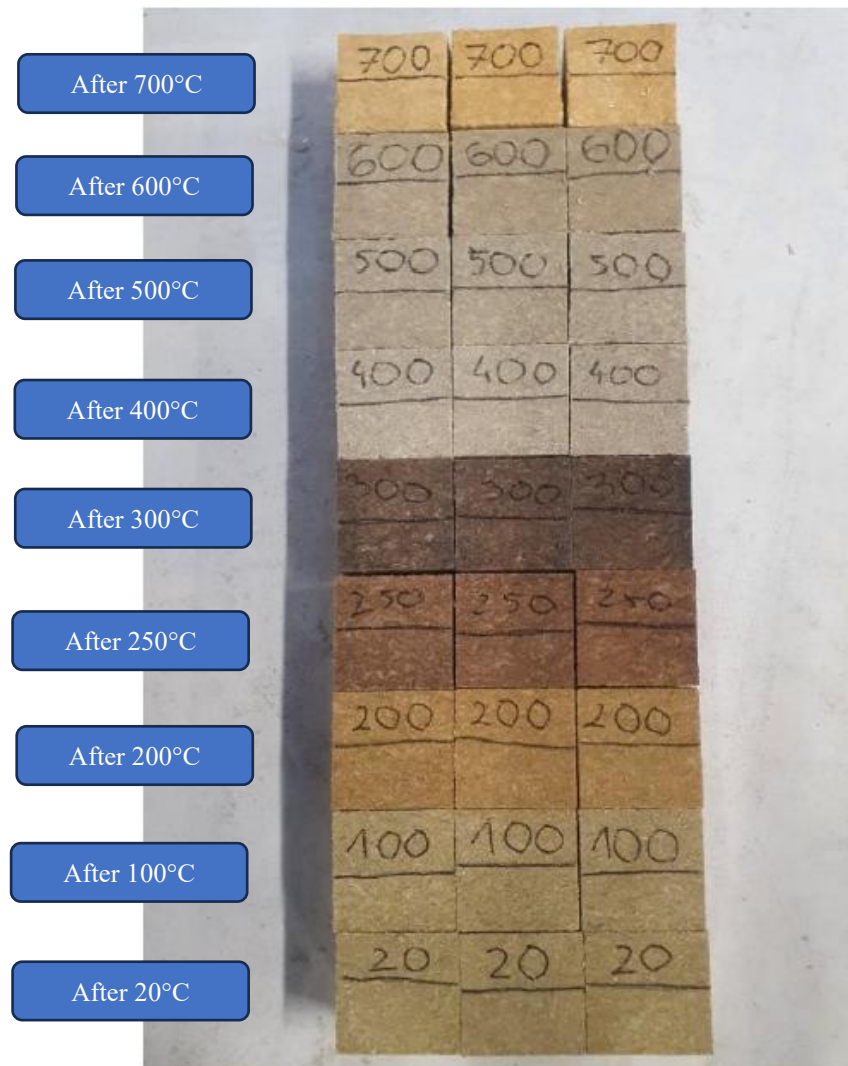


Figure 12. Mineral wool samples after removal from the furnace, at different temperatures.

A noticeable change in color occurs as the firing temperature increases. Samples at lower temperatures (20°C to 100°C) retain a light yellowish-brown color, which darkens slightly by 200°C. At 250°C, the samples take on a reddish-brown hue, transitioning to deep brown at 300°C. By 400°C and 500°C, the color lightens to a greyish brown, becoming a more neutral gray at 600°C, and finally a light-yellow gray at 700°C. Each row shows consistent color, indicating uniform exposure within each group. These color changes suggest thermal degradation or chemical transformations in the mineral wool, providing insight into its thermal properties and behavior under elevated temperatures, which is crucial for the fire resistance of sandwich panels. Mineral wool has been selected for detailed investigation in this study due to its most used core material in fire-resistant

sandwich panels, as well as the observed lack of comprehensive and accurate characterization of its thermal response in the existing scientific literature.

#### **2.4.1 Thermal properties of mineral wool at elevated temperatures**

The significant influence of thermal properties on material behavior at elevated temperatures has been previously analyzed in [31]. In this study [31], we emphasize importance in understanding the thermal response of core materials. In last years, many studies have been focused on the influence of structural property when it is exposed to fire [32, 33, 34]. To comprehensively understand the behavior of sandwich panels under various thermal conditions, it is essential to analyze the material properties in relation to temperature, with particular emphasis on the core material.

The thermal properties of insulation materials are critical for their effectiveness in fire conditions. [35], as they significantly impact the panels' performance and safety during thermal exposure, as illustrated in previous sections. There are three key thermal parameters that are relevant to fire behavior: thermal conductivity ( $\lambda$ ), mass density ( $\rho$ ) and specific heat ( $C_p$ ). Nevertheless, the engineering approach to calculating transient heat propagation in a sandwich panel can be based on information about thermal diffusivity. As was mentioned, thermal diffusivity is the quantity that combines all the thermal properties mentioned above ( $\lambda$ ,  $\rho$ ,  $C_p$ ). The thermal diffusivity ( $\alpha$ ) is crucial because it directly affects the heat flow described by the heat transfer differential equation. It is shown below that based on a relatively simple experimental setup, the effective thermal diffusivity of an insulating core material can be assessed, which can then be used to model the heat transfer process.

Several authors have specifically focused on determining the thermal properties of mineral wool or assemblies containing mineral wool and other materials, such as gypsum boards, thin metal sheets or plasterboards [36, 37, 38]. The thermal conductivity of mineral wool with a density of 80 kg/m<sup>3</sup> was derived in [39] using a prediction-correction method. This method was applied to fit the computation results to those obtained during standard fire tests. However, the paper does not specify the orientation of the fibers, the number of measurement points or the geometry of the sample. In [40], a detailed thermal analysis of mineral wool in nitrogen and oxygen atmospheres was conducted. The authors reported two exothermic peaks and attributed them to the burning of the binder and



crystallization of the amorphous material. The thermal behavior of mineral wool was investigated and modelled in [41, 42]. In [41], a multiphysics model of heat and mass transfer coupled with the chemical decomposition of the organic content was developed while in [42] models for predicting the temperature of the unexposed side of sandwich composites made of mineral wool with stainless steel or plasterboard cladding were presented.

The thermal properties of insulation materials vary depending on their type. At ambient temperature, mineral wool exhibits thermal conductivity in the range of 0.030–0.046 W/(m·K) [43]. In the case of elevated temperature, different values of thermal conductivity of mineral wool are given in numerous studies. For example, a constant value of 0.036 W/(m·K) was utilized in [39], whereas in [31, 44], different thermal conductivity versus temperature functions were used. It is crucial to consider the relationship between thermal conductivity and temperature to accurately evaluate the effectiveness of insulation materials.

There are several sources as [45, 46, 47] that give MW conductivity as a function of temperature, but they refer to different material densities. There is no standard function that determines the conductivity of MW as a function of temperature (and wool density) or a simple test method that can be used to determine thermal conductivity as a function of temperature. Determining the  $\lambda - \theta$  relationship is difficult because during the production of mineral wool, several types of binders and chemical preparations are used to glue or bind mineral fibers, which affect the thermal processes occurring in the material. To illustrate the problem, the dependence of thermal conductivity on temperature (and density) according to sources [42, 45, 46] is presented in Figure 13. The graphs show the significant differences in thermal conductivity observed in numerous studies. This can be attributed to differences in the structure of the material or the chemical composition of the materials, but the reason should also be sought in the use of different test methods. In the case of ambient temperature, differences may also result from the humidity of insulating materials [47].

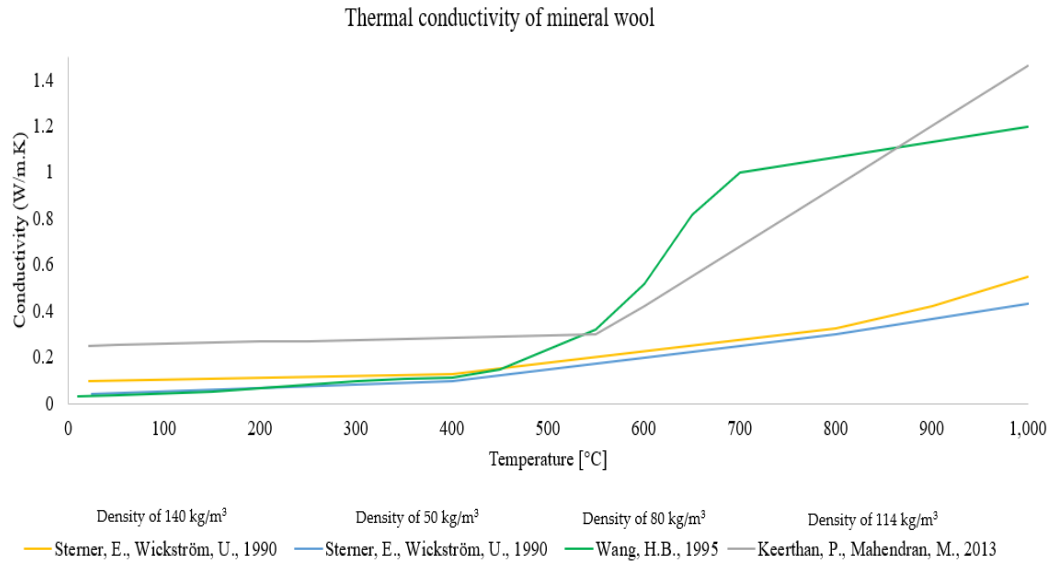


Figure 13. Thermal conductivity of mineral wool as a function of temperature [31].

Another critical material parameter is specific heat. The difficulty of measuring the specific heat of insulating materials results from the fact that these materials are porous and have low thermal conductivity and low heat capacity. In [31, 48], a constant value of the specific heat of mineral wool is given, equal to 850 J/(kg·K). The density of mineral wool can also be affected by temperature; insulating materials tend to decrease in density slightly with increasing temperature. This is primarily due to thermal expansion; the material absorbs heat and expands, resulting in lower density. The analysis of available publications shows that, currently, the most general and useful source of mineral wool properties at elevated temperature is the upcoming Eurocode prEN 1995-1-2 (design of timber structures state for 2022) [49], in which the effective thermal properties of mineral wool are generalized based on fundamental experimental and numerical analyses (see Table 3).

Table 3. Thermal properties of MW insulation with density more than 26 kg/m<sup>3</sup> [49].

Temperature [°C]	$\lambda$ [W/m·K]	$C_p$ [kJ/(kg·K)]	$\rho/\rho_{20}$ [-]
20	0.036	0.880	1.00
100	0.047	1.040	1.00
200	*	1.160	0.980
400	$0.09 \cdot (11 \cdot e^{-0.05 \cdot \rho_{20}} + 1.9)$	1.280	0.977
600	$0.15 \cdot (11 \cdot e^{-0.05 \cdot \rho_{20}} + 1.9)$	1.355	0.973
800	$0.23 \cdot (11 \cdot e^{-0.05 \cdot \rho_{20}} + 1.9)$	1.430	0.970
925	$0.30 \cdot (11 \cdot e^{-0.05 \cdot \rho_{20}} + 1.9)$	1.477	0.967
1200	$0.45 \cdot (11 \cdot e^{-0.05 \cdot \rho_{20}} + 1.9)$	1.580	0.88

\* Linear interpolation can be applied.



Different laboratory methods can be utilized to measure thermal properties, including Transient Plane Source (TPS) [50], Heat Flow Meter Apparatus [35] or Guarded Hot Plate (GHP) [51]. Each of these methods has its advantages, but also notable limitations regarding the transient properties that are of interest in our investigation. The heat transfer inside nonporous and non-transparent materials takes place via conduction. For porous materials, heat is transmitted by conduction, radiation and convection. Decoupling those three ways of heat transfer for the assessment of temperature in mineral wool is impractical. Moreover, the measured thermal conductivity will vary with test conditions and test methods (e.g., transient and steady-state methods). According to [44], the applicability of the thermal conductivity obtained with any particular method is limited to heat flow patterns similar to those used in the measurement method. Therefore, typical methods used for insulation materials, such as guarded hot plate and heat flow meter, are applicable when steady-state values are of interest. For some applications, transient methods are used, for example, with the TPS method. During a fire, the conditions are far from a steady-state and differ from typical transient tests. Due to the above-mentioned issues, establishing the so-called effective thermal properties is a prerequisite for building materials. The effective properties are meant to give a good agreement between the experimental data and the calculations [52, 53] without the burden of complicated calculations.

None of the methods described above was used in our study [31]. The proposed method is not expensive and does not require specialized equipment. It is low-cost and requires no specialized equipment. A large heat source was applied to one surface, ensuring one-dimensional heat transfer. Thermocouples measured temperature at fixed points. Thermal diffusivity was calculated. The method allows analysis of fiber orientation and chemical reactions.

While the study [31] employs a methodology for evaluating the thermal properties of mineral wool insulation, it is important to note that the scope of the investigation is limited to temperatures up to 700°C. Although the method utilized in [31] provides reliable results within its specified range, the present studies in chapter 4 and 5 will adopt the prEN 1995-1-2[49] standard Table 3 to ensure comprehensive analysis across a broader temperature range. This approach allows for the integration of standardized methodologies in the assessment of thermal properties as function of temperature.

### 2.4.2 Thermal diffusivity of porous materials

In this subsection, the theoretical background and methodological framework employed in the investigation [31] are outlined. The concept of thermal diffusivity, which is fundamental for understanding heat transfer mechanisms in porous materials, is discussed. Although the study in [31] provides a methodology for evaluating thermal diffusivity, a detailed review and explanation of various models tested for its calculation were not included in the publication due to the extensive scope. Therefore, this section aims to present a broader theoretical context, offering insights into different approaches tested to determine thermal diffusivity.

Thermal diffusivity is a critical thermophysical property that describes how fast heat spreads through a material when subjected to a temperature gradient. It is a measure of how efficiently a material conducts thermal energy relative to how much it stores. [54] explained thermal diffusivity as the rate at which the temperature of the material conducting the heat changes. [55] defined thermal diffusivity as it measures the ability of a material to conduct thermal energy relative to its ability to store thermal energy. It is often confusing with thermal conductivity, but they are distinct properties. While thermal conductivity measures a material's ability to conduct heat, thermal diffusivity relates to how fast the heat spreads through the material. It depends not just on conductivity but also on the material's ability to store heat (specific heat capacity and its density). For example, two materials may have similar thermal conductivities but different thermal diffusivities due to differences in their heat capacities or densities.

The concept of thermal diffusivity ( $\alpha$ ) can be rigorously analyzed using the heat diffusion equation (also known as the heat conduction equation) in cartesian coordinates. The heat diffusion equation describes how heat flows and is derived from the law of conservation of energy combined with Fourier's law of heat conduction. The heat diffusion equation in the Cartesian coordinate system  $x, y, z$  is given by:

$$\frac{\partial}{\partial x} \left( \lambda_x \frac{\partial \theta}{\partial x} \right) + \frac{\partial}{\partial y} \left( \lambda_y \frac{\partial \theta}{\partial y} \right) + \frac{\partial}{\partial z} \left( \lambda_z \frac{\partial \theta}{\partial z} \right) + q = \rho C_p \frac{\partial \theta}{\partial t}, \quad (2.3)$$

Equation (2.3) describes heat transfer through a material considering anisotropic thermal conductivities (different values in the  $x, y$ , and  $z$  directions).

Porous material, such as foams or fiber-based insulations as mineral wool, exhibit complex thermal behavior due to the interaction between the solid matrix and the air-filled pores. The overall thermal diffusivity of porous materials is lower than that of dense materials with similar compositions. This reduction is largely because the air within the pores has an extremely low thermal conductivity, which serves as a barrier to heat transfer. The function of thermal diffusivity can vary based on the spatial point considered. In general, the equation (2.3) will be different depending on the considered point in space. If internal heat sources are neglected (No energy generated),  $q$  can be omitted from equation (2.3). If, in addition, the conduction heat rate associated with one direction is much greater than in the other two directions, then Equation (2.3) reduces to a 1-D problem:

$$\frac{\partial}{\partial x} \left( \lambda_x \frac{\partial \theta}{\partial x} \right) = \rho C_p \frac{\partial \theta}{\partial t}. \quad (2.4)$$

In the case of constant thermal conductivity  $\lambda_x$ , which is independent of the position variable, the heat equation is simplified to:

$$\frac{\partial^2 \theta}{\partial x^2} = \frac{1}{\alpha} \frac{\partial \theta}{\partial t}, \quad (2.5)$$

The method in [31] is to determine the thermal diffusivity of mineral wool as a function of temperature based on the use of Equation (2.5). Knowledge of such a function makes it possible to model thermal phenomena occurring in variable thermal conditions.

From Equation. (2.5), the function of the thermal diffusivity  $\alpha(\theta)$  can be obtained knowing the 2nd order derivative of the temperature with respect to distance and the derivative of the temperature with respect to time:

$$\alpha(\theta) = \frac{\partial \theta}{\partial t} / \frac{\partial^2 \theta}{\partial x^2}. \quad (2.6)$$

Experimental data supply spatial and temporal distribution of temperature in a material at distinct position and specific time steps. It allows approximate derivatives in Equation (2.6) based on experimental results and consequently calculates thermal

diffusivity. To compute thermal diffusivity, three approaches—Model I, Model II, and Model III are presented below. Model III, originally developed and validated in our prior research [31], has been utilized in the present dissertation as part of the methodological framework. Specifically, the content from the referenced study [31] has been adopted as Chapter 3 of this dissertation. This model (Model III) utilizes regression curve fitting to improve the prediction of heat propagation under one-dimensional heat flow conditions. It assumes a uniform temperature profile across the sample cross-section, enabling accurate estimation of thermal properties without the influence of lateral temperature deviations.

▪ Model I

From the finite difference approximations of the derivatives of  $\frac{\partial^2 \theta}{\partial x^2}$  and  $\frac{\partial \theta}{\partial t}$  we get:

$$\frac{\partial^2 \theta}{\partial x^2} \cong \frac{\theta_{i+1}^t - 2\theta_i^t + \theta_{i-1}^t}{\Delta x^2}, \quad (2.7)$$

$$\frac{\partial \theta}{\partial t} \cong \frac{\theta_i^{t+1} - \theta_i^{t-1}}{2\Delta t}. \quad (2.8)$$

Substituting Equation (2.7) and Equation (2.8) into Equation (2.6) one obtains Equation (2.9).

$$\frac{\theta_{i+1}^t - 2\theta_i^t + \theta_{i-1}^t}{\Delta x^2} \cong \frac{1}{\alpha(\theta_i)} \cdot \frac{\theta_i^{t+1} - \theta_i^{t-1}}{2\Delta t}, \quad (2.9)$$

rewriting of (2.9), the thermal diffusivity is expressed as in (2.10)

$$\alpha(\theta_i) \cong \frac{\theta_i^{t+1} - \theta_i^{t-1}}{\theta_{i+1}^t - 2\theta_i^t + \theta_{i-1}^t} \cdot \frac{\Delta x^2}{2\Delta t}, \quad (2.10)$$

where:  $i$  is the number of the reference node,  $t$  is time,  $\Delta x$  and  $\Delta t$  represent uniform increments of the depth and time in  $x$ -direction. Please note that the application of the Equation (2.10) requires three temperature profiles at two distinct time levels ( $\theta_i^{t+1}, \theta_i^{t-1}$ ).

Equation (2.10) has been utilized in prior studies [56, 57, 58, 59] to evaluate the apparent thermal diffusivity within the active layer and permafrost. Additionally, [59] presents alternative formulations for  $\alpha(\theta_i)$  to address cases with non-uniform spatial and temporal discretization.

#### ▪ Model II

The coefficients of the central differences can be used to calculate the time derivative of temperature,  $\frac{\partial \theta}{\partial t}$ . This can be improved by using a higher-order central difference scheme for approximating the first derivative, which achieves eighth-order accuracy in  $\frac{\partial \theta}{\partial t}$ . Higher-order accuracy means more precise results with less numerical error for the same time step size.

In this model, the derivative is approximated using a central difference scheme that incorporates multiple time levels symmetrically distributed around the current time step (from  $t - 4$  to  $t + 4$ ). The use of carefully selected coefficients results in an approximation that is accurate up to the eighth power of the time step, hence eighth-order accurate. Thus,  $\frac{\partial \theta}{\partial t}$  will be written as:

$$\begin{aligned} \frac{\partial \theta}{\partial t} = \frac{1}{\Delta t} & \left( \frac{1}{280} \theta_i^{t-4} - \frac{4}{105} \theta_i^{t-3} + \frac{1}{5} \theta_i^{t-2} - \right. \\ & \frac{4}{5} \theta_i^{t-1} + \frac{4}{5} \theta_i^{t+1} - \frac{1}{5} \theta_i^{t+2} + \frac{4}{105} \theta_i^{t+3} - \\ & \left. \frac{1}{280} \theta_i^{t+4} \right), \end{aligned} \quad (2.11)$$

following the derivation presented in Equation (2.11), the time derivative of temperature can be approximated using the eighth-order central difference scheme. The expression in the brackets of (2.11) will be denoted as  $\Delta'_t \theta$ :

$$\begin{aligned} \Delta'_t \theta = \frac{1}{280} \theta_i^{t-4} - \frac{4}{105} \theta_i^{t-3} + \frac{1}{5} \theta_i^{t-2} - \frac{4}{5} \theta_i^{t-1} + \frac{4}{5} \theta_i^{t+1} - \\ \frac{1}{5} \theta_i^{t+2} + \frac{4}{105} \theta_i^{t+3} - \frac{1}{280} \theta_i^{t+4}. \end{aligned} \quad (2.12)$$

Substituting the spatial derivative from Equation (2.7) and the derivative from Equation (2.12) into Equation (2.6), a refined expression for thermal diffusivity is obtained (see Equation (2.13)). This formulation incorporates eight-time levels for

high accuracy (from  $t - 4$  to  $t + 4$ ) and three spatial nodes ( $i + 1, i, i - 1$ ). Therefore, the application of Equation (2.14) requires eight temperature profiles across time and three spatial levels centered around the reference node  $i$ .

$$\frac{\theta_{i+1}^t - 2\theta_i^t + \theta_{i-1}^t}{\Delta x^2} \cong \frac{1}{\alpha(\theta_i)} \cdot \frac{\Delta'_t \theta}{\Delta t}, \quad (2.13)$$

$$\alpha(\theta_i) \cong \frac{\Delta'_t \theta}{\theta_{i+1}^t - 2\theta_i^t + \theta_{i-1}^t} \cdot \frac{\Delta x^2}{\Delta t}, \quad (2.14)$$

where:  $i$  is the number of the reference node,  $t$  is time,  $\Delta x$  and  $\Delta t$  represent uniform increments of the depth and time in  $x$ -direction.

#### ▪ Model III

To expect more accurate results, the calculation of the 2nd order derivative of the temperature with respect to distance based on regression curve equations can be used. In [31] was used the regression curves of the 2<sup>nd</sup> order polynomial, 3<sup>rd</sup> order polynomial, 4<sup>th</sup> order polynomial, and exponential functions. The aim of the regression analysis is to determine parameter values that ensure the best fit to the experimental data. This approach is chosen to minimize temperature peaks caused by chemical reactions within the mineral wool samples (see chapter 3).

## 2.5 Thermomechanical modelling of sandwich panels

Thermomechanical problems are crucial in evaluating the performance and integrity of structural materials subjected to combined thermal and mechanical loads. This becomes particularly relevant in the context of sandwich panels, where temperature-induced deformations can affect both the structural integrity and performance of the panel. Therefore, accurate modelling of these interactions is essential for predicting the performance and failure of sandwich panels, especially under extreme environments such as fire exposure. Sandwich panels designed for fire-resistance applications are often assessed under both thermal and mechanical loads to ensure their integrity during fire exposure. In such tests, fully coupled thermomechanical analysis is essential to predict how the panels will behave as they are exposed to rapidly changing temperatures and high thermal gradients.

Additionally, [60] demonstrated that a coupled thermal–mechanical model could predict the temperature rise, stiffness degradation, and failure time of sandwich composites exposed to one-sided fire, closely aligning with experimental data. [61] showed that integrating a thermo-mechanical damage model significantly improved the prediction of strength and stiffness deterioration in steel structures under elevated temperatures. [62] conducted fire simulations of lightweight sandwich panels with Gypsum plasterboard core material and found that both panel thickness and core material density had a marked impact on thermal insulation and structural stability. [20] confirmed through full-scale fire testing and two-scale simulations that accounting for local failure mechanisms, such as adhesive bond degradation, was essential for reliably estimating panel deflection and load-bearing performance during fire exposure.

Hence, during fire scenarios the face sheets, which provide structural strength, may experience significant thermal stresses, while the core insulation material degrades, leading to delamination and potential structural failure. Therefore, in thermomechanical analysis, the interaction between thermal and mechanical effects must be carefully considered. Therefore, Predictive models that couple thermal and mechanical fields are essential for ensuring the reliability of sandwich panels in high-temperature environments. To capture these interactions, coupled thermo-mechanical analysis using both fully coupled and sequentially coupled approaches has been employed in finite element modelling (FEM) software ABAQUS [63]. These methods are pivotal for predicting the behavior of sandwich panels under varying thermal and mechanical conditions. Fully coupled thermal-displacement analysis simultaneously solves both the temperature field and the mechanical displacement field, making it a robust method for applications where thermal and mechanical responses are highly interdependent. Studies as [64] specifically focus on the thermo-mechanical behavior of sandwich panels exposed to fire, exploring how thermal and mechanical fields interact during fire conditions. This study serves as a key reference for understanding the fire performance of these materials. Additionally, advanced theories have been employed to simulate the thermal response of sandwich structures, as discussed in [65]. Accounting for temperature gradients across the core and face sheets. These gradients significantly influence deformation, stress distribution, and overall panel stability, providing critical insights into how temperature variations impact structural behavior. Similarly, [19] presents thermo-mechanical models for sandwich panels, focusing on their connections during fire resistance tests. This study

offers valuable insights into fire-induced displacements and structural failures, enhancing understanding of sandwich panel behavior under extreme conditions. However, limitations in existing simulations remain. For example, study [66] investigates the PIR behavior of sandwich panels using coupled thermo-mechanical analysis. Despite this, the results show discrepancies when comparing the horizontal displacement from test results with numerical analysis for the tested wall panel. The primary reason for these inaccuracies is the simultaneous delamination of the steel face, which causes local buckling in a sinusoidal manner. This highlights the challenges in achieving accurate predictions using current simulation methods.

For high-temperature environments, ABAQUS software offers the ability to incorporate temperature-dependent cohesive elements to model the weakening of adhesive bonds, as well as the fasteners, providing a realistic prediction of failure points. However, one of the main limitations of fully coupled analysis is the high computational cost, as both fields are solved concurrently. This makes it more suitable for complex cases involving rapid thermal changes, where predicting the interaction between thermal and mechanical responses is essential. In contrast, sequentially coupled analysis simplifies the problem by first solving the temperature field independently and then using the resulting temperature distribution as input for the mechanical analysis, where large displacements or dynamic thermal loads are not expected. The mechanical response in such cases is influenced by the steady-state temperature field, making the sequential approach sufficient for predicting overall panel performance without requiring the high fidelity of a fully coupled model.

The prediction of structure displacement and failures in sandwich panels is key to understanding how these structures perform under extreme environments in different fire scenarios. Coupled thermomechanical analysis, whether fully or sequentially coupled, plays a crucial role in predicting the behavior of sandwich panels under fire conditions.

In this investigation, fully coupled analysis will be used, as it is the most used method for simulating dynamic environments such as fire exposure, where both thermal and mechanical responses evolve simultaneously. However, as will be explained in Chapter 5, fully coupled analysis presents significant challenges, and substantial improvements in modelling methodology are required to simulate the behavior of sandwich panels.



## 2.6 Summary of literature review

The literature review focused on the fire behavior of sandwich panels, particularly their performance under elevated temperatures and the role of core materials as mineral wool. These panels face significant challenges in ensuring fire safety, with a limited understanding of their thermal and mechanical responses during fire exposure posing serious risks to structural integrity. The mentioned gap in knowledge highlights the need for further investigation to enhance the fire resistance and overall safety of sandwich panels.

The review also explores the motivation for this research, driven by the increasing demand for safer and more energy-efficient construction materials. The chapter highlights the reactions of sandwich panels, detailing the behavior of each material that could be used under elevated temperatures. It also discusses the differences between standardized and non-standardized functions regarding the thermal properties of core materials as a function of temperature. Furthermore, the chapter addresses simplified approaches that can be employed for calculating the thermal diffusivity of porous materials. The literature emphasizes limited research on critical aspects such as thermal diffusivity and the behavior of porous materials. It also highlights the importance of simulations using thermo-mechanical analysis, considering all aspects such as boundary conditions, the interaction properties between steel and core materials, and heating parameters. This approach is crucial for predicting the interaction between thermal and mechanical responses during fire events.

## **Chapter 3. Experimental and numerical investigation on the thermal properties of mineral wool**

### **3.1 Introduction**

Sandwich panels with a mineral wool (MW) core are examined in this chapter. The modelling of their fire behavior increasingly relies on performance-based design, which requires an accurate definition of thermophysical material parameters at elevated temperatures. As indicated in Section 2.4.1, thermal diffusivity ( $\alpha$ ) is of primary importance, as it incorporates the effects of thermal conductivity ( $\lambda$ ), density ( $\rho$ ), and specific heat ( $C_p$ ). Due to the significance of this parameter, an experimental method for determining the thermal diffusivity of mineral wool as a function of temperature ( $\theta$ ) is discussed.

The main idea of the method has been previously published and is cited as reference [31]. The aim herein is to briefly re-present the simplified experimental method for determining the thermal diffusivity of MW. Given the characteristically low diffusivity of mineral wool, its measurement is associated with considerable challenges. The method is designed for practical implementation and is presented in Appendix A. Furthermore, additional results for other MW samples are provided to extend the original study.

### **3.2 Experimental setup on mineral wool at elevated temperature**

A cuboid mineral wool specimen is exposed to one-dimensional heat flow in a laboratory furnace under controlled thermal conditions. Lateral insulation is applied to minimize side heat transfer, with heating applied from the top. Seven type K thermocouples are placed at predefined vertical intervals to measure internal temperature distributions. Their positions are horizontally offset to allow reduced vertical spacing and are verified after each test to provide reliable data for the calculation. This configuration ensured accurate thermal data acquisition for evaluating thermal diffusivity. The arrangement is illustrated in Figure 14 and Figure 15.

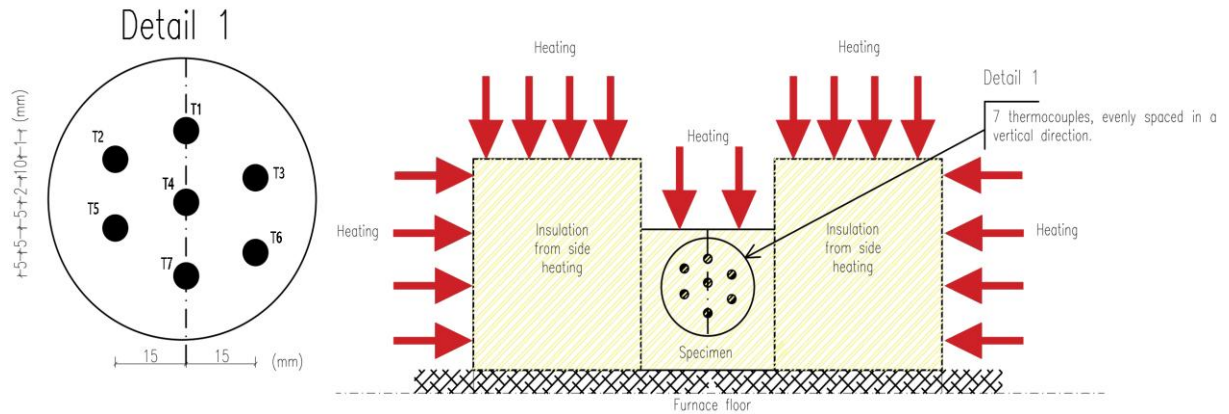


Figure 14. Sketch of a specimen inside the furnace.

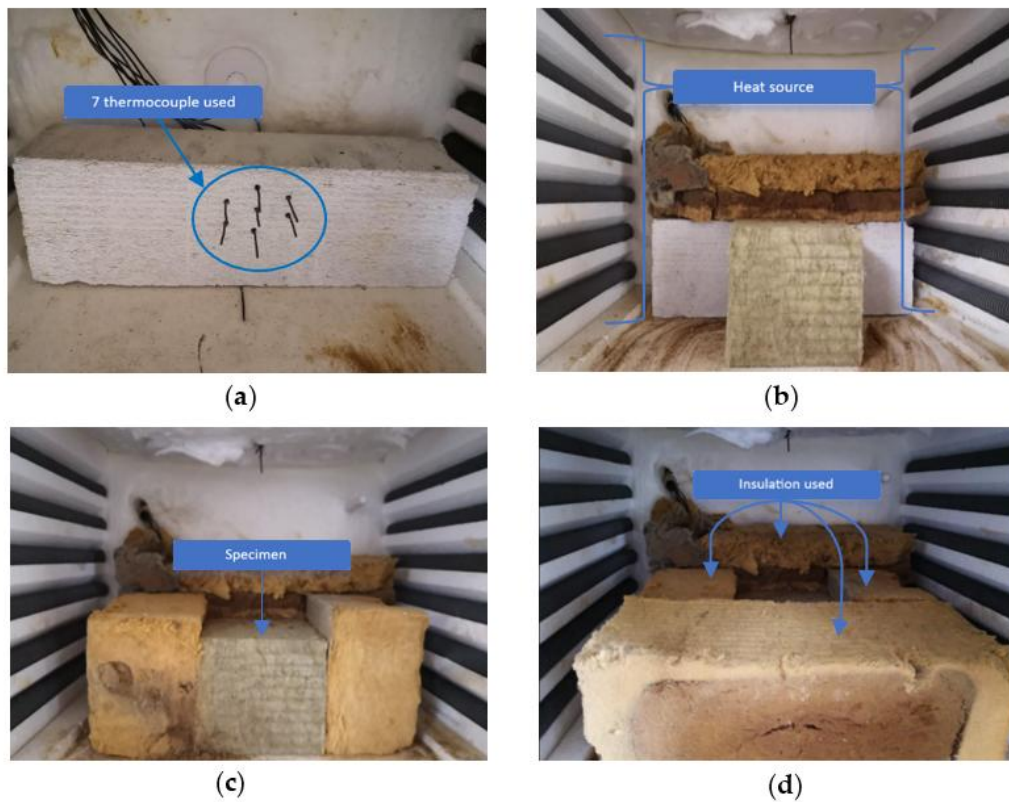


Figure 15. The test specimen inside the electrical furnace: (a) fixing position of a thermocouple using an aerated concrete brick at the back of the furnace; (b) sticking a mineral wool specimen on the thermocouples; (c, d) insulating the specimen from all-around.

### 3.3 Calculation method for thermal diffusivity

Thermal diffusivity is a critical thermophysical property that characterizes the rate at which heat propagates through a material under a temperature gradient. To apply the proposed method, internal heat sources is eliminated, and one-dimensional heat transfer

is ensured (see Appendix A - Reduction of 3-D problem to 1-D problem). Inaccuracies resulting from these simplifications are also estimated.

As outlined in Section 2.4.2 and based on the formulation presented in Equations (2.3) and (2.6), the determination of thermal diffusivity  $\alpha(\theta)$  requires the evaluation of the second spatial derivative and the first temporal derivative of temperature.

Experimental data provided spatial and temporal temperature distributions at defined positions in time intervals. These data are used to approximate the required derivatives and calculate thermal diffusivity accordingly. Two approaches are investigated to determine the derivatives, a central difference approach (Model II – Section 2.4.2) and a regression-based method (Model III – Section 2.4.2). To prevent redundancy in the present research, the theoretical background and the derivation steps underlying the applied methodology have been comprehensively described in [31].

### **3.4 Experimental procedure**

The experimental setup and calculation method described in sections above were used. The tested specimens were made of mineral wool with a density of  $114 \text{ kg/m}^3$ . The specimens were extracted from a sandwich panel. Two consecutive tests on three samples were performed: Sample A, Sample B and Sample C. The first two samples were assessed with fibers perpendicular to the furnace floor, as they were aligned in the panels. The third sample (Sample C) was evaluated with fiber orientation parallel to the furnace floor.

In preliminary tests, it was found that during the heating of the fresh mineral wool, the temperature increased significantly after reaching about  $200^\circ\text{C}$ . This was due to the burning out of the binder that was used in the production of mineral wool. Therefore, tests on samples A, B and C consisted of two heating cycles. The first, which aimed to capture the effect of binder burning. The second is to check the behavior of mineral wool without the burnt binder. A detailed description of the tests is presented in Table 9 Appendix A.

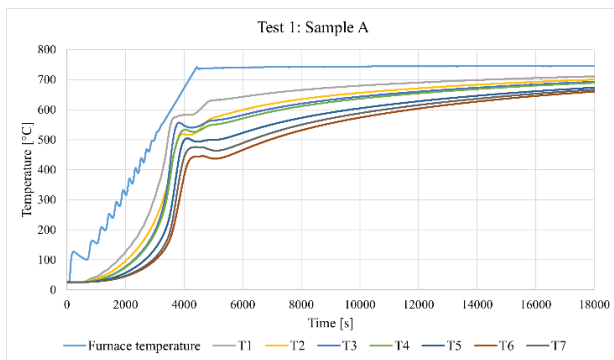
After each experimental test, the furnace and samples were cooled about 12 h. In all tests, the temperature was measured at points T1, T2, T3, T4, T5, T6 and T7, for the test period  $5 \text{ h} = 18000 \text{ s}$ , with the values recorded every 1 s.

### 3.5 Results

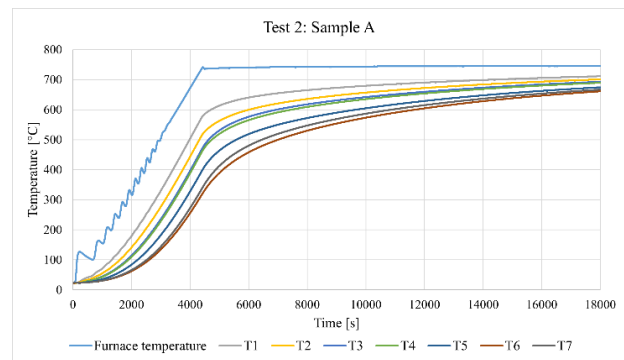
#### 3.5.1 Experimental results

Temperatures at measurement points T1–T7 were recorded as functions of time during the experiments. Figures 16 provides the temperature profiles for samples A, B, and C. Figures 16 (a), (c), and (e) correspond to Tests 1, 3, and 5, in which fresh samples were used.

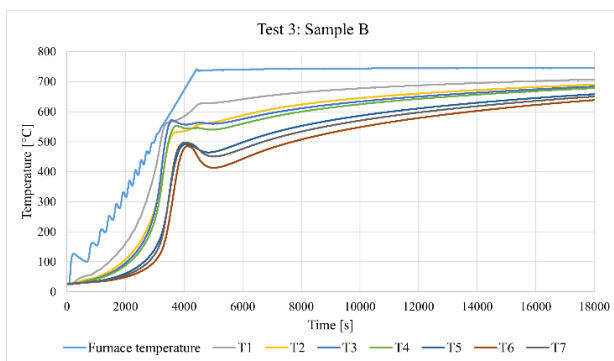
A noticeable disturbance between  $t = 3500$  s and  $t = 5500$  s was observed, attributed to the combustion of the binder within the mineral wool, leading to a temporary rise in internal temperature. This effect was absent in the second heating cycle (Tests 2, 4, and 6), indicating that preheating effectively eliminated internal heat generation. After approximately 4400 s, the heating phase ended, and the furnace temperature stabilized, leading to a steady-state condition within the samples.



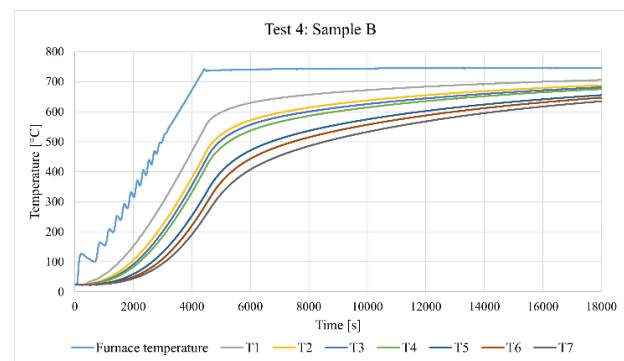
(a)



(b)



(c)



(d)

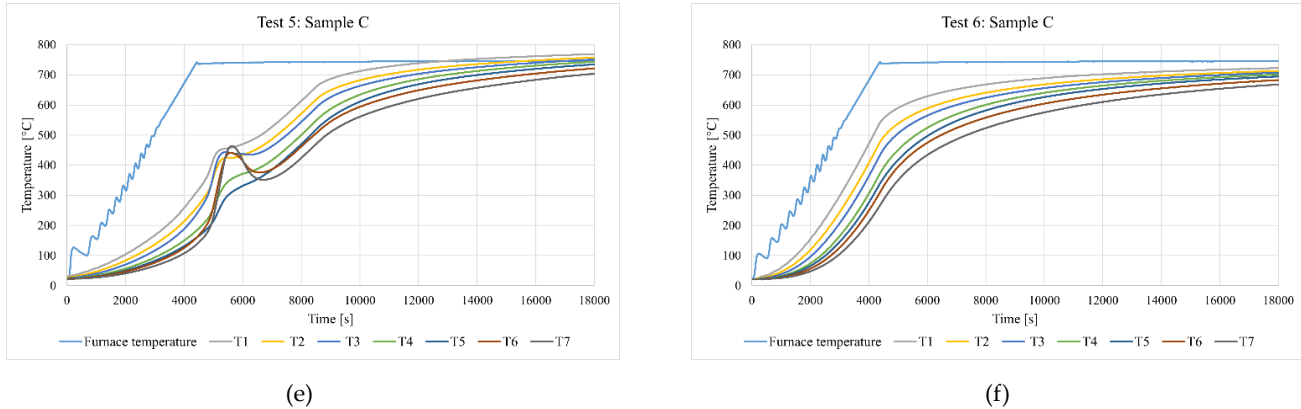


Figure 16. Time-temperature dependence for the tested samples: (a) Sample A – first heating cycle; (b) Sample A – second heating cycle; (c) Sample B – first heating cycle; (d) Sample B – second heating cycle; (e) Sample C – first heating cycle; and (f) Sample C – second heating cycle.

All tests mentioned were conducted using the same furnace heating rate. However, binder combustion was observed latest in sample C (Test 5), occurring after approximately 1 hour and 30 minutes. In this sample, the fibres were oriented parallel to the heated plane. In contrast, earlier binder combustion (after about 1 hour) was observed in samples A and B, where the fibres were oriented perpendicularly. The results from Tests 1, 2, and 5 clearly indicate that fibre orientation significantly influences heat transfer within mineral wool. This orientation affects the mechanisms of conduction, convection, and radiation, thereby altering the material's thermal response.

### 3.5.2 Thermal diffusivity results

The recorded temperature histories were used to calculate thermal diffusivity, as defined in Equation (2.6), with derivatives approximated using the Model II central difference scheme described in Section 2.4.2 chapter 2. Thermal diffusivity values, calculated at different nodes (see Figures. 17–18), are presented as a function of nodal temperature, revealing significant peaks that illustrate the influence of chemical reactions on heat flow.

Figures 17 and 18 display the thermal diffusivity values derived from the data of two experimental tests (Test 1 and Test 2) for points T2–T6. In the first test (Test 1), diffusivity was calculated at increments of 100 seconds, whereas, in the second test (Test 2), diffusivity was calculated at 1-second intervals. This reduction in time intervals enhances the accuracy in predicting heat diffusion and propagation across the sample's

cross-section, aiming to account for and minimize any effects of chemical reactions within the mineral wool.

As shown in Figure 17, a chemical reaction occurs across all nodes within the 350°C to 400°C range, resulting in an unstable diffusivity profile.

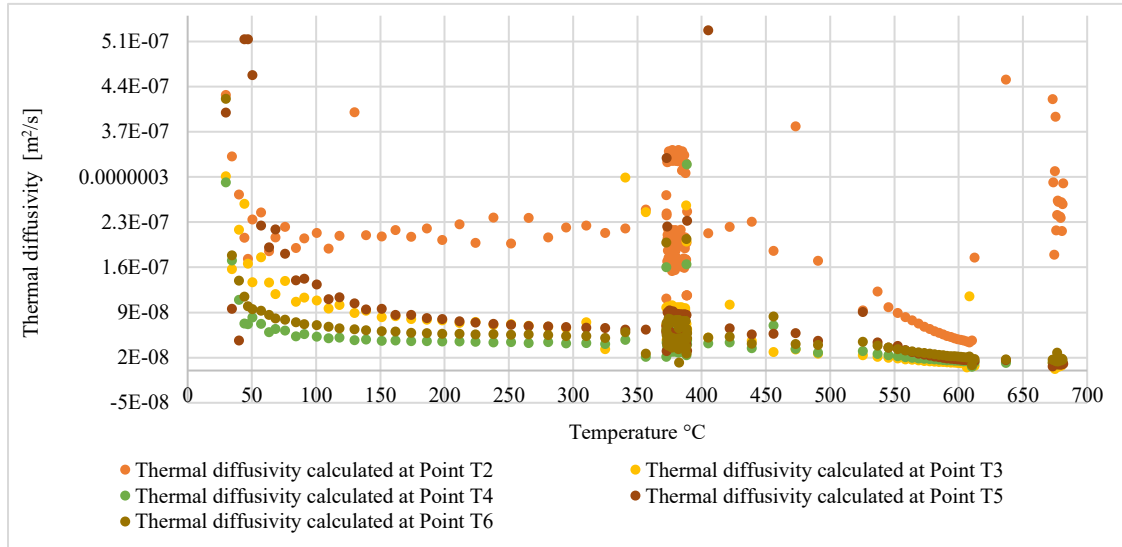


Figure 17: Thermal diffusivity of mineral wool calculated for each 100 s – first experimental test.

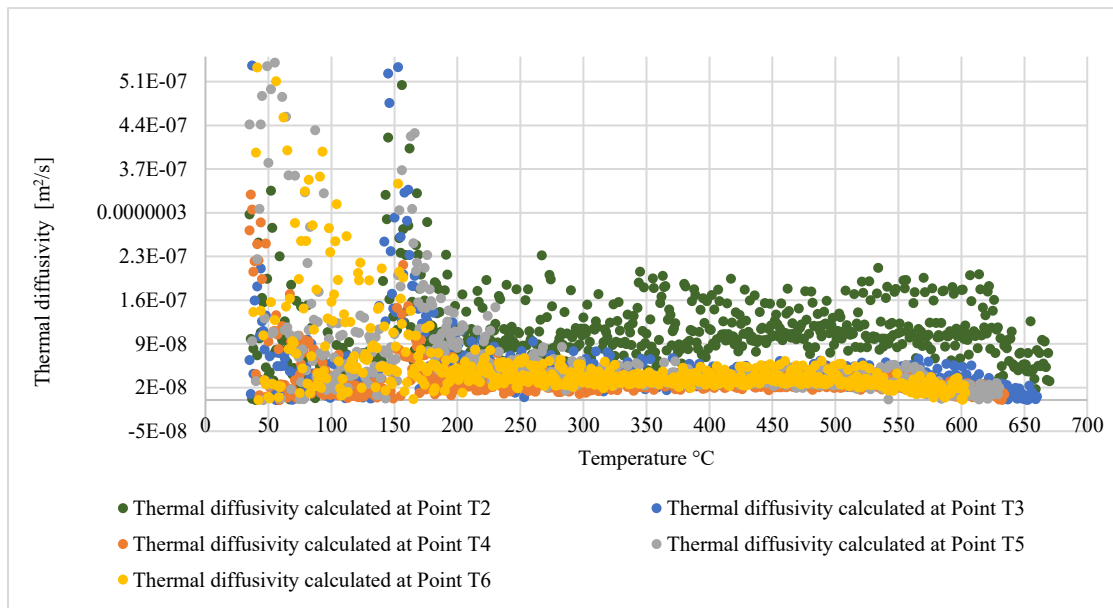


Figure 18: Thermal diffusivity of mineral wool calculated for each 1 s – second experimental test.

It has been found that the malfunction of the calculations is related to the noise of experimentally obtained temperatures, which enhances when derivatives are approximately calculated. Using Model III procedures, which was presented in above section 2.4.2 can solve this problem. On the other hand, differences in heating rates could



influence the value of the thermal diffusivity. Each node of the specimen heats up at different rates, so the results could be affected by that.

As was also mentioned in Section 2.4.2, to determine the thermal diffusivity, it is necessary to calculate the second derivative of the temperature with respect to the spatial coordinate. The possibility of using a second-order polynomial, a third-order polynomial, a fourth-order polynomial and an exponential function was explored. The respective results for Sample A, Test 2, for measurement points T2–T6 are presented in Figure 19. Furthermore, the second derivative of temperature with respect to the spatial coordinate of the other tests are presented in Appendix A. The curves below are to illustrate significant changes in the results of the regression curve. In the case of polynomials of the second and third degree, a large variability of the second derivative is obtained. To obtain a good prediction of thermal diffusivity, the exponential regression was chosen for further investigation. Calculations of the derivative for each recorded time  $t$ , for points T2–T6, were performed using the MATLAB R2017a software.

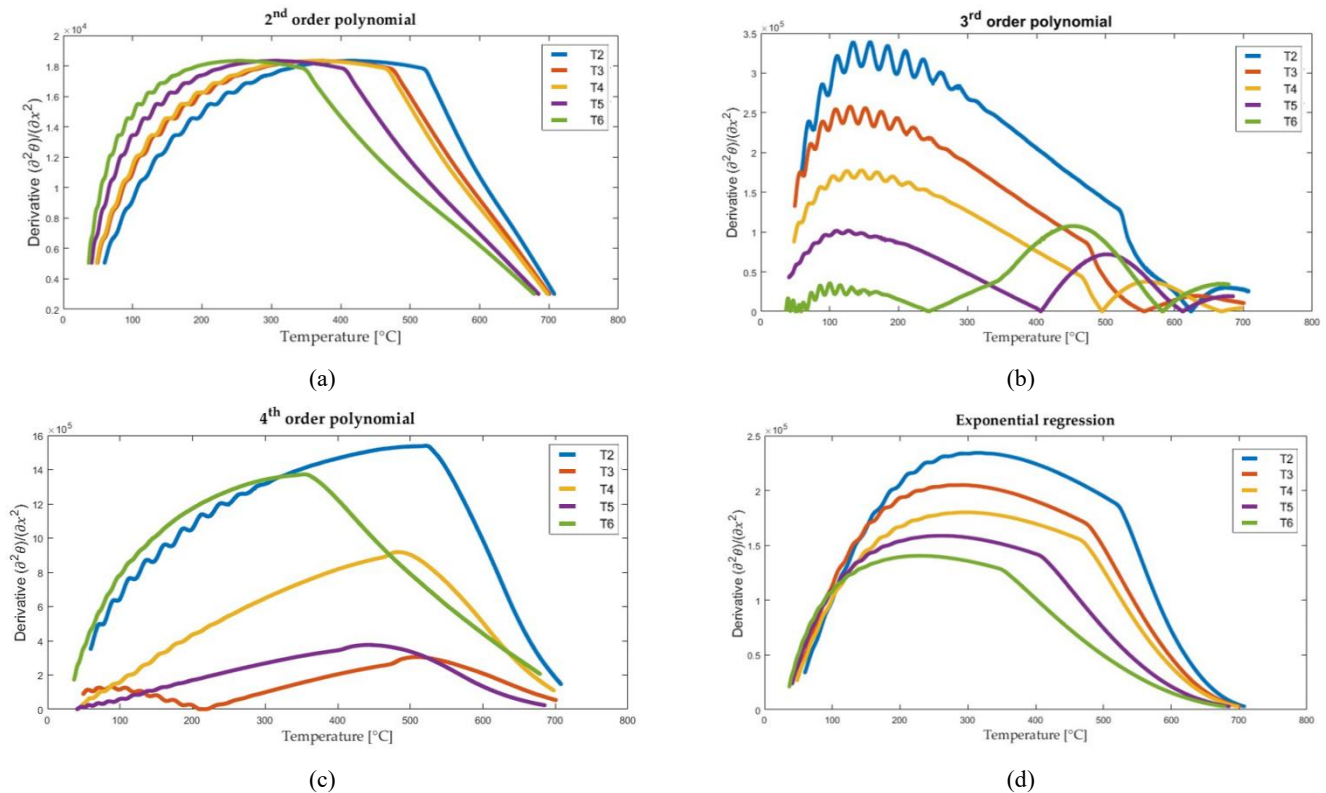


Figure 19. The second derivative of temperature with respect to the spatial coordinate, obtained for Test 2, sample A using the regression curve function: (a) 2nd order polynomial; (b) 3rd order polynomial; (c) 4th order polynomial and (d) exponential function.



Following the completion of the derivative calculations, the thermal diffusivity values for points T2–T6 were determined using Equation (2.6). The thermal diffusivity results for samples (A, B and C) are presented in Figures 20–25. These Figures illustrate the variation of thermal diffusivity as a function of temperature, providing valuable insights into the heat transfer properties of the materials at different temperature levels. Some differences can be noticed in the results obtained for the same temperature but for different measurement points (T2 to T6).

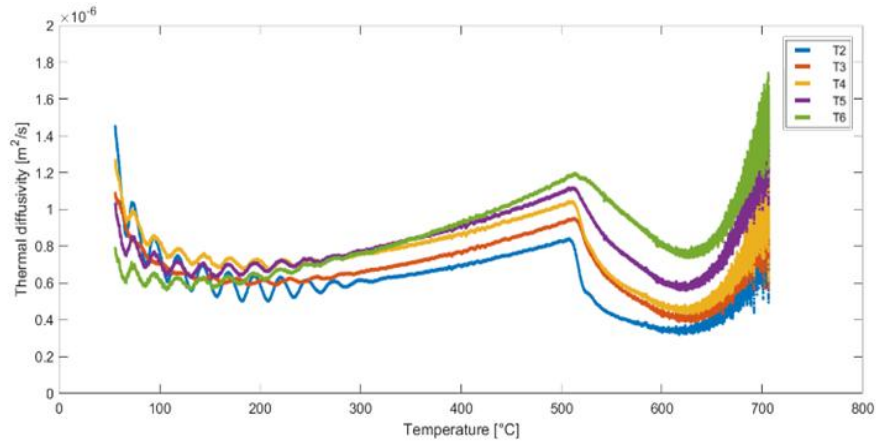


Figure 20. Thermal diffusivity as a function of temperature for nodes T2, T3, T4, T5 and T6 – Sample A, Test 1.

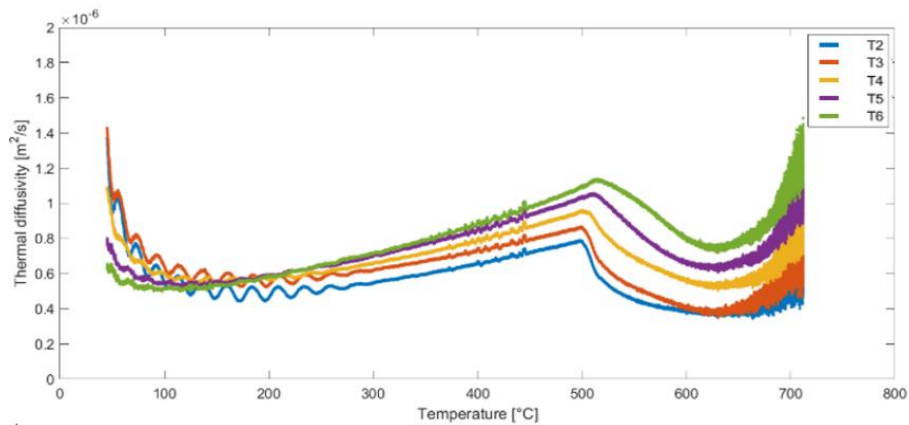


Figure 21. Thermal diffusivity as a function of temperature for nodes T2, T3, T4, T5 and T6 – Sample A, Test 2.

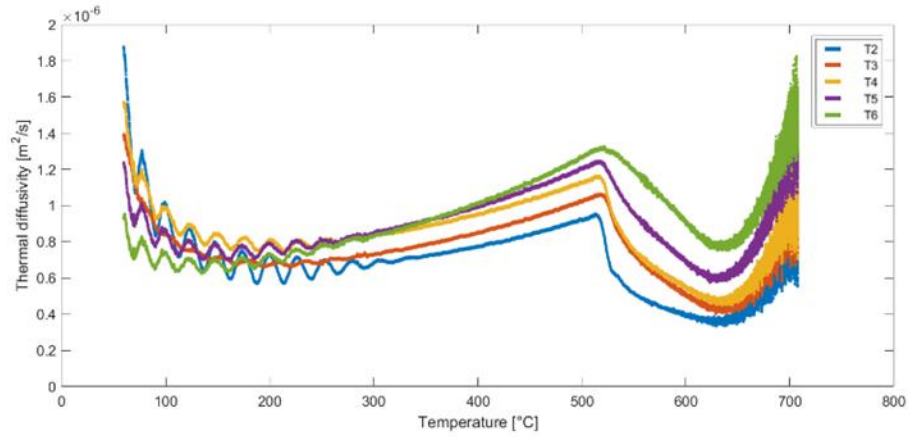


Figure 22. Thermal diffusivity as a function of temperature for nodes T2, T3, T4, T5 and T6 – Sample B, Test 1.

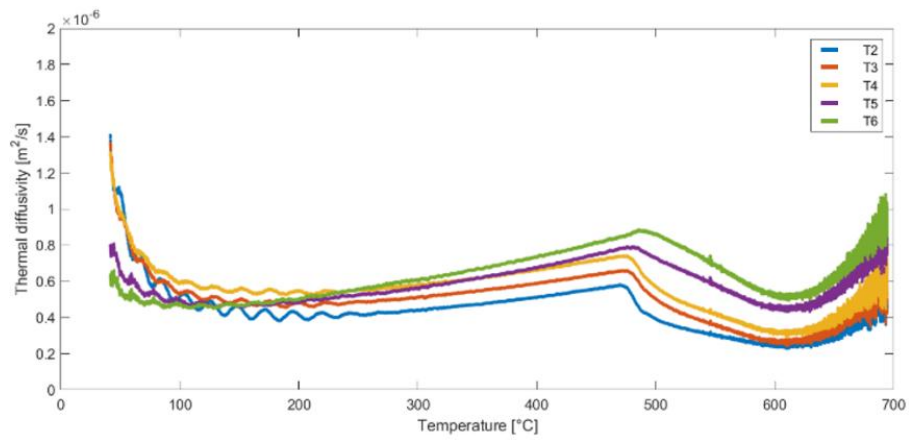


Figure 23. Thermal diffusivity as a function of temperature for nodes T2, T3, T4, T5 and T6 – Sample B, Test 2.

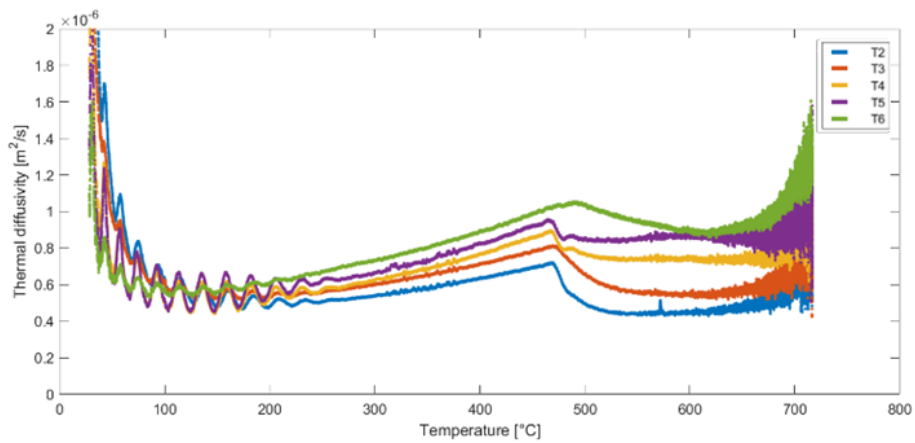


Figure 24. Thermal diffusivity as a function of temperature for nodes T2, T3, T4, T5 and T6 – Sample C, Test 1.

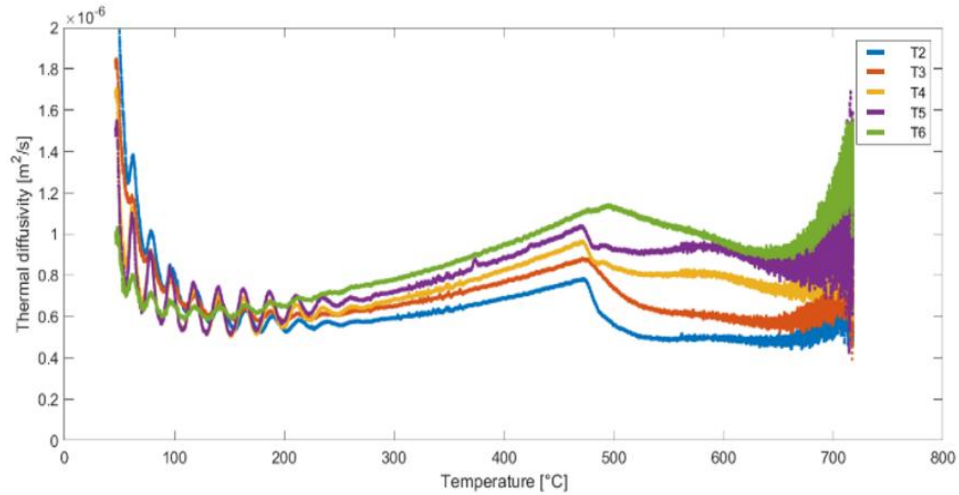


Figure 25. Thermal diffusivity as a function of temperature for nodes T2, T3, T4, T5 and T6 – Sample C, Test 2.

Figures 26 and Figure 27 presents the average thermal diffusivity values derived from the curves obtained for measurement points T2–T6. In Figure 26, each curve represents one test conducted on fresh samples taken directly from the sandwich panel as was mentioned. Similarly, Figure 27 shows the average thermal diffusivity values for tests performed on pre-heated samples.

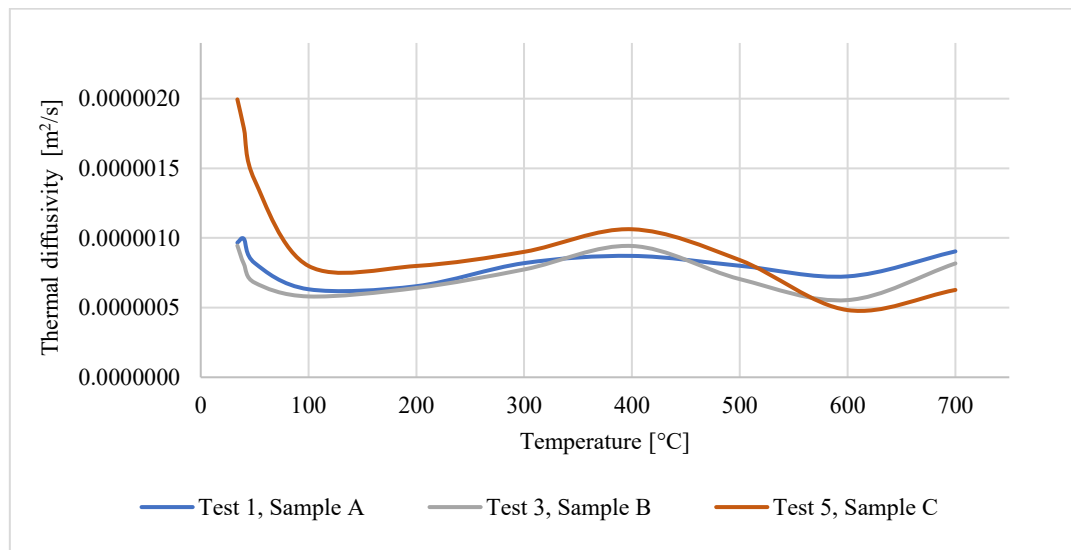


Figure 26. Thermal diffusivity (average value) as a function of temperature – fresh samples.

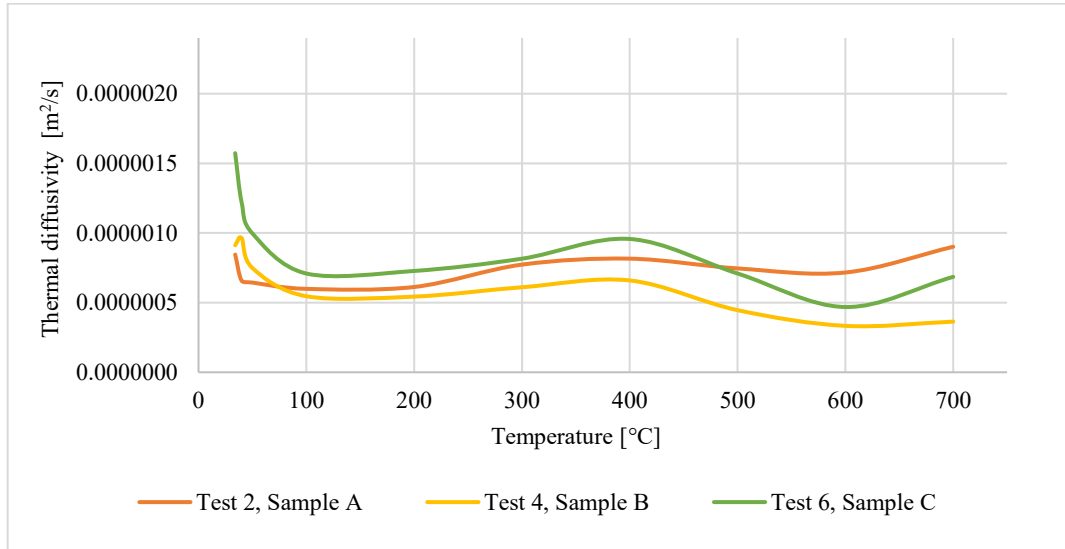


Figure 27. Thermal diffusivity (average value) as a function of temperature – pre-heated samples.

The average functions shown in Figures 26 and Figure 27 represent the characteristics of the behavior of mineral wool subjected to temperature. The results obtained for samples A and B are remarkably similar (especially in the range up to 450 °C), which means that the results are characterized by a certain reproducibility. The thermal diffusivity obtained for sample C is higher in the entire temperature range than for the other samples, which once again confirms the influence of fiber orientation on the thermal properties of mineral wool.

### 3.6 Validation Procedure

To validate the method of determining thermal diffusivity, a comparison was made between experimental results and a numerical model using the experimentally obtained thermal diffusivity values, as described in [31]. The comparison was referring to the temperature versus time values determined for different points located in the sample, see Figure 16.

A one-dimensional numerical model was developed in ABAQUS software using DC1D2 elements to simulate heat transfer through mineral wool. The model was defined by thermal diffusivity values obtained from the experimental results (cf. Figures 26 and 27). Boundary conditions were set using temperatures measured at nodes T1 and T7 from experimental tests. The model simplification is illustrated below in Figure 28.

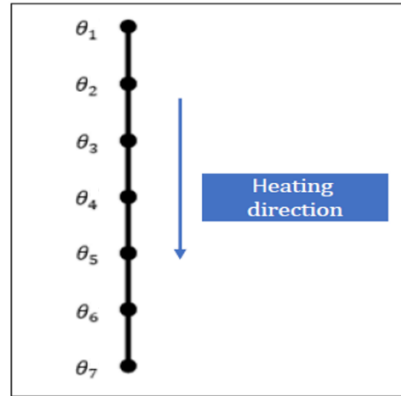
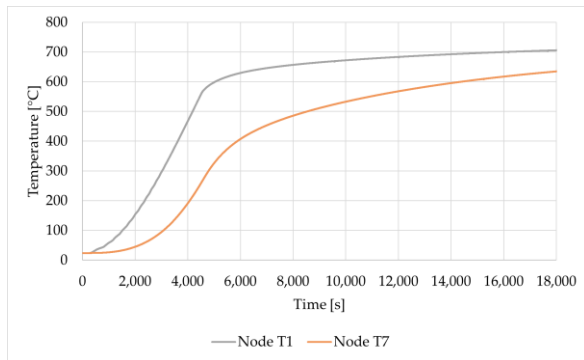
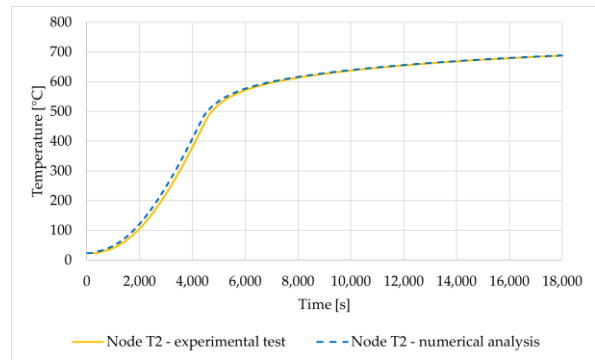


Figure 28. 1-D model of heat transfer.

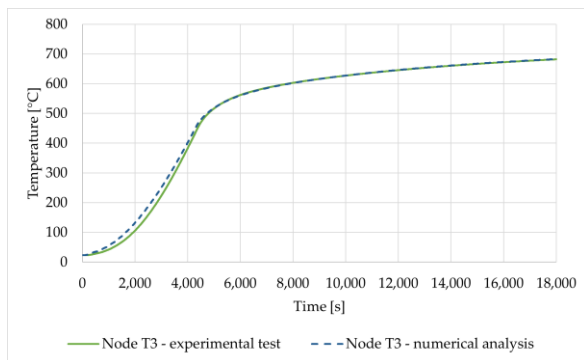
Test 4 on sample B was used to validate the method, representing the second heating cycle without temperature disturbances, indicating no binder combustion. Figure 29a shows the boundary conditions (T1 and T7) applied in the numerical model. Figures 29b – 29f compare experimental and numerical temperatures at points T2–T6, demonstrating quite consistency between the results.



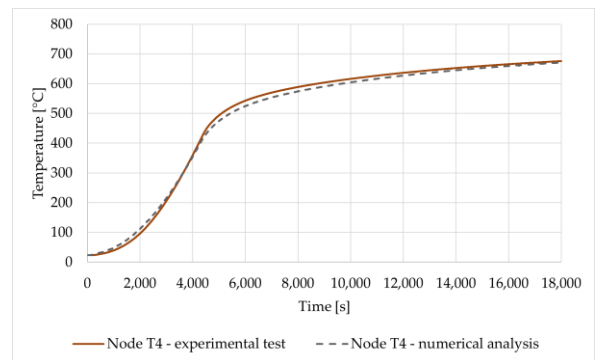
(a)



(b)



(c)



(d)

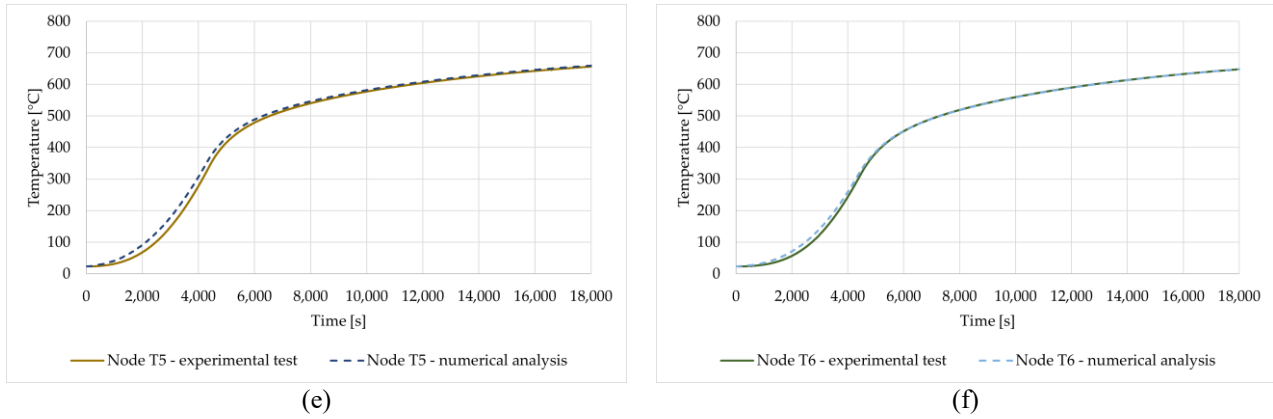


Figure 29. Comparison of the experimental and numerical results: (a) boundary conditions for the numerical problem—temperatures at nodes T1 and T7; (b) time–temperature relationship at node T2; (c) time–temperature relationship at node T3; (d) time–temperature relationship at node T4; (e) time–temperature relationship at node T5 and (f) time–temperature relationship at node T6.

A similar agreement of the experimental and numerical results was obtained for the remaining samples, i.e., for Test 1 (Sample A), Test 2 (Sample A), Test 3 (Sample B), Test 5 (Sample C), and Test 6 (Sample C), are presented in Appendix A. The validation process was noted as crucial for verifying the effectiveness of the numerical approach in predicting the temperature behavior of mineral wool under specific boundary conditions. Consistence between experimental and numerical results indicates a successful model that can then be used to predict the thermal behavior of mineral wool.

### 3.7 Summary and conclusion

This chapter examined the thermal behavior of mineral wool used in sandwich panels when subjected to elevated temperatures. A novel experimental method was proposed, based on direct temperature measurements within a thermally loaded specimen, enabling the determination of thermal diffusivity as a function of temperature.

The presented approach required the determination of the second derivative of temperature after the spatial variable. This was accomplished by using a regression curve in the form of an exponential function. It was also required to determine the time derivative of temperature, which was achieved using the linear regression function. The experiments shows that mineral wool contains a binder, which acts as an internal heat source upon heating; however, this effect was shown to be eliminated by pre-heating the material to approximately 200 °C. A simplified heat flow condition was ensured by

applying lateral thermal insulation, resulting in near one-dimensional heat transfer, as confirmed through numerical validation. Fibre orientation was found that it influences thermal diffusivity, indicating that mineral wool exhibits anisotropic thermal behavior.

This chapter has been presented to maintain the coherence and integrity of the overall research framework. It should be noted that the core methodology and part of findings presented in this chapter have been previously published and are referenced as [31]. However, the current work extends the original study by incorporating additional data and results from all tested samples, providing a broader evaluation of the material behavior. It should be also, noted that the thermal diffusivity values established in this chapter will not be applied in the subsequent analyses due to the different density characteristics of the materials employed in the forthcoming large-scale tests.

Therefore, in Chapters 4 and 5, the thermal parameters provided in Table 3, as referenced in [49], will be utilized as the standard basis for simulation and analysis. The observed inconsistencies and variations in the available literature have highlighted the need for an alternative approach. This prompted the development of a method that is both simplified and cost-effective, enabling the efficient determination and calculation of thermal diffusivity for each type of mineral wool insulation.

## **Chapter 4. Experimental and numerical investigation on thermal behavior**

### **4.1 Introduction**

In this chapter, the thermal response of sandwich panel walls incorporating a mineral wool (MW) core material was examined, with the aim of evaluating and validating their thermal performance. To achieve this, results from series of laboratory fire tests were used. Full-scale samples with different thermal and mechanical parameters were exposed to fire load on one side, while temperatures were monitored on the unheated side. This setup allowed for precise measurement of heat transfer through the panel, providing insights into its insulation effectiveness and structural integrity under thermal load. The experimental findings offer valuable data on how these panels respond when exposed to fire scenarios, reflecting their reliability and limitations.

In addition to the experimental test, numerical simulations were developed to replicate the thermal behavior captured in the tests. By presenting and comparing experimental results with numerical modelling, this chapter provides a detailed view of the thermal behavior sandwich panels with mineral wool core material. This chapter aims to validate the effectiveness of numerical models in predicting the thermal response of mineral wool sandwich panels.

This chapter outlines the experimental setup and laboratory testing methods used, details the thermal responses observed in the mineral wool panels, and discusses the numerical simulations conducted to replicate these responses. Finally, the findings and insights from both experimental and numerical analyses are discussed, offering a deeper understanding of the fire resistance capabilities of these panels.

### **4.2 Experimental setup for fire resistance testing**

The experimental data is taken from tests, which were conducted at the Fire Research Department of the Instytut Techniki Budowlanej (ITB) in Warsaw. The tests described in this chapter involved four large-scale sandwich panels with mineral wool core material. The tests were carried out by the laboratory in accordance with the procedures specified in references [1, 5, 23]. The cooperation with ITB was essential due



to the lack of availability of accredited facilities for conducting large-scale fire resistance tests.

The mounting structure was constructed within a steel testing frame and consisted of aerated concrete blocks with a density of  $600 \text{ kg/m}^3$  and a thickness of 240 mm, along with a reinforced concrete lintel measuring  $240 \times 240 \text{ mm}$ . Hot-rolled angle brackets  $L80 \times 80 \times 8$  were attached to three edges, secured to the aerated concrete blocks using self-drilling steel anchors with a diameter of 8 mm and length of 100 mm, spaced every 500 mm on the horizontal edges and approximately every 1000 mm on the vertical edge. The upper vertical edge was left as a free edge. The gaps between the tested samples free edges and the mounting structure was filled with mineral wool, 50 mm thick on the upper free edges and 25 mm on vertical gaps - with a density of  $140 \text{ kg/m}^3$ . The  $L80 \times 80 \times 8$  hot-rolled angle brackets serving as load-bearing elements which were protected with mineral wool density  $140 \text{ kg/m}^3$ . Figure 30 shows the elements used in the mounting structure for assembling the tested panels. This configuration is also utilized in all tests, Test 1', Test 2', Test 3', and Test 4', as the panels used in each experimental test conformed to the cross-sectional views presented in Figures 34–36.

- Test 1', Test 2', and Test3'

The samples were mounted on two horizontal edges to hot-rolled angle brackets using self-drilling screws, with a diameter of 5.5 mm and a length of 190 mm, spaced every 530 mm (three fasteners across the panel width). The down vertical edge of the sandwich panel wall was also attached to hot-rolled angle bracket using the same self-drilling screws, spaced every 1000 mm (four fasteners along the panel length). The fourth edge (the upper vertical) was left free as free edge 50 mm. More details about specimen fixing are shown in Figures 30-32. The orientation of the specimens during the testing is horizontal orientation, with symmetrical construction.

- Test 4'

The samples were mounted on two horizontal edges to hot-rolled angle brackets using self-drilling screws, with a diameter of 5.5 mm and a length of 190 mm, spaced every 300 mm (three fasteners across the panel width). One vertical edge of the sandwich panel wall was also attached to hot-rolled angle bracket using the same self-drilling screws, spaced every 300 mm (four fasteners

along the panel length). The fourth edge (the upper vertical) was left free as free edge 50 mm. More details about specimen fixing are shown in Figure 33 below. The orientation of the specimen during the testing is horizontal orientation, with symmetrical construction.

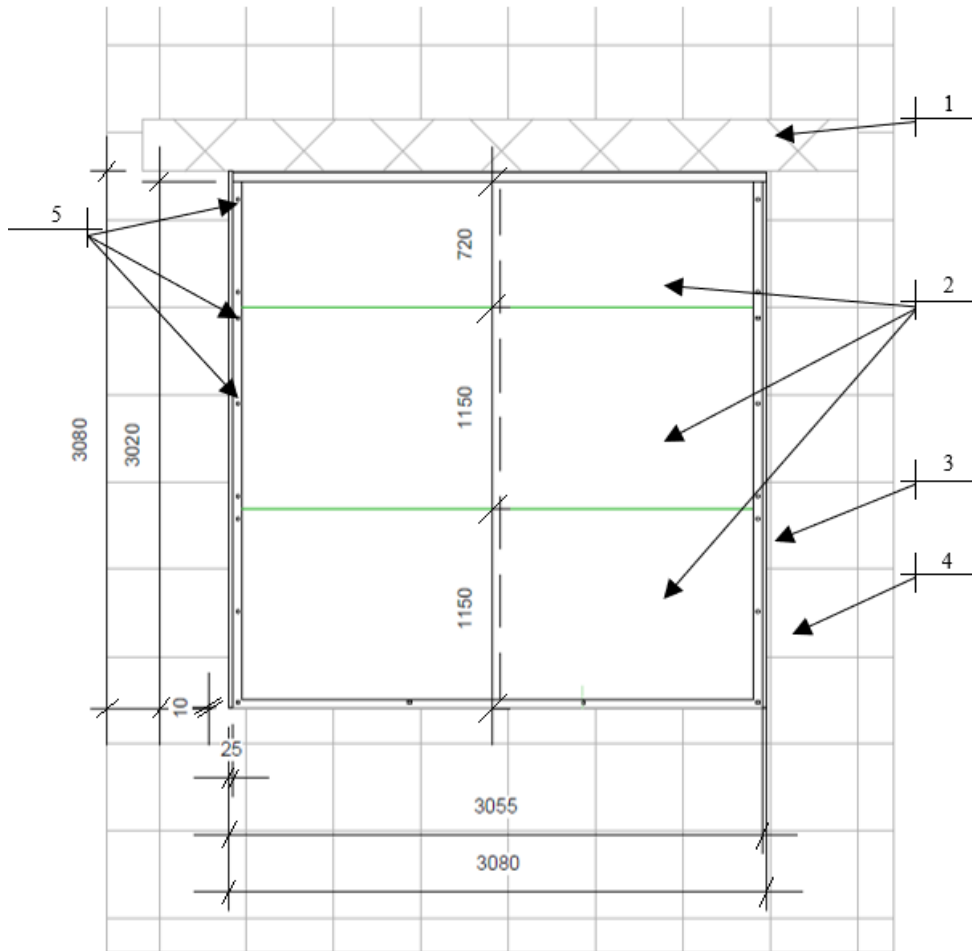


Figure 30. Front view of the assembly of the first sandwich panel wall – Test 1'. The numbered elements correspond to the following components: (1) reinforced concrete lintel with a cross-section of  $240 \times 240$  mm, (2) sandwich panel made of mineral wool – samples described in Section 4.3, (3) free edge filled with insulation material, (4) concrete blocks with a thickness of 24 cm, and (5) self-drilling screws with a diameter of 5.5 mm and a length of 190 mm.

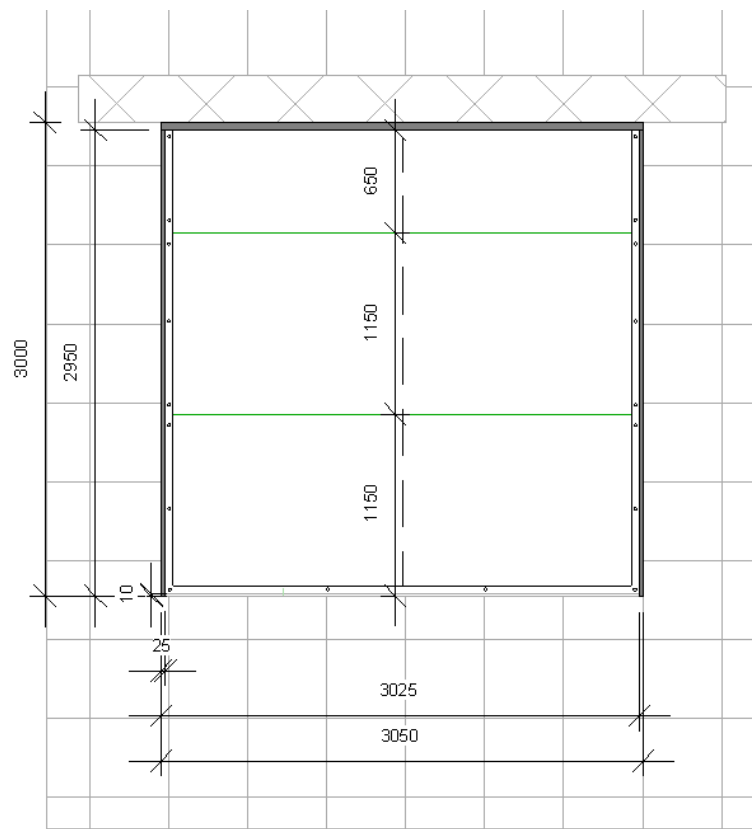


Figure 31. Front view of the assembly of the first sandwich panel wall – Test 2'.

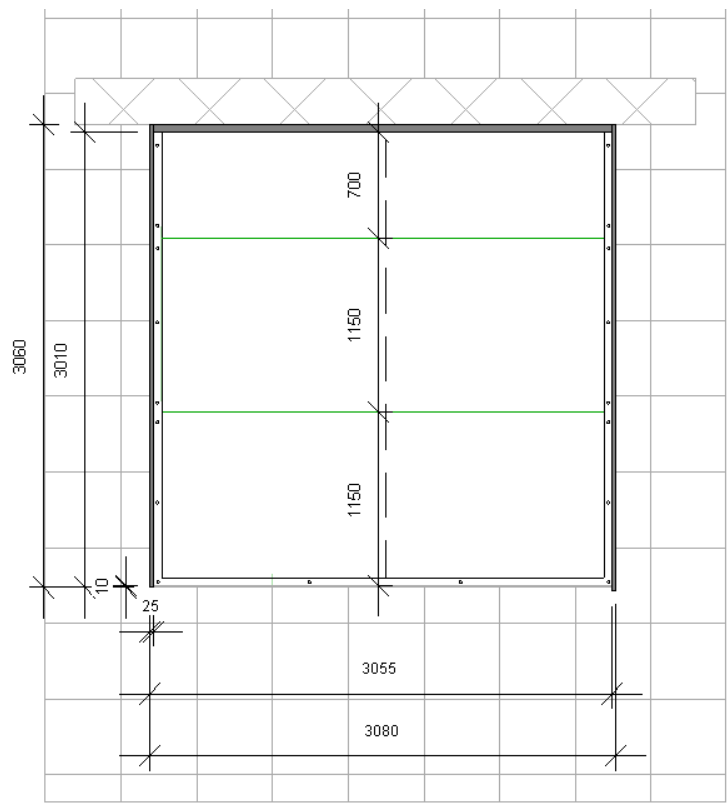


Figure 32. Front view of the assembly of the first sandwich panel wall – Test 3'.

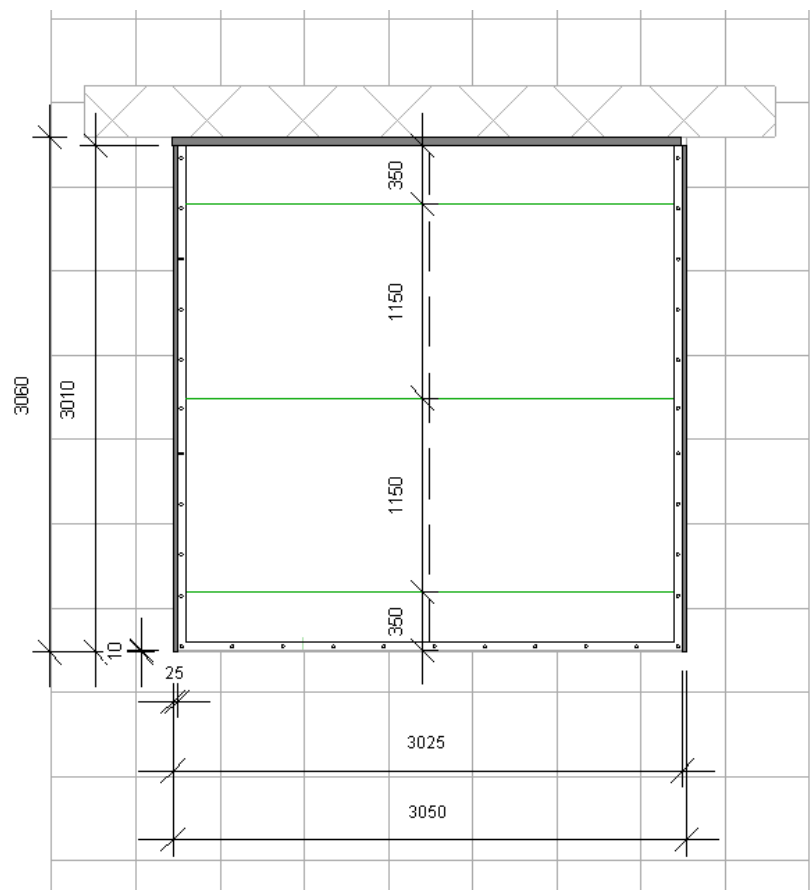


Figure 33. Front view of the assembly of the first sandwich panel wall – Test 4'.

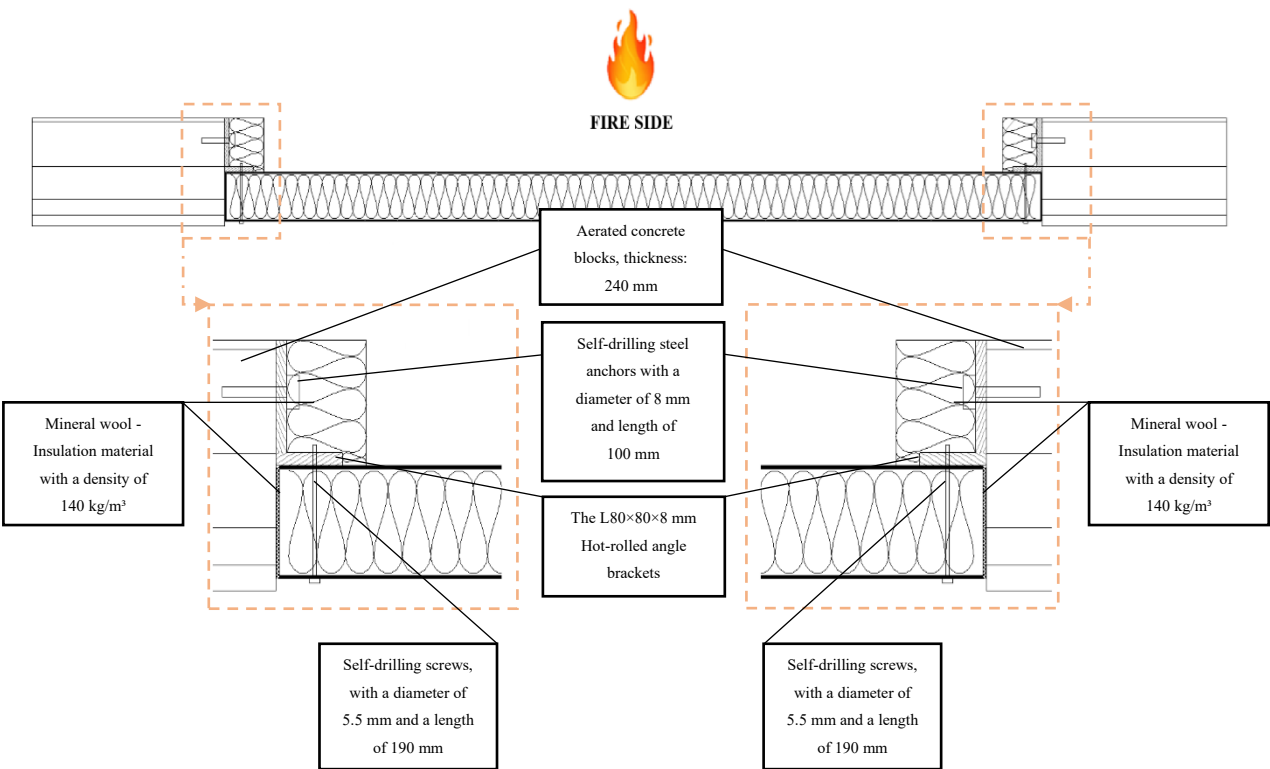


Figure 34. Horizontal cross section of samples evaluated assembled on mounting structure.

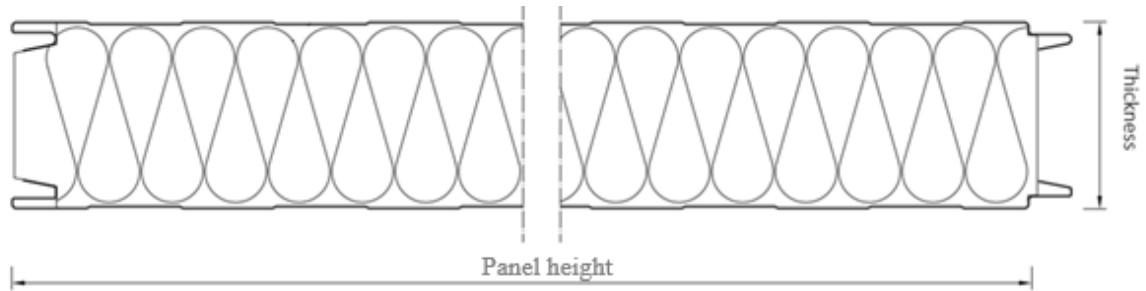


Figure 35. Cross-section of the geometry of the sandwich panel used.

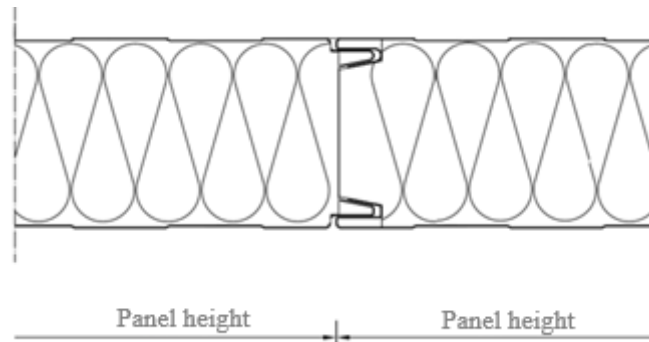


Figure 36. The assembly of sandwich panel during testing.

Figure 37 illustrates the wall view from unheated side for Test 1', Test 2', and Test 3'. Figure below presents the thermocouples positions and the measurement points of the horizontal displacement of the wall – see Appendix C. The description of the symbols used in Figure 37 are as follows:

- thermocouples for average and maximum temperature measurements from T1 to T5,
- thermocouples for maximum temperature measurement from T6 to T17,
- ▲ displacement measurement points from A to J.

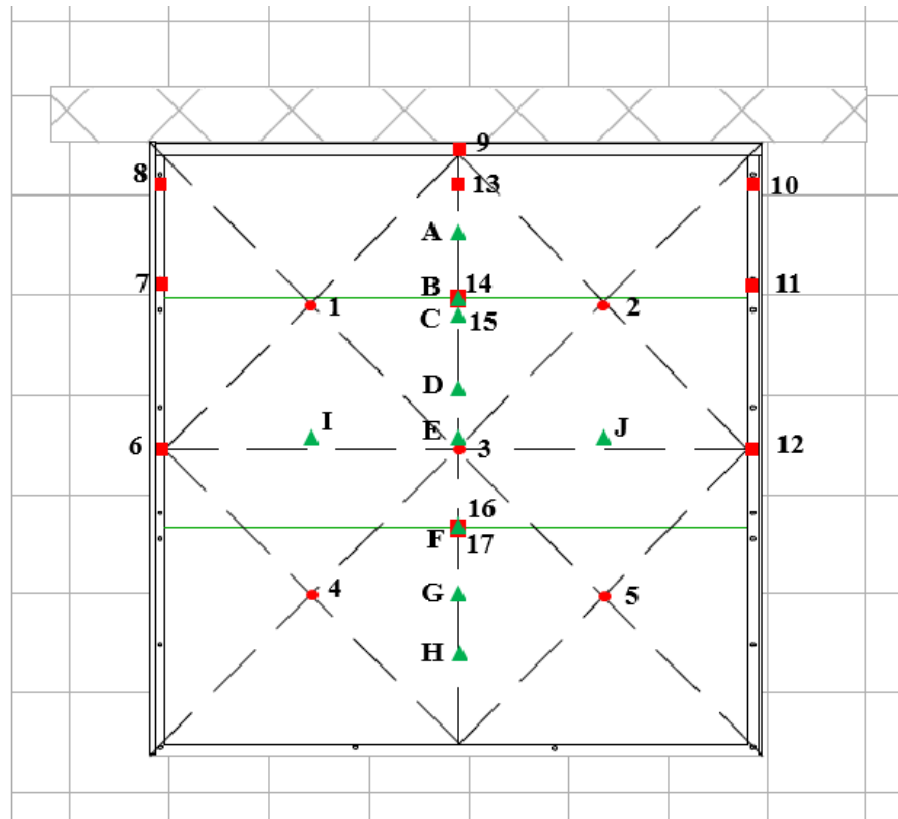


Figure 37. Measurement localizations of horizontal displacements and localizations of temperature sensors - view from unexposed side – Test 1', Test 2', and Test 3'.

Figure 38 illustrates the wall view from unheated side of the Test 4', due to different geometry of samples used to made tested. Figure presents the thermocouples positions and the measurement points of the horizontal displacement of the wall – see Appendix C. The description of the symbols used in Figure 38 are as follows:

- thermocouples for average and maximum temperature measurements from T1 to T5,
- thermocouples for maximum temperature measurement from T6 to T23,
- ▲ displacement measurement points from A to I.

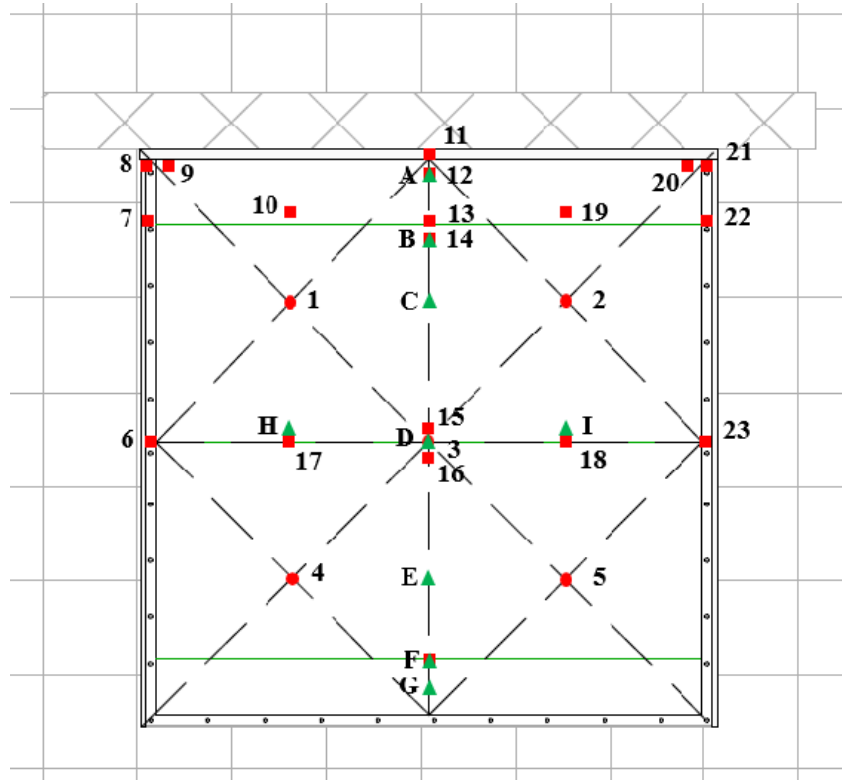


Figure 38. Measurement localizations of horizontal displacements and localizations of temperature sensors - view from unexposed side – Test 4'.

The thermocouples were installed with careful arrangement for the wires to be protected for as long as possible during the fire test. Thermal data were continuously monitored and recorded throughout the test for every 15 seconds, while the horizontal displacement of every wall structure was also measured. These displacement results will be discussed in the next chapter, as this chapter focuses on thermal behavior and cross-sectional heat transfer.

The prepared samples were assembled at an ambient air temperature approximately 21.1°C, with a relative humidity between 46% to 62%. Additionally, the furnace temperature was measured and monitored using multiple thermocouples arranged in accordance with EN 1363-1 [23] to ensure the accuracy of the furnace temperature in relation to the ISO standard fire curve [12]. The pressure sensor in the furnace was located at 0.37 m above the top edge of the test piece and was maintained at 23.1 Pa, which corresponds to a pressure of 20 Pa at the reference point (at the top edge of the wall).

Figure 39 shows the recorded temperatures, displayed as average, minimum, and maximum values, alongside the standard time-temperature fire curve for the duration of the test. The maximum temperature recorded on the heated side reached 1120°C.

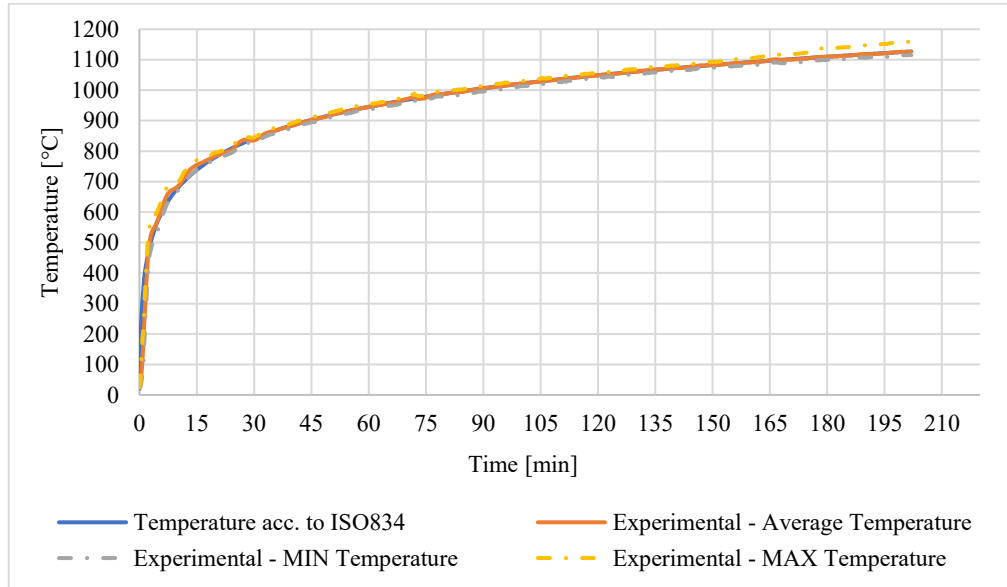


Figure 39. The time–temperature from the experimental test compared with the ISO 834.

### 4.3 Experiments of large-scale fire resistance tests

The fire test methods for a non-load-bearing wall were chosen in accordance with references [1] and [5], as previously mentioned, and following the assembly specified for each test (Section 4.2 Experimental setup). The tests were conducted with parameters presented in Table 4.

Table 4. Description of experimental large-scale tests.

Experiments	Durations	
Test 1'	3 h 02 min = 10,880 s	<p>Test 1': The tested wall assembly consisted of sandwich panels with a core material density of 100 kg/m<sup>3</sup> and a thickness of 150 mm. Each panel measured 150 mm in thickness, 3050 mm in height (3080 mm including the free edge insulation), and 1150 mm in width. The wall assembly was composed of three panels: two full panels with a width of 1150 mm and one cut panel with a width of 720 mm (measured as the external dimension). The panels were arranged horizontally, and their edges were interlocked using a</p>



		<p>specialized joint design to ensure a secure fit between them (Figure 36).</p> <p>The faces of the panels were made of steel sheets with a nominal thickness of 0.50 mm, manufactured from S280 GD + Z115 steel and coated with polyester. The core consisted of mineral wool lamellas, 150 mm thick, with a nominal density of 100 kg/m<sup>3</sup>. These lamellas were adhered to the steel facings using a one-component adhesive with an application rate of approximately 0.26 kg/m<sup>2</sup>.</p>
Test 2'	3 h 36 min = 12,120 s	<p>Test 2': The tested wall assembly consisted of sandwich panels with a core material density of 100 kg/m<sup>3</sup> and a thickness of 150 mm. Each panel measured 150 mm in thickness, 2950 mm in height (3010 mm including the free edge insulation), and 3010 mm in width. The wall assembly was composed of three panels: two full-width panels measuring 1150 mm, and one cut panel with a width of 650 mm (external dimension). The panels were arranged horizontally, and the edges of adjacent panels were interlocked using a specialized joint design, ensuring a secure fit between them (Figure 36).</p> <p>The faces of the sandwich panels were made of steel sheets with a nominal thickness of 0.50 mm, produced from steel grade S280 GD + Z115 and coated with polyester. The core material of the panels consisted of 150 mm thick mineral wool lamellas with a nominal density of 100 kg/m<sup>3</sup>. These lamellas were adhered to the steel facings using a one-component adhesive with an application rate of approximately 0.26 kg/m<sup>2</sup>.</p>

Test 3'	1 h 52 min = 5,500 s	<p>Test 3': The tested wall assembly consisted of sandwich panels with a core material density of <math>120 \text{ kg/m}^3</math> and a thickness of 100 mm. Each panel measured 100 mm in thickness, 3000 mm in height (3080 mm including the free edge insulation), and 3030 mm in width. The wall assembly was composed of three panels: two full-width panels measuring 1150 mm, and one cut panel with a width of 700 mm (external dimension). The panels were arranged horizontally, and the edges of adjacent panels were interlocked using a specialized joint design, ensuring a secure fit between them (Figure 36).</p> <p>The faces of the sandwich panels were made of steel sheets with a nominal thickness of 0.50 mm, produced from steel grade S280 GD + Z115 and coated with polyester. The core material of the panels consisted of 100 mm thick mineral wool lamellas with a nominal density of <math>120 \text{ kg/m}^3</math>. These lamellas were adhered to the steel facings using a one-component adhesive with an application rate of approximately <math>0.26 \text{ kg/m}^2</math>.</p>
Test 4'	3 h 01 min = 10,860 s	<p>Test 4': The tested wall assembly consisted of sandwich panels with a core material density of <math>95 \text{ kg/m}^3</math> and a thickness of 120 mm. Each panel measured 120 mm in thickness, 3000 mm in height (3050 mm including the free edge insulation), and 3000 mm in width. The wall assembly was composed of four panels: two full-width panels measuring 1150 mm, and two cut panels, each with a width of 350 mm (external dimension),</p>

mounted at the top and bottom. The panels were arranged horizontally, and the edges of adjacent panels were interlocked using a specialized joint design, ensuring a secure fit between them (Figure 36).

The faces of the sandwich panels were made of steel sheets with a nominal thickness of 0.60 mm, produced from steel grade S280 GD + Z and coated with polyester. The core material of the panels consisted of 120 mm thick mineral wool lamellas with a nominal density of 95 kg/m<sup>3</sup>. The lamellas were bonded to the steel facings using a one-component adhesive, applied at a rate of 0.21 kg/m<sup>2</sup>.

---

#### 4.4 Numerical modelling of thermal behavior

To simulate the thermal behavior of the sandwich panel, it is sufficient to model only a single representative element rather than the entire wall. This approach focuses specifically on the thermal response, which is the primary focus of this chapter. Additionally, it reduces analysis time and cost. In this study, ABAQUS software was used to conduct a numerical analysis of the specimen under test conditions. Each component of the model was designed with linear geometry to ensure accurate representation of real test behavior.

The facing was modelled as a 2D deformable shell extrusion with homogeneous and nonlinear geometry. For Tests 1', 2', and 3', the facing thickness was defined as 0.5 mm, while Test 4' had a facing thickness of 0.6 mm, in accordance with the specifications of each experiment. The core material, on the other hand, was modelled as a 3D solid extrusion, homogeneous, with nonlinear geometry. The core's thickness varied based on the parameters of each individual test.

The thermal analysis of the sandwich panel was conducted using a transient heat transfer step, to capture time-dependent heat flow. The response was configured for transient analysis, with the total duration of each test specified in the preceding section. Additionally, nonlinear geometric effects were disabled to focus exclusively on thermal

behavior. An automatic increment control was applied with an initial increment size of 15 s, as was captured experimentally. The direct method with the full Newton solution technique was used for the equation solver, with severe discontinuities set to propagate from the previous step. The thermal load variation with time was defined as instantaneous, with linear extrapolation of the previous state at the start of each increment. This setup was optimized to ensure precise and stable results in capturing the transient thermal response of the sandwich panel.

Thermal boundary conditions were implemented to account for heat fluxes due to convection and radiation across surfaces. Two convection interactions were defined as surface film conditions. For the surface with room temperature region, a film coefficient of  $0.009 \text{ W/mm}^2\cdot^\circ\text{C}$  ( $9 \text{ W/m}^2\cdot\text{K}$ ) was applied to the surface within the room temperature region, with a uniform room temperature of  $21.1^\circ\text{C}$  and an instantaneous amplitude, as specified in EN 1991-1-2 [67], which define standard ambient temperature conditions. For the fire exposed surface, a film coefficient of  $0.025 \text{ W/mm}^2\cdot^\circ\text{C}$  ( $25 \text{ W/m}^2\cdot\text{K}$ ) was assigned, in accordance with EN 1991-1-2 [67], which establishes convective heat transfer coefficients for fire resistance analysis.

Additionally, radiation interactions were incorporated into the analysis. For the room temperature surface, radiation was defined with an emissivity of 0.7, an ambient temperature of  $21.1^\circ\text{C}$ , and an instantaneous amplitude, consistent with the values provided in EN 1991-1-2 [67], which specify emissivity for construction materials in thermal assessments. Similarly, for the fire-exposed surface, an emissivity of 0.7 was applied, in line with the values recommended by EN 1993-1-2 [28], which define fire resistance testing conditions.

These interactions, applied as boundary conditions in the thermal analysis, were crucial in replicating the experimental thermal loading conditions as closely as possible.

To model on thermal contact behavior between the steel facing and core material, a Tie constraint was used. The core material, which consisted of mineral wool, was represented by 3D 8-node heat transfer linear solid elements with reduced integration points (DC3D8R). For the steel facing, an 8-node quadrilateral shell element (DS8) was selected. The temperature-dependent material properties were based on the tested specimen. Thermal properties of the core material were obtained from Table 3 reference [49], while the properties of the steel (S280GD+Z) were referenced from [29]. The thermal diffusivity values determined in Chapter 3 were not directly used in these

numerical simulations, because the study focus was on methodology development and presenting the heat behavior for a fresh sample rather than providing simulation inputs (thermal conductivity ( $\lambda$ ), specific heat capacity ( $C_p$ ), and density ( $\rho$ )). Additionally, Chapter 3 presents core material that differs in terms of the density used in the current chapter and next chapter.

A mesh sensitivity analysis was conducted, revealing that a mesh size of 20 mm was optimal for achieving presented results in our analysis. The initial temperature for the model was predefined at 21°C, with the temperatures on the heated surfaces set to match the values recorded in the furnace during the tests.

## 4.5 Thermal analysis results

In the results section of this chapter, we explore how each unheated side of the panel responds to fire scenario, based on four tests conducted with various configurations but the same composite materials (S280GD+Z, and mineral wool). Our focus is on thermocouples T1 to T5 for average and maximum temperature measurements, while data from thermocouples T6 to T17, which record maximum temperatures, is included in Appendix B. Each experimental and numerical graph is presented and discussed below, with attention given to the average values, as these will be used for our numerical comparisons. We will also compare the experimental averages from thermocouples T1 to T5 with the values calculated through our numerical models.

### 4.5.1 Experimental results

- **Test 1': Panel with 100 kg/m<sup>3</sup> core density, 150 mm core thickness, and 0.5 mm steel thickness**

The unheated surface of the panel with a core density of 100 kg/m<sup>3</sup> and a thickness of 150 mm exhibited a steady increase in temperature until 6000 s (Figure 40). After this point, temperatures began to stabilize, ranging between 120 °C to 140 °C. T2, to T4 showed similar profiles, stabilizing around 130 °C to 140 °C, while T1, and T5 recorded a slightly lower stabilization temperature of around 120 °C.

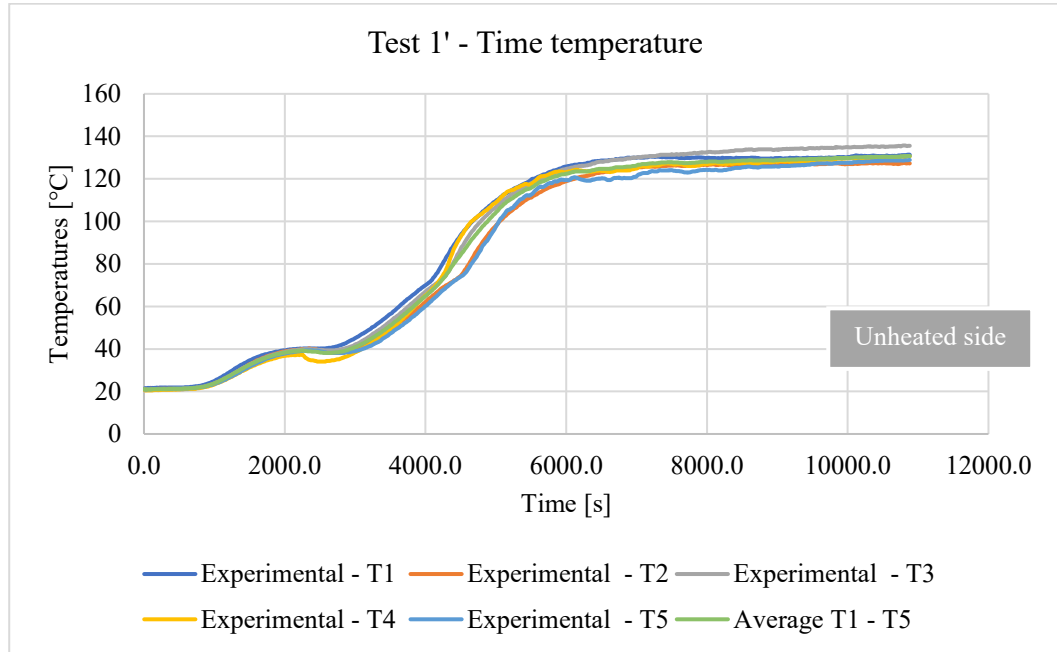


Figure 40. Time–temperature for the tested samples: (Test 1') — unheated face.

The consistent thermal profiles across T1 to T4 suggest uniform thermal properties and effective heat distribution within the panel. The slightly lower temperature at T5 could be due to localized differences in heat absorption or delamination of composite materials.

➤ Experimental test observations of test 1'

The first experimental test began with the heating process. After 55 s, cracking sounds were heard from the furnace. At 1 minute 50 s, slightly yellow smoke appeared from the top edge of the wall. By the 8 min, smoke was observed coming from the gap around T6 and T7. At 75 min, slight smoking was noted from the edges. At 163 min, a continuous flame appeared in the left corner. Theoretical the test should stop, but upon our request, heating was continued. The test concluded at 181 min 33 s.

▪ **Test 2': Panel with 100 kg/m<sup>3</sup> core density, 150 mm core thickness, and 0.5 mm steel thickness**

The unheated surface of the panel with a core density of 100 kg/m<sup>3</sup> and a thickness of 150 mm demonstrated a consistent initial temperature across all measurement points, starting at approximately 21.1 °C (Figure 41). As the thermal exposure continued, the temperature at all points rose steadily until 5000 s. During

this phase, the panel showed uniform heat absorption, indicating good thermal conductivity within the material.

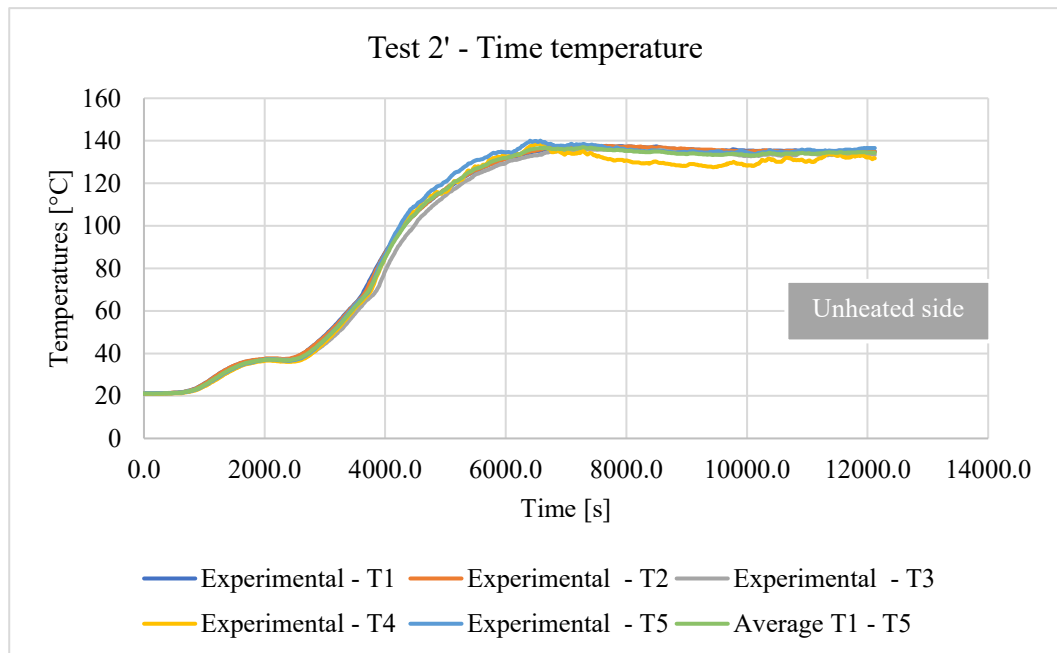


Figure 41. Time–temperature for the tested samples: (Test 2') — unheated face.

At time, 5000 s, the temperatures began to stabilize, ranging between 120 °C to 140 °C. This stabilization suggests that the panel reached a thermal equilibrium where the heat absorbed balanced with the heat dissipated. T4 showed a slightly lower peak temperature of about 100°C compared to the other measured points. This variation could be attributed to slight differences in material properties or local heat exposure at the measurement point – See deviations on Appendix B.

➤ Experimental test observations of test 2'

The second experimental test began with the start of heating. At 36 s to 1 min 40 s, cracking sounds were heard coming from the furnace. At 6 min 17 s, smoke was observed coming from the upper joint of the plates on the right side. By 13 min 20 s, a gap on the right side of the upper joint near T11 had started to widen, with a small leakage noted. As time progressed, periodic observations recorded further changes in gap widths. The test continued without significant incidents and concluded successfully until 202 minutes. The test continued without stopping because it did not encounter any criteria for failure. In fire resistance testing, the test duration is often predetermined

to assess how long a material or structure can maintain its integrity, insulation, and stability under prolonged exposure to elevated temperatures.

- **Test 3':** Panel with 120 kg/m<sup>3</sup> core density, 100 mm core thickness, and 0.5 mm steel thickness

The unheated surface of the panel in the third test with 120 kg/m<sup>3</sup> density and 100 mm thickness showed a similar initial temperature rise from around 21.1°C. The temperature increase was gradual, peaking between 3000 to 4000 s, and then stabilizing. T1 recorded the highest temperature, peaking just above 200 °C, while T2 and T5 stabilized around 180°C. T3 and T4 showed stabilization at slightly lower temperatures, between 160 °C and 180 °C.

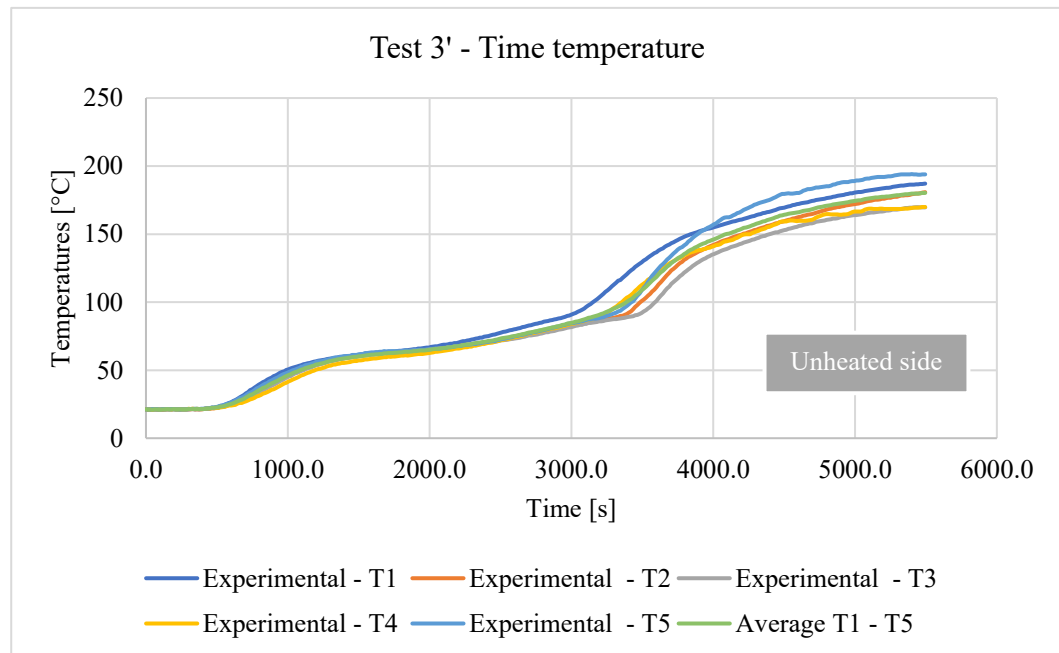


Figure 42. Time–temperature for the tested samples: (Test 3') — unheated face.

These results in Figure 42 highlight consistent thermal behavior across most measurement points, with T1 showing slightly higher thermal activity. This could indicate localized variations in material properties or differences in heat exposure, influencing the thermal equilibrium.

➤ Experimental test observations of the test 3'

The third experimental test began with the start of heating. At 36 s to 1 min 40 s, cracking sounds were heard from the furnace. From 5 min to 12 min, smoke was observed coming from under the top edge of the wall and the joint



of the full plates. At 61 min, slight browning appeared at the free edge of the material. By 75 min, some smoke gaps appear near T5. The test was concluded at 91 min 66 s as agreed, with no significant failures and meeting the required fire resistance and insulation standards.

- **Test 4': Panel with 95 kg/m<sup>3</sup> core density, 120 mm core thickness, and 0.6 mm steel thickness**

Figure 43 illustrates the temperature changes over time for T1 to T5. Each thermocouple shows a similar trend of a gradual increase in temperature, with all curves stabilizing around 160°C after approximately 10,000 s.

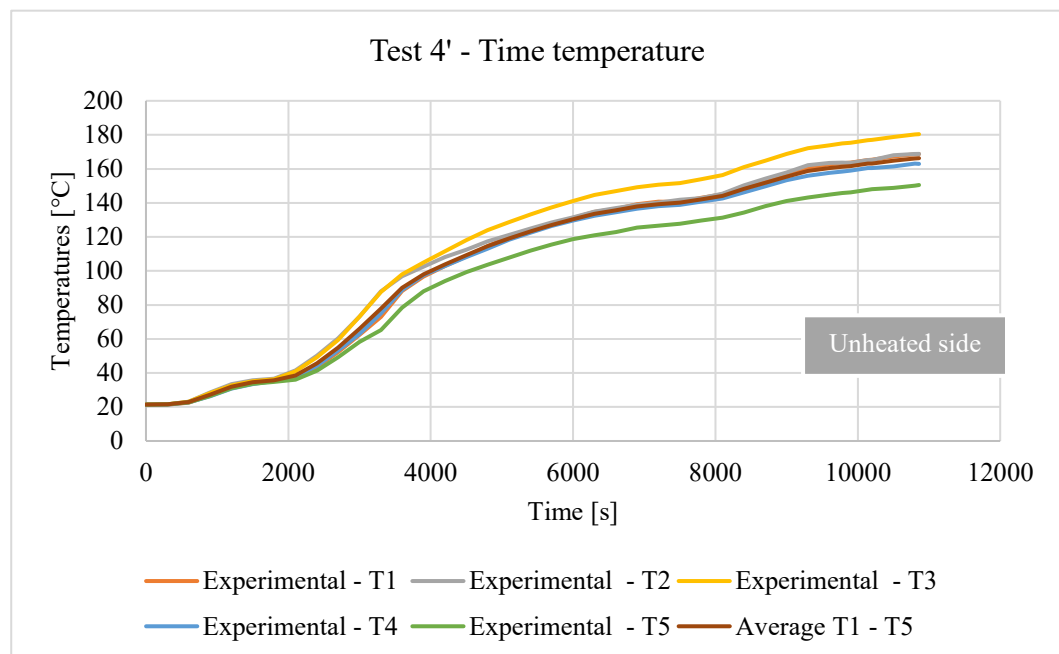


Figure 43. Time–temperature for the tested samples: (Test 4') — unheated face.

This close alignment among the individual thermocouple readings suggests that the panel's thermal response is consistent across its surface, with minimal variation between points. The average curve follows the same pattern, reflecting a steady heat increase that reaches equilibrium after prolonged exposure. This stability in temperature after 10,000 s implies effective heat distribution within the panel.

➤ **Experimental test observations of the test 4'**

The test began with the application of heat as the test before. At 50 s, cracking sounds were heard from the furnace resulting delamination of the panels on

the heated side. After 45 min, no significant changes were visible on the unheated side. This lack of visible changes continued at intervals of 60 min, 120 min, and 180 min. However, at 94 min, an increase in the gap width was noted between panels in joint D. The test was terminated at 181 min without further significant observations.

Figure 44 serves as a concise summary, capturing the average values from all previously presented results of Experimental Tests 1', 2', 3', and 4' into a single, comprehensive visualization.

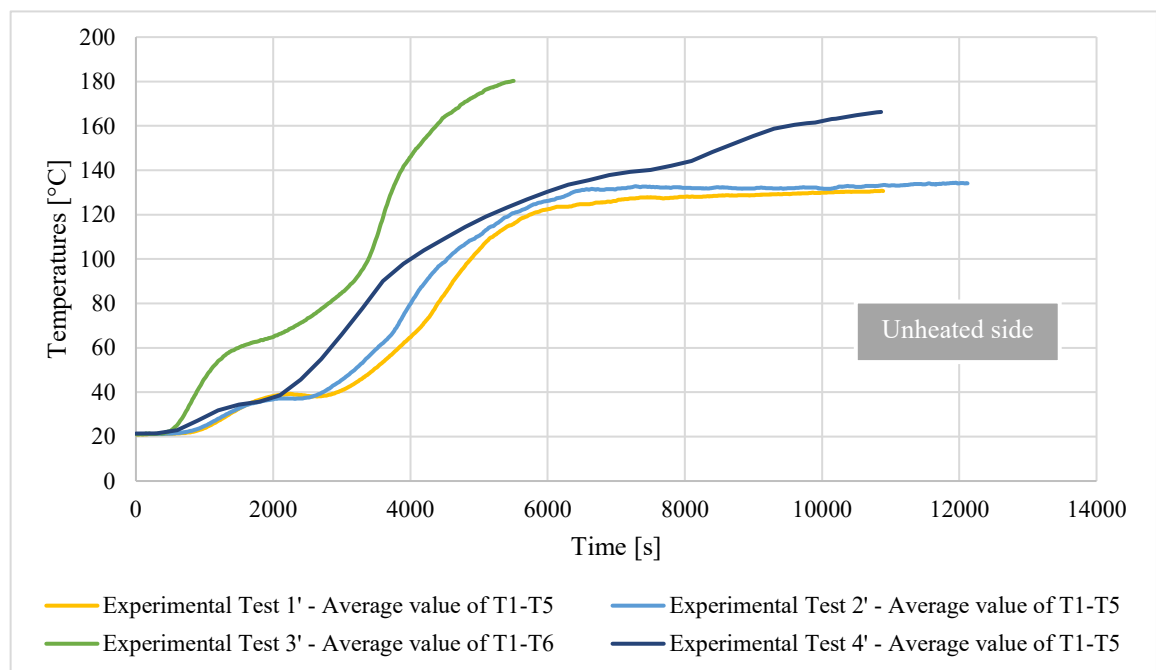


Figure 44. Average Time-temperature for all tested samples — unheated face.

The chart effectively illustrates both the common patterns and deviations between the tests. The consistent initial temperature rise observed across all configurations reflects the uniform thermal behavior of the mineral wool core material during the early stages of heat exposure. However, as the tests progress, the variations in temperature progression become apparent, highlighting the distinct structural responses and fire resistance capabilities of each panel configuration.

- Average of Test 1' reflects a gradual and steady rise in temperature over time. This aligns with the early cracking sounds observed at 55 seconds and smoke emissions detected by 110 seconds. The continuous flame recorded at 9,780 seconds (163 minutes) corresponds with the slight increase in the temperature curve toward the

later stages. Despite this critical point, the test continued until 10,893 seconds (181 minutes and 33 seconds) without abrupt failure.

- Average of Test 2' shows a steady increase similar to Test 1', with periodic rises corresponding to smoke observations at 377 seconds (6 minutes 17 seconds) and gap widening starting at 800 seconds (13 minutes 20 seconds). The sustained plateau observed near 12,120 seconds (202 minutes) reflects the panel's structural stability under prolonged heat exposure, as no significant failures were recorded.
- Average of Test 3' displays a much steeper initial temperature rise, corresponding to early cracking sounds and smoke emissions between 36 seconds and 100 seconds (1 minute 40 seconds). The rapid thermal increase aligns with visual signs of degradation and smoke gaps observed from 300 seconds (5 minutes) to 720 seconds (12 minutes). The test concluded earlier at 5,506 seconds (91 minutes and 66 seconds) while still meeting fire resistance standards [5].
- Average of Test 4' presents a gradual but persistent increase in temperature, corresponding with early cracking sounds heard at 50 seconds and panel delamination on the heated side. A widening of the gap at joint D, observed at 5,640 seconds (94 minutes), aligns with a slight acceleration in the temperature curve. The steady progression until 10,860 seconds (181 minutes) reflects the panel's maintained structural integrity throughout the test.

Overall, experimental tests highlight both the material's response to heat exposure and the variations in behavior under prolonged thermal stress. These results mark a significant achievement in understanding the fire resistance and durability of mineral wool core panels.

#### **4.5.2 Numerical results**

In this section, the numerical results concerning the thermal behavior of mineral wool sandwich panels with varying core densities, core thicknesses, and steel facing thicknesses are analyzed based on the preceding experimental investigations. Tests 1' and 2' produced comparable thermal responses due to their identical core density, core thickness, and steel facing thickness. In contrast, Tests 3' and 4', characterized by variations in core densities, core thicknesses, and steel facing thicknesses, demonstrated the significant influence of these parameters on the distribution and progression of temperature throughout the panel section.

Figures 45, 46, 47 illustrates the numerically simulated nodal temperature distributions in the sandwich panel at three selected time points:  $t = 1$  minute,  $t = 10$  minutes, and  $t = 67$  minutes, corresponding to heated side surface temperatures of approximately  $72^\circ\text{C}$ ,  $664^\circ\text{C}$ , and  $905^\circ\text{C}$ , respectively. The results demonstrate the transient development of the thermal field across the panel thickness under standard fire exposure conditions. By comparing all tests, the numerical analysis highlights the influence of material properties and structural configuration on temperature stability.

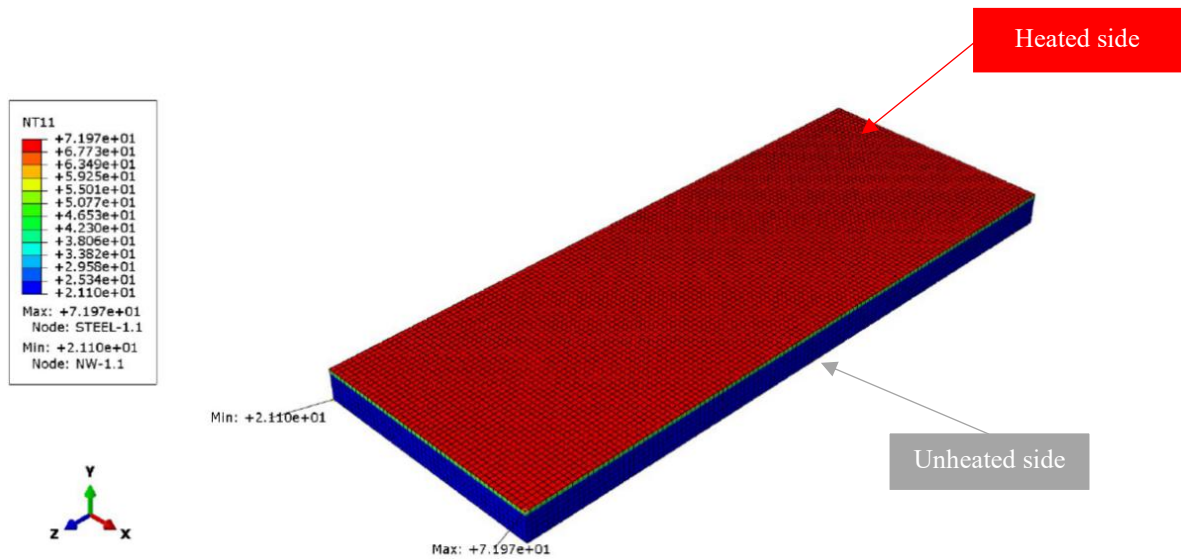


Figure 45. 3D Nodal temperature distribution at  $t = 1$  min (Heated side:  $72^\circ\text{C}$ ) – Test 1'.

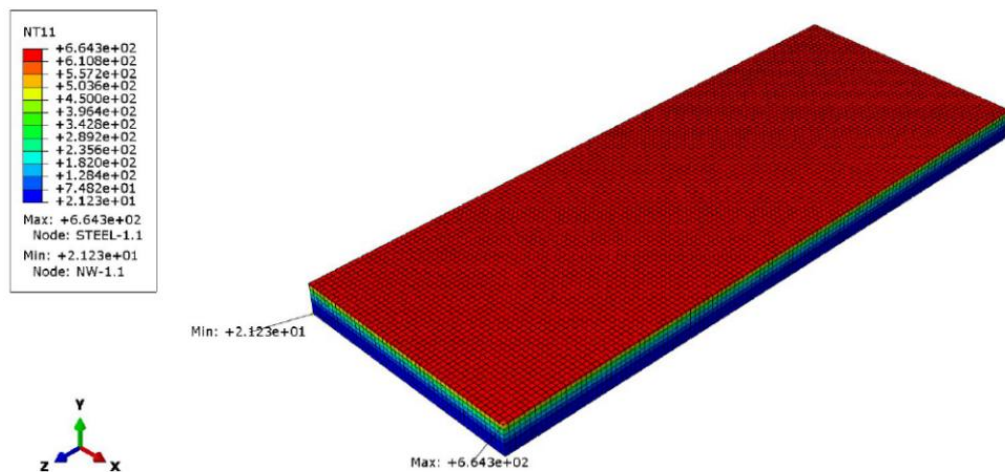


Figure 46. 3D Nodal temperature distribution at  $t = 10$  min (Heated side:  $664^\circ\text{C}$ ) – Test 1'.

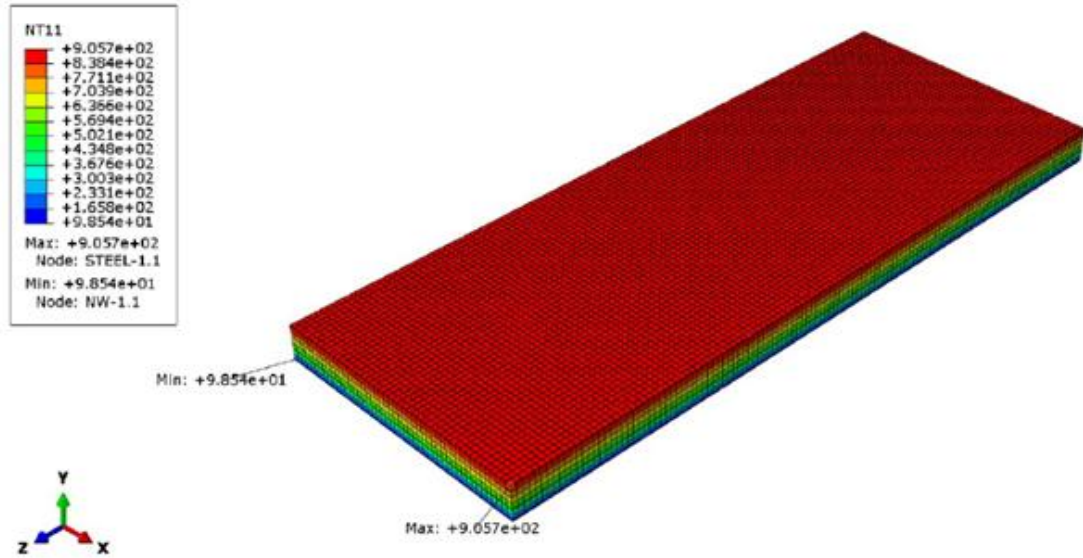


Figure 47. 3D Nodal temperature distribution at  $t = 67$  min (Heated side:  $905^{\circ}\text{C}$ ) – Test 1'.

- **Test 1' & Test 2': Panel with core material  $100\text{ kg/m}^3$  density and  $150\text{ mm}$  thickness -  $0.5\text{ mm}$  steel thickness**

Figure 48 illustrates temperature changes over time between experimental tests (1' and 2') and numerical analysis results. Both experimental tests show a rapid temperature rise in the initial phase, stabilizing around  $120^{\circ}\text{C}$  after approximately  $5000\text{ s}$ . A noticeable deviation occurs around  $1500\text{ s}$ , due to the delamination of the face material from the core, which initiates radiative heat transfer between facing and core material.

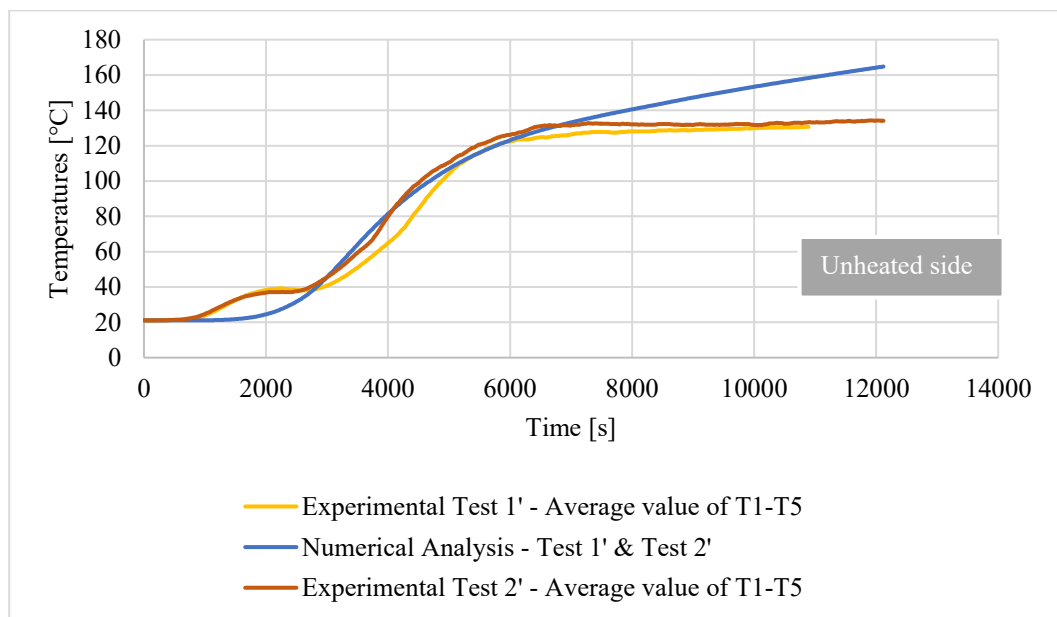


Figure 48. Thermal response of panels in Tests 1', and 2'- Experimentally and numerically.

In contrast, the numerical analysis initially aligns with the experimental results but continues to rise beyond the stabilization point of the experimental tests. Although the numerical model includes temperature-dependent thermal properties, this alone does not fully capture the physical behavior, as it omits mechanical changes that may occur in the first minutes or around 30 min. This suggests that incorporating both thermal and mechanical factors is necessary for modelling the material's behavior over time.

- **Test 3': Panel with  $120 \text{ kg/m}^3$  core density, 100 mm core thickness, and 0.5 mm steel thickness**

The second comparison between the experimental and numerical results for Test 3' reveals notable differences in the temperature development over time. Both results (experimental, numerical) initially exhibit a rapid temperature increase, indicating good agreement in the early phase of thermal exposure. However, a deviation emerges after approximately 1000 s, where the numerical simulation begins to predict consistently higher temperatures than those recorded experimentally. This behavior is illustrated in Figure 49, which presents the temperature progression for both tests.

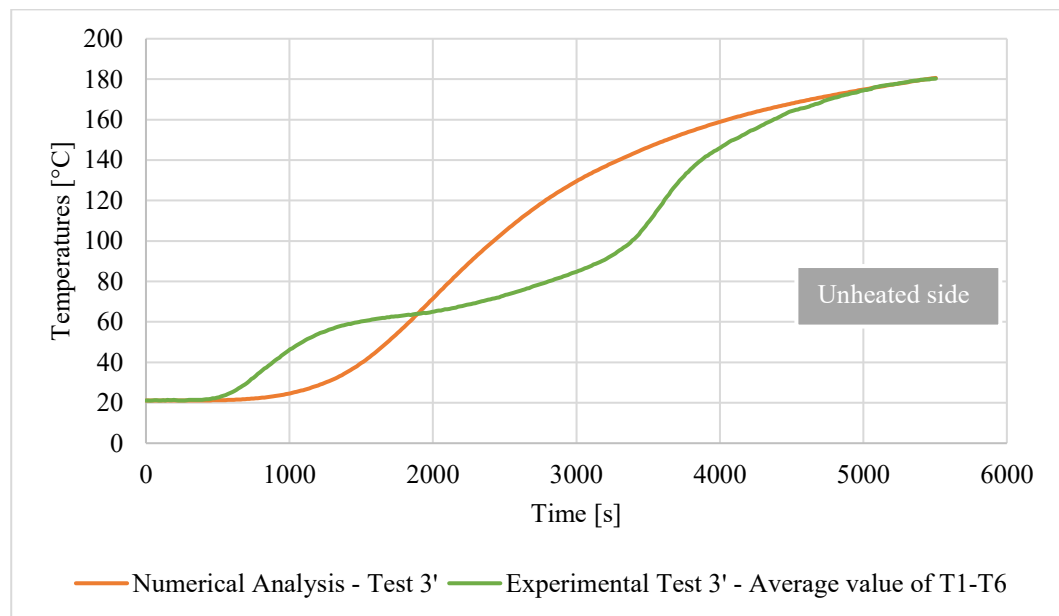


Figure 49. Thermal response of panels in Tests 3'- Experimentally and numerically.

In the experimental setup, the temperature stabilizes at approximately 175 °C, whereas the numerical results continue to increase, only reaching a similar value

near the end of the analyzed time interval. This discrepancy suggests that, although the numerical model accurately captures the general thermal trend, it does not fully account for physical phenomena present in the experimental conditions. Such phenomena may include material delamination, radiative heat transfer, and chemical transformations within the mineral wool insulation, all of which can significantly influence thermal conductivity and heat retention during fire exposure.

- **Test 4': Panel with 95 kg/m<sup>3</sup> core density, 120 mm core thickness, and 0.6 mm steel thickness**

Similarly, the thermal response of the sandwich panel in Test 4' was evaluated by comparing the experimental results with the results of numerical analysis. Initially, both the experimental and numerical curves follow a similar upward trend. However, a noticeable divergence occurs around 2000 s, with the numerical analysis predicting significantly higher temperatures than observed experimentally. This behavior is illustrated in Figure 50, which presents the temperature development over time on the unexposed side of the panel. The experimental temperature curve gradually stabilizes below 160°C, whereas the numerical model continues to rise, reaching over 200°C by the end of the time.

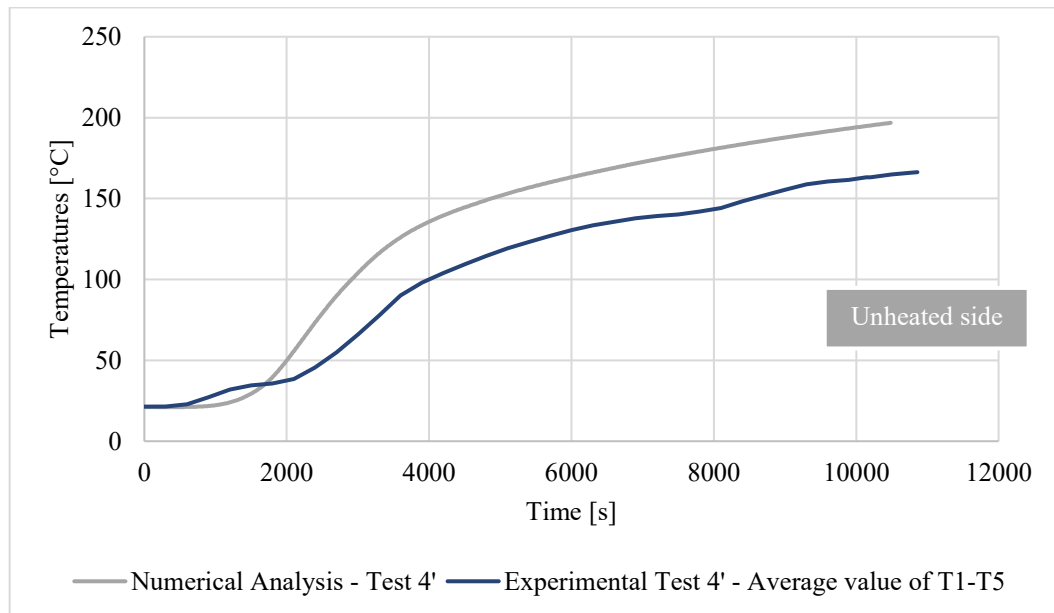


Figure 50. Thermal response of panels in Tests 4'- Experimentally and numerically.

This divergence highlights potential limitations in the thermal model developed, particularly regarding the influence of physical behaviors. This discrepancy underscores the importance of incorporating cohesive behavior in thermomechanical analysis, which will be discussed in the next chapter. Integrating these cohesive properties is essential for capturing interactions and material separation under thermal stress, aligning the numerical predictions more closely with experimental observations.

Based on the results of Tests 1', 2', 3', and 4', it can be noticed that the thermal response of sandwich panels is significantly influenced by variations in core density, core thickness, and steel facing thickness. Higher core densities, as in Test 3' (120 kg/m<sup>3</sup>), enhance thermal resistance, leading to a higher stabilization temperature, while lower-density cores, as in Test 4' (95 kg/m<sup>3</sup>), allow for faster temperature increases over time. Thicker cores, such as the 150 mm core in Tests 1' and 2', provide additional thermal resistance and contribute to a slower initial temperature rise. However, when paired with lower core density or thinner steel, as seen in some tests, this advantage is lessened, indicating that an optimal balance of core density and thickness is essential for achieving improved thermal performance.

Across all tests, the numerical model diverges from experimental data at higher temperatures and extended time frames, particularly due to the lack of consideration for mechanical effects like delamination and radiation between separate layers. These mechanical behaviors, which are significant in real test scenarios, impact thermal performance by altering heat transfer dynamics. Incorporating cohesive behavior in thermomechanical analysis, including delamination and separation phenomena, will be crucial for modelling the material's behavior, as discussed in the upcoming chapter. This overall analysis underscores the importance of both thermal and mechanical considerations in panel design for reliable, long-term performance.

#### **4.6 Summary and conclusions**

The chapter underscores the influence of core density and thickness on the thermal performance of sandwich panels. The study examines the construction method, test conditions, and results obtained when a specific element with the described structure is assessed in accordance with the procedures outlined in section 4.2 and section 4.3.

The time-temperature analysis of sandwich panels with mineral wool cores highlights the significant influence of core density and thickness on both thermal and



mechanical behavior. The consistent initial temperature rise followed by stabilization across different configurations underscores the panels' ability to manage thermal exposure effectively. The variations between measurement points shown in appendix B suggest that local material properties and heat exposure play a role in thermal performance. This analysis enhances the understanding of the thermal dynamics of sandwich panels, supporting their effective use in engineering and construction.

The numerical analysis presented in the chapter provides proximate results near to reality as it was described and illustrated. Additionally, the numerical results of this chapter indicate the importance of the sensitivity of microstructural parameters. Additionally, highlight the effect or influence of stress strain of the structure on thermal behavior.

Due to the nature of fire resistance tests and the associated difficulties in quantifying the uncertainty of fire resistance measurements, it may be possible to determine the precise accuracy level of the heat transfer results from the experimental test if additional behaviors are considered. The data presented in the chapter supports the panel designs for applications requiring specific thermal performance characteristics, thereby contributing valuable knowledge to the field.

## **Chapter 5. Thermomechanical evaluation and finite element analysis**

### **5.1 Introduction**

In this chapter, the thermomechanical response of sandwich panels with a MW core material is analyzed based on the experimental tests presented in the previous chapter, alongside comparisons with numerical analysis findings. The horizontal displacement results from the previous tests are presented in a dedicated section and will be utilized for comparison with finite element model (FEM) results. The horizontal displacement is examined through two finite element groups, providing a detailed exploration of their structural performance under thermal and mechanical influences.

In the first developed group of analysis, a 3D shell composite model was used to gain a detailed view of global displacement. Simplified support conditions such as fixed beam, fixed-pinned beam, and fixed-roller configurations were applied to streamline the approach and serve as a basis for comparison. This simple setup allows for the observation of boundary condition influences on displacement directions on the models behavior and that will be presented as a section with corresponding results.

In the second developed group of analysis, a coupled thermal-stress analysis is employed to investigate the impact of a large fire scenario on the structural stability of the wall panel. The numerical analysis is compared with the experimental tests presented in the previously, with a specific focus on evaluating the horizontal displacement of the panel. This is achieved through the development of a 3D thermomechanical model. This chapter includes an outline of the numerical simulation setup and a detailed description of key considerations for the analysis. This approach provides a structured framework for assessing and interpreting displacement, delamination effects, and thermomechanical interactions within the tested materials. The chapter concludes with key findings from the thermomechanical analysis.

### **5.2 Deformation of sandwich panels**

Before discussing the modelling process, it is important to present the results of the previously conducted tests described above, providing a general visualization of the displacement behavior of sandwich panels when subjected to fire. This section focuses on analyzing the horizontal displacement behavior panel wall under fire scenarios, based

on the large-scale tests conducted. The Test 1', Test 2', Test 3', and Test 4' were performed following the experimental setup and procedures outlined in Sections 4.2 and 4.3. Figures 37 and 38, introduced in Section 4.2, serve as references to identify the specific displacement locations of each measured point discussed below on the tested wall panels.

From results below the Tests 1' and 2' reveal both expansion and contraction trends, demonstrating the considerable influence of boundary conditions and localized thermal effects. Meanwhile, Tests 3' and 4' show dominant contraction responses, with more pronounced negative displacement influenced by thermal contraction, material properties, and asymmetrical constraints. These results highlight the significance of thermal gradients, material variability, and boundary configurations in influencing the structural performance of sandwich panels. All measurements presented below were taken on the unheated surface, with negative values indicating panel displacement toward the heated side.

- **Test 1': Panel with 100 kg/m<sup>3</sup> core density, 150 mm core thickness, and 0.5 mm steel thickness**

The horizontal displacement trends observed in the graph below (Figure 51) indicate distinct behaviors across the tested wall regions. The measured points are indicated as mentioned before in Figure 37. In the upper panel, points A, B, and C show the most significant positive displacement trends, reflecting progressive outward movement due to reduced structural constraints and exposure to thermal or mechanical effects. These points, being less constrained, experience greater deformation, with point C exhibiting slightly lower displacement than A and B, as it is influenced by panel joints effects.

In the middle panel, points D and E display moderate and stabilized positive displacement trends, indicating balanced deformation due to structural rigidity. Points I and J, located near the edges, exhibit contrasting displacement behaviors. Point J shows significant positive displacement, indicating progressive outward movement. In contrast, point I displays a trend of slight negative displacement followed by stabilization over time.

In the lower panel, point F shows an initial increase in positive displacement, followed by a temporary decline around 4000–6000 s, and then a significant upward trend toward the end. Points G and H exhibit similar patterns of initial displacement

increase, subsequent stabilization, and moderate positive movement afterward, with H showing slightly lower values than G. This behavior indicates varying deformation responses influenced by time and positioning within the lower panel.

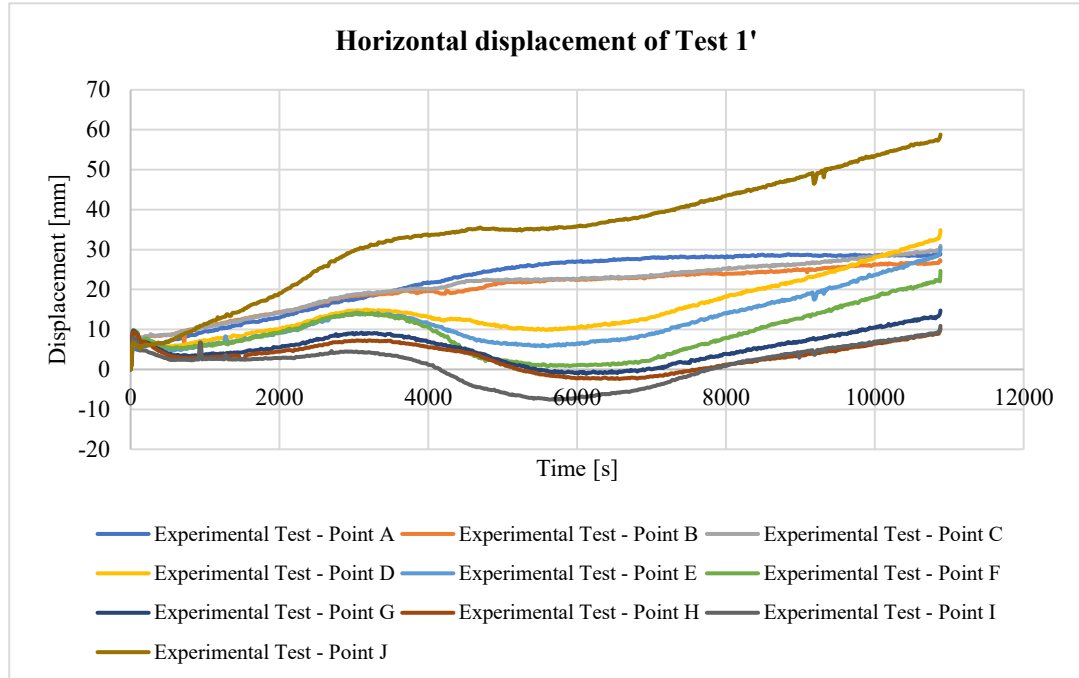


Figure 51. Horizontal displacement at measured points in Test 1'.

The overall behavior indicates greater outward movement in less constrained areas (upper panel and middle panel), while the boundary conditions effects in lower panel and edge points moderate the deformation. These trends are driven by a combination of thermal expansion and mechanical loading. However, the variability in displacement trends across points A to J highlights the non-uniform deformation of the panel, which may be attributed to factors such as material anisotropy, thermal gradients, or boundary conditions.

- **Test 2': Panel with 100 kg/m<sup>3</sup> core density, 150 mm core thickness, and 0.5 mm steel thickness**

The horizontal displacement trends observed in Test 2' (Figure 52) exhibit distinct behaviors across the upper, middle, and lower panels of the wall. The measured points are indicated as mentioned before in Figure 37. In the upper panel (points A, B, and C), significant positive displacement trends are evident, with

points A and B showing the greatest outward movement. Point C exhibits slightly lower displacement, as it is influenced by joints effects.

In the middle panel (points D, E, I, and J), moderate and stabilized positive displacement trends are observed for points D and E, indicating balanced deformation. Points I and J, located near the edges, also display positive displacement, though slightly reduced compared to central points, reflecting the moderating influence of boundary conditions.

In the lower panel, point H initially deviates into negative displacement, followed by a steady transition where the panel changes direction, leading to positive displacement trends. Point F shows a continuous and significant increase in positive displacement over time, while point G exhibits a gradual upward trend, maintaining slightly higher values than point H throughout the test.

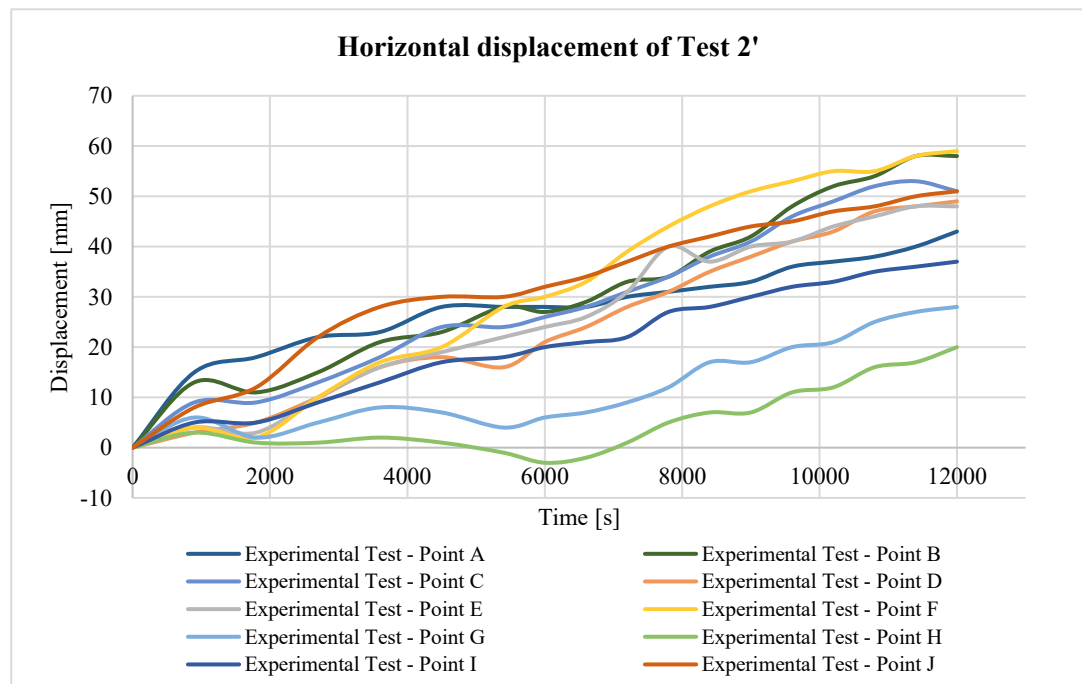


Figure 52. Horizontal displacement trends at measured points in Test 2'.

The overall behavior demonstrates greater outward movement in less constrained areas, including the upper, middle, and lower panels, while boundary effects at the lower panel and edge points moderate the deformation. The variability in displacement trends across points A to J also underscores the non-uniform deformation observed throughout the panel.

- **Test 3':** Panel with 120 kg/m<sup>3</sup> core density, 100 mm core thickness, and 0.5 mm steel thickness

The horizontal displacement trends observed in Test 3' (Figure 53) show distinct behaviors across the upper, middle, and lower panels. The measured points are indicated as mentioned before in Figure 37. In the upper panel (points A, B, and C), point C exhibits slightly positive displacement, while points A and B transition to negative displacement over time, indicating varying deformation responses.

In the middle panel (points D, E, I, and J), negative displacement trends are observed, with point E showing the largest downward movement. Points I and J, located near the edges, exhibit slightly less negative displacement compared to central points, suggesting the influence of boundary effects.

In the lower panel (points F, G, and H), negative displacement is evident and varies among the points. Point F initially shows moderate negative displacement, but it deviates significantly downward, reaching the lowest value among the points, before recovering slightly. Points G and H exhibit more constrained negative displacement trends, with H showing the least downward movement, reflecting localized deformation and boundary influences.

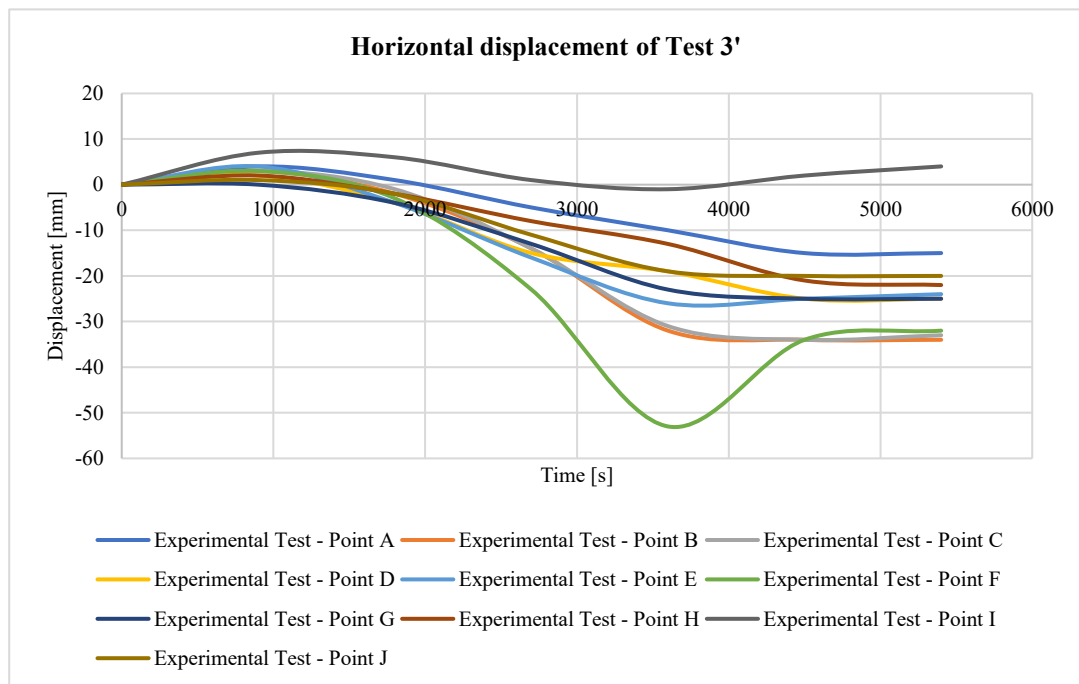


Figure 53. Horizontal displacement at measured points in Test 3'.

- Test 4': Panel with 95 kg/m<sup>3</sup> core density, 120 mm core thickness, and 0.6 mm steel thickness

The horizontal displacement trends observed in Test 4' (Figure 54) reveal varied deformation behaviors across the upper, middle, and lower panels. The measured points are indicated as mentioned before in Figure 38. In the upper panel (points A, B, and C), points A and B exhibit moderate negative displacement, while point C shows slight positive displacement, suggesting localized expansion or reduced constraints.

In the middle panel (points D, E, H, and I), significant negative displacement is observed, with points D and E showing the greatest contraction. Points H and I, located near the boundaries, display slightly less negative displacement, as it is influenced by their proximity to structural edges.

In the lower panel (points F, G), point F shows significant positive displacement, while point G exhibits substantial negative displacement. The displacement of all points highlights dominant negative displacement across most regions, with localized positive displacement at points F and G.

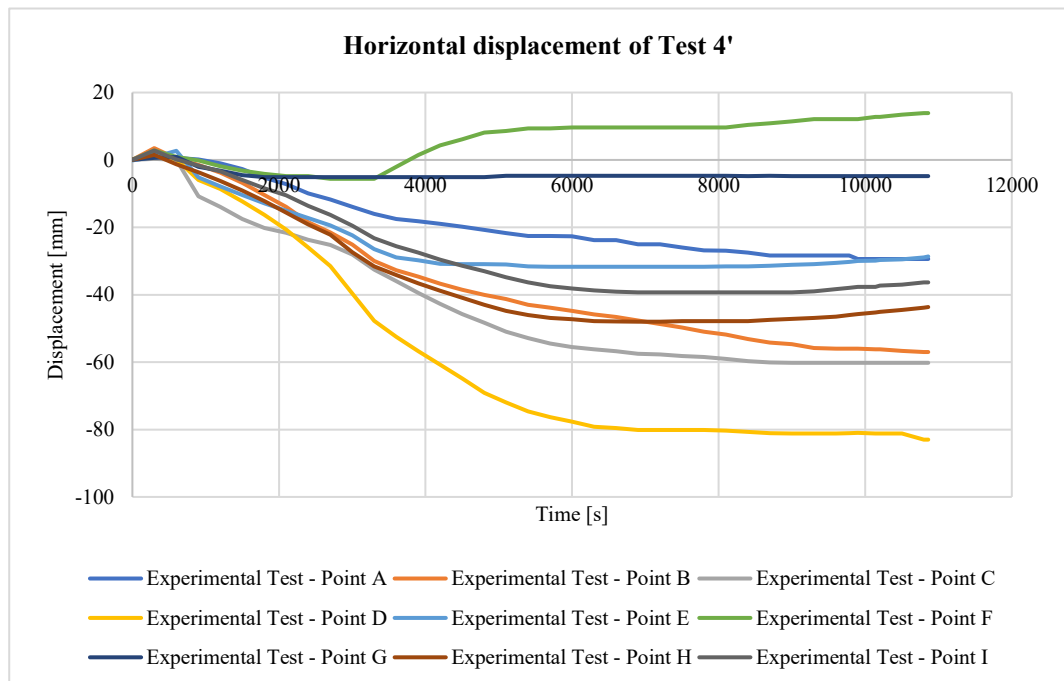


Figure 54. Horizontal displacement at measured points in Test 4'.

In Test 1' and Test 2', the heated steel facing underwent outward displacement primarily due to thermal expansion. The design of these panels allowed the thermal elongation to manifest as a bowing outward rather than structural collapse. During the fire scenario, the heated side pushed outward because its expansion was partly restrained by cooler regions and edge fixings, creating a bowing effect. The magnitude of outward displacement in these tests was moderated by the panel's mechanical properties: a thicker face and rigid core can distribute the thermal strain more evenly, preventing early instability.

The panel thickness and core density in Tests 1' and 2' were higher than in later tests, contributing to their outward displacement behavior. A thicker cross-section increases the panel's flexural stiffness, making it less prone to bending inward. Meanwhile, a high-density core firmly supports the steel skins, keeping them parallel and resisting instability. As known, the core material role is to hold the steel faces and prevent buckling either inward or outward.

In Test 3', and Test 4' exhibited a pronounced inward displacement of the heated facing, meaning the panel bowed towards the heat-exposed side (concave on the fire side). This occurred because the expansion of the steel was restrained enough to build significant compressive stress in the hot face, but the panel's configuration made outward bulging less feasible. In this test, the combination of panel thickness and core stiffness may have been such that the panel resisted uniform outward bending, leading the steel sheet to wrinkle or buckle toward the core (inward).

Across Tests 1' through 4', the displacements of the composite panels under heat were governed by a competition between thermal expansion and mechanical stability. In Tests 1' and 2', the steel faces expanded outward, creating a bulging deformation. The combination of thick facings, dense cores, and moderate restraint allowed thermal expansion to be relieved by outward bowing without immediate loss of structural integrity. Audible cracking in these tests signaled the onset of face-core delamination, but the panels remained largely intact as the expansion was accommodated by outward deflection. In contrast, Tests 3' and 4' showed that when thermal expansion is highly restrained, the resulting compressive forces can trigger buckling of the steel face. Test 3', with slightly less robust parameters, reached a point of instability where the hot face buckled inward. Test 4, with the weakest core and most rigid boundary conditions, experienced the most severe inward displacement. This demonstrates a clear relationship



with stronger, thicker panel with better support tend to bow outward under heat (dominated by thermal expansion), whereas more slender or constrained panels buckle inward (dominated by mechanical instability). Furthermore, boundary conditions critically influence these outcomes: a freely expanding panel will deform more benignly, while a tightly restrained panel accumulates stress and is prone to sudden failure.

In summary, the displacement trends differ between the tests because of variations in boundary condition. Tests 1' and 2' were governed by thermal expansion producing outward deflection, whereas Tests 3' and 4' were governed by structural buckling producing inward deflection. Understanding this interplay is crucial for predicting sandwich panel behavior in fire.

### **5.3 Parameters considered for thermomechanical analysis**

Modelling sandwich panels using FEM under elevated temperatures or fire conditions, it is essential to consider several factors could influence overall performance of the panel simulated. As the material properties must be defined as a function of temperature, which was illustrated in chapter 3. The definition of interactions and contact properties at the interface allows also for realistic simulation of interfacial behavior, including potential detachment. Fasteners, boundary conditions, and model size also play key roles in capturing stress distribution and panel stability. Key considerations include in the investigation of the following aspects:

- Material properties as a function of temperature

Defining the temperature-dependent material properties of each material such as thermal expansion, conductivity, and degradation characteristics is crucial for realistic simulation results. These properties ensure that the model captures the behavior of both the facing and core materials under thermal exposure, as was mentioned in above chapters.

- Boundary conditions

Defining boundary conditions is essential to reflect realistic constraints and support conditions that the panel may experience. Boundary conditions influence stress distributions particularly near the panel edges, which can affect interfacial stability under thermal loads.

- Adhesive layer modelling (interaction properties)

ABAQUS software offers Cohesive Zone Modeling (CZM) tools that are based on the traction–separation law and enable progressive simulation of damage initiation and evolution. Accurate definition of cohesive interaction is essential for predicting interfacial behavior under thermal stress, particularly the onset and propagation of delamination. The significance of cohesive contact in such analyses has also been highlighted by [66, 68,74], as it becomes particularly important when debonding occurs between the steel face sheets and the mineral wool insulation.

Experimental observations have reported audible signs of interfacial failure within the first 36–60 seconds of heating, underscoring that the traditional assumption of a perfectly bonded interface is unrealistic under fire exposure. To simulate this behavior, ABAQUS provides cohesive contact modeling capabilities that allow for the capture of interface degradation due to thermomechanical effects.

In the research, the maximum separation criterion was used to take into account the dominant role of large interfacial displacements in the debonding of materials under the influence of temperature. This criterion provides improved numerical stability and corresponds well with observed delamination behavior, especially under conditions where adhesive stiffness is significantly reduced. In ABAQUS, the maximum separation criterion specifies that damage initiates when the relative separation attains a critical value in either the normal or shear direction [63]. This approach was selected due to the unavailability of direct cohesive strength data (i.e., stress at failure) between the steel and mineral wool core material. Instead, a tolerable separation before bond failure under thermal loading could be more reliably estimated. The discussion and justification for parameter selection are presented in section 5.4.2.

Furthermore, similarly to [69], a linear softening behavior was used to characterize the progressive loss of load-carrying capacity after peak traction. The implementation of a cohesive contact formulation has been considered essential for capturing the failure mechanisms in sandwich panel systems exposed to elevated thermal loading. Various cohesive formulations, including linear softening [69, 70], trapezoidal [71], and bilinear softening models [72], have been utilized to describe interface degradation mechanisms within such frameworks, enabling a robust

characterization of mixed-mode delamination and impact-induced damage phenomena in composite structures.

To facilitate an efficient and physically meaningful representation of adhesive behavior under thermal loading, the cohesive model in ABAQUS was implemented. This implementation comprised three principal components: the Traction–Separation Law, the Damage Initiation Criteria, and the Damage Evolution Law.

➤ Traction–Separation Relationship

In the initial (undamaged) phase, the interaction between the nominal traction stress vector  $\mathbf{T}$  and the separation vector  $\boldsymbol{\delta}$  is governed by the linear elastic traction–separation law, expressed as:

$$\mathbf{T} = \mathbf{K} \boldsymbol{\delta}. \quad (5.1)$$

The stiffness matrix, separation vector, and traction vector are defined as:

$$\mathbf{K} = \begin{bmatrix} K_{nn} & 0 & 0 \\ 0 & K_{ss} & 0 \\ 0 & 0 & K_{tt} \end{bmatrix}, \quad \boldsymbol{\delta} = \begin{bmatrix} \delta_{nn} \\ \delta_{ss} \\ \delta_{tt} \end{bmatrix}, \quad \mathbf{T} = \begin{bmatrix} T_{nn} \\ T_{ss} \\ T_{tt} \end{bmatrix}, \quad (5.2)$$

where  $\mathbf{K}$  denote the stiffness matrix, whose components  $K_{nn}$ ,  $K_{ss}$ , and  $K_{tt}$  represent the normal, first tangential, and second tangential stiffnesses, respectively;  $\boldsymbol{\delta}$  is the separation vector comprising the components  $\delta_{nn}$ ,  $\delta_{ss}$ , and  $\delta_{tt}$ , which correspond to the normal, first tangential, and second tangential separations; and  $\mathbf{T}$  is the traction vector composed of the traction components  $T_{nn}$ ,  $T_{ss}$ , and  $T_{tt}$  in the respective directions. This linear formulation describes the elastic response of the adhesive layer before damage occurs.

➤ Damage Initiation Criterion

Damage initiation was assumed to occur once the maximum effective separation  $\delta_{eff}$  exceeded a critical threshold  $\delta_0$ , which was defined as:

$$\delta_{eff} = \max(|\delta_{nn}|, |\delta_{ss}|, |\delta_{tt}|) \geq \delta_0. \quad (5.3)$$

The displacement-based failure criterion utilized in has been identified as particularly suitable for applications subjected to thermomechanical loading conditions, such as those encountered during fire exposure. This suitability is attributed to the criterion's independence from stress-based limits of material resistance, which are known to deteriorate significantly at elevated temperatures due to the thermally induced degradation of mechanical properties.

#### ➤ Damage Evolution

The evolution of damage following initiation was modelled using the formulation available in ABAQUS [63], which requires the specification of the final effective separation  $\delta_f$ . Additionally, the evolution of damage is characterized by a scalar variable  $D$ , ranging from 0 (undamaged) to 1 (fully damaged), and was expressed as a function of the effective separation  $\delta_{eff}$ . The damage variable  $D$  was defined according to the linear degradation model available in ABAQUS as:

$$D = \frac{\delta_{eff} - \delta_0}{\delta_f - \delta_0}, \quad \text{for } \delta_0 \leq \delta_{eff} \leq \delta_f. \quad (5.4)$$

When the effective separation  $\delta_{eff}$  exceeds the critical value  $\delta_0$  and remains below the final separation  $\delta_f$ , i.e.,  $\delta_0 < \delta_{eff} < \delta_f$ , the cohesive interface is subjected to progressive softening. Under this regime, the nominal cohesive tractions in the normal and tangential directions are expressed as:

$$T_{nn} = (1 - D) K_{nn} \delta_{nn}, \quad (5.5)$$

$$T_{ss} = (1 - D) K_{ss} \delta_{ss},$$

$$T_{tt} = (1 - D) K_{tt} \delta_{tt}.$$

This formulation could provide a comprehensive description of the interface behavior from damage onset to complete separation, ensuring accurate modelling of delamination under combined thermal and mechanical loading conditions.

Figure 55 presents the traction–separation response of the cohesive interface under mechanical loading. Initially, the response is elastic up to the critical separation  $\delta_0$ , where damage initiates. Beyond this point, progressive degradation of traction occurs according to the defined damage evolution law, until complete separation at  $\delta_f$ . The curve reflects the transition from an undamaged to a fully damaged state of the adhesive layer.

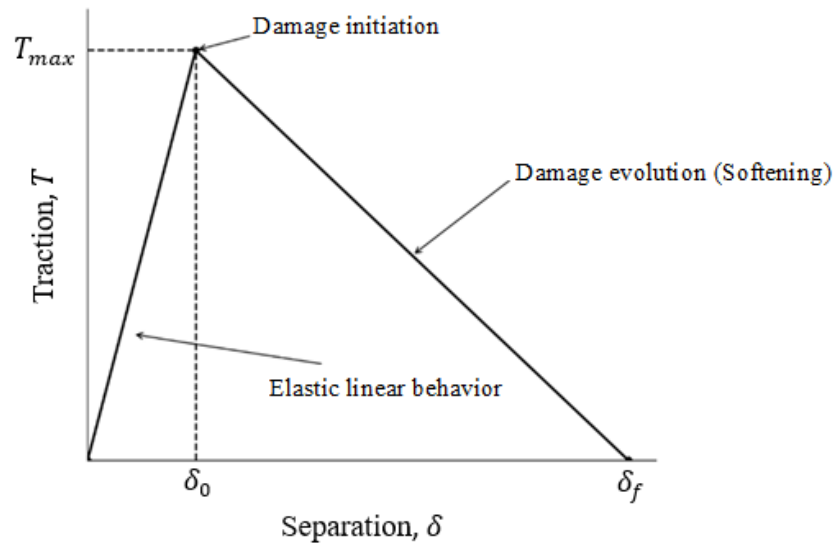


Figure 55. Traction – separation curve illustrating a damage evolution.

#### ▪ Fasteners

In cases where mechanical fasteners or screws are used, that should be modelled with appropriate constraints and properties to account for additional stress points, load distribution, and potential movement under thermal expansion.

- Model size

The large scale of the tested samples, combined with the geometric complexity of the joints, makes the thermomechanical analysis computationally intensive and time-consuming. To address this, the model size of the joints has been simplified by implementing a proposed approach, as detailed in the following section. Similar approach was used in [73]. This simplification reduces computational demands while maintaining the accuracy required to capture the essential mechanical and thermal behaviors of the model.

#### **5.4 Numerical modelling of thermomechanical problem**

Two different types of numerical models were developed and implemented using ABAQUS software to investigate the thermomechanical response of a sandwich panel structure under elevated temperature conditions. Each type of model represents a specific analytical strategy, enabling comprehensive assessment of coupled temperature–displacement behavior.

In the first group, a simplified numerical model was employed, wherein the sandwich panel was represented as a layered shell structure. This model included a shell layer for steel and a mineral wool (MW) layer, structured as a composite to simulate basic displacement behavior. This model section, defined as "Shell/Continuum Shell, Composite", facilitated the representation of distinct material layers with predefined thicknesses, thereby enabling an efficient representative analysis of directional displacements within the panel.

In the second group, a more detailed numerical model was utilized. This model integrated a 3D solid representation of the MW material with 2D shells for the steel, thereby capturing the full geometric and material complexities of the sandwich panel. This model enabled advanced thermomechanical analysis by accounting interactions and potential failure mechanisms. Additionally, the second group will be developed based on the experimental results from Test 1', which shares similarities with Test 2', as detailed in Section 4.3 of the preceding chapter.

For both groups, a shared configuration was implemented to ensure consistency and comparability across simulations. This configuration included uniform definitions of material properties, model types, meshing strategies, and step settings. Both groups were defined using the "Standard & Explicit" procedure, which is well-suited for explicit

dynamic analysis and provides high fidelity in capturing transient thermal and mechanical behaviors, including stress distributions under dynamic loading conditions.

Another common configuration shared between the models as mentioned above, is the definition of material properties, with steel (S280GD+Z) used as the face material of the panel and mineral wool as the core material. The thermal properties of the steel (S280GD+Z) were referenced from [29], and mechanical properties were taken from [28]. For the mineral wool, the thermal properties of the core material were obtained from reference [49]. The thermal diffusivity values determined in Chapter 3 were not directly used in these numerical simulations, because the study focus was on methodology development and presenting the heat behavior for a fresh sample rather than providing simulation inputs (thermal conductivity ( $\lambda$ ), specific heat capacity ( $C_p$ ), and density ( $\rho$ )).

As the mechanical proprieties of mineral wool reflect the low stiffness and moderate lateral deformation of mineral wool fibrous, porous structure, consistent with its role as a non-load-bearing insulation material. The thermal expansion coefficient of approximately  $7 \times 10^{-6} \text{ 1/}^\circ\text{C}$  according to [75], indicates high dimensional stability, ensuring minimal expansion or contraction under temperature fluctuations. Moreover, the yield stress of mineral wool at ambient temperature ( $21.1^\circ\text{C}$ ) is approximately 30 MPa as was reported in [20]. By  $500^\circ\text{C}$ , is estimated that the yield stress decreases to approximately 5 MPa, and by  $850^\circ\text{C}$ , the yield stress approaches zero as the mineral fibers soften and it can no longer resist compressive forces effectively.

The step analysis configuration is another shared aspect between both model groups. A coupled temperature-displacement step is employed, set to transient response mode, to accurately capture time-dependent changes in temperature and displacement. The time-period for both simulations is set according to experimental tests, allowing for an extensive analysis window to capture long-term temperature-displacement effects. The Full Newton solution technique is applied with unsymmetrical matrix storage, which is ideal for managing non-linear thermal-mechanical interactions. Heat load application is set to instantaneous, to observe the effects immediately at each step, which is well-suited for the explicit analysis approach.

Thermal boundary conditions in both groups were simulated as heat fluxes from convection and radiation. For the room-temperature surface, convection was defined with a film coefficient of  $0.009 \text{ W}/(\text{mm}^2 \cdot ^\circ\text{C})$  and a room temperature of  $21.1^\circ\text{C}$ , following the guidelines in EN 1991-1-2 [67]. On the heated surface, a film coefficient of

0.025 W/mm<sup>2</sup>·°C with accordance to [67] was applied, based on furnace data radiation effects were modelled using recommended value in [28] an emissivity of 0.7, consistent with ambient or furnace conditions. The model's initial temperature was set to 21°C, and heated surfaces were according to the recorded furnace values.

For element type and controls, both shell and solid elements are defined with the "Coupled Temperature-Displacement" element type. Default settings are maintained for hourglass stiffness, viscosity, and scaling factors, while element deletion is set to "No" to preserve structural integrity throughout the simulation. Reduced integration is applied across both shell and solid elements to speed up computation without sacrificing accuracy. The meshing strategy in both groups is designed to balance computational efficiency with result accuracy. A structured mesh is generated for both shell and solid geometries, with element type and size carefully selected to capture thermal gradients and displacements. This approach could ensure that critical details in thermal and mechanical response are well-resolved, contributing to reliable simulation results.

The above modelling configuration, incorporating standardized parameters, boundary conditions, material properties, and meshing strategies within ABAQUS, enables effective simulation of thermomechanical behavior in both groups' scenarios. The explicit dynamic approach is advantageous for managing rapid changes in temperature and displacement, especially in scenarios involving transient thermal events, such as fire simulations.

#### **5.4.1 Analysis of panels displacement under thermal and boundary effects**

The purpose of this subsection is to analyze and evaluate the displacement behavior of the 3D composite shell model, as introduced in the previous section, under one-sided thermal loading and varying mechanical boundary conditions, with simplified support configurations. This initial investigation is conducted using simplified model cases from the first numerical modelling group, enabling a fundamental understanding of panel response under basic constraints.

Using a 3D shell composite model, horizontal displacement was analyzed under support conditions such as fixed, simply supported, and fixed-roller configurations (see Figure 56 and Table 5). This approach emphasizes the influence of boundary conditions on displacement direction, with results provided in the corresponding section.



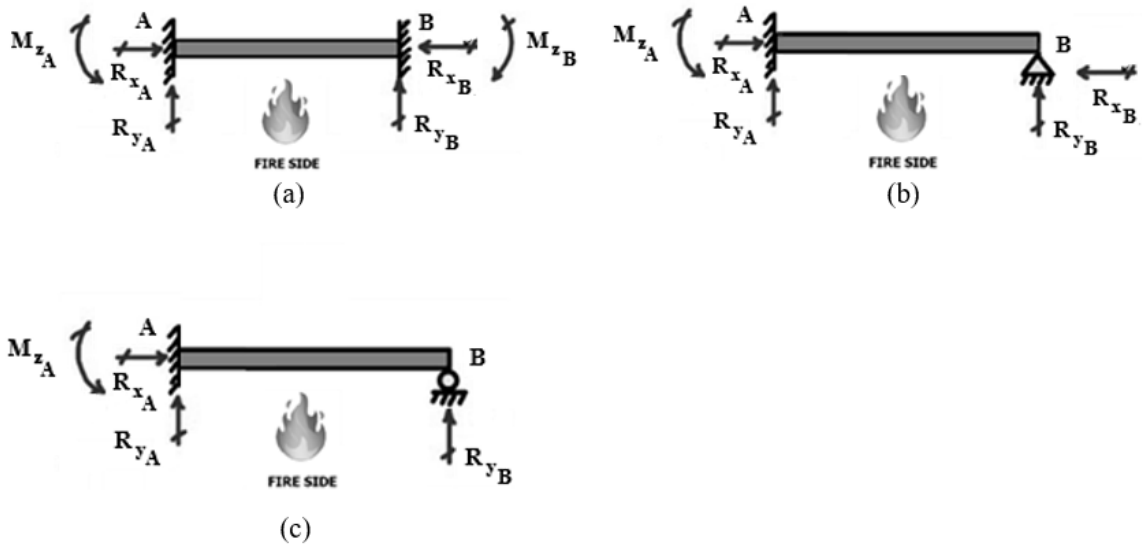
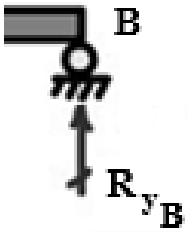
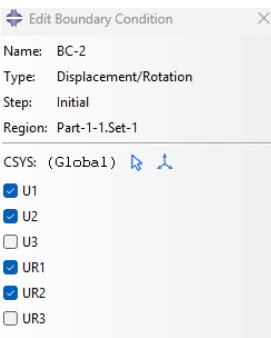
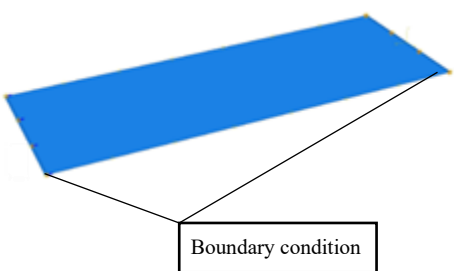
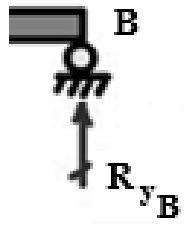
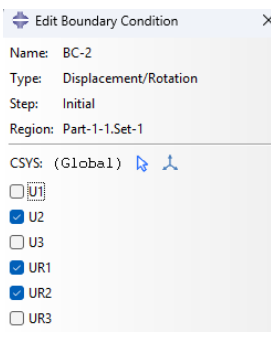
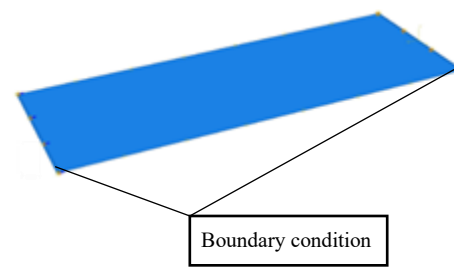


Figure 56. Simplified support conditions. (a) fixed, (b) fixed pinned, and (c) fixed roller.

Three boundary configurations were analyzed: (a) both ends fixed, (b) one end pinned while the other end is fixed, and (c) one end supported on a roller while the other end is fixed. Each configuration results in distinct displacement directions as the panel responds to the temperature gradient, transitioning from the heated side to the unheated side. All measurements are conducted on the unheated surface. Negative values indicate that the panels are displacing toward the heated side.

Table 5. Fixation types, schematics, boundary conditions, and graphical representations

Fixation type	Schematic representative	ABAQUS boundary condition	Graphical representation
Fixed			

Pinned			
Roller			

In the thermomechanical simulation conducted from the first numerical modelling group using the composite shell model, with both ends of the panel are fixed – (see Figure 57) illustrates the mid-span deflection under thermal loading. This configuration results in the most significant displacement, with a rapid and steady increase that stabilizes at approximately 80 mm. The fixed ends restrict thermal expansion, leading to considerable stress build-up within the panel, which manifests as substantial displacement toward the unheated side.

In contrast, when one end is pinned and the other is fixed, the displacement is significantly reduced and stabilizes much earlier. The pinned support provides a degree of rotational freedom, alleviating some of the thermal stress and resulting in a lower overall displacement.

In the third configuration, where one end is supported on a roller while the other is fixed, the panel exhibits a maximum deflection of approximately 40 mm directed toward the heated side. Roller support permits unrestricted horizontal movement, accommodating the panel's natural thermal expansion and effectively minimizing thermal stress build-up.

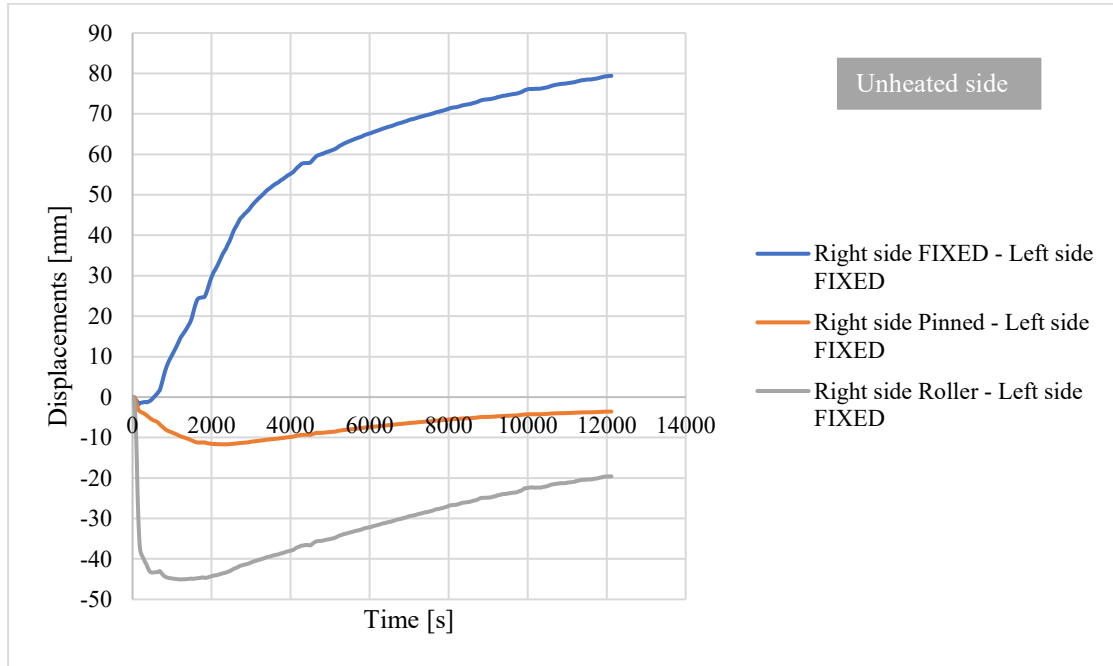


Figure 57. Effect of boundary conditions on horizontal displacement of sandwich panels under thermal loading.

The displacement trends obtained from the first numerical modelling group (Figure 57), which incorporates different mechanical boundary configurations, demonstrate that thermal expansion induces outward deflection when both panel ends are fixed, while pinned or roller supports reduce or redirect displacement. These trends are evaluated with the experimental results shown in the above Figures 51 - 54 (corresponding to Tests 1' - 4'). The experimental results, referenced here to contextualize and support these findings. Specifically, from above results (Figure 57) indicates both positive and negative displacements depending on constraint type, and these are consistent with the experimental observations, where displacement occurs either toward the heated or the unheated side, depending on the applied boundary conditions.

In the first modelling configuration from the first group of numerical modelling, when the panel edges were fully fixed, the thermal expansion was resisted, causing the panel to buckle outward. This was observed in Test 1', wherein the panel deformed outward due to constrained expansion. Similarly, significant outward displacement was predicted by the numerical configuration under such conditions. When the panel edges were partially restrained (pinned), the displacement trend was less pronounced, with the panel expanding outward to a smaller degree. This was consistent with Test 2', in which moderate restraints resulted in smaller outward deflection. In the simulation, pinned

boundary conditions produced a smoother outward curve compared to fully restrained cases, reflecting similar experimental results.

In second or third numerical configurations from first group of numerical modelling, where the panel edges were free to expand (either unrestrained or sliding), natural expansion was allowed, preventing significant out-of-plane deformation. As a result, the second numerical model predicted a nearly flat displacement curve with only slight outward movement. This aligned with Tests 3' and 4', where no significant outward deflection was observed under minimal restraint. These results demonstrate that boundary conditions permitting free expansion prevented large deflection.

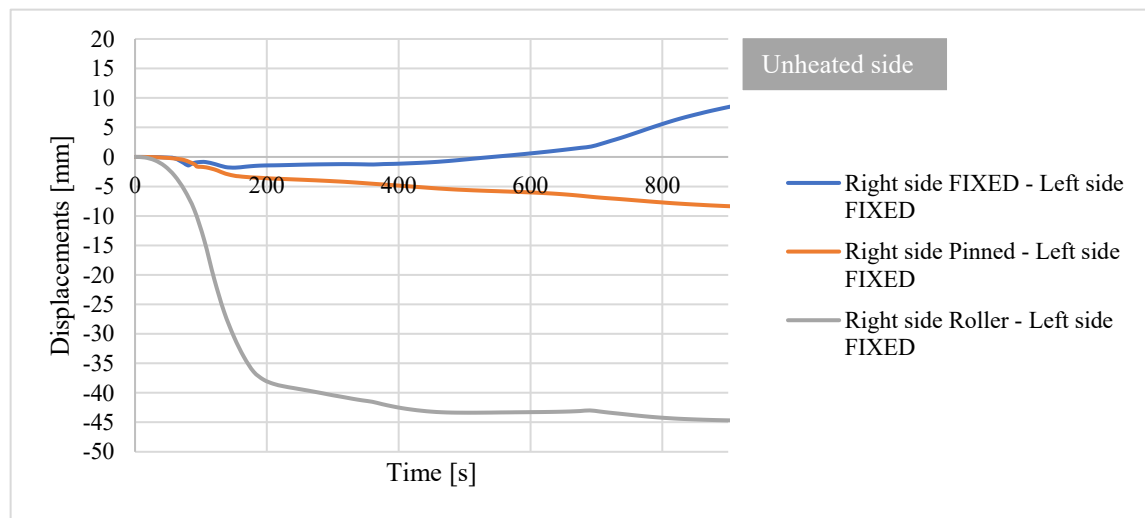


Figure 58. Early-stage displacement response under various boundary conditions (extracted from Figure 57).

Figure 58 presents extracted numerical results from Figure 57, focusing only on the displacement response on the first minutes. The fixed–fixed configuration exhibits an initial outward deflection, followed by a reversal to inward displacement. This notable behavior captured in the experimental results was the transition from outward deflection to inward buckling in certain scenarios. After reaching peak outward displacement, inward displacement began in panels with significant boundary restraint, as observed in Tests 1' and 2'. This shift occurred when compressive stresses built up due to the restrained expansion, eventually causing the panel to buckle inward. This trend was also predicted by the numerical simulation, where the panel transitioned from outward deflection to inward pull due to mechanical instability, but it was noted only in the initial minutes. In Tests 3' and 4', inward displacement was more pronounced due to more rigid support conditions. The numerical analysis showed that, under severe boundary

constraints, thermal expansion led to inward displacement, as the panel's stiffness prevented outward expansion. These results confirmed that boundary restraint played a critical role in determining whether thermal expansion led to outward bowing or inward buckling. Panel stiffness and boundary conditions were key factors determining whether the panel deformed outward or inward. A stiffer panel resisted bending, and if boundary conditions were restrictive, higher internal compressive forces developed, leading to inward buckling at elevated temperatures. This matched the experimental results, where more rigid panels exhibited delayed inward movement after initial outward deflection. Conversely, flexible panels exhibited more pronounced outward displacement under thermal expansion, as thermal strain was less effectively resisted. In the simulations, panel behavior was directly related to boundary conditions and stiffness, showing that rigid supports (fully fixed) caused more significant outward displacement, while free supports resulted in minimal deflection. As thermal load increased, inward displacement was predicted in Tests 3' and 4' under constrained boundary conditions, where inward buckling occurred after outward expansion.

The key factors influencing displacement behavior in the modelling and experimental tests included thermal expansion, boundary conditions, and panel stiffness. Thermal expansion, initiated displacement, typically causing outward deflection. Both experimental tests and simulations showed outward displacement as material temperature increased. Boundary conditions significantly influenced displacement patterns. Fully fixed edges caused more outward displacement, while pinned or sliding supports reduced deflection. Free expansion resulted in minimal or no out-of-plane displacement. Stiffer panels resisted outward bending and led to inward buckling when thermal strain was not accommodated. Flexible panels exhibited more pronounced outward displacement under thermal expansion. When thermal expansion was highly restrained, compressive forces accumulated, leading to inward displacement.

The numerical displacement results confirmed the experimental findings, showing that thermal expansion and boundary conditions were critical in determining whether a panel deformed outward or inward. Rigid boundary conditions led to larger outward deflections, which resulted in inward buckling as compressive forces accumulated. More flexible support allowed expansion with minimal deflection, preventing inward buckling. The interplay of thermal expansion, stiffness, and mechanical restraint determined the

overall displacement trend, and the first group of numerical modelling accurately predicted these behaviors in alignment with the experimental tests.

The analysis above highlights the importance of boundary effects in predicting the behavior of sandwich panels under heat. Tests with fixed edges show more pronounced outward displacement and eventual inward buckling, while less restrained systems exhibit smaller displacement or no significant out-of-plane deformation.

#### **5.4.2 Modelling methodology and numerical simulation framework**

This section focuses on using the second numerical modelling group. The group will present two configurations based on experimental data. The first configuration is based on Test 1' and second is based on Test 2'. The purpose of both configurations is to simulate and study how sandwich panels behave under large-scale fire conditions. The configurations models integrate a detailed 3D representation of mineral wool with a 3D shell for the steel layers, offering a perspective on how the core material interacts with the steel sheets. By capturing the full depth mentioned and with simplicity of the design joints between panels, the 3D models enable precise analysis of displacements, deformations, and failure points. This approach is crucial for understanding the panels' performance and response to thermal stresses in three-dimensional models, with a primary focus on analyzing horizontal displacement of the panels.

This detailed analysis is essential for understanding the mechanical and thermal performance of sandwich panels under fire conditions in a large-scale testing, providing insights into their displacement.

The methodology outlined below is a detail of considerations discussed in Section 5.3. These include the use of screws for panel fixation, springs to simplify the joints between panels, interaction-contact modelling to capture the interaction between the core material and the sheet face, and cohesive contact incorporating damage initiation and evolution. Additionally, the methodology accounts for thermal conductance and radiative heat transfer for a more representation of heat transfer mechanisms, as well as geometric properties tailored for enhanced precision.

Furthermore, the second modelling group is based on the experimental tests from Test 1', which is similar to Test 2' in terms of assembly, described in Section 4.3 of the previous chapter, as a reminder for context.

▪ Mechanical boundary conditions

The mechanical boundary conditions are designed to provide a simplified realistic representation of the sandwich wall panel behavior under fire conditions, consistent with experimental tests. The panels' edges are fixed with an Encastre boundary condition, fully restricting all degrees of freedom to simulate complete fixation, as seen in the mounting structure constructed using angle brackets. The connection mechanism is modelled using L80×80×8 mm brackets, which provide structural support and facilitate realistic load transfer. This simplified modelling approach reduces computational complexity by abstracting detailed physical interactions while ensuring accuracy in capturing critical responses, such as structural fixation and contact behavior. However, the primary focus of the analysis is on the transversal displacement of the panel.

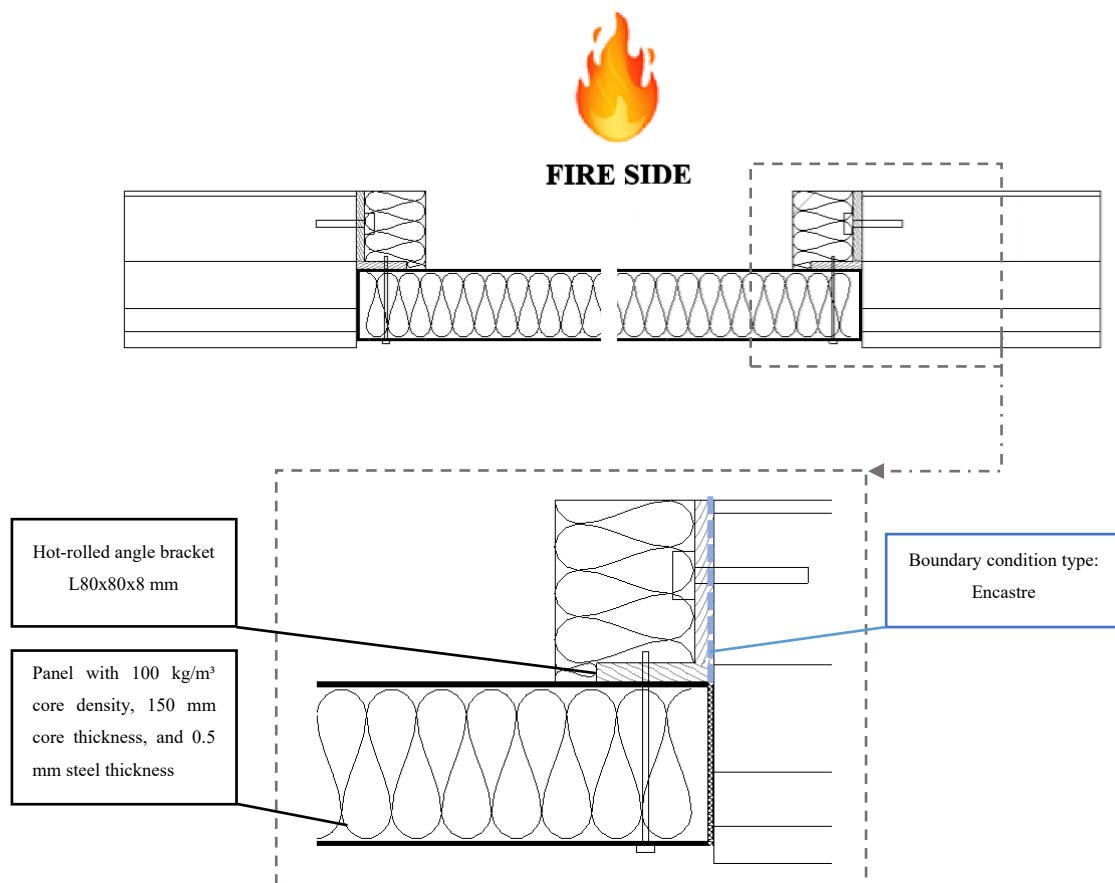


Figure 59. Structural setup and boundary conditions for fire exposure on sandwich panels.

### ▪ Bolts modelling (Connectors)

The bushing connector used in this analysis. It is specifically configured to model the behavior of screws under mechanical and thermal loads. In the assembly, as described in Test 1' describe in chapter 4, section 4.2, the two lower panels are secured using three bushing connectors (three screws) on each side, while the upper panel is attached with two connectors (two screws) on each side. These bushing connectors are incorporated in our ABAQUS model, where they are designed to simulate flexible connections that allow relative motion between materials. This motion can occur in translational and/or rotational degrees of freedom, depending on the configuration, enabling the connectors to realistically represent the elastic and deformable behavior of screws under varying mechanical and thermal conditions.

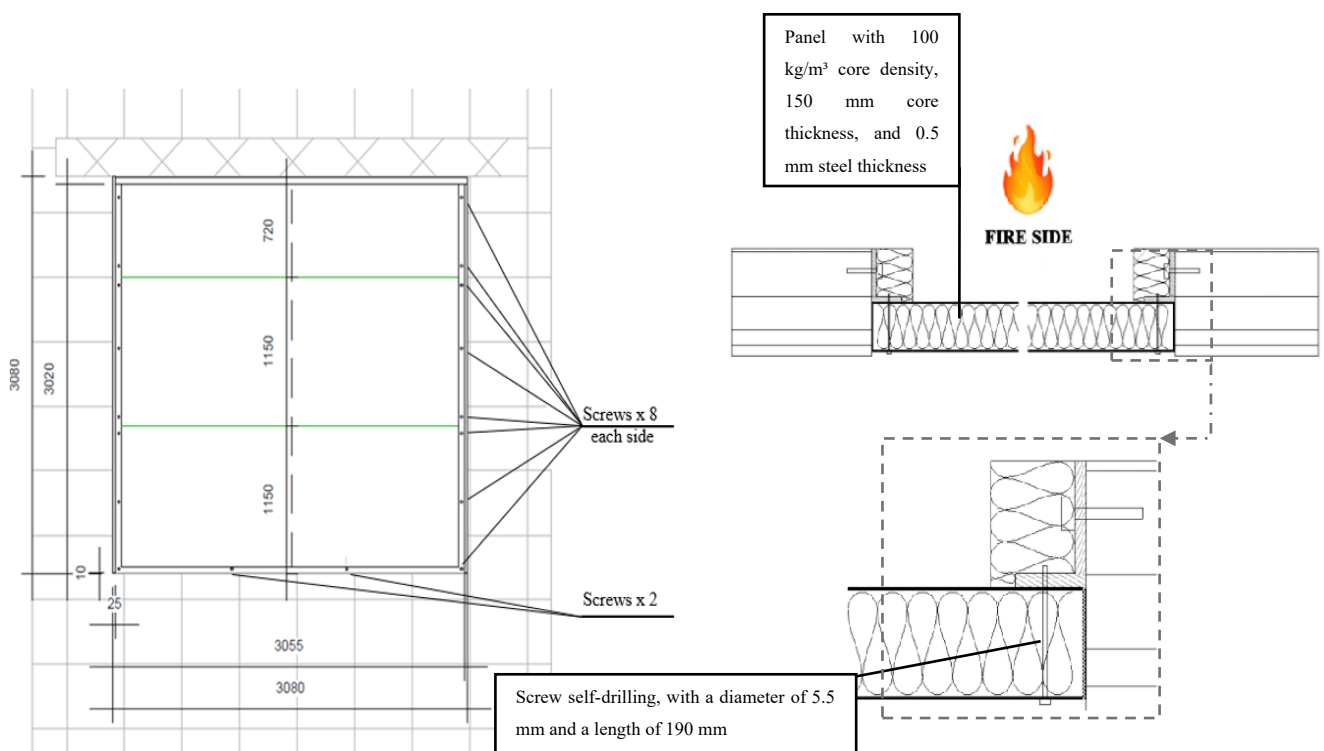


Figure 60. Assembly details and structural configuration of tested samples.

Generally, as mentioned the bushing connector will simulate the elastic and deformable response of screws, allowing translational motion along  $x$  and  $y$  axes (F1 and F2) with a focus on nonlinear elasticity to represent the realistic behavior of the screw material under varying forces. Nonlinear elasticity ensures that the stiffness of the screws changes with increasing deformation, reflecting their



ability to manage high loads while maintaining functionality. The uncoupled configuration is used as well to ensure that forces and displacements in different directions are treated independently.

In this context, the reference axial displacement of a 5.5 mm diameter, 190 mm long steel screw under a 200 N load is calculated to be 0.0076 mm, based on Hooke's Law. This value serves as a valid basis for defining the initial connector stiffness in the model. A summary of the calculated force–displacement relationship for different load levels is presented in Table 6.

Table 6. Force-displacement relationship for bolt – bushing connectors.

Force [N]	Displacement [mm]
0	0
100	0.0038
200	0.0076
500	0.0190

▪ Joint connections modelling (springs)

The modelling approach adopted in this study for simulating the joint connections between adjacent sandwich panels is grounded in the methodology presented in [76], wherein spring elements were employed to capture the mechanical behavior of tongue and groove joints along longitudinal panel edges. In [76] finite element model, spring elements were positioned between the inner plates of adjoining panels, with a defined spring stiffness of 1 kN/mm and a center-to-center spacing of 100 mm, in order to represent the out-of-plane stiffness of the joint interface.

In the second modelling group, the same spring-based modelling strategy has been applied. However, a geometric adaptation has been introduced. Specifically, the springs have been positioned not only between the upper and lower plates, as in the referenced configuration, but also between the upper face sheets and between the lower face sheets. This arrangement can be clearly observed in Figure 61, where springs are located across all corresponding face sheet interfaces. By placing the springs between the upper face sheets, between the lower face sheets, and between the upper and lower plates, the model more accurately reflects physical joint layout of the current panel design.

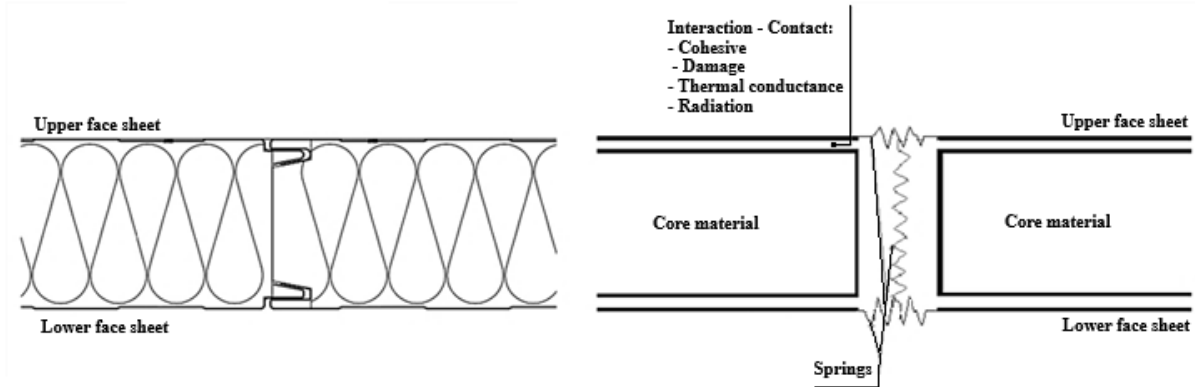


Figure 61. Schematic representation of simplified joint connection and interface properties with interaction details.

The use of springs in the numerical model serves to represent the mechanical behavior of joint connections, enabling the abstraction of joint stiffness into simplified parameters. This approach reduces computational complexity by eliminating the need for detailed geometric modelling of the connection. This not only minimizes computational costs but also facilitates rapid adjustments and tuning of parameters, making it easier to match experimental results or optimize the design. Overall, using springs to simulate joint connections in sandwich panels is a practical and efficient approach that enhances the model's usability and reliability.

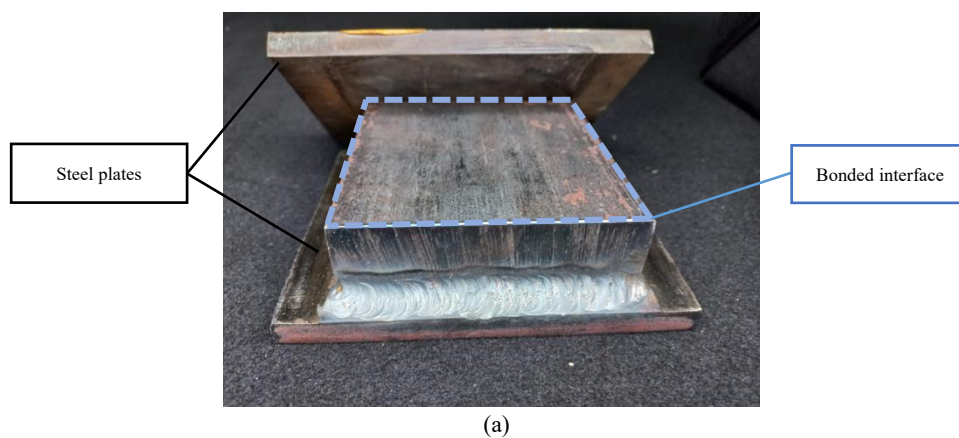
- Adhesive layer modelling (interaction properties)

The interaction between the core material and steel sheets is a significant focus of this modelling section. Experimental tests consistently recorded cracking sounds starting at 36 s - 55 s, indicating early delamination caused by adhesive bonding, thermal expansion of the steel, and material degradation at elevated temperatures. These observations highlight the need for modelling the interaction using cohesive contact, which captures the initiation and evolution of damage at the interface under thermal loading. Hence, cohesive contact models are used to represent the bonding behavior at the interface, simulating the initiation and evolution of damage under thermomechanical loads. This includes damage initiation, where cracks or separations begin due to thermal expansion or applied stresses, and damage evolution, which reflects how degradation propagates, ultimately leading to failure.

In the absence of relevant experimental data in the literature, the performance of the polyurethane adhesive layer was determined based on a tensile test of the

adhesive layer. Figure 62 shows a test in which two steel elements with an area of  $10\text{ cm} \times 10\text{ cm}$  were glued with an adhesive designed for bonding steel facing of sandwich panels and mineral wool core. The gluing process was carried out on a functioning production line. After the adhesive was applied, in order to simulate the conditions on the production line, the specimen was transferred to an incubator, where the adhesive bond was matured for 20 minutes at  $60^\circ\text{C}$ . After a minimum of 6 hours after bonding, the specimen was subjected to axial tension on an Instron Electropuls e10000 testing machine. Based on the results, the parameters of the cohesive layer model were determined, with the results related to a unit interface thickness of 1 mm. Figure 62 presents: (a) the initial condition prior to bonding, showing the steel plates and designated bonding interface, (b) the specimen mounted in the uniaxial tensile testing apparatus, with the adhesive layer visible at the interface, and (c) the post-failure appearance of the bonded interface following uniaxial tensile loading, highlighting the failure characteristics of the adhesive joint.

Figure 63 shows an initial disturbance in the force-displacement relationship (in the range of up to about 0.4 mm). This probably results from taking out all the clearances in the system. Then the force-displacement relationship is close to linear until the moment of damage. The damage is sudden and no slow degradation of the connection is observed. The maximum load values recorded for the three tested samples were 8.210 kN, 7.329 kN and 7.045 kN. Based on the linear range of the force-displacement relationship, the stiffness  $K_{nn}$  was determined for each sample (see, Table 7).



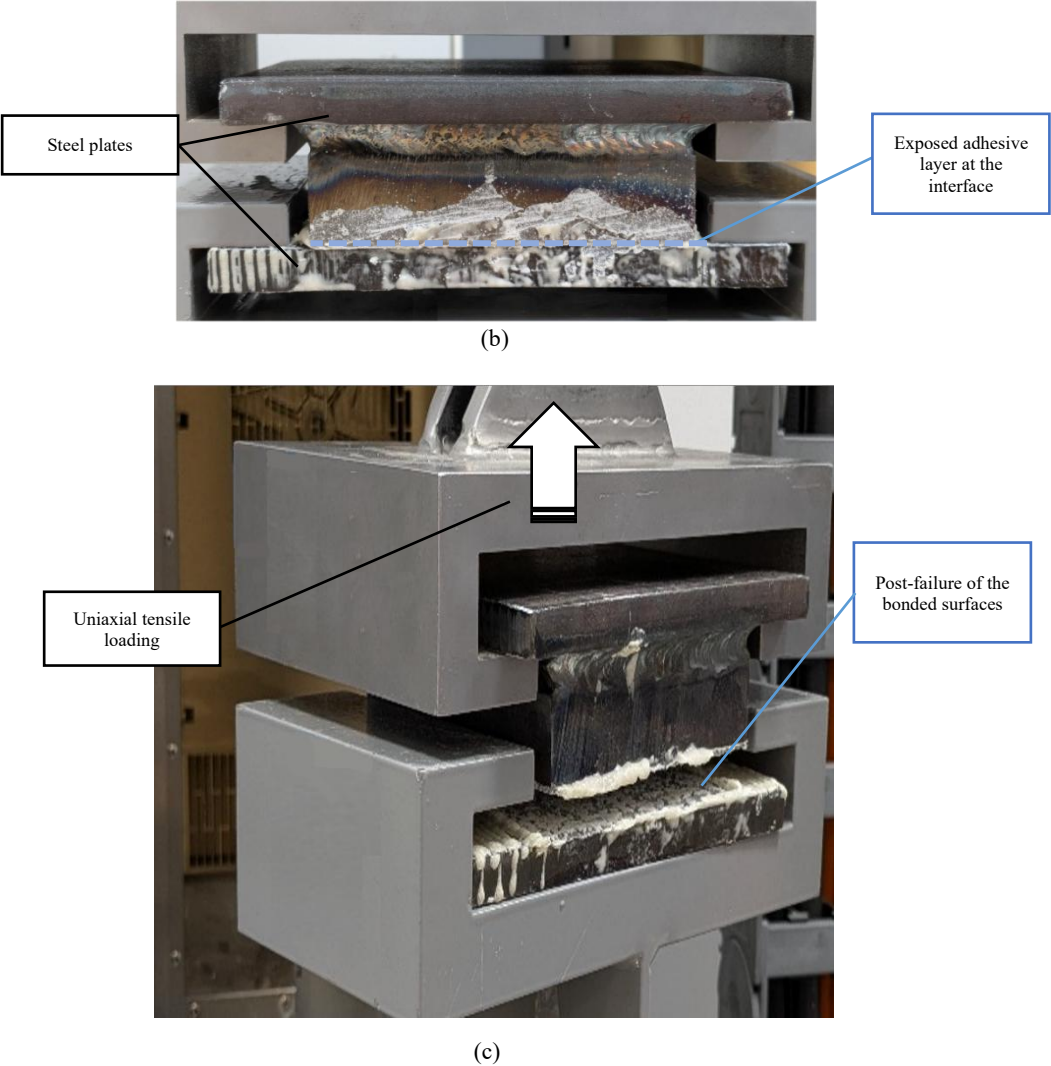


Figure 62. Steel plate specimens bonded with polyurethane adhesive: (a) pre-bonding condition; (b) mounted samples in tensile testing machine; (c) post-failure appearance after uniaxial loading.

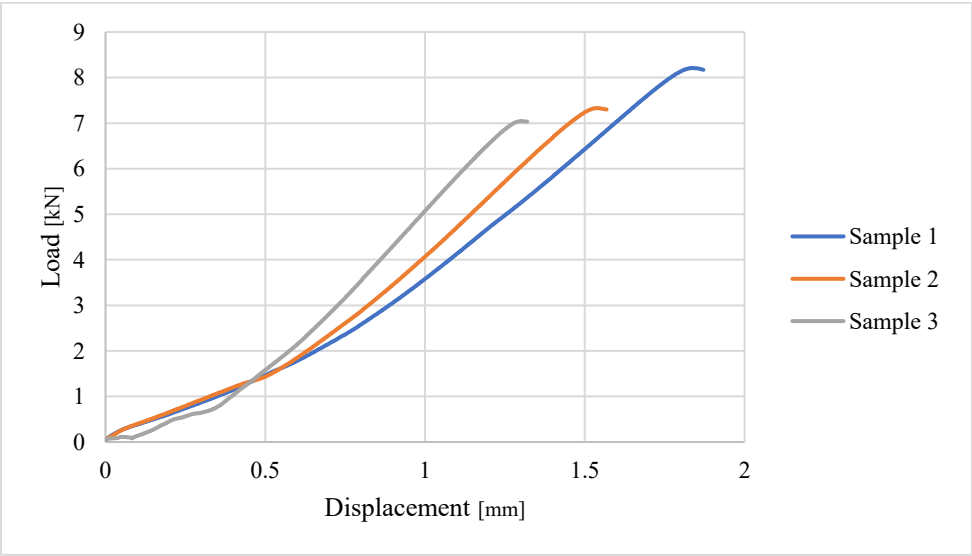


Figure 63. Tensile response of adhesive-bonded steel plate specimens.

Table 7. Experimental results of stretching the adhesive layer.

Samples	Max load [kN]	Interface traction $T_{nn}$ [MPa]	Determined stiffness $K_{nn}$ [MPa/mm]
1	8.210	0.8210	0.5164
2	7.329	0.7329	0.5791
3	7.045	0.7045	0.6782
Average	7.528	0.7528	0.5912

Based on the average values of  $T_{nn}$  and  $K_{nn}$ , the separation value  $\delta_0$  was determined, indicating the beginning of damage:

$$\delta_0 = \frac{T_{nn}}{K_{nn}} = \frac{0.7528}{0.5912} = 1.273 \text{ mm}, \quad (5.6)$$

Of course, this value is lower than the displacements recorded during the tests performed (1.838 mm, 1.539 mm, and 1.304 mm).

Due to the lack of visible effect of gradual degradation of the adhesive joint, the final separation  $\delta_f$  was assumed to be 10% higher than the separation initiating damage, i.e.

$$\delta_f = \delta_0 \times 1.10 = 1.400 \text{ mm}. \quad (5.7)$$

Due to the lack of available information on the behavior of the adhesive during shearing, as well as based on the fact that the shear strength of polyurethanes used in sandwich panels is of a similar order to the tensile strength, the following were assumed:

$$T_{nn} = T_{ss} = T_{tt} = 0.752 \text{ MPa}, \quad (5.8)$$

$$\delta_{nn} = \delta_{ss} = \delta_{tt} = 1.273 \text{ mm}. \quad (5.9)$$

Moreover, to take into account the dependence of the interface stiffness on temperature, the relationship presented in Table 8 was introduced. The tests presented in Figure 64 below conducted in the same furnace used in chapter 3 on 10 cm × 10 cm sandwich panel samples show that at a temperature of approximately 250°C, the connection between the facing and the core loses its load-bearing capacity.

Table 8. Temperature dependence of interface stiffness for polyurethane adhesive layer.

Temperature [°C]	Interface shear stiffness $K_{nn}$ [MPa/mm]	Interface shear stiffness $K_{ss}, K_{tt}$ [MPa/mm]
21	0.591	0.591
100	0.40	0.40
150	0.30	0.30
200	0.10	0.10
250	0.00	0.00

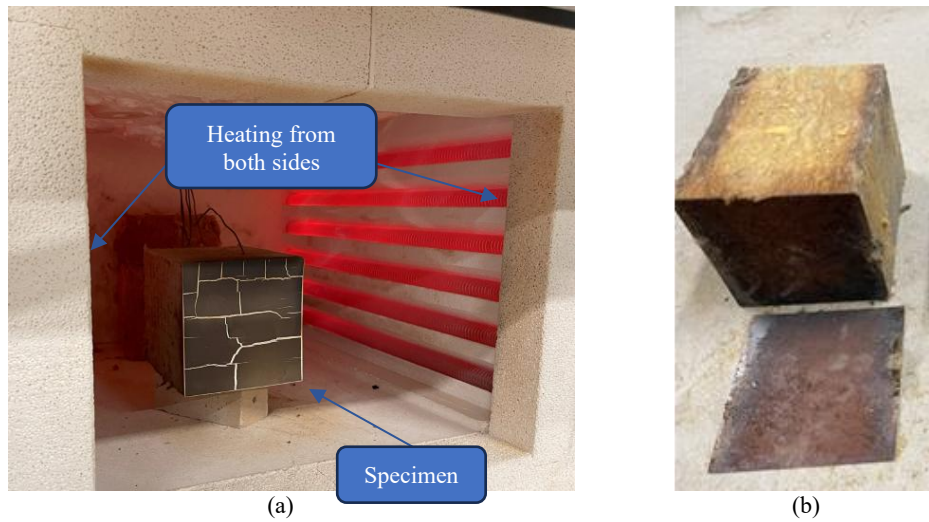


Figure 64. Sandwich panel sample tested up to 250°C: (a) specimen placed in a furnace with bilateral heating configuration; (b) failure mode showing delamination between facing and core material after thermal exposure.

As mentioned in Section 5.3, a simple linear model of damage evolution was adopted. Based on experimental observations, complete failure of the adhesive interface at room temperature was defined to occur at an average separation displacement of  $\delta_f = 1.40$  mm (see Equation 5.7). A temperature-dependent relationship was subsequently introduced, as presented in Table 9, where the final separation at failure increases with temperature. This trend reflects the assumption that the polyurethane adhesive layer becomes more ductile under elevated thermal conditions.

Table 9. Temperature dependence of failure displacement for polyurethane adhesive layer.

Temperature [°C]	Final separation $\delta_f$ [mm]	Strain at failure [%]
21	1.40	140
100	2.00	200
150	2.50	325
200	3.00	300
250	3.50	350

The traction separation response follows the linear relation defined in Equation (5.1), using the stiffness matrix described in Equation (5.2). The effective separation  $\delta_{eff}$ , which governs damage initiation, is calculated as the maximum of the absolute separations in the normal and tangential directions, as described in Equation (5.3). The evolution of damage is then computed using the linear degradation law given in Equation (5.4). Figure 65 is a graphical representation used to visually explain the described model.

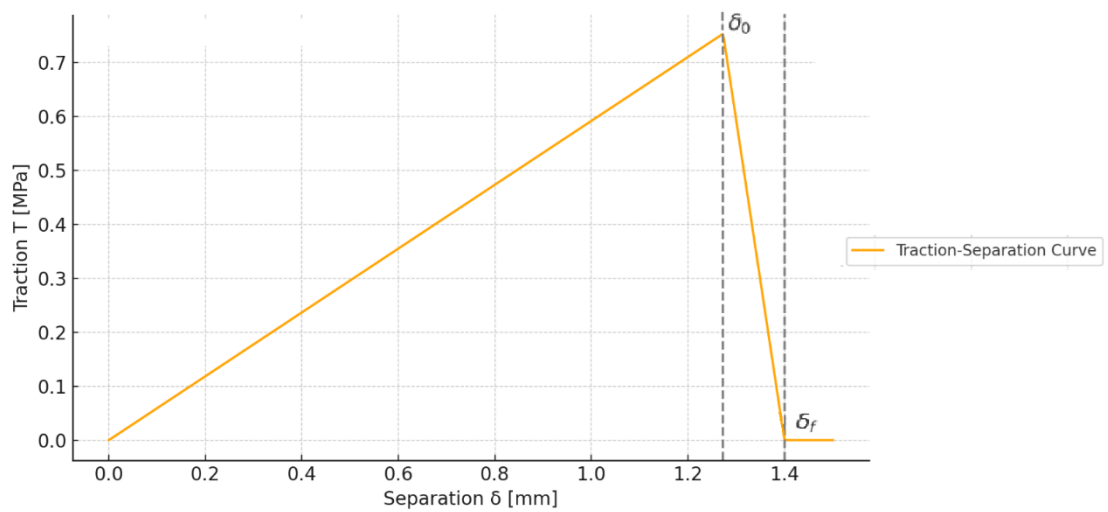


Figure 65. Traction – separation curve representing the cohesive zone model

#### ■ Thermal conductance & radiative heat transfer modelling

Following the implementation of cohesive elements to represent the adhesive layer, ABAQUS was unable to complete the contact configuration due to the absence of defined thermal contact conductance and radiative heat transfer interactions. These two mechanisms are essential for modelling interface detachment. Thermal contact conductance was therefore defined as a function of interfacial clearance, enabling the model to account for reduction in conductive heat transfer efficiency as the gap between the steel sheet and the mineral wool core increased. In parallel, radiative heat transfer was modelled using surface emissivity values and clearance-dependent view factors, providing a physical representation of heat exchange across separated surfaces under fire exposure conditions.

#### ➤ Thermal conductance

A thermal contact conductance value of  $35 \text{ W/m}^2\cdot\text{K}$  was assigned at the steel–mineral wool interface under full contact assumptions, following the



methodology employed by [77]. This value reflects the expected interfacial thermal performance between metallic and microporous insulating materials, considering surface roughness, limited real contact area, and conduction suppression due to the fibrous structure of mineral wool.

To capture the thermal behavior under complete detachment, the conductance values were defined as a function of increasing separation. When the separation exceeded  $\delta_f = 1.40$  mm, the conductance is reduced to  $0 \text{ W/m}^2\cdot\text{K}$ , as physical contact was no longer present. This definition reflects the physical elimination of conductive paths.

➤ Radiation

Under this detached condition, radiative heat transfer became the dominant interfacial mechanism. In the absence of conductive contact, the radiative exchange between the steel sheet and the mineral wool core was governed by the geometrical configuration of the gap, represented by the radiative view factor. Based on the assumption of two parallel, and planar exposed surfaces, and in accordance with the principles outlined in [78], a view factor of 1 was assigned in our analysis when the separation exceeded  $\delta_f = 1.40$  mm, representing full radiative exposure. When physical contact existed, the view factor was set to 0, indicating complete suppression of radiative exchange. This methodology, consistent with the view factor summation rule, ensured compliance with energy conservation and enabled a physically realistic transition.

### **5.4.3 Model configuration and graphical representations**

This section presents the graphical and visual outputs obtained from the numerical simulation for Test 1', which was conducted under conditions analogous to those of Test 2'. The configuration of the model is discussed. Particular emphasis is placed on the graphical illustration of the displacements of the sandwich panels, which are presented in cross-sections taken along the longitudinal and transverse directions (cf. Figure 66).



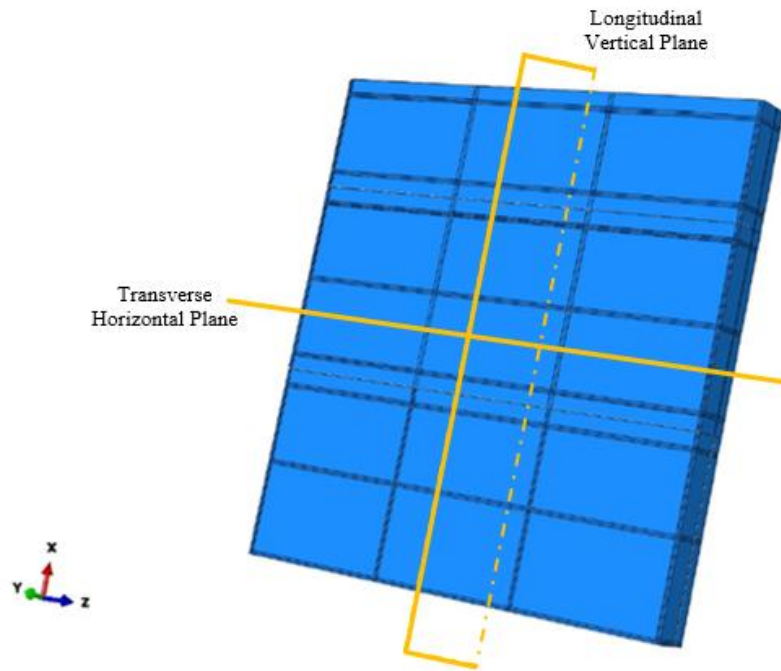


Figure 66. 3D model of the tested panels showing cross-sections along the longitudinal and transverse directions.

The boundary conditions in ABAQUS were defined to replicate the experimental setup described in Chapter 4, Section 4.2, which outlined fire test configuration, and further detailed in Section 5.4.2, where the numerical modelling methodology was presented. Specifically, the fixation of the sandwich panels to the concrete wall using screws and brackets was represented in the model by applying ‘Encastre’ boundary conditions to simulate the rigid connection at the bracket locations and by employing bushing connectors to model the mechanical behavior of the screws, as previously explained.

To reflect the physical constraints observed in the experimental configuration, mechanical boundary conditions were implemented accordingly (see Figure 59). Furthermore, the use of bushing connectors, configured to model the behavior of screws under mechanical and thermal loads, as illustrated in Figure 60, was numerically replicated in order to capture both displacement and deformation behavior of the panels under these loading conditions.

This modelling approach was complemented by the use of springs, as illustrated in Figure 61, to represent joint flexibility and to reduce computational complexity. These configurations were applied consistently within the second numerical modelling group and were graphically represented in Section 5.4.2 to support transparency in the

simulation setup. Figure 67 further demonstrates the geometry of the frame used in the simulations and explicitly indicates the locations of the boundary conditions applied. The connection between the numerical boundary conditions and the experimental test frame has thus been established both in textual and graphical form, ensuring a coherent integration of modelling assumptions into the numerical framework.

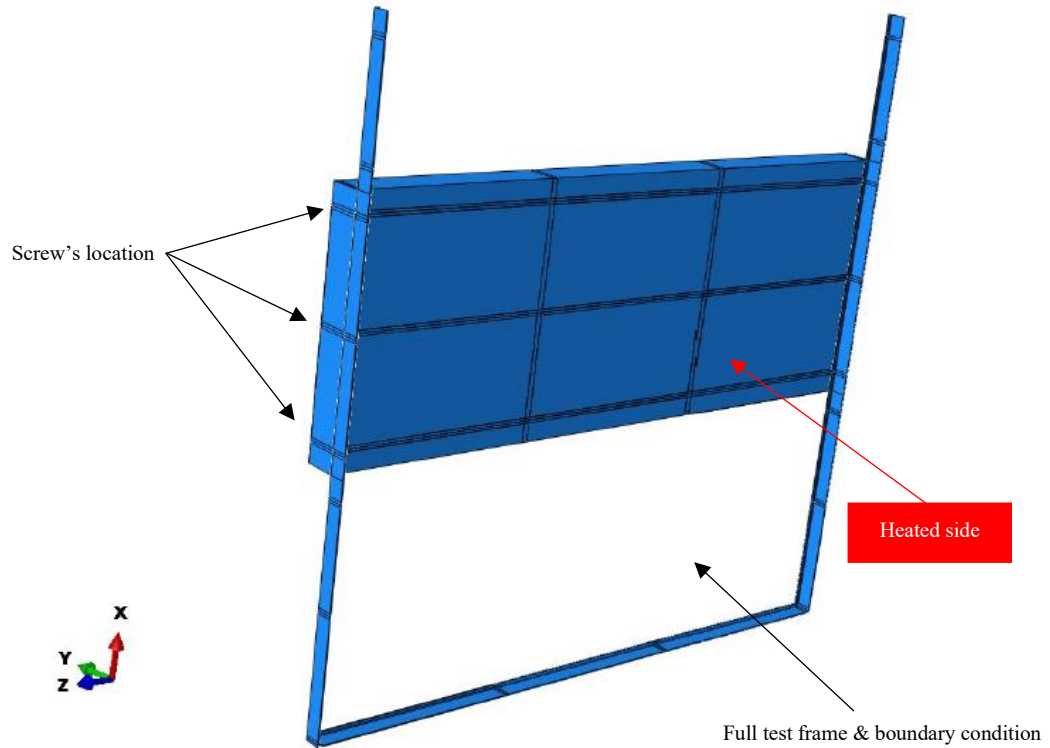


Figure 67. Structural test frame with screw locations for middle panel and boundary conditions.

The visual outputs below illustrates the structural response of the sandwich panels under thermal loading. Figure 68 provides a visualization of the longitudinal cross-sectional plane ( $y$   $z$ -plane), while Figure 69 illustrates the transverse cross-sectional plane ( $x$   $y$ -plane). These representations show how displacements evolve under heat exposure applied to one face of the panel assembly.

The longitudinal cross-section (Figure 68) reveals horizontal displacement distribution through the panel height, with the heating applied from the bottom. The displacement vectors indicate the movement along the  $y$ -axis, reflecting thermal expansion behavior during the first minute of testing. The highest displacement is observed in the middle panel near to joint connection, which is less constrained than the upper panel.

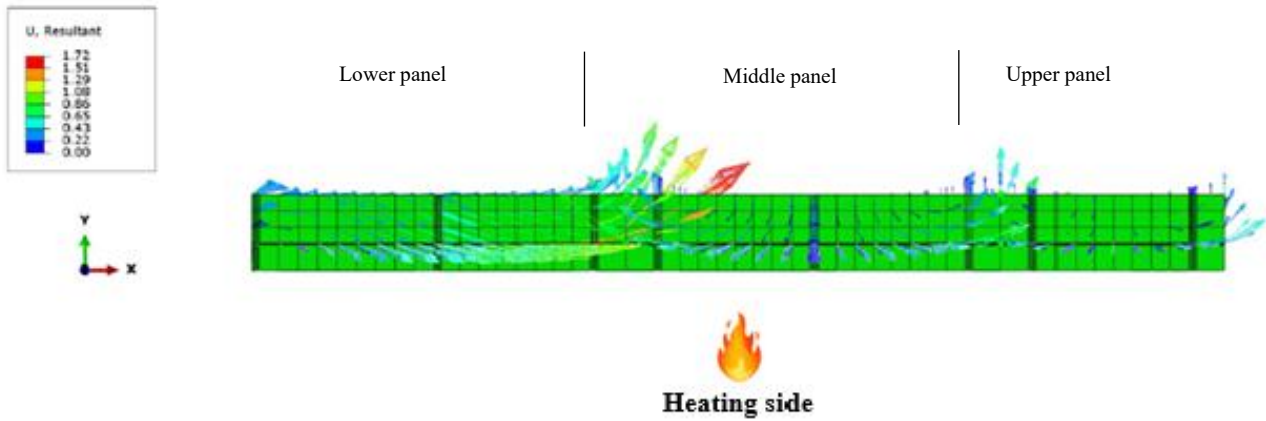


Figure 68. Displacement directions [max 1.72 mm] at initial thermal exposure, illustrated in the longitudinal cross-sectional plane ( $y$ - $x$  plane).

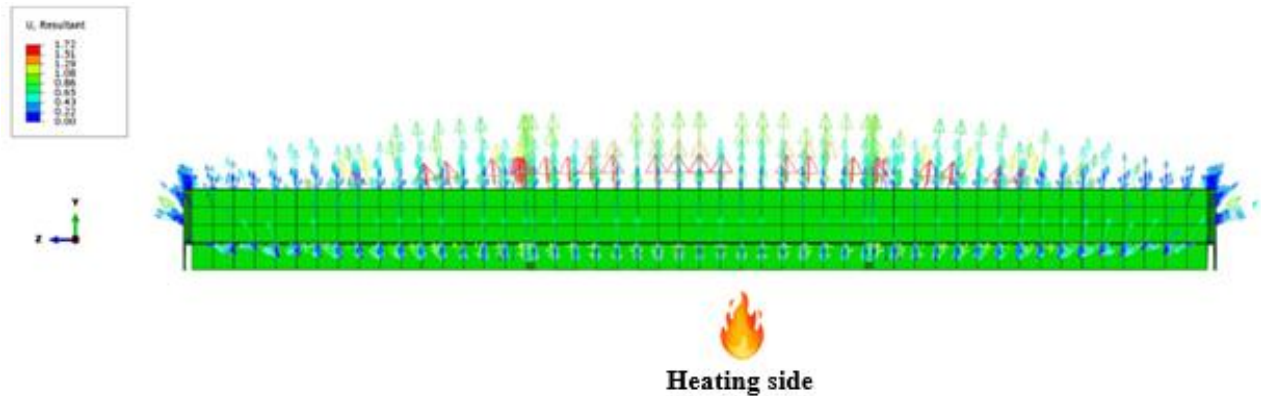


Figure 69. Displacement directions [max 1.72 mm] at initial thermal exposure, illustrated in the transverse cross-sectional plane ( $y$ - $z$  plane).

This uniform heating causes distributed thermal expansion, with deformation propagating along the  $x$ -,  $y$ -, and  $z$ - planes. However, the most significant displacement is captured in the  $y$ -direction and is visualized in the transverse cross-section. The lower panel, located on the left side, exhibits the highest upward displacement due to constraint effects. The middle and upper panels also deform, with displacement patterns influenced by thermal expansion and the interaction between the core and facings. In this initial phase, the interfaces between the panels emerge as critical zones where deformation and stress concentrations are most pronounced.

At the end of the test, these effects are amplified (cf. Figures 70 and 71). The lower panel continues to experience significant displacement, and the middle and upper panels show increased movement due to accumulated damages. These visual displacements confirm the locations of structural weakness under prolonged fire exposure.

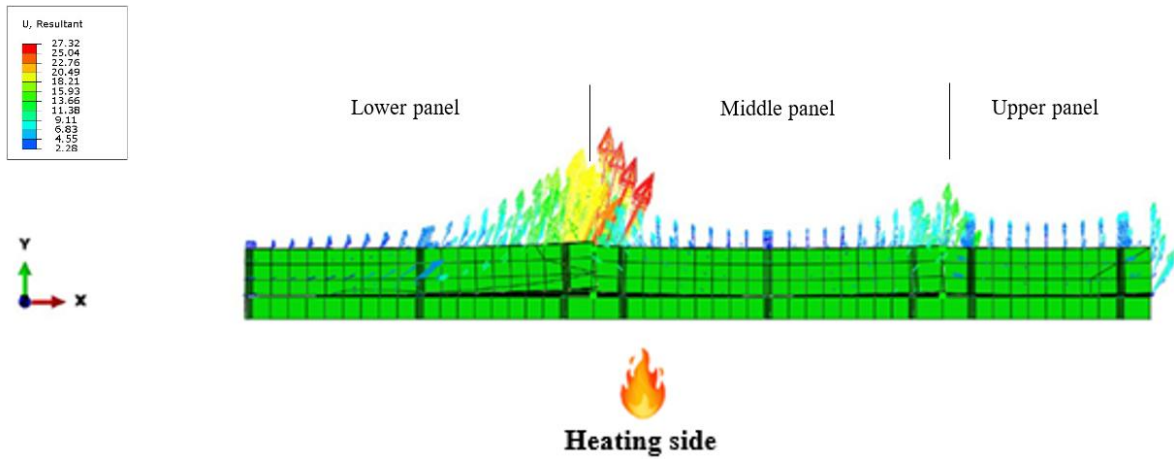


Figure 70. Displacement directions [max 27.32 mm] at the end of thermal testing, illustrated in the longitudinal cross-sectional plane ( $y$ - $x$  plane).

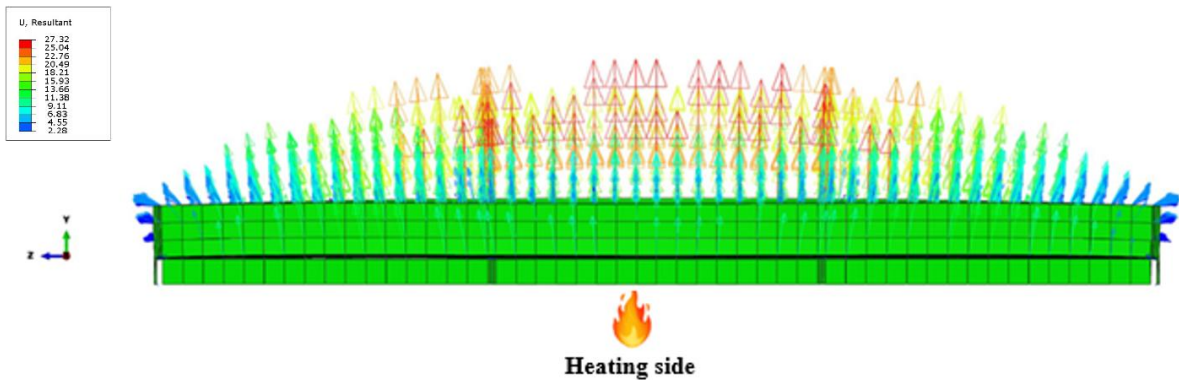


Figure 71. Displacement directions [max 27.32 mm] at the end of thermal testing, illustrated in the transverse cross-sectional plane ( $y$ - $z$  plane).

To illustrate the visual results comprehensively, Figure 72 provides a 3D visualization of the resultant displacement at the end of the test (10,880 s). This view encompasses all wall assembly and illustrates cumulative displacements in all spatial directions ( $x$ -,  $y$ -, and  $z$ - plane). Displacement vectors and the associated contour scale confirm that the greatest deformation occurred in the lower central region, aligning with the prior cross-sectional observations.

In addition, Figure 73 presents the corresponding 3D temperature distribution at the end of thermal exposure. This visualization illustrates the heat propagation across the full panels, with the maximum surface temperature reaching approximately 1123 °C on the heated side and decreasing to 179 °C on the unheated side. The temperature gradient induced by one-sided heating contributes to the thermomechanical response observed in the displacement results.

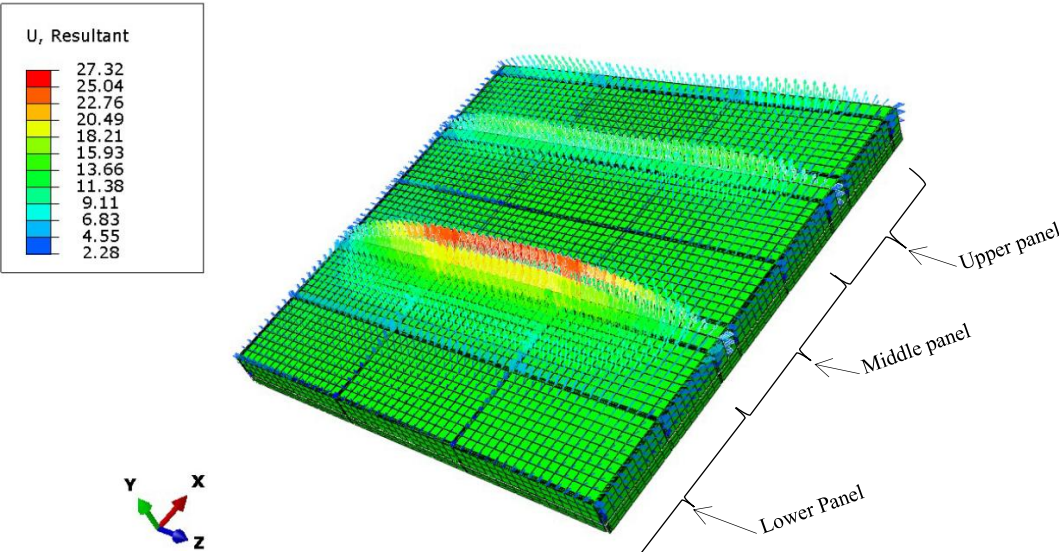


Figure 72. 3D visualization of resultant displacement field at the end of testing [10,880 s], viewed from the unheated side.

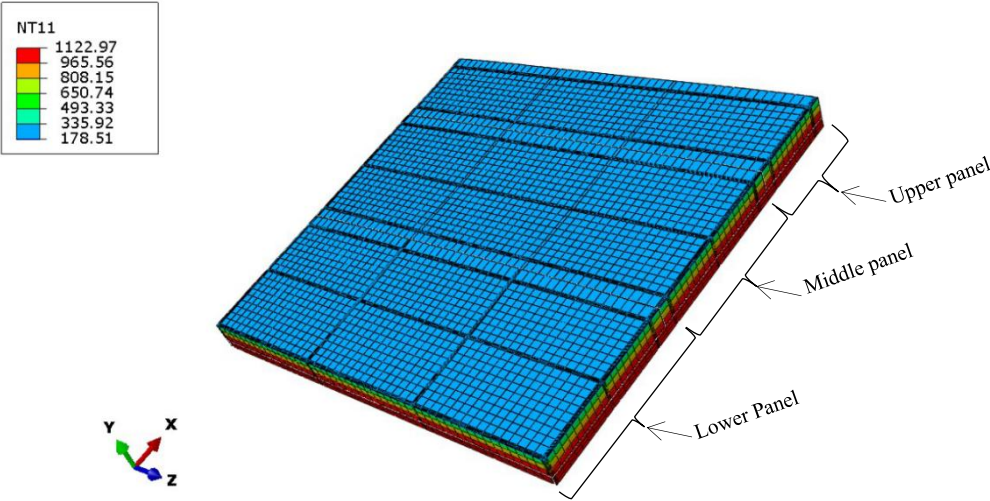


Figure 73. 3D visualization of temperature distribution at the end of thermal exposure, showing heat propagation across wall panels.



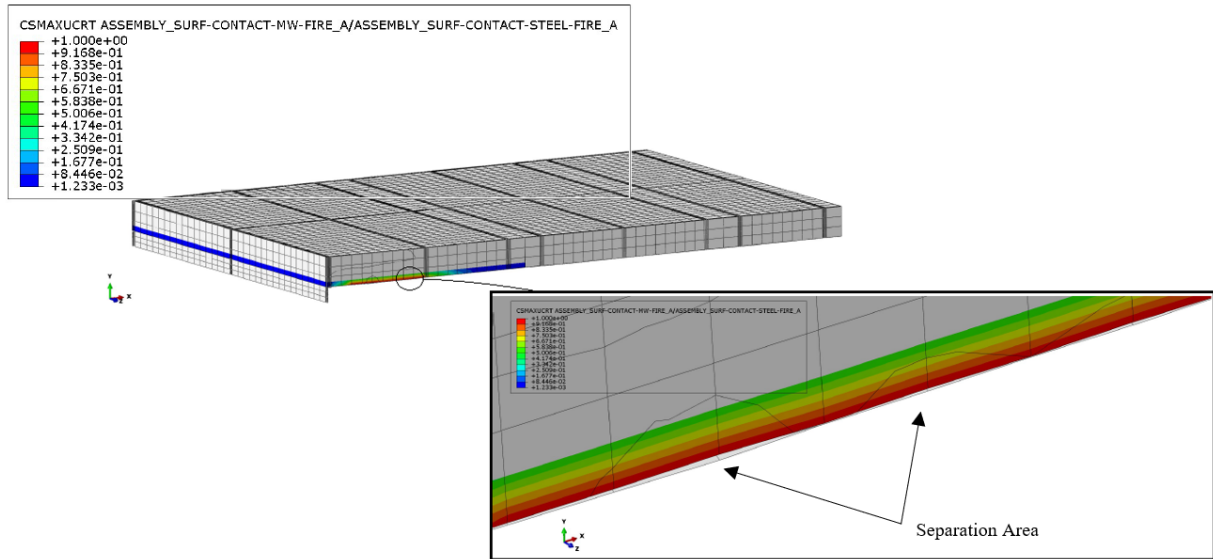


Figure 74. Numerical prediction of interface separation at  $t = 315$  s under fire load.

The failure process, encompassing both damage initiation and complete separation, was captured through the simulation. The criteria for damage evolution were consistent with the cohesive zone modelling approach implemented in ABAQUS. As illustrated in Figure 74, regions where the maximum effective separation reached a value equal to 1 correspond to full separation at the cohesive interface, thereby indicating complete damage (i.e.,  $D = 1$ ). The color gradient represents progressive damage, with red zones confirming interface failure.

After outlining the numerical model and presenting the graphical and visual outputs for Test 1', the subsequent section compares the experimental results with the numerical predictions obtained from the second modelling group. The purpose of this comparison is to interpret the horizontal displacement response (along the  $y$ -axis). The comparison is conducted for each measurement points (from A to J) defined experimentally, as described earlier in Chapter 4, Section 4.2 (cf. Figures 37 and 38).

## 5.5 Numerical and experimental displacement results

This section focuses on the comparison of numerical analysis results with the experimental outcomes from Test 1' and Test 2'. These tests have been selected for comparison due to their similar structural configurations, with the only distinction in the upper dimension of the panel assembly, as detailed in Section 4.3.

The comparison aims to evaluate and quantify the agreement between the second modelling group and the experimental measurements obtained at different measurement

points from unheated side, in order to identify displacement deviations in all structural response under thermal loading.

- **Test 1': Panel with 100 kg/m<sup>3</sup> core density, 150 mm core thickness, and 0.5 mm steel thickness**

The chart below compares the horizontal displacement at Point A (near the center of the upper panel) for Test 1', highlighting the relationship between the experimental data and the numerical simulation.

Initially, the change in the direction of displacement observed in the FEM results (Figure 58) is influenced by the interaction between thermal expansion, and boundary conditions. As the material heats up, thermal expansion causes the material to expand outward. The boundary conditions play a critical role in this process.

From Figure 75, it is evident that the experimental displacement increases more sharply than the FEM prediction. This difference arises because the boundary conditions in the experiment partially restrain the expansion. This restraint leads to the panel bowing outward, but without structural collapse. As the test progresses, the experimental displacement rises more rapidly, stabilizing at approximately 28 mm, while the FEM prediction reaching at around 20 mm, suggesting that the model slightly underestimates the displacement magnitude.

Despite these differences, the FEM results capture the overall trend and direction of displacement effectively. The comparison demonstrates the numerical model reliability in representing general behavior.

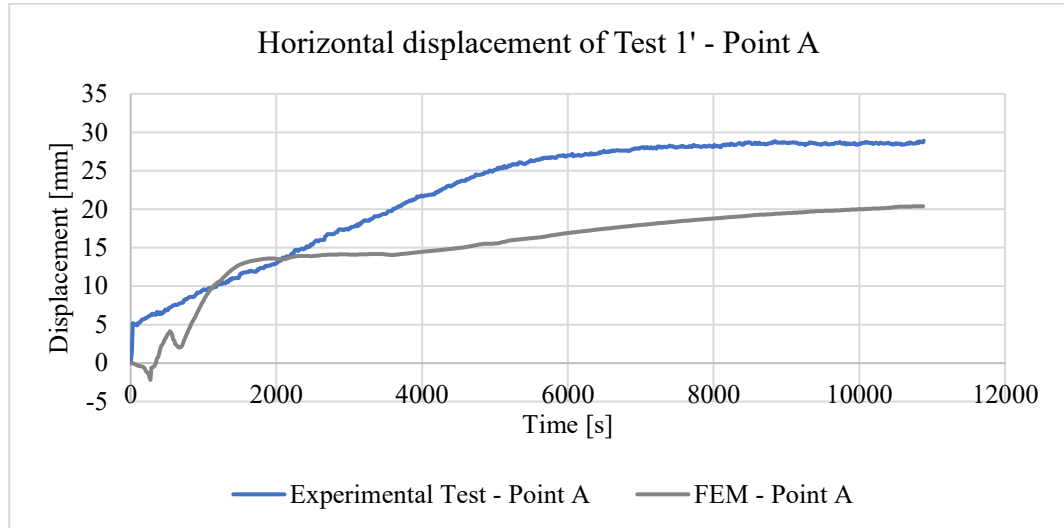


Figure 75. Horizontal displacement - experimental and FEM results at point A - Test 1'.

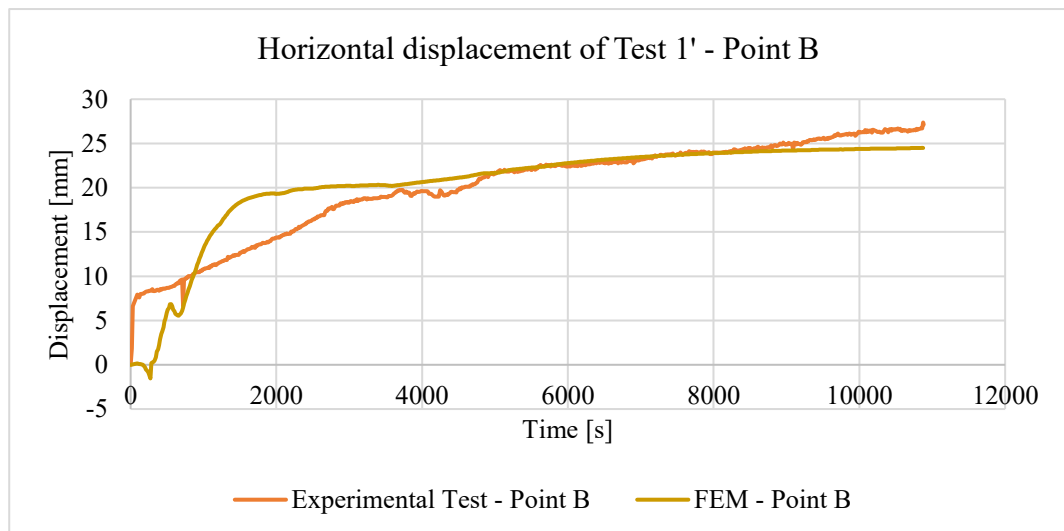


Figure 76. Horizontal displacement - experimental and FEM results at point B - Test 1'.

The graph (Figure 76) at Point B exhibits strong consistency between the experimental and FEM results, both testes near 25–30 mm after 10,000 seconds. A slight deviation in the FEM curve is observed during the initial phase, where the FEM underpredicts displacement for a short period before converging with the experimental trend. However, the change in direction of the FEM displacement at the beginning of the test as mentioned above is due to interaction between thermal expansion, and boundary conditions. Initially, as the material begins to expand due to thermal loading, the FEM model might not fully account for the restrained expansion caused by boundary conditions, leading to a temporary negative displacement before the model stabilizes.



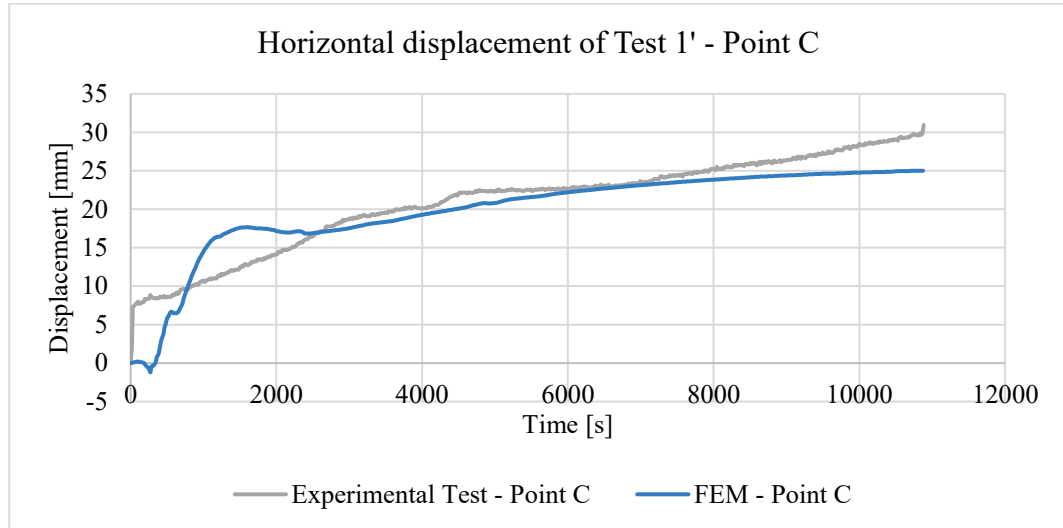


Figure 77. Horizontal displacement - experimental and FEM results at point C - Test 1'.

For Point C (Figure 77), also situated on the upper panel near to the upper joint panels, the experimental displacement finished at approximately 30 mm, while the FEM curve slightly underestimates the displacement throughout the test, around 25 mm. The early-phase variation is minimal, as both curves align closely.

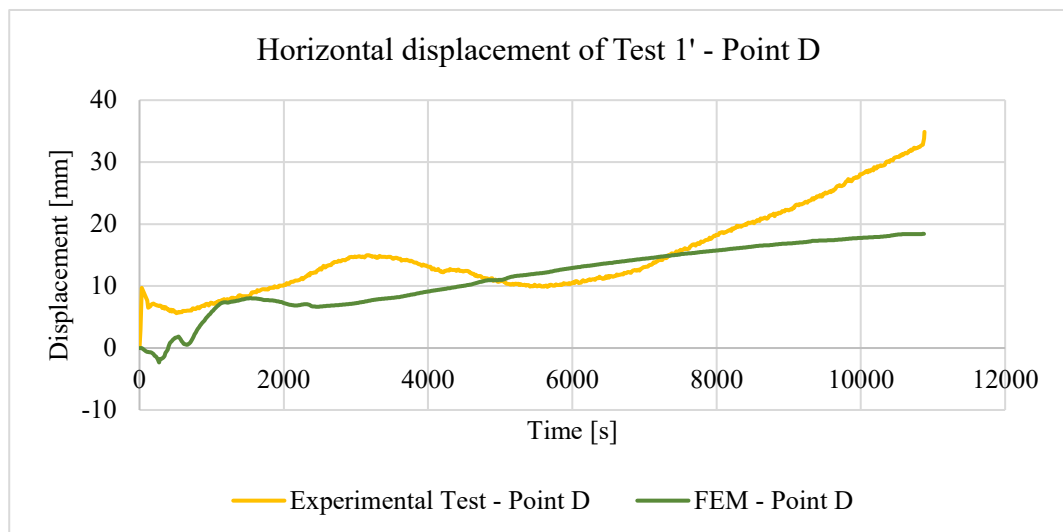


Figure 78. Horizontal displacement - experimental and FEM results at point D - Test 1'.

At Point D (Figure 78), located in the middle section of the panel, the experimental displacement initially exhibits fluctuations before end near 30 mm, while the FEM curve follows a smoother trend, finished around 25 mm. The early-stage divergence reflects potential challenges in modelling complex localized effects or transient behaviors in this region. Despite this, the FEM results effectively capture the general thermal displacement trend.

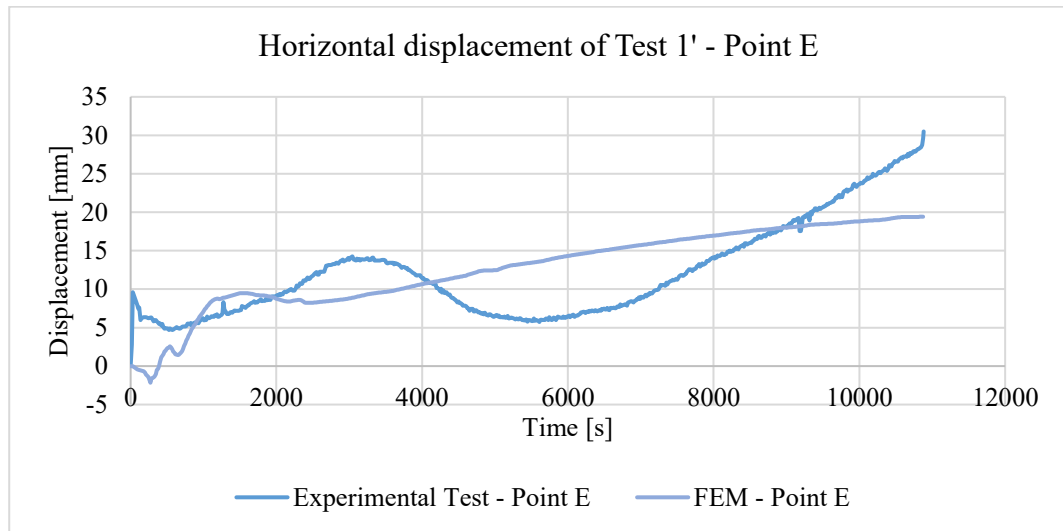


Figure 79. Horizontal displacement - experimental and FEM results at point E - Test 1'.

At Point E (Figure 79), located at the center of the middle panel, significant differences between the experimental and FEM results are observed because this region experiences more complex interactions that are not fully captured in the FEM model. The center of the panel is more susceptible to thermal gradients and localized phenomena, such as material interactions, panel self-load, and plastic deformation, which may cause fluctuations in the displacement. These effects result in more dynamic behavior in the experimental results. In contrast, the FEM model tends to represent the material as more uniform, leading to a smooth and gradual increase in displacement that does not account for these localized and nonlinear effects. After around 6,000 seconds, the experimental displacement surpasses the FEM prediction, indicating that the FEM model underestimates the magnitude and complexity of the displacement behavior, as it does not fully simulate the nonlinear or time-dependent effects occurring in the experiment.

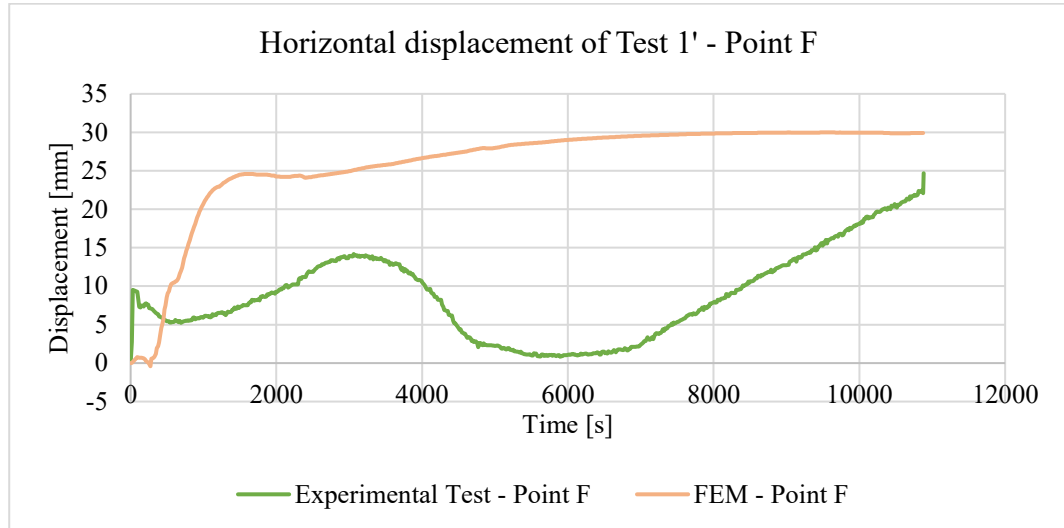


Figure 80. Horizontal displacement - experimental and FEM results at point F - Test 1'.

The graph for Point F (Figure 80), located near to upper joints of the lower panel, reveals noticeable differences between the experimental and FEM results. The FEM curve follows a smooth and steady increase in displacement, at approximately 35 mm. Conversely, the experimental displacement initially increases, then fluctuates significantly between 2,000 and 6,000 seconds, before gradually increasing again, ultimately ending at a lower value than the FEM prediction. This early-phase mismatch indicates that the FEM model struggles to accurately simulate the transient effects of combined thermal and gravitational forces in this lower region. Improved representation of material response under complex loading conditions could enhance alignment.

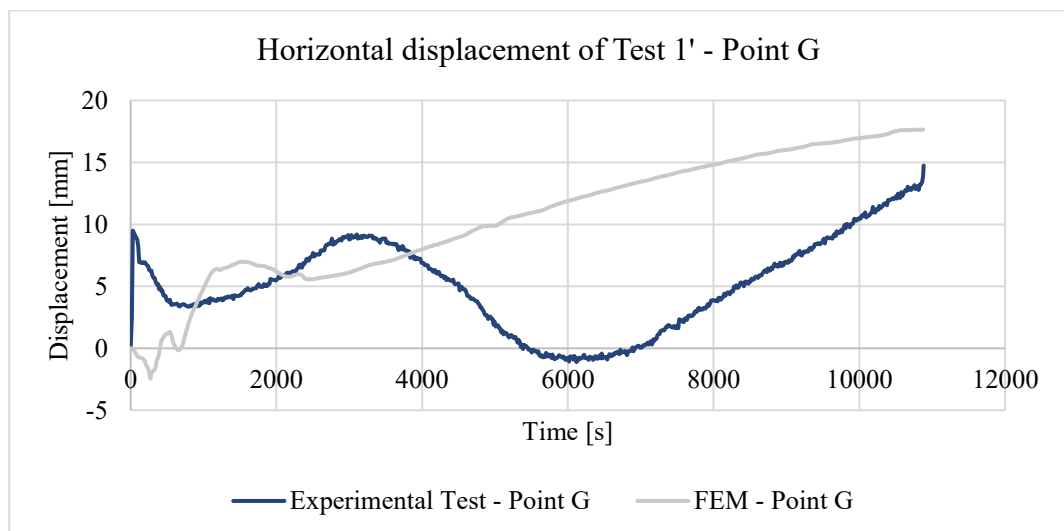


Figure 81. Horizontal displacement - experimental and FEM results at point G - Test 1'.

The graph for Point G (Figure 81), located at the middle of the lower panel, reveals distinct differences between the experimental and FEM results. Initially, the FEM curve shows a smooth and continuous increase in displacement, reflecting the overall thermal expansion of the panel, with displacement reaching approximately 15 mm by the end of the test. In contrast, the experimental displacement shows more complex behavior. Initially, there is a slight downward trend, due to thermal gradients and restraint effects from the boundary conditions. This is followed by a rapid increase in displacement, peaking at around 2,000 seconds, after which fluctuations dominate the displacement between 2,000 and 6,000 seconds. These fluctuations are due to the interaction between the material and boundary conditions at the panels' lower edge, where the thermal gradients and restrained expansion are more pronounced.

After 6,000 seconds, the experimental displacement transitions into a gradual upward trend, partially aligning with the FEM curve but consistently remaining below it. This indicates that the FEM model captures the overall trend but underestimates the localized effects and time-dependent variability seen in the experimental results. The experimental data highlights the importance of boundary conditions, material interactions, and thermal gradients near the lower edge of the panel, which the FEM model simplifies or overlooks. The fluctuations observed experimentally suggest that these factors significantly influence the displacement at this point, whereas the FEM model, with its more generalized assumptions, does not fully account for these complex interactions.

The experimental results at Point G show complex localized behavior and time-dependent fluctuations, reflecting the impact of boundary conditions and material interactions, especially at the panel's lower edge. The FEM model

underestimates these effects, capturing only the general trend of the displacement without accounting for the localized fluctuations observed experimentally.

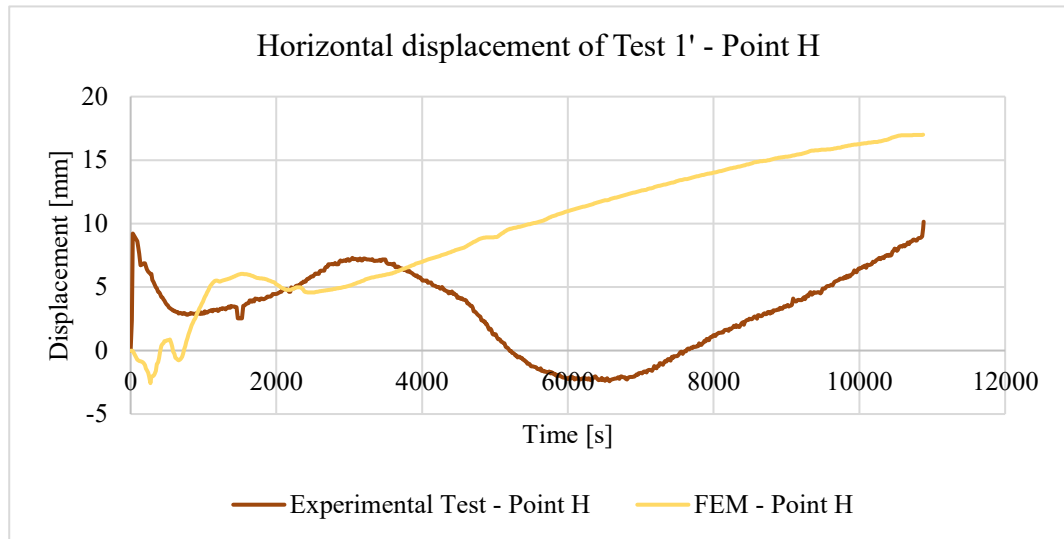


Figure 82. Horizontal displacement - experimental and FEM results at Point H - Test 1'.

Point H (Figure 82), also located on the lower panel, the displacement graph shows a notable divergence between the experimental data and the FEM results, emphasizing a complex interaction at this location on the lower panel. The experimental displacement initially exhibits fluctuations, followed by a significant decrease, reaching a negative displacement phase (indicating contraction), before gradually recovering around 10 mm. In contrast, the FEM results predict a consistent positive upward trend, near 15 mm, with no indication of contraction or recovery. This early-stage variation indicates that the FEM model does not fully capture the nonlinear or fluctuating behavior observed experimentally.

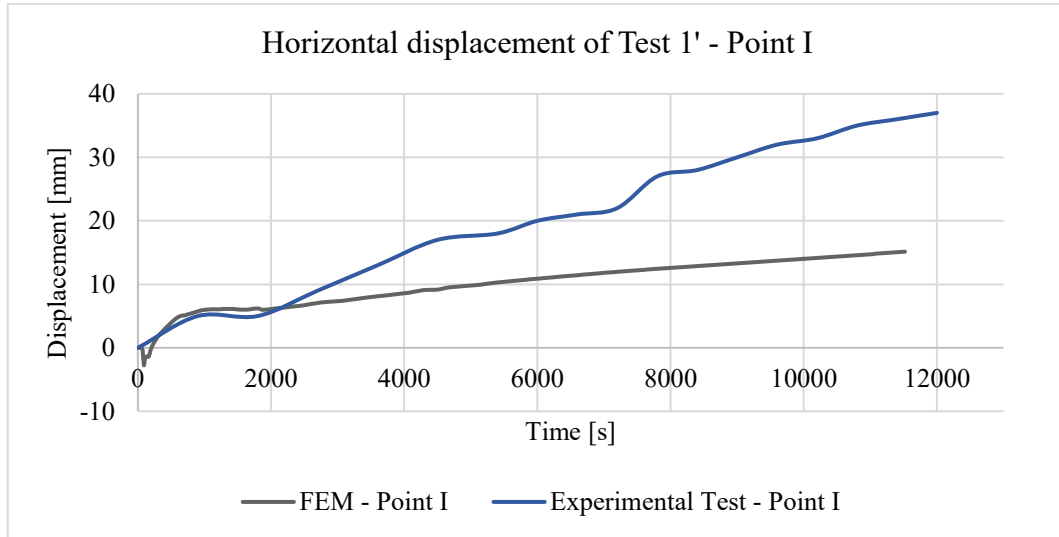


Figure 83. Horizontal displacement - experimental and FEM results at point I - Test 1'.

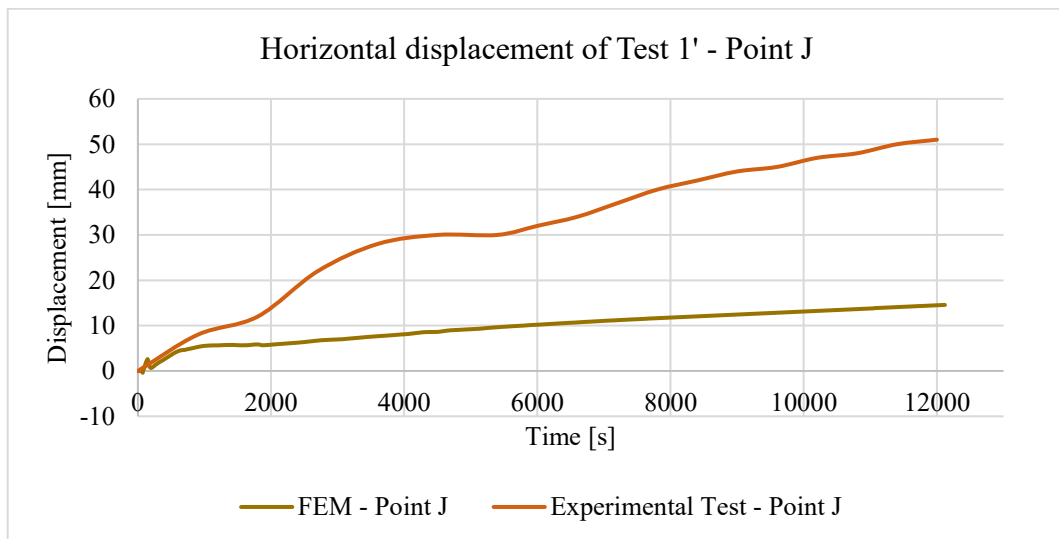


Figure 84. Horizontal displacement - experimental and FEM results at point J - Test 1'.

In Figures 83 and 84, no displacement trend changed is observed at Points I and J, as at Points E, F, G, and H, where Point E is located in the same panel and at the same vertical level of point I, and J. Instead, a continuous increase in displacement occurs, indicating sustained deformation in these boundary regions. At Point I, the experimental displacement exceeds FEM predictions, suggesting progressive damage such as micro-cracking or interface separation. At Point J, even higher displacement magnitudes indicate stress concentration effects and boundary conditions influence.

- **Test 2':** Panel with 100 kg/m<sup>3</sup> core density, 150 mm core thickness, and 0.5 mm steel thickness

The results of Test 2' were analyzed as well, to evaluate the same aim is the ability of the numerical simulation to replicate the experimental data, considering the modification of the upper dimension of the panel assembly. With the boundary conditions and assembly configurations unchanged from Test 1', the displacement behavior reflects the combined effects of the structural alteration and consistent thermal and mechanical loading.

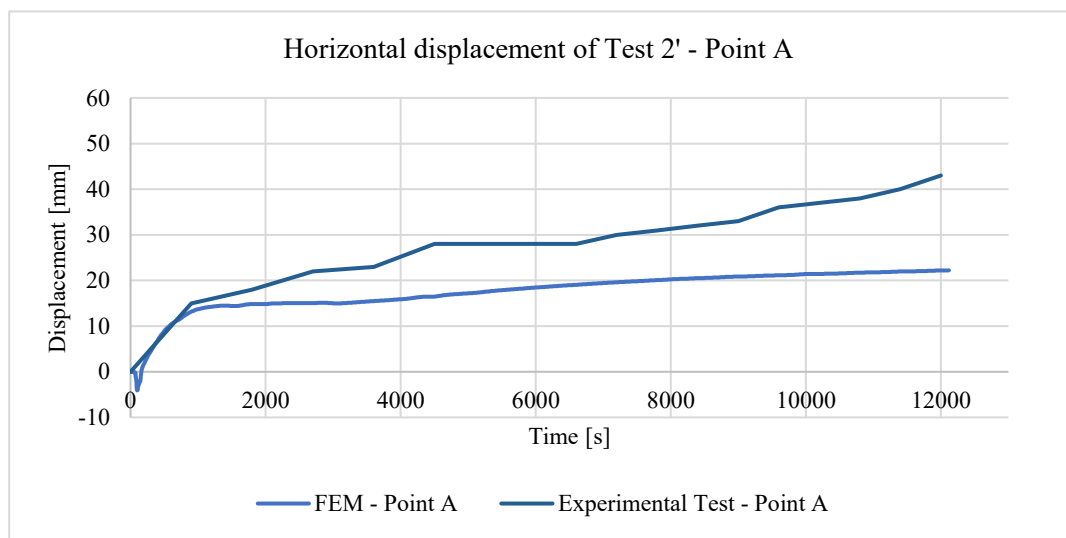


Figure 85. Horizontal displacement - experimental and FEM results at point A - Test 2'.

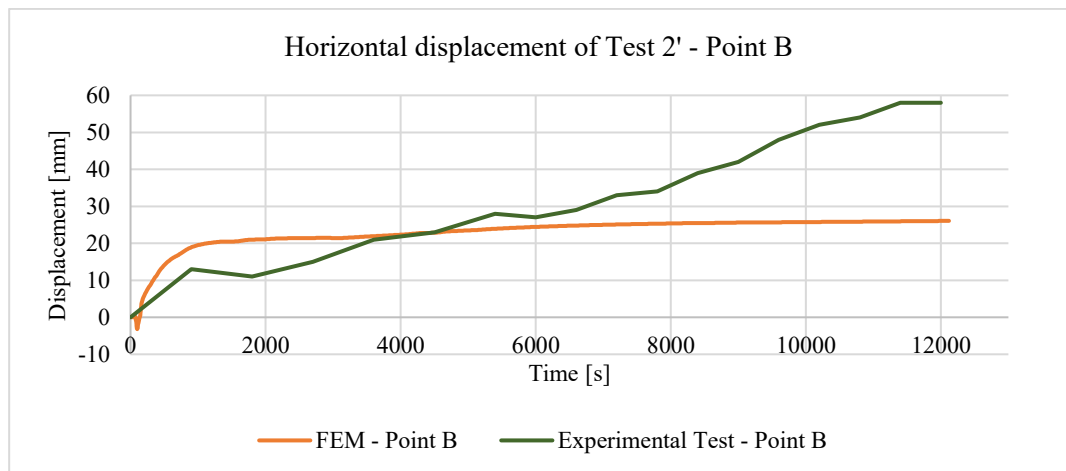


Figure 86. Horizontal displacement - experimental and FEM results at Point B - Test 2'.

The analysis highlights the similarity of the findings of Test 1' and the influence of thermal expansion and gravitational load transfer on displacement. The

points located on the lower panel (e.g., F, G, and H) show higher displacement variability and nonlinear behavior, as these regions are subjected to the cumulative load and stresses transferred from the upper sections. This redistribution amplifies the deformation in the lower regions, a phenomenon effectively captured by the FEM model. Conversely, points on the upper panel (e.g., A, B, and C) exhibit smoother and more uniform displacement trends, with closer alignment between the FEM predictions and experimental observations, as these areas experience less load concentration and more uniform thermal expansion.

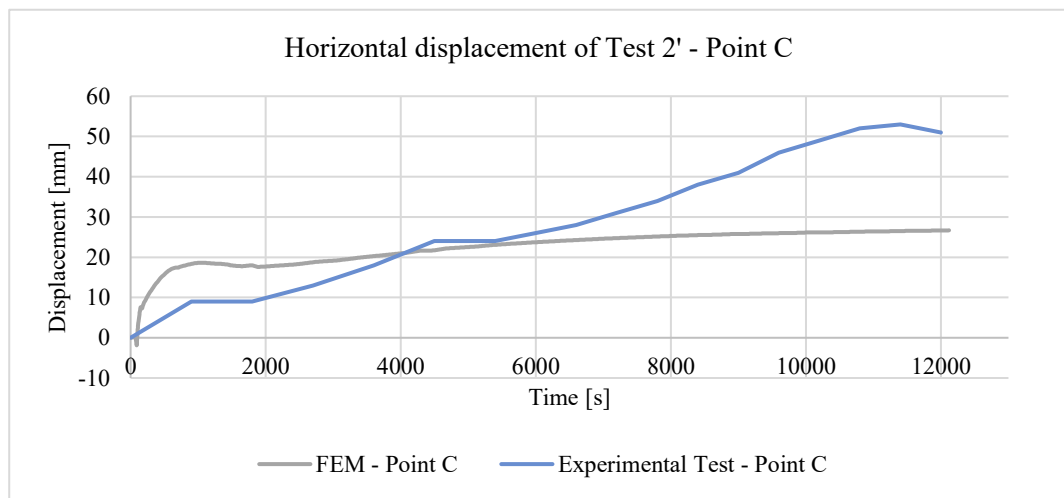


Figure 87. Horizontal displacement - experimental and FEM results at point C - Test 2'.

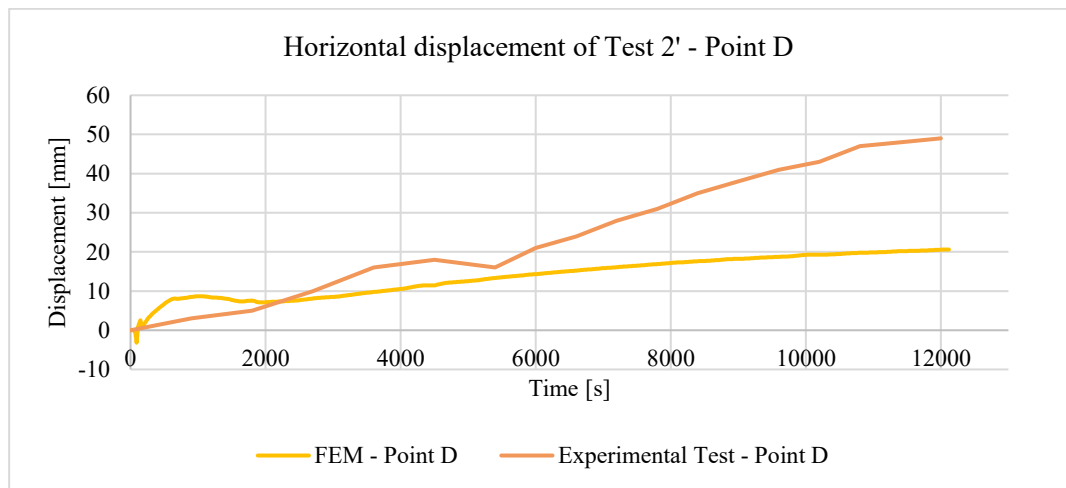


Figure 88. Horizontal displacement - experimental and FEM results at Point D - Test 2'.



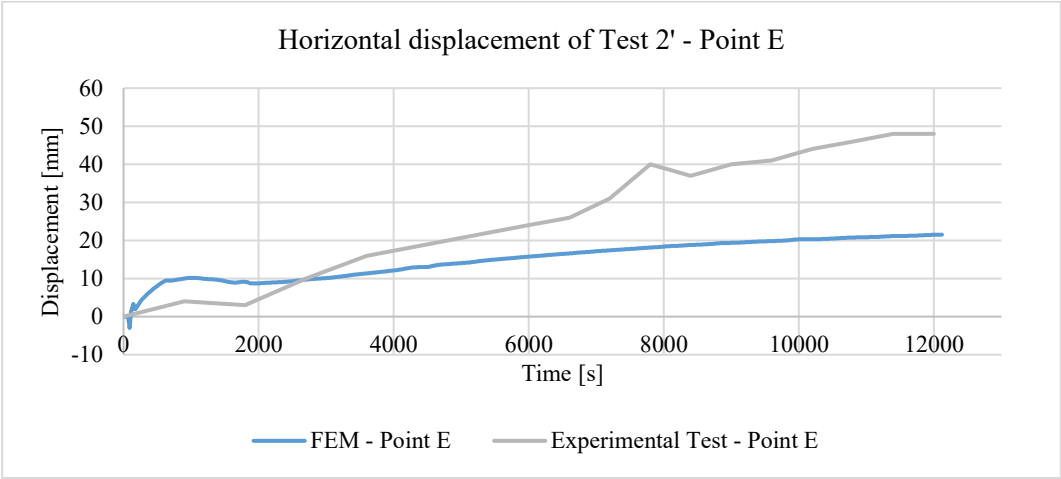


Figure 89. Horizontal displacement - experimental and FEM results at point E - Test 2'.

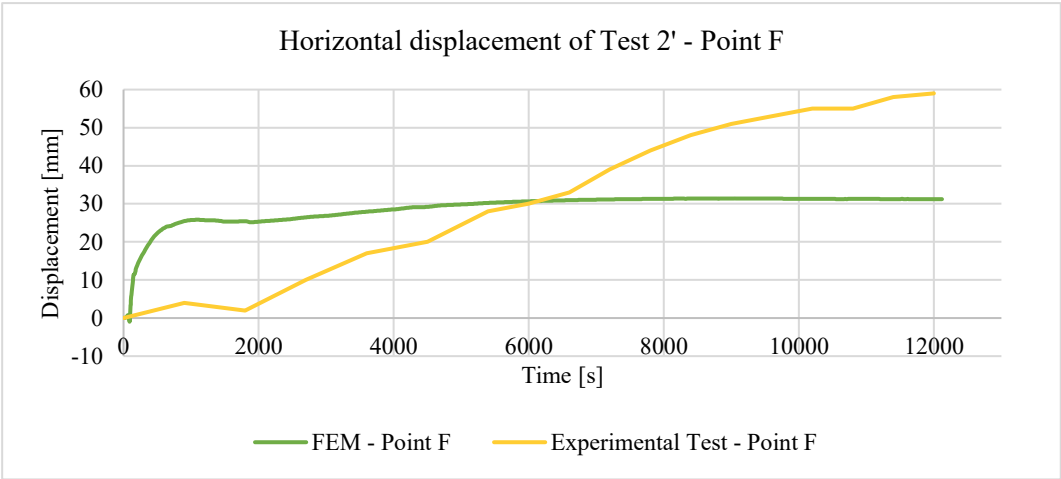


Figure 90. Horizontal displacement - experimental and FEM results at Point F - Test 2'.

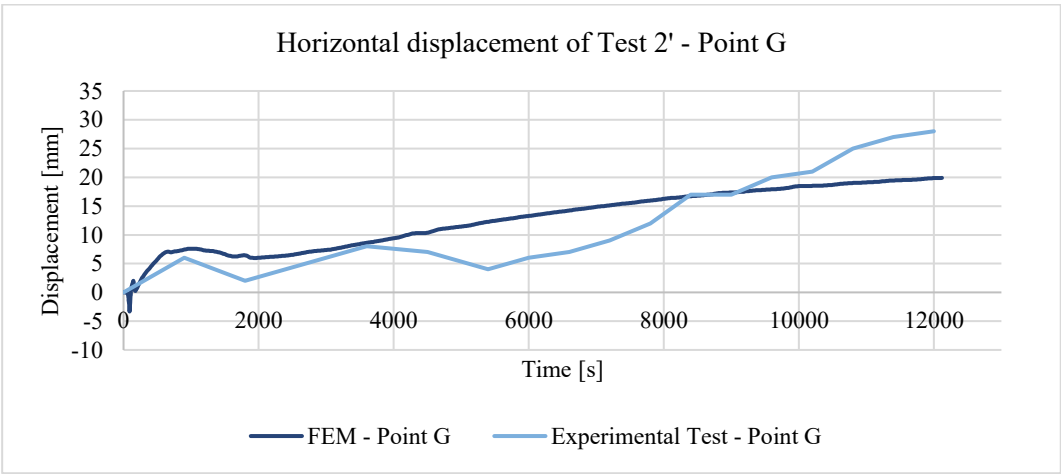


Figure 91. Horizontal displacement - experimental and FEM results at Point G - Test 2'.

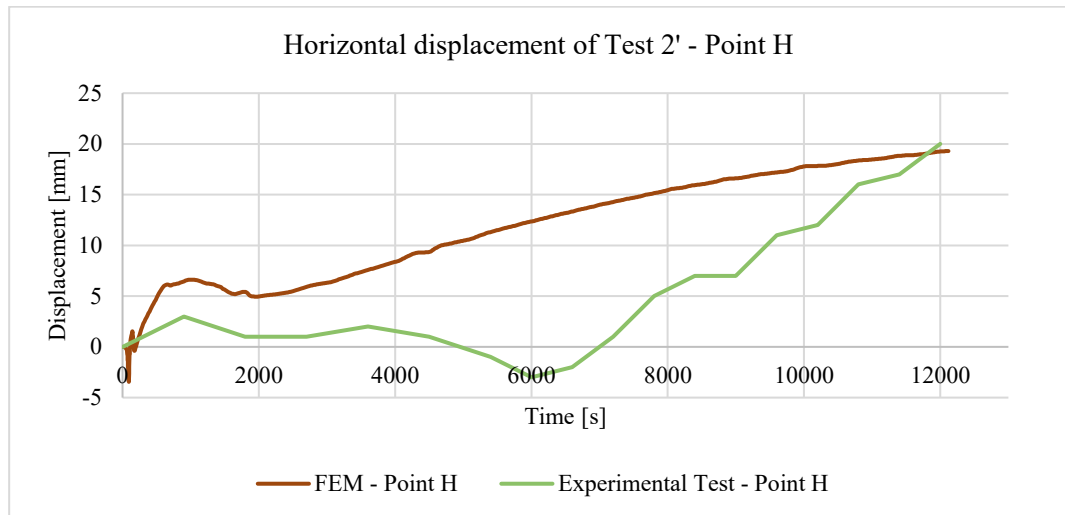


Figure 92. Horizontal displacement - experimental and FEM results at Point H - Test 2'.

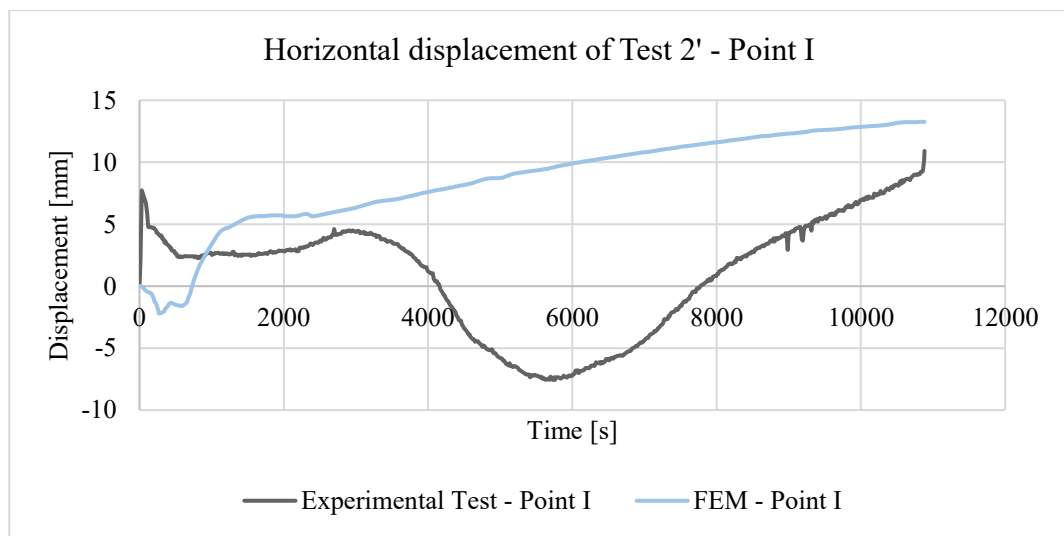


Figure 93. Horizontal displacement - experimental and FEM results at point I - Test 2'.

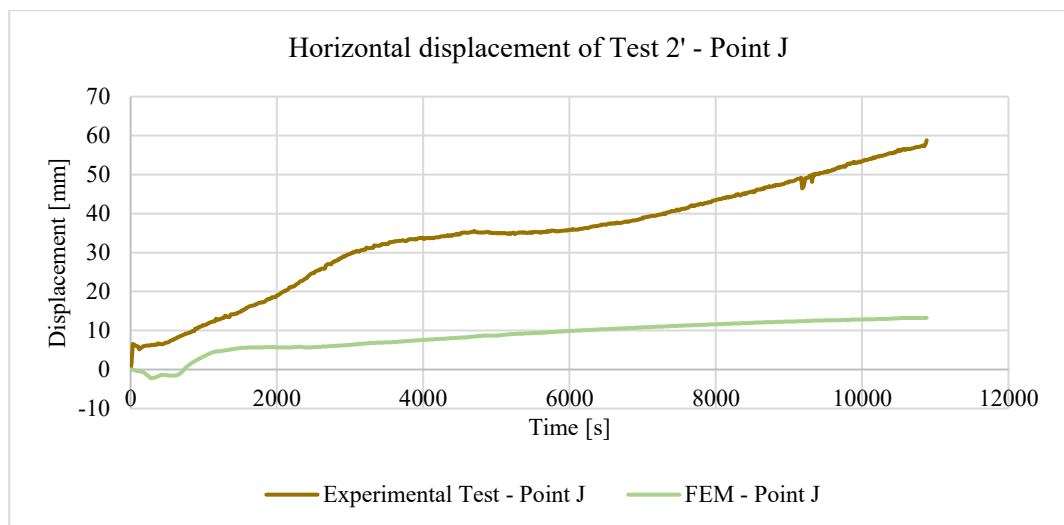


Figure 94. Horizontal displacement - experimental and FEM results at point J - Test 2'.

In Figures 93 and 94, the displacement behavior at Points I and J differs significantly, despite being in the same panel and vertical level as Point E (Figure 89). At Point I, the experimental displacement initially decreases before reversing direction and increasing, suggesting an initial contraction due to restraint effects followed by progressive expansion as stress redistributes. This behavior indicates local stress relaxation or facing delamination. At Point J, the displacement continuously increases, significantly exceeding FEM predictions, implying gradual weakening or delamination at the panel edge. As Point E, where stress redistribution shifts the displacement trend, Points I and J experience sustained deformation due to localized boundary.

Based on the provided displacement data for Test 1' and Test 2' at various points across the panels, a short summary can be drawn regarding the comparison between the experimental results and FEM predictions.

In both tests, the experimental results show more complex displacement behavior, characterized by fluctuations, sharp increases, and more pronounced deviations, particularly in the middle and lower regions of the panels. These fluctuations are caused by localized effects such as boundary conditions, thermal gradients, and material interactions that vary across the panels. The FEM results, on the other hand, tend to follow a smoother, more gradual displacement pattern, reflecting a more general thermal expansion without fully capturing these localized complexities.

Despite these discrepancies, the FEM model generally captures the overall trend of displacement, though it underestimates the magnitude and time-dependent behavior observed experimentally. The differences highlight the need for further refinement in the model to better account for nonlinear effects, boundary constraints, and thermal behavior at different locations on the panel.

## **5.6 Summary and conclusions**

The finite element models developed in this investigation demonstrate their capacity to capture directional trends, and the overall deformation behavior of sandwich panels subjected to fire loads. The model also demonstrated its capability to simulate bond degradation, and separation behavior, providing valuable insights into the progressive failure of adhesive layers under extreme thermal load. The cohesive zone modelling approach effectively represented damage initiation and evolution, ensuring a realistic depiction of the thermal and mechanical response of sandwich panels. Despite these

achievements, certain limitations were identified, particularly in regions where load redistribution plays a significant role. These localized discrepancies underline the need for further refinement of the analysis to enhance its accuracy.

The findings underscore the importance of improving the definition of material properties, boundary conditions, and interaction effects within the model to account for phenomena such as localized delamination, material degradation, and thermal expansion more effectively. While the current FEM approach provides a foundation for understanding the thermomechanical behavior of sandwich panels made by mineral wool. The limitations encountered, including time constraints, precluded the evaluation of alternative simulation techniques or the development of more detailed models within this investigation.

---

## Chapter 6. Conclusions

The fire behavior of sandwich panels has been presented based on an analysis of their thermal and mechanical performance at elevated temperatures, with a focus on panels with mineral wool cores. To support this analysis, material properties, geometric configurations, and boundary conditions have been integrated into finite element simulations. These simulations included thermal conductivity and cohesive interactions to more accurately replicate real conditions. This multi-faceted approach allows a detailed prediction of fire resistance by capturing the parameters influencing the structural performance of sandwich panels. The numerical simulations closely replicate experimental observations, including displacement patterns. This provides a basis for understanding the performance of sandwich panels and informs further design and safety optimization strategies.

### Main conclusions based on the conducted research

The research conducted aimed to explain and predict the behavior of sandwich panels subjected to fire temperatures and to determine the influence of material properties, geometric properties and boundary conditions on this behavior. These explications and predictions were achieved by means of a combination of small-scale and large-scale experiments, as well as numerical simulations results. It was possible to analyze the fire performance of these panels with respect to their material composition, boundary conditions, and geometric characteristics. The outcomes confirm and address hypotheses formulated at the beginning of the study.

- Prediction of fire resistance

Based on material tests, known geometrical properties, and technological solutions, it is possible to predict the fire resistance of sandwich panels.

This hypothesis was verified by developing an advanced FEM model and comparing the numerical simulation results with the results of large-scale fire tests. The FEM model included the material parameter values from laboratory tests, detailed panel geometry and construction details corresponding to the conditions of large-scale tests. The numerical simulation results showed good agreement of the temperature distributions and displacement trends with the results measured during the actual tests. The graphs of

the temperature dependence of the unheated panel surface on time presented in Figures 48–50 corresponded to the experimental curves. Similarly, the predicted horizontal displacements at specific measurement points reflected the general trend of displacements observed during the tests (see Figures 75–94). The obtained agreement of the results confirms the possibility of predicting the behavior of sandwich panels subjected to fire temperatures, including fire resistance, for the established geometric, material, temperature and support conditions.

▪ Influential parameters

It is possible to specify a group of parameters that significantly affect the fire resistance of sandwich panels.

The fire test results showed that core density, core thickness and thickness of steel facing have a measurable effect on both thermal insulation and structural response of the panels. Core thickness was identified as a parameter that significantly affects the performance of the panels. Panels with a mineral wool core of 100 kg/m<sup>3</sup> density and 150 mm thickness (Test 1' and Test 2') showed a prolonged heat transfer process and longer-lasting structural integrity, which resulted in better fire resistance. In the case of panels with a core of 95 kg/m<sup>3</sup> density and 120 mm thickness (Test 4'), the temperature rise on the unheated facing was faster and the debonding and buckling of the heated facing towards the heat source occurred faster than in the tests Test 1' and Test 2'. Even with a higher core density (120 kg/m<sup>3</sup> in Test 3'), the thinner core thickness (100 mm) led to faster heat transfer and premature failure, confirming that a thicker panel is essential for thermal and mechanical stability.

The thickness of the steel facing is not the main factor influencing the performance of the panels in the fire tests. The use of a 0.60 mm facing (Test 4') did not provide higher fire resistance due to the thinner core thickness. The effect of core density on fire resistance is not unequivocal. Although there is some evidence to suggest that higher density provides better fire resistance, the small number of fire tests analyzed do not allow such a clear statement.

In addition to material characteristics, structural and boundary conditions were found to exert a significant influence on panel behavior. The influence of support conditions was demonstrated through comparative simulations, which revealed that changes in constraint types—such as fixed, pinned, or roller supports—led to distinct

displacement outcomes. The effect of geometric variation was also evident. Although Tests 1' and 2' employed panels with identical material compositions, differences in upper panel geometry, particularly in panel height, led to measurable changes in displacement behavior. These outcomes, both numerically predicted and experimentally confirmed, demonstrate that even minor adjustments in geometry or restraint conditions significantly influence thermomechanical response.

#### Original contribution of the dissertation

- **Advanced analytical model for thermal diffusivity**

A novel regression-based analytical model was developed that takes into account the anisotropy of mineral wool due to fiber orientation. The proposed approach, described in detail in Chapter 3, allows obtaining thermal parameters for simulation under fire exposure conditions.

- **Parameters significantly influencing the behavior of sandwich panels**

A systematic experimental and numerical study was conducted to explain the influence of material property and configuration changes on the behavior of sandwich panels under fire temperature conditions. It was found that the influence of core density and the thickness of the core and steel facings is particularly important.

- **FEM-based framework for fire resistance analysis**

A finite element method (FEM)-based approach was presented, capable of extrapolating laboratory fire test results to other panel geometries and boundary conditions. This framework facilitates predictive assessments of the thermal and structural performance of sandwich panels without the necessity for extensive experimental campaigns.

- **The impact of boundary conditions**

A systematic comparison between numerical results under varied boundary conditions was performed, demonstrating the critical role of boundary constraints in influencing the direction and magnitude of displacement, thereby contributing to a more refined understanding of fire-induced deformation mechanisms.

---

*Limitation of the research*

The research is limited to mineral wool (MW) core material, excluding other materials such as polyisocyanurate (PIR), which may exhibit different fire behavior. Material degradation, in particular the temperature-dependent mechanical properties of mineral wool, have been simplified, potentially affecting displacement accuracy. Thermal boundary conditions were idealized and may not fully represent non-uniform heat exposure or radiative effects, which may also affect structural response predictions under fire conditions. Despite these limitations, this research provides a strong starting point for modelling and shows where improvements can be made in future fire studies.

*Recommendation for future research*

Future research should incorporate progressive conduction and radiation models during the early separation phase to enhance thermal accuracy. Additionally, more realistic temperature-dependent material properties and non-idealized thermal boundary conditions should be considered. Furthermore, experimental investigations are recommended to accurately determine cohesive parameters under elevated temperatures, which will improve the predictive capabilities under fire exposure conditions.



---

## Literature

- [1] European Committee for Standardization, EN 14509: Self-supporting double skin metal faced insulating panels – Factory made products – Specifications, CEN, Brussels, 2013.
- [2] Brushlinsky, N.N., Ahrens, M., Sokolov, S.V., and Wagner, World Fire Statistics, CTIF, International Association of Fire and Rescue Services, 2017, p. 22.
- [3] Davies, J.M., Lightweight Sandwich Construction, published on behalf of CIB Working Commission W056 Sandwich Panels (joint CIB-ECCS Commission), Manchester, UK, 2001.
- [4] International Organization for Standardization, ISO 13784-2:2020.
- [5] European Committee for Standardization, EN 1364-1: Fire Resistance Tests for Non-Loadbearing Elements—Part 1: Walls, CEN, Brussels, Belgium, 2015.
- [6] European Committee for Standardization, EN 1364-2: Fire Resistance Tests for Non-Loadbearing Elements—Part 2: Ceilings, CEN.
- [7] European Committee for Standardization, prEN 13381-1: Test Methods for Determining the Contribution to the Fire Resistance of Structural Members—Part 1: Applied Passive Protection, CEN.
- [8] European Committee for Standardization, EN 13501-1: Fire Classification of Construction Products and Building Elements—Part 1: Classification Using Data from Reaction to Fire Tests, CEN.
- [9] American Society for Testing and Materials (ASTM), ASTM E84: Standard Test Method for Surface Burning Characteristics of Building Materials, ASTM International.
- [10] National Fire Protection Association (NFPA), NFPA 286: Standard Methods of Fire Tests for Evaluating Contribution of Wall and Ceiling Interior Finish to Room Fire Growth, NFPA.

- 
- [11] Zhongji Machines, How Do You Manufacture Sandwich Panels?, Retrieved from <https://zhongji-machines.com/blogs/news/how-do-you-manufacture-sandwich-panels>.
- [12] International Organization for Standardization, ISO 834: Fire-Resistance Tests—Elements of Building Construction, ISO.
- [13] Hardy, C.C., Wildland Fire Hazard and Risk: Problems, Definitions, and Context, USDA Forest Service—Rocky Mountain Research Station, Missoula Fire Sciences Laboratory, Missoula, MT, USA.
- [14] Buchanan, A.H., and Abu, A.K., Structural Design for Fire Safety, Wiley, University of Canterbury, New Zealand, 2017.
- [15] Kodur, V., Properties of Concrete at Elevated Temperatures, ISRN Civil Engineering, vol. 2014, 2014, pp. 1–15.
- [16] Warrington Fire Research, Fire Resistance Test in Accordance with BS 476: Part 22, 1987, Section 5, on a Paroc Asymmetrical Non-loadbearing Partition Assembly, Report WARRES 58390, UK, 1993.
- [17] Roszkowski, P., & Sulik, P. (2016, January). Sandwich panels – behavior in fire based on fire resistance tests. In Applications of Structural Fire Engineering. <https://doi.org/10.14311/asfe.2015.065>
- [18] European Committee for Standardization, EN 15254-5: Extended Application of Results from Fire Resistance Tests—Non-loadbearing Walls—Part 5: Metal Sandwich Panel Construction, CEN.
- [19] Xu, Q., Hofmeyer, H., Maljaars, J., and van Herpen, R.A.P., Thermomechanical Modelling of Sandwich Panels with Connections in Fire Resistance Tests. In Jiang, L., Real, P.V., Huang, X., Orabi, M.A., Qiu, J., Chu, T., Nan, Z., Chen, C., Wang, Z., and Usmani, A. (Eds.), Proceedings SiF 2022 - The 12th International Conference on Structures in Fire, 2022, pp. 703–714.

- 
- [20] Xu, Q., Hofmeyer, H., Maljaars, J., and van Herpen, R.A.P., Full-Scale Fire Resistance Testing and Two-Scale Simulations of Sandwich Panels with Connections, *Fire Technology*, vol. 60, 2023, pp. 2461–2488. <https://doi.org/10.1007/s10694-023-01463-y>.
- [21] De Paula, D.J., Rodrigues, J.P.C., Camargo, A.L., and Lopes, R.F.R., Performance Fire Tests on Building External Walls Made of Sandwich Panels, *Fire Safety Journal*, vol. 150, 2024, p. 104273. [doi:10.1016/j.firesaf.2023.104273](https://doi.org/10.1016/j.firesaf.2023.104273).
- [22] American Society for Testing and Materials (ASTM), ASTM E119-20: Standard Test Methods for Fire Tests of Building Construction and Materials, ASTM International.
- [23] European Committee for Standardization, EN 1363-1:2020 - Fire Resistance Tests—Part 1: General Requirements, CEN.
- [24] European Committee for Standardization, EN 14509:2013 - Self-Supporting Double Skin Metal Faced Insulating Panels—Factory Made Products—Specifications, CEN, 2013.
- [25] Franssen, J.-M., and Vila Real, P., *Fire Design of Steel Structures*, Wiley, 2016.
- [26] Hurley, M.J., Gottuk, D.T., Hall, J.R., Harada, K., Kuligowski, E.D., Puchovsky, M., Torero, J.L., Watts, J.M., and Wieczorek, C.J., *SFPE Handbook of Fire Protection Engineering* (5th ed.), Springer, 2016. ISBN: 978-1-4939-2564-3.
- [27] Dallaev, R., Pisarenko, T., Sobola, D., Orudzhev, F., Ramazanov, S., & Trčka, T. (2022). Brief review of PVDF properties and applications potential. *Polymers*, 14(21), 4793. <https://doi.org/10.3390/polym14224793>
- [28] European Committee for Standardization, EN 1993-1-2: Eurocode 3—Design of Steel Structures—Part 1-2: General Rules—Structural Fire Design, CEN.

- 
- [29] Raveiro, H.D., Rodrigues, J.P.C., Santiago, A., and Laím, L., Review of the High Temperature Mechanical and Thermal Properties of the Steels Used in Cold-Formed Steel Structures – The Case of the S280GD+Z Steel, Thin-Walled Structures, vol. 98, 2016, pp. 154–168.
- [30] Olso, B. G., Hauko, A.-M., & Risholt, B. (2024). Experimental study of fire exposed expanded polystyrene (EPS) insulation protected by selected coverings. *Heliyon*, 10(2), e26309. <https://doi.org/10.1016/j.heliyon.2024.e26309>
- [31] Abblaoui, E.M., Malendowski, M., Szymkuć, W., and Pozorski, Z., Determination of Thermal Properties of Mineral Wool Required for the Safety Analysis of Sandwich Panels Subjected to Fire Loads, *Materials*, vol. 16, no. 17, 2023, pp. 5852-1–5852-18.
- [32] Mouritz, A.P., and Mathys, Z., Post-Fire Mechanical Properties of Marine Polymer Composites, *Composite Structures*, vol. 47, 1999, pp. 643–653.
- [33] Allison, D.M., Marchand, A.J., and Morchat, R.M., Fire Performance of Composite Materials in Ships and Offshore Structures, *Marine Structures*, vol. 4, 1991, pp. 129–140.
- [34] McManus, H.L., Prediction of Fire Damage to Composite Aircraft Structures, *Proceedings of the 9th International Conference on Composite Materials*, Madrid, Spain, July 1993, pp. 929–936.
- [35] Buck, W., and Rudtsch, S., Thermal Properties. In *Springer Handbook of Metrology and Testing*, Czichos, H., Saito, T., and Smith, L. (Eds.), Springer-Verlag, Berlin/Heidelberg, Germany, 2011, Chapter 8, pp. 453–483.
- [36] Keerthan, P., and Mahendran, M., Thermal Performance of Composite Panels Under Fire Conditions Using Numerical Studies: Plasterboards, Rockwool, Glass Fibre, and Cellulose Insulations, *Fire Technology*, vol. 49, 2013, pp. 329–356. doi:10.1007/s10694-012-0269-6.
- [37] Malaska, M., Alanen, M., Cábová, K., Lišková, N., Mela, K., Pajunen, S., and Wald, F., Experimental Study on Temperature Distribution of Sandwich Panel

- Joints in Fire, Nordic Steel 2019: The 14th Nordic Steel Construction Conference, 2019, pp. 3–4. doi:10.1002/cepa.1123.
- [38] Roszkowski, P., and Sulik, P., Sandwich Panels – Behavior in Fire Based on Fire Resistance Tests, Applications of Structural Fire Engineering - Proceedings of the International Conference in Dubrovnik, 2015. doi:10.14311/asfe.2015.065.
- [39] Feng, M., Wang, Y.C., and Davies, J.M., Thermal Performance of Cold-Formed Thin-Walled Steel Panel Systems in Fire, Fire Safety Journal, vol. 38, 2003, pp. 365–394. doi:10.1016/S0379-7112(02)00090-5.
- [40] Sjöström, J., and Jansson, R., Measuring Thermal Material Properties for Structural Fire Engineering, 15th International Conference on Experimental Mechanics, 2012, vol. 2846, pp. 22–27.
- [41] Paudel, D., Rinta-Paavola, A., Mattila, H.-P., and Hostikka, S., Multiphysics Modelling of Stone Wool Fire Resistance, Fire Technology, vol. 57, 2020, pp. 1283–1312. doi:10.1007/s10694-020-01050-5.
- [42] Andres, B., Livkiss, K., Bhargava, A., and van Hees, P., Using Micro-Scale and Solid Material Data for Modelling Heat Transfer in Stone Wool Composites Under Heat Exposures, Fire Technology, vol. 57, 2021, pp. 1541–1567. doi:10.1007/s10694-021-01122-0.
- [43] Hung Anh, L.D., and Pásztor, Z., An Overview of Factors Influencing Thermal Conductivity of Building Insulation Materials, Journal of Building Engineering, vol. 44, 2021, p. 102604. doi:10.1016/j.jobe.2021.102604.
- [44] Kodur, V.K.R., and Harmathy, T.Z., Properties of Building Materials. In SFPE Handbook of Fire Protection Engineering (5th ed.), edited by M.J. Hurley, Springer, 2016, pp. 277–324. doi:10.1007/978-1-4939-2565-0\_9.
- [45] Sterner, E., and Wickström, U., TASEF - Temperature Analysis of Structures Exposed to Fire: User's Manual, Appendix A8 Materials, Swedish National Testing Institute, Borås, Sweden, 1990.

- 
- [46] Wang, H.B., Heat Transfer Analysis of Components of Construction Exposed to Fire—A Theoretical, Numerical, and Experimental Approach, PhD thesis, Civil Engineering and Construction, University of Salford, 1995.
- [47] Gusyachkin, A.M., Sabitov, L.S., Khakimova, A.M., and Hayrullin, A.R., Effects of Moisture Content on Thermal Conductivity of Thermal Insulation Materials, IOP Conference Series: Materials Science and Engineering, vol. 570, 2008, p. 012029. doi:10.1088/1757-899X/570/1/012029.
- [48] Chen, W., Ye, J., and Li, X., Thermal Behavior of Gypsum-Sheathed Cold-Formed Steel Composite Assemblies Under Fire Conditions, Journal of Constructional Steel Research, vol. 149, 2018, pp. 165–179. doi:10.1016/j.jcsr.2018.07.023
- [49] European Committee for Standardization, prEN 1995-1-2: Eurocode—Design of Timber Structures—Part 1-2: General—Structural Fire Design, CEN, 2022.
- [50] Log, T., and Gustafsson, S.E., Transient Plane Source (TPS) Technique for Measuring Thermal Transport Properties of Building Materials, Fire and Materials, vol. 19, 1995, pp. 43–49. doi:10.1002/fam.810190107.
- [51] Hammerschmidt, U., Guarded Hot-Plate (GHP) Method: Uncertainty Assessment, International Journal of Thermophysics, vol. 23, 2002, pp. 1551–1570.
- [52] Pimienta, P., Alonso, M.C., Jansson McNamee, R., and Mindeguia, J.-C., Behaviour of High-Performance Concrete at High Temperatures: Some Highlights, RILEM Technical Letters, vol. 2, 2017, pp. 45–52. doi:10.21809/rilemtechlett.2017.53.
- [53] Wickström, U., Chapter 7: Numerical Methods. In Temperature Calculation in Fire Safety Engineering, Springer, 2016.
- [54] Textbook, Thermal Diffusivity - Concept and Formula: Comprehensive Insights into the Definition of Thermal Diffusivity in Porous Materials, Including Its

- Dependency on Porosity, Thermal Conductivity, and Density of the Medium, Textbook, 2023. Available at: <https://testbook.com/physics/thermal-diffusivity>.
- [55] Bergman, T.L., Lavine, A.S., Incropera, F.P., and DeWitt, D.P., *Fundamentals of Heat and Mass Transfer* (7th ed.), John Wiley & Sons, 2011. ISBN: 978-0470-50197-9.
- [56] McGaw, R.W., Outcalt, S.I., and Ng, E., Thermal Properties of Wet Tundra Soils at Barrow, Alaska. In *Proceedings of the Third International Conference on Permafrost*, Edmonton, Alberta, National Research Council of Canada, Ottawa, vol. 1, 1978, pp. 47–53.
- [57] Nelson, F.E., Outcalt, S.I., Goodwin, C.W., and Hinkel, K.M., Diurnal Thermal Regime in a Peat-Covered Palsa, Toolik Lake, Alaska, *Arctic*, vol. 38, no. 4, 1985, pp. 310–315.
- [58] Zhang, T., *Climate, Seasonal Snow Cover, and Permafrost Temperatures in Alaska North of the Brooks Range*, PhD thesis, Geophysical Institute, University of Alaska, Fairbanks, 1993, 232 pp.
- [59] Zhang, T., *Thermal Regime of Permafrost Within the Depth of Annual Temperature Variation at Prudhoe Bay, Alaska*, M.Sc. thesis, Geophysical Institute, University of Alaska, Fairbanks, 1989, 145 pp.
- [60] Anjang, A., Mouritz, A. P., & Gibson, A. G. (2014). Tension modelling and testing of sandwich composites in fire. *Composite Structures*, 113, 446–454. <https://doi.org/10.1016/j.compstruct.2014.03.016>
- [61] Lu, W., Ayoub, A., & D'Mello, C. (2021). Effectiveness of coupled thermo-mechanical damage modelling in steel structural fire engineering. *Fire Safety Journal*, 121, 103314. <https://doi.org/10.1016/j.firesaf.2021.103314>
- [62] Upasiri, I. R., Konthesigha, K. M. C., Nanayakkara, S. M. A., Poologanathan, K., Gatheeshgar, P., & Nuwanthika, D. (2021). Finite element analysis of lightweight composite sandwich panels exposed to fire. *Journal of Building Engineering*, 40, 102329. <https://doi.org/10.1016/j.jobbe.2021.102329>

- 
- [63] Dassault Systèmes. (2016). ABAQUS 6.14 documentation. Providence, RI: Dassault Systèmes Simulia Corp.
- [64] Cutter, P.A., Shenoi, R.A., and Phillips, H., Thermal and Mechanical Response of Sandwich Panels in Fire. In Gdoutos, E.E. (Ed.), *Experimental Analysis of Nano and Engineering Materials and Structures*, Springer, 2007, pp. 763–769.
- [65] Frostig, Y., and Thomsen, O.T., Thermomechanical Nonlinear Response of Sandwich Panels. In Gdoutos, E.E. (Ed.), *Experimental Analysis of Nano and Engineering Materials and Structures*, Springer, 2014, pp. 5999–6011. [https://doi.org/10.1007/978-94-007-2739-7\\_430](https://doi.org/10.1007/978-94-007-2739-7_430).
- [66] Foster, A., Understanding, Predicting, and Improving the Performance of Foam-Filled Sandwich Panels in Large-Scale Fire Resistance Tests, PhD thesis, The University of Manchester, School of Mechanical, Aerospace and Civil Engineering, 2014.
- [67] European Committee for Standardization, EN 1991-1-2: Eurocode 1—Actions on Structures—Part 1-2: General Actions—Actions on Structures Exposed to Fire, CEN.
- [68] Girolamo, D., Dávila, C. G., Leone, F. A., & Lin, S.-Y. (n.d.). Cohesive laws and progressive damage analysis of composite bonded joints: A combined numerical/experimental approach. NASA Langley Research Center, Hampton, VA, USA.
- [69] Bustamante-Gómez, L. M., Chica-Arrieta, E., & Villarraga Ossa, J. A. (2019). Assessment of cohesive traction–separation relationship according to stiffness variation. *Revista UIS Ingenierías*, 18(2), 67–76. <https://doi.org/10.18273/revuni.v18n2-2019006>
- [70] Camanho, P. P., Davila, C. G., & de Moura, M. F. (2003). Numerical simulation of mixed-mode progressive delamination in composite materials. *Journal of Composite Materials*, 37(16), 1415–1438. <https://doi.org/10.1177/0021998303034505>



- 
- [71] Tvergaard, V., & Hutchinson, J. W. (1993). The influence of plasticity on mixed mode interface toughness. *Journal of the Mechanics and Physics of Solids*, 41(6), 1119–1135. [https://doi.org/10.1016/0022-5096\(93\)90072-U](https://doi.org/10.1016/0022-5096(93)90072-U)
- [72] Geubelle, P. H., & Baylor, J. S. (1998). Impact-induced delamination of composites: A 2D simulation. *Composites Part B: Engineering*, 29(5), 589–602. [https://doi.org/10.1016/S1359-8368\(98\)00018-6](https://doi.org/10.1016/S1359-8368(98)00018-6)
- [73] De Boer, J.G.G.M., Hofmeyer, H., Maljaars, J., and van Herpen, R.A.P., Two-Way Coupled CFD Fire and Thermomechanical FE Analyses of a Self-Supporting Sandwich Panel Façade System, *Fire Safety Journal*, vol. 105, 2019, pp. 154–168.
- [74] Banea, M. D., da Silva, L. F. M., & Campilho, R. (2010). Temperature dependence of the fracture toughness of adhesively bonded joints. *Journal of Adhesion Science and Technology*, 24(11), 2011–2026. <https://doi.org/10.1163/016942410X507713>
- [75] ASHRAE Handbook—Fundamentals (2017), Chapter 26: Heat, Air, and Moisture Control in Building Assemblies.
- [76] De Boer, J. G. G. M., Hofmeyer, H., Maljaars, J., & van Herpen, R. A. P. (2019). Two-way coupled CFD fire and thermomechanical FE analyses of a self-supporting sandwich panel façade system. *Fire Safety Journal*, 105, 19–36. <https://doi.org/10.1016/j.firesaf.2019.02.011>
- [77] Ortwein, R., Esposito, B., Marocco, D., Kotula, J., Dongiovanni, D., Maciocha, W., Bocian, D., & Moro, F. (2023). Design and FEM modeling of a fire-resistant cabinet for fusion environment. *Fusion Engineering and Design*, 192, 113840. <https://doi.org/10.1016/j.fusengdes.2023.113840>
- [78] Incropera, F. P., DeWitt, D. P., Bergman, T. L., & Lavine, A. S. (2007). *Fundamentals of heat and mass transfer* (6th ed.). John Wiley & Sons.

## List of figures

Figure 1. Development of fire. ....	13
Figure 2. Graphical decomposition of structural sandwich panel. ....	19
Figure 3. Core material classification of homogeneous and structured sandwich panels. ....	21
Figure 4. Example of homogeneous sandwich panel used for industrial construction. ....	21
Figure 5. Evolution curve of fire behavior. ....	23
Figure 6. Time-temperature curve of the ISO 834 standard. ....	25
Figure 7. Time-temperature of hydrocarbon curve. ....	26
Figure 8. The concept of fire resistance test on wall specimens. ....	27
Figure 9. The concept of fire resistance test on roof and ceiling specimens. ....	27
Figure 10. General aspects of sandwich panels exposed to fire according to [18]. ....	28
Figure 11. View of the fire-damaged PIR core material after fire laboratory test. (a) charred foam, (b) cross-section view, (c) full damage of PIR. ....	36
Figure 12. Mineral wool samples after removal from the furnace, at different temperatures..	37
Figure 13. Thermal conductivity of mineral wool as a function of temperature [31]. ....	40
Figure 14. Sketch of a specimen inside the furnace. ....	51
Figure 15. The test specimen inside the electrical furnace: (a) fixing position of a thermocouple using an aerated concrete brick at the back of the furnace; (b) sticking a mineral wool specimen on the thermocouples; (c, d) insulating the specimen from all-around. ....	51
Figure 16. Time-temperature dependence for the tested samples: (a) Sample A – first heating cycle; (b) Sample A – second heating cycle; (c) Sample B – first heating cycle; (d) Sample B – second heating cycle; (e) Sample C – first heating cycle; and (f) Sample C – second heating cycle. ....	54
Figure 17: Thermal diffusivity of mineral wool calculated for each 100 s – first experimental test. ....	55
Figure 18: Thermal diffusivity of mineral wool calculated for each 1 s – second experimental test. ....	55
Figure 19. The second derivative of temperature with respect to the spatial coordinate, obtained for Test 2, sample A using the regression curve function: (a) 2nd order polynomial; (b) 3rd order polynomial; (c) 4th order polynomial and (d) exponential function. ....	56
Figure 20. Thermal diffusivity as a function of temperature for nodes T2, T3, T4, T5 and T6 – Sample A, Test 1. ....	57
Figure 21. Thermal diffusivity as a function of temperature for nodes T2, T3, T4, T5 and T6 – Sample A, Test 2. ....	57
Figure 22. Thermal diffusivity as a function of temperature for nodes T2, T3, T4, T5 and T6 – Sample B, Test 1. ....	58
Figure 23. Thermal diffusivity as a function of temperature for nodes T2, T3, T4, T5 and T6 – Sample B, Test 2. ....	58
Figure 24. Thermal diffusivity as a function of temperature for nodes T2, T3, T4, T5 and T6 – Sample C, Test 1. ....	58
Figure 25. Thermal diffusivity as a function of temperature for nodes T2, T3, T4, T5 and T6 – Sample C, Test 2. ....	59

Figure 26. Thermal diffusivity (average value) as a function of temperature – fresh samples.	59
Figure 27. Thermal diffusivity (average value) as a function of temperature – pre-heated samples. ....	60
Figure 28. 1-D model of heat transfer. ....	61
Figure 29. Comparison of the experimental and numerical results: (a) boundary conditions for the numerical problem—temperatures at nodes T1 and T7; (b) time–temperature relationship at node T2; (c) time–temperature relationship at node T3; (d) time–temperature relationship at node T4; (e) time-temperature relationship at node T5 and (f) time–temperature relationship at node T6.....	62
Figure 30. Front view of the assembly of the first sandwich panel wall – Test 1'. The numbered elements correspond to the following components: (1) reinforced concrete lintel with a cross-section of $240 \times 240$ mm, (2) sandwich panel made of mineral wool – samples described in Section 4.3, (3) free edge filled with insulation material, (4) concrete blocks with a thickness of 24 cm, and (5) self-drilling screws with a diameter of 5.5 mm and a length of 190 mm. ....	66
Figure 31. Front view of the assembly of the first sandwich panel wall – Test 2'.....	67
Figure 32. Front view of the assembly of the first sandwich panel wall – Test 3'.....	67
Figure 33. Front view of the assembly of the first sandwich panel wall – Test 4'.....	68
Figure 34. Horizontal cross section of samples evaluated assembled on mounting structure. ....	68
Figure 35. Cross-section of the geometry of the sandwich panel used. ....	69
Figure 36. The assembly of sandwich panel during testing. ....	69
Figure 37. Measurement localizations of horizontal displacements and localizations of temperature sensors - view from unexposed side – Test 1', Test 2', and Test 3'.....	70
Figure 38. Measurement localizations of horizontal displacements and localizations of temperature sensors - view from unexposed side – Test 4'.....	71
Figure 39. The time–temperature from the experimental test compared with the ISO 834.....	72
Figure 40. Time–temperature for the tested samples: (Test 1') — unheated face.....	78
Figure 41. Time–temperature for the tested samples: (Test 2') — unheated face.....	79
Figure 42. Time–temperature for the tested samples: (Test 3') — unheated face.....	80
Figure 43. Time–temperature for the tested samples: (Test 4') — unheated face.....	81
Figure 44. Average Time–temperature for all tested samples — unheated face. ....	82
Figure 45. 3D Nodal temperature distribution at $t = 1$ min (Heated side: $72^{\circ}\text{C}$ ) – Test 1'.....	84
Figure 46. 3D Nodal temperature distribution at $t = 10$ min (Heated side: $664^{\circ}\text{C}$ ) – Test 1'..	84
Figure 47. 3D Nodal temperature distribution at $t = 67$ min (Heated side: $905^{\circ}\text{C}$ ) – Test 1'..	85
Figure 48. Thermal response of panels in Tests 1', and 2'- Experimentally and numerically..	85
Figure 49. Thermal response of panels in Tests 3'- Experimentally and numerically. ....	86
Figure 50. Thermal response of panels in Tests 4'- Experimentally and numerically. ....	87
Figure 51. Horizontal displacement at measured points in Test 1'.....	92
Figure 52. Horizontal displacement trends at measured points in Test 2'.....	93
Figure 53. Horizontal displacement at measured points in Test 3'.....	94
Figure 54. Horizontal displacement at measured points in Test 4'.....	95
Figure 55. Traction – separation curve illustrating a damage evolution. ....	101
Figure 56. Simplified support conditions. (a) fixed, (b) fixed pinned, and (c) fixed roller. ..	105

Figure 57. Effect of boundary conditions on horizontal displacement of sandwich panels under thermal loading.....	107
Figure 58. Early-stage displacement response under various boundary conditions (extracted from Figure 57). .....	108
Figure 59. Structural setup and boundary conditions for fire exposure on sandwich panels. ....	111
Figure 60. Assembly details and structural configuration of tested samples. ....	112
Figure 61. Schematic representation of simplified joint connection and interface properties with interaction details. ....	114
Figure 62. Steel plate specimens bonded with polyurethane adhesive: (a) pre-bonding condition; (b) mounted samples in tensile testing machine; (c) post-failure appearance after uniaxial loading. ....	116
Figure 63. Tensile response of adhesive-bonded steel plate specimens. ....	116
Figure 64. Sandwich panel sample tested up to 250°C: (a) specimen placed in a furnace with bilateral heating configuration; (b) failure mode showing delamination between facing and core material after thermal exposure. ....	118
Figure 65. Traction – separation curve representing the cohesive zone model .....	119
Figure 66. 3D model of the tested panels showing cross-sections along the longitudinal and transverse directions. ....	121
Figure 67. Structural test frame with screw locations for middle panel and boundary conditions. ....	122
Figure 68. Displacement directions [max 1.72 mm] at initial thermal exposure, illustrated in the longitudinal cross-sectional plane ( $y$ $x$ - plane). ....	123
Figure 69. Displacement directions [max 1.72 mm] at initial thermal exposure, illustrated in the transverse cross-sectional plane ( $y$ $z$ - plane). ....	123
Figure 70. Displacement directions [max 27.32 mm] at the end of thermal testing, illustrated in the longitudinal cross-sectional plane ( $y$ $x$ - plane). ....	124
Figure 71. Displacement directions [max 27.32 mm] at the end of thermal testing, illustrated in the transverse cross-sectional plane ( $y$ $z$ - plane). ....	124
Figure 72. 3D visualization of resultant displacement field at the end of testing [10,880 s], viewed from the unheated side. ....	125
Figure 73. 3D visualization of temperature distribution at the end of thermal exposure, showing heat propagation across wall panels. ....	125
Figure 74. Numerical prediction of interface separation at $t = 315$ s under fire load.....	126
Figure 75. Horizontal displacement - experimental and FEM results at point A - Test 1'.....	128
Figure 76. Horizontal displacement - experimental and FEM results at point B - Test 1'.....	128
Figure 77. Horizontal displacement - experimental and FEM results at point C - Test 1'.....	129
Figure 78. Horizontal displacement - experimental and FEM results at point D - Test 1'.....	129
Figure 79. Horizontal displacement - experimental and FEM results at point E - Test 1'.....	130
Figure 80. Horizontal displacement - experimental and FEM results at point F - Test 1'. ....	131
Figure 81. Horizontal displacement - experimental and FEM results at point G - Test 1'.....	131
Figure 82. Horizontal displacement - experimental and FEM results at Point H - Test 1'. ...	133
Figure 83. Horizontal displacement - experimental and FEM results at point I - Test 1'. ....	134
Figure 84. Horizontal displacement - experimental and FEM results at point J - Test 1'.....	134

Figure 85. Horizontal displacement - experimental and FEM results at point A - Test 2'.....	135
Figure 86. Horizontal displacement - experimental and FEM results at Point B - Test 2'.....	135
Figure 87. Horizontal displacement - experimental and FEM results at point C - Test 2'.....	136
Figure 88. Horizontal displacement - experimental and FEM results at Point D - Test 2'. ...	136
Figure 89. Horizontal displacement - experimental and FEM results at point E - Test 2'. ....	137
Figure 90. Horizontal displacement - experimental and FEM results at Point F - Test 2'. ....	137
Figure 91. Horizontal displacement - experimental and FEM results at Point G - Test 2'. ...	137
Figure 92. Horizontal displacement - experimental and FEM results at Point H - Test 2'. ...	138
Figure 93. Horizontal displacement - experimental and FEM results at point I - Test 2'. ....	138
Figure 94. Horizontal displacement - experimental and FEM results at point J - Test 2'.....	138
Figure 95. Cross sectional view–nodal temperatures for $t = 53$ min at the temperature of heated surfaces $537^{\circ}\text{C}$ .....	160
Figure 96. Numerical result of the heat flux on $x$ -, $y$ - and $z$ -directions of the specimen evaluated. ....	161
Figure 97. The comparison of the 1st derivatives of the heat flux at nodes T1 and T2 obtained from numerical analysis. ....	162
Figure 98. The second derivative of temperature with respect to the spatial coordinate, obtained for Test 1, sample A (first heating cycle) using the regression curve function: (a) 2nd order polynomial; (b) 3rd order polynomial; (c) 4 <sup>th</sup> order polynomial and (d) exponential function. ....	164
Figure 99. The second derivative of temperature with respect to the spatial coordinate, obtained for Test 2, sample A (second heating cycle) using the regression curve function: (a) 2nd order polynomial; (b) 3rd order polynomial; (c) 4 <sup>th</sup> order polynomial and (d) exponential function. ....	164
Figure 100. The second derivative of temperature with respect to the spatial coordinate, obtained for Test 3, sample B (first heating cycle) using the regression curve function: (a) 2nd order polynomial; (b) 3rd order polynomial; (c) 4 <sup>th</sup> order polynomial and (d) exponential function.....	165
Figure 101. The second derivative of temperature with respect to the spatial coordinate, obtained for Test 4, sample B (second heating cycle) using the regression curve function: (a) 2nd order polynomial; (b) 3rd order polynomial; (c) 4 <sup>th</sup> order polynomial and (d) exponential function.....	165
Figure 102. The second derivative of temperature with respect to the spatial coordinate, obtained for Test 5, sample C (first heating cycle) using the regression curve function: (a) 2nd order polynomial; (b) 3rd order polynomial; (c) 4 <sup>th</sup> order polynomial and (d) exponential function.....	166
Figure 103. The second derivative of temperature with respect to the spatial coordinate, obtained for Test 6, sample C (second heating cycle) using the regression curve function: (a) 2nd order polynomial; (b) 3rd order polynomial; (c) 4 <sup>th</sup> order polynomial and (d) exponential function.....	166
Figure 104. Comparison of the experimental and numerical results: (a) boundary conditions for the numerical problem—temperatures at nodes T1 and T7; (b) time–temperature relationship at node T2; (c) time–temperature relationship at node T3; (d) time–temperature relationship at	

node T4; (e) time-temperature relationship at node T5 and (f) time-temperature relationship at node T6 – Test 1, Sample A (first heating cycle).....	167
Figure 105. Comparison of the experimental and numerical results: (a) boundary conditions for the numerical problem—temperatures at nodes T1 and T7; (b) time-temperature relationship at node T2; (c) time-temperature relationship at node T3; (d) Time-temperature relationship at node T4; (e) time-temperature relationship at node T5 and (f) time-temperature relationship at node T6 – Test 3, Sample B (first heating cycle).....	168
Figure 106. Comparison of the experimental and numerical results: (a) boundary conditions for the numerical problem—temperatures at nodes T1 and T7; (b) time-temperature relationship at node T2; (c) time-temperature relationship at node T3; (d) time-temperature relationship at node T4; (e) time-temperature relationship at node T5 and (f) time-temperature relationship at node T6 – Test 4, Sample B (second heating cycle). ....	169
Figure 107. Comparison of the experimental and numerical results: (a) boundary conditions for the numerical problem—temperatures at nodes T1 and T7; (b) time-temperature relationship at node T2; (c) time-temperature relationship at node T3; (d) time-temperature relationship at node T4; (e) time-temperature relationship at node T5 and (f) time-temperature relationship at node T6 – Test 5, Sample C (first heating cycle).....	170
Figure 108. Comparison of the experimental and numerical results: (a) boundary conditions for the numerical problem—temperatures at nodes T1 and T7; (b) time-temperature relationship at node T2; (c) time-temperature relationship at node T3; (d) time-temperature relationship at node T4; (e) time-temperature relationship at node T5 and (f) time-temperature relationship at node T6 – Test 6, Sample C (first heating cycle).....	170
Figure 109. Time-temperature of all points – sample: (Test 1') — unheated face.....	171
Figure 110. Time-temperature of all points – sample: (Test 2') — unheated face.....	172
Figure 111. Time-temperature of all points – sample: (Test 3') — unheated face.....	172
Figure 112. Time-temperature of all points – sample: (Test 4') — unheated face.....	173
Figure 113. Initial setup of the tested wall specimen - unheated side of test 1'. ....	174
Figure 114. Condition of the tested wall specimen – unheated side of test 1' at 30 minutes. ....	174
Figure 115. Condition of the tested wall specimen – unheated side of test 1' at the end of the test. ....	175
Figure 116. Condition of the tested wall specimen – heated side of test 1' at the end of the test. ....	175
Figure 117. Initial setup of the tested wall specimen - unheated side of test 4'. ....	176
Figure 118. Condition of the tested wall specimen – unheated side of test 2' at 95 minutes. ....	176
Figure 119. Condition of the tested wall specimen – unheated side of test 4' at 181 minutes. ....	177
Figure 120. Condition of the tested wall specimen – heated side of test 4' at the end of the test. ....	177

---

**List of tables**

Table 1. Time-temperature values for the ISO 834 curve.....	24
Table 2. Properties of common steel sheet and metallic coatings use in sandwich panel [3]..	33
Table 3. Thermal properties of MW insulation with density more than 26 kg/m <sup>3</sup> [49].....	40
Table 4. Description of experimental large-scale tests.....	72
Table 5. Fixation types, schematics, boundary conditions, and graphical representations....	105
Table 6. Force-displacement relationship for bolt – bushing connectors. ....	113
Table 7. Experimental results of stretching the adhesive layer. ....	117
Table 8. Temperature dependence of interface stiffness for polyurethane adhesive layer. ...	118
Table 9. Temperature dependence of failure displacement for polyurethane adhesive layer.	118
Table 10. Description of performed small-scale tests. ....	162



## Appendix A. Thermal response of mineral wool

### ▪ Reduction of 3-D problem to 1-D problem

A 3-D thermal model replicating the experimental setup was developed using ABAQUS software, employing DC3D8 elements. The cross-sectional view of the model is given in Figure 95. The analysis confirmed that the heat flux in the  $x$ -direction significantly exceeded those in the  $y$ - and  $z$ -directions, thereby justifying the 1-D assumption. Temperature-dependent thermal diffusivity, derived from the results of this chapter, was applied. Tie constraints were used between the specimen and surrounding materials, and heat flux boundary conditions due to convection and radiation were implemented. A mesh size of 0.005 m was determined sufficient. For validation, the furnace temperature during testing was imposed on the heated surfaces, with an initial temperature of 21 °C.

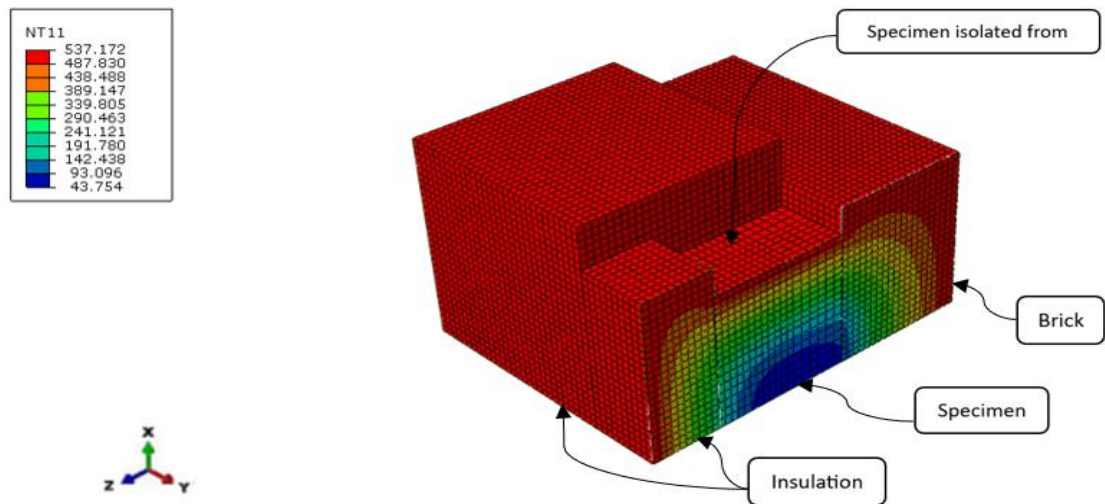


Figure 95. Cross sectional view–nodal temperatures for  $t = 53$  min at the temperature of heated surfaces 537 °C.

Figure 96 presents the magnitude of the heat flux components ( $x$ ,  $y$  and  $z$ ) for points T1-T7. The results were obtained from numerical analysis. It is clear from the illustration below that the amount of the heat transfer in the  $x$ -direction was much greater than the heat flux in the  $y$ - and  $z$ -direction. However, the comparison of the expressions  $\frac{\partial}{\partial x} \left( \lambda_x \frac{\partial \theta}{\partial x} \right)$ ,  $\frac{\partial}{\partial y} \left( \lambda_y \frac{\partial \theta}{\partial y} \right)$  and  $\frac{\partial}{\partial z} \left( \lambda_z \frac{\partial \theta}{\partial z} \right)$  was needed to show that the 1-D heat flow assumption was close to reality.



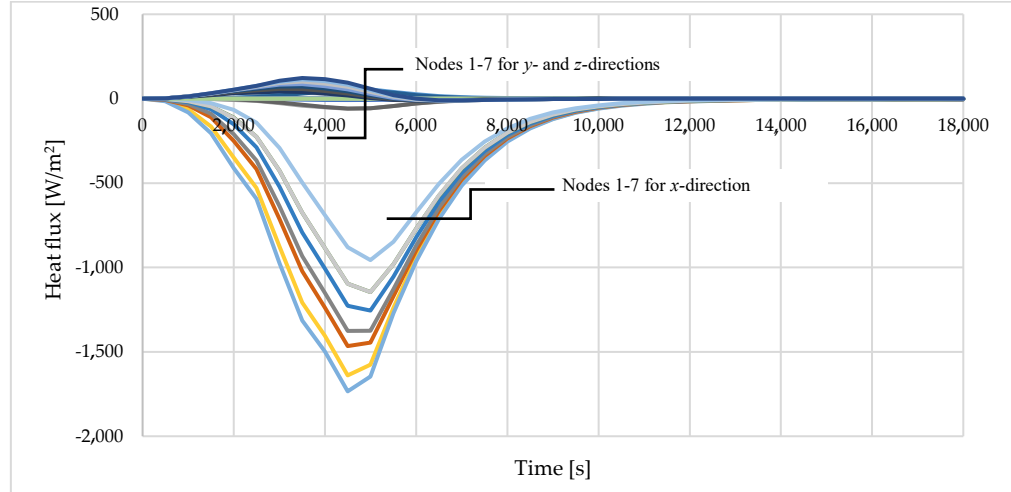


Figure 96. Numerical result of the heat flux on  $x$ -,  $y$ - and  $z$ -directions of the specimen evaluated.

To compare the partial derivatives  $\frac{\partial}{\partial x} \left( \lambda_x \frac{\partial \theta}{\partial x} \right)$ ,  $\frac{\partial}{\partial y} \left( \lambda_y \frac{\partial \theta}{\partial y} \right)$  and  $\frac{\partial}{\partial z} \left( \lambda_z \frac{\partial \theta}{\partial z} \right)$ , the numerical model was applied, in which nodes were evenly spaced in each spatial direction (distances between nodes were:  $\Delta x = 0.02$  m,  $\Delta y = 0.02$  m and  $\Delta z = 0.02$  m). The terms in the brackets represent the components of heat flux (e.g.,  $\lambda_x \frac{\partial \theta_i}{\partial x} = -q_{x_i}$ ). To determine the increments of these components in node  $i$ , the heat flux values  $q$  in the neighboring nodes and the finite difference method were used. For the  $x$ -direction, it is:

$$\frac{\partial}{\partial x} \left( \lambda_x \frac{\partial \theta_i}{\partial x} \right) = \frac{-q_{x_{i+1}} + q_{x_{i-1}}}{2\Delta x}, \quad (3.4)$$

where  $q_{x_{i+1}}$  and  $q_{x_{i-1}}$  are the heat fluxes in the  $x$ -direction for the nodes  $i + 1$  and  $i - 1$ , respectively. Figure 96 shows the first derivatives of the heat flux in the  $x$ -,  $y$ -, and  $z$ -directions at positions T1 and T2. The derivative in the  $x$ -direction was found to be approximately one order of magnitude greater than in the other directions, confirming the dominance of heat flow along this axis. A slight deviation in the  $z$ -direction at  $t = 5500$  s was attributed to the higher thermal conductivity of the aerated concrete brick in contact with the specimen. This effect may be mitigated in future studies by introducing a mineral wool layer between the brick and specimen. Overall, the results support the validity of the one-dimensional heat flow assumption.

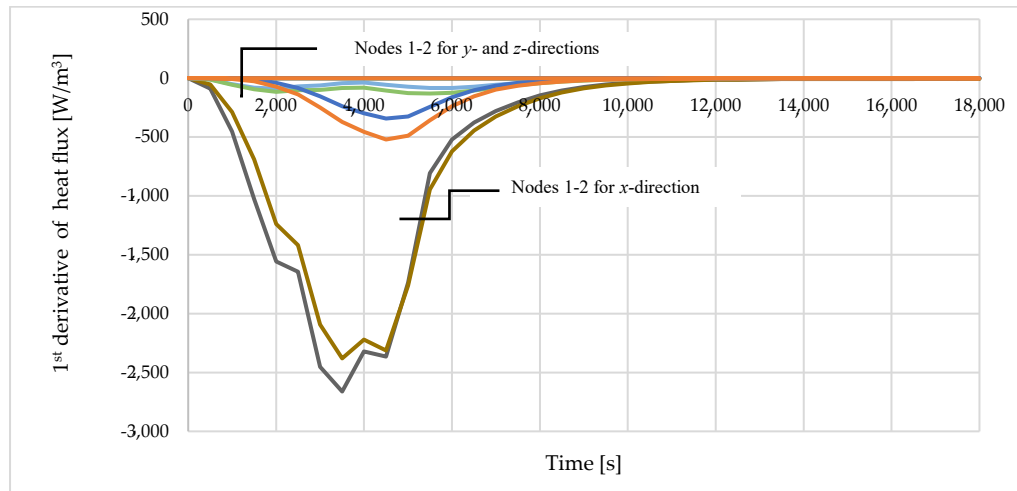


Figure 97. The comparison of the 1st derivatives of the heat flux at nodes T1 and T2 obtained from numerical analysis.

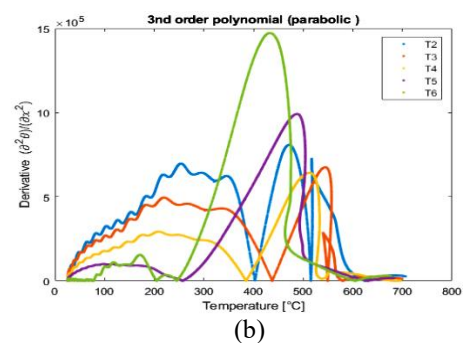
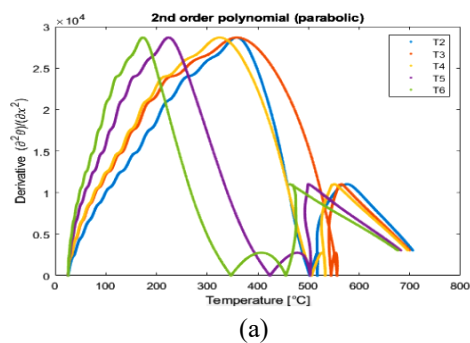
## Experiments

Table 10. Description of performed small-scale tests.

Experiments	Heat Rate	Durations	
Test 1, Sample A (density of 114 kg/m <sup>3</sup> )	10 °C per 60 s	5 h	Test 1: fresh sample  Heating from 21 °C to 750 °C during a period of 1 h 14 min = 4400 s, then a constant temperature of 750 °C for the rest of duration.
Colling Sample A	Room Temperature	12 h	Cooling to room temperature.
Test 2, Sample A (density of 114 kg/m <sup>3</sup> )	10 °C per 60 s	5 h	Test 2: sample after Test 1  Heating from 21 °C to 750 °C during a period of 1 h 14 min = 4400 s, then a constant temperature of 750 °C for the rest of duration.
Test 3. Sample B (density of 114 kg/m <sup>3</sup> )	10 °C per 60 s	5 h	Test 3: fresh sample  Heating from 21 °C to 750 °C during a period of 1 h 14 min = 4400 s, then a constant temperature of 750 °C for the rest of duration.

Colling Sample B	Room Temperature	12 h	Cooling to room temperature.
Test 4, Sample B (density of 114 kg/m <sup>3</sup> )	10 °C per 60 s	5 h	Test 4: sample after Test 1  Heating from 21 °C to 750 °C during a period of 1 h 14 min = 4400 s, then a constant temperature of 750 °C for the rest of duration.
Test 5, Sample C (density of 114 kg/m <sup>3</sup> )	10 °C per 60 s	5 h	Test 5: fresh sample  Heating from 21 °C to 750 °C during a period of 1 h 14 min = 4400 s, then a constant temperature of 750 °C for the rest of duration.
Colling Sample C	Room Temperature	12 h	Cooling to room temperature.
Test 6, Sample C (density of 114 kg/m <sup>3</sup> )	10 °C per 60 s	5 h	Test 6: sample after Test 1  Heating from 21 °C to 750 °C during a period of 1 h 14 min = 4400 s, then a constant temperature of 750 °C for the rest of duration.

▪ Derivatives of temperature with respect to distance



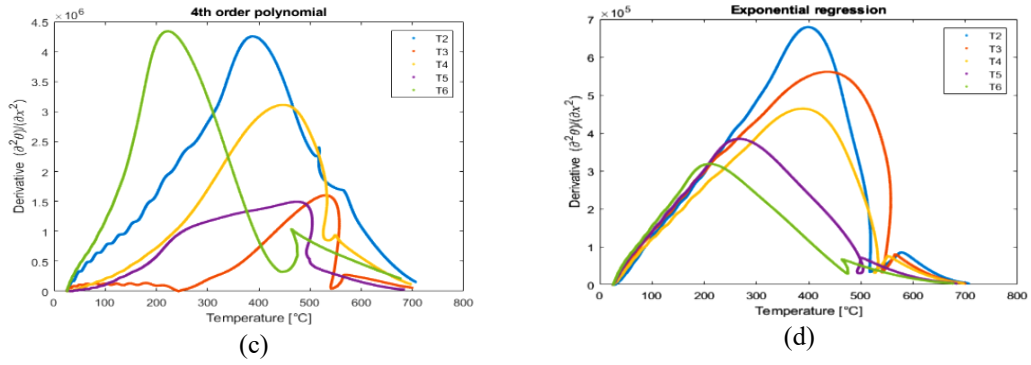


Figure 98. The second derivative of temperature with respect to the spatial coordinate, obtained for Test 1, sample A (first heating cycle) using the regression curve function: (a) 2nd order polynomial; (b) 3rd order polynomial; (c) 4<sup>th</sup> order polynomial and (d) exponential function.

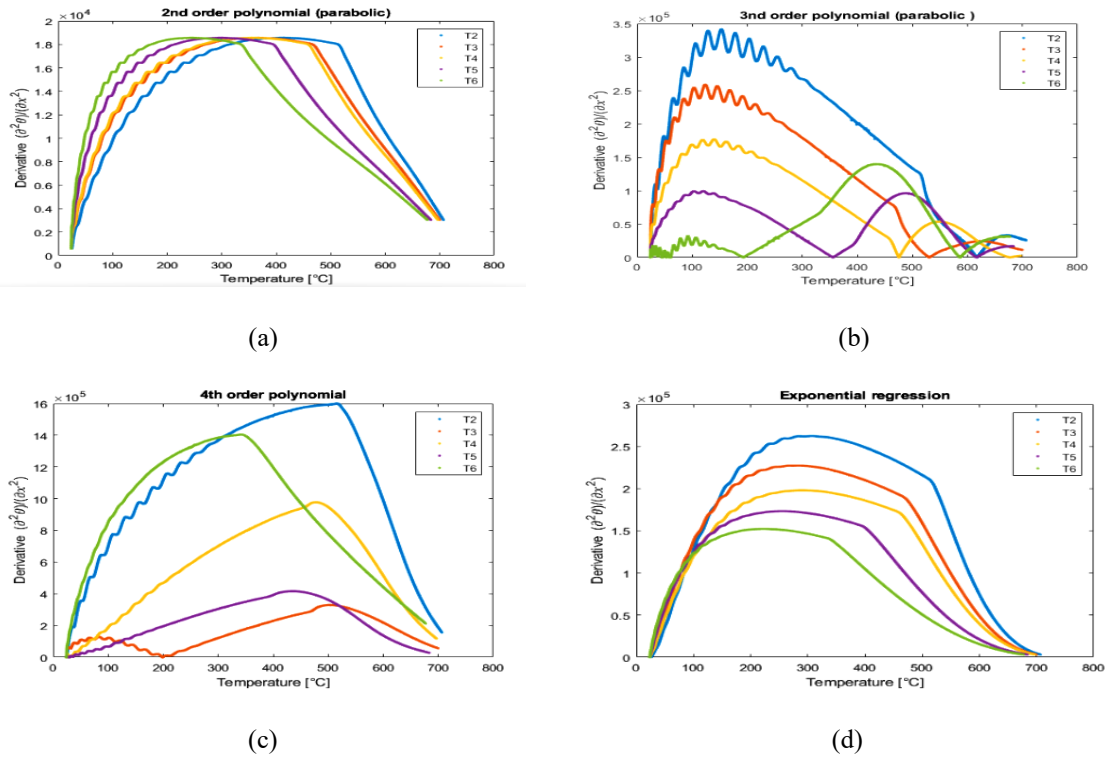


Figure 99. The second derivative of temperature with respect to the spatial coordinate, obtained for Test 2, sample A (second heating cycle) using the regression curve function: (a) 2nd order polynomial; (b) 3rd order polynomial; (c) 4<sup>th</sup> order polynomial and (d) exponential function.

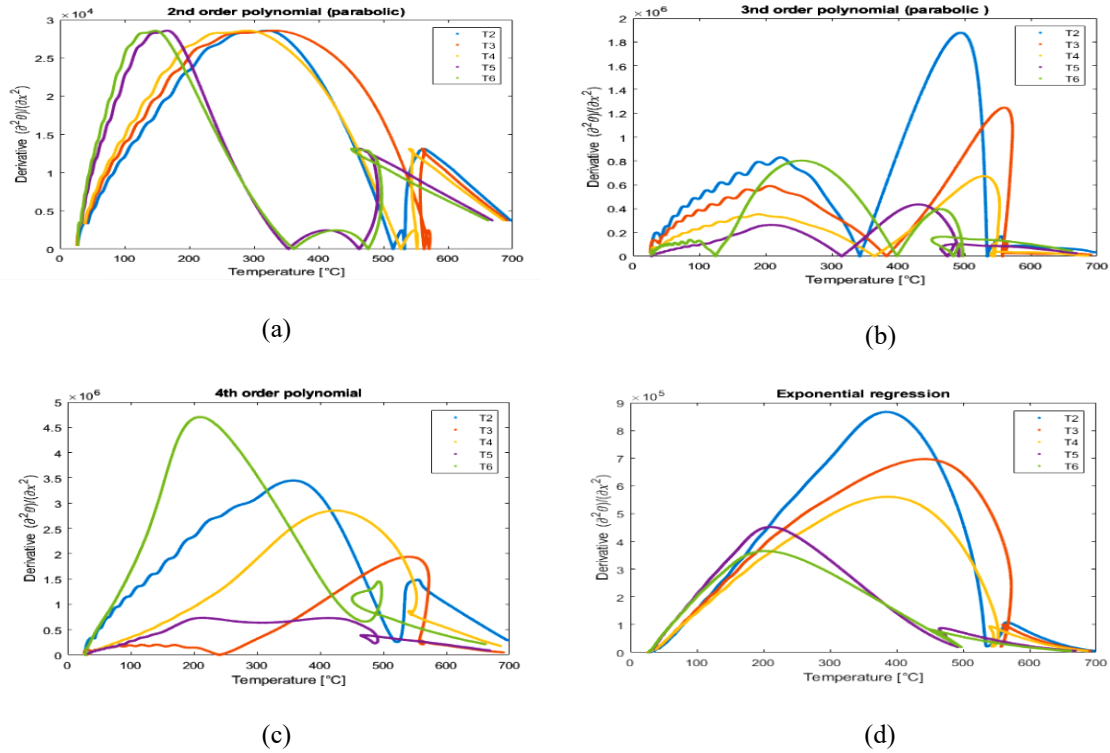


Figure 100. The second derivative of temperature with respect to the spatial coordinate, obtained for Test 3, sample B (first heating cycle) using the regression curve function: (a) 2nd order polynomial; (b) 3rd order polynomial; (c) 4<sup>th</sup> order polynomial and (d) exponential function.

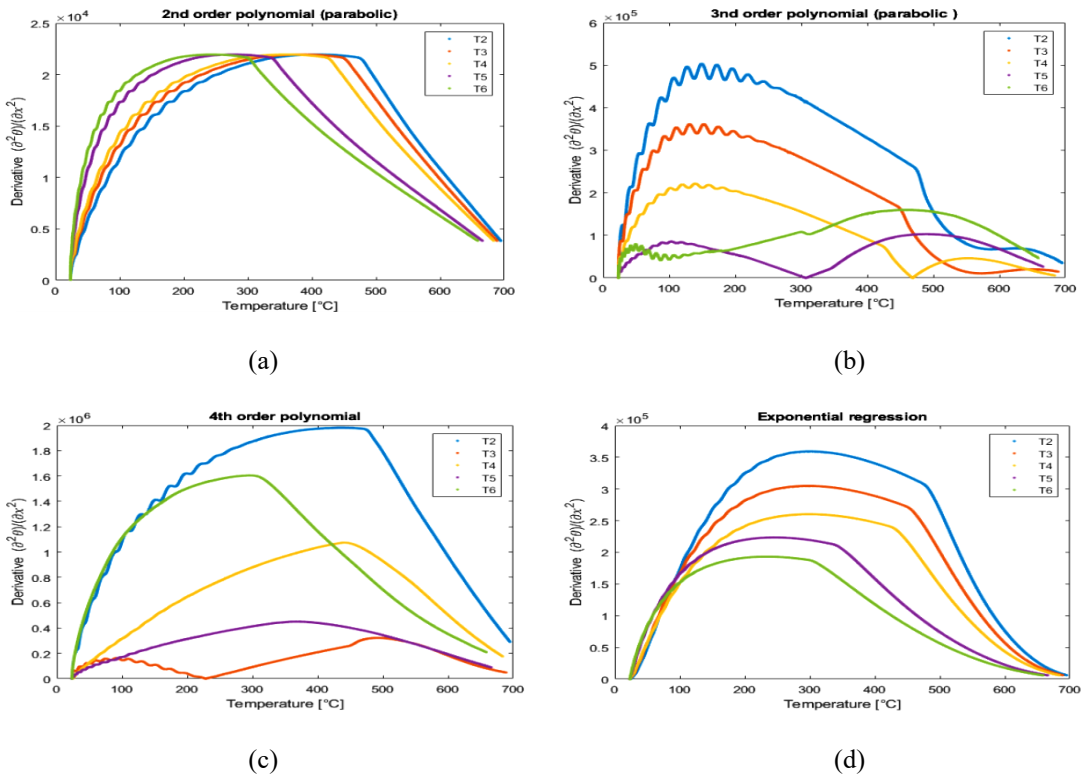


Figure 101. The second derivative of temperature with respect to the spatial coordinate, obtained for Test 4, sample B (second heating cycle) using the regression curve function: (a) 2nd order polynomial; (b) 3rd order polynomial; (c) 4<sup>th</sup> order polynomial and (d) exponential function.

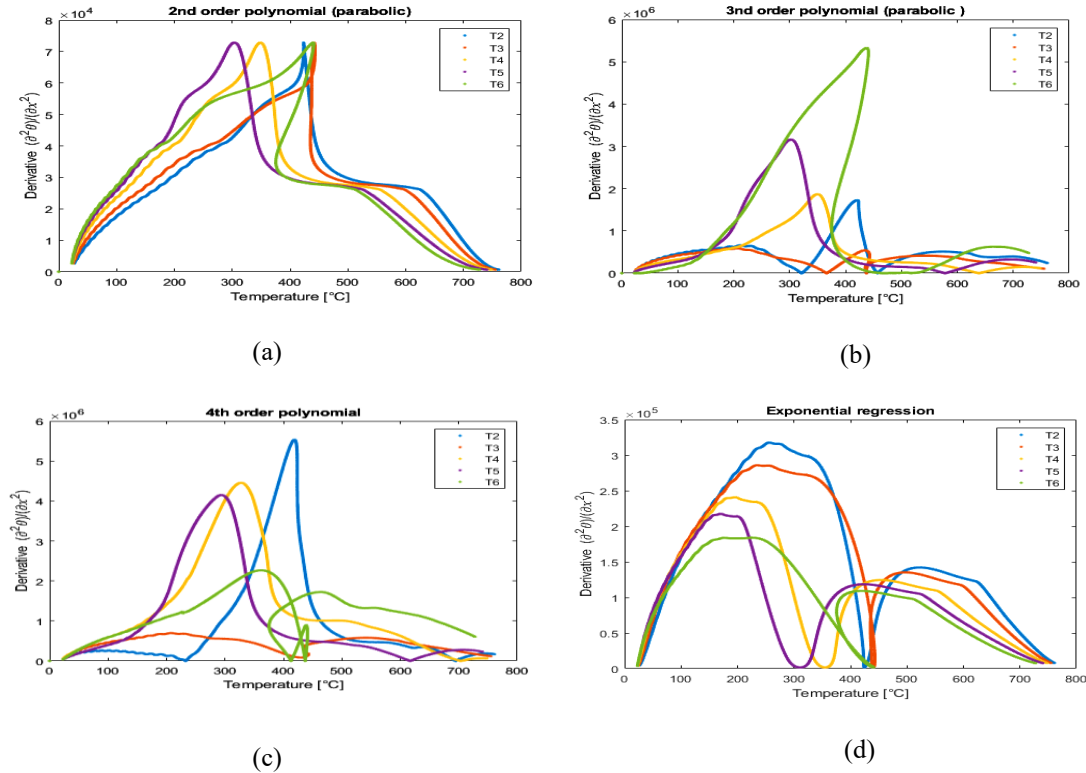


Figure 102. The second derivative of temperature with respect to the spatial coordinate, obtained for Test 5, sample C (first heating cycle) using the regression curve function: (a) 2nd order polynomial; (b) 3rd order polynomial; (c) 4<sup>th</sup> order polynomial and (d) exponential function.

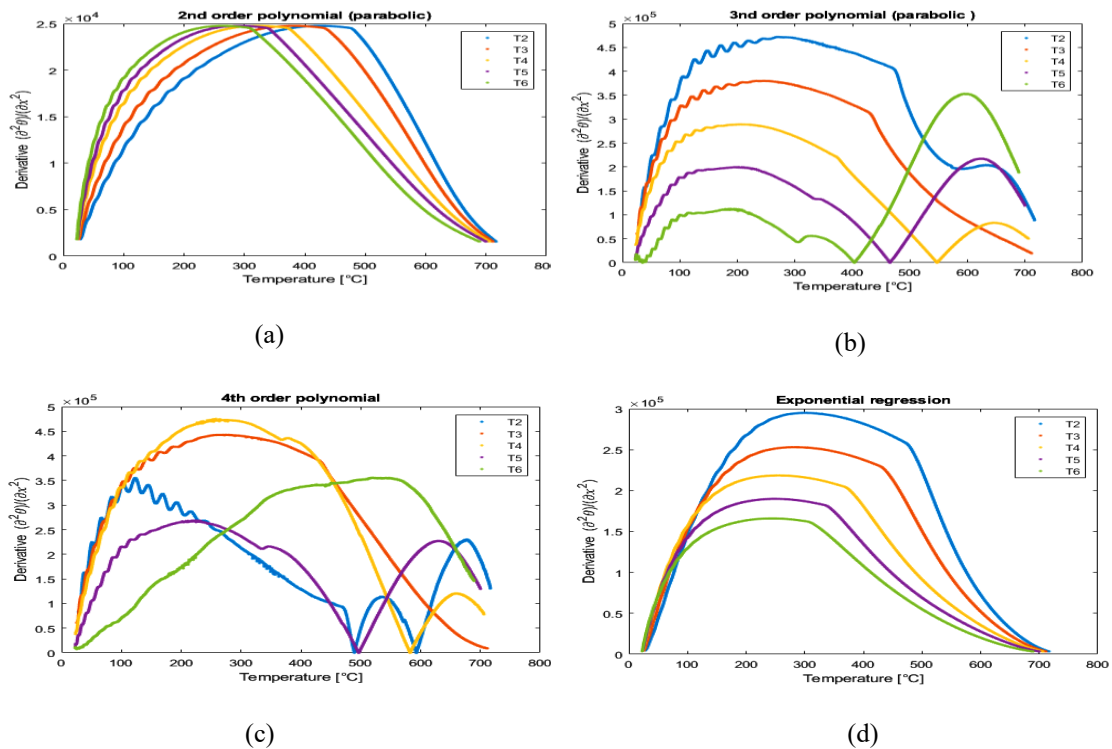


Figure 103. The second derivative of temperature with respect to the spatial coordinate, obtained for Test 6, sample C (second heating cycle) using the regression curve function: (a) 2nd order polynomial; (b) 3rd order polynomial; (c) 4<sup>th</sup> order polynomial and (d) exponential function.

## Results of validation process

The validation results presented below encompass both the straightforward and more complex aspects of heat flow, like the impact of fibre alignment and binder combustion. Altogether, this validation reassures us that the model can effectively represent the thermal responses in mineral wool samples, making it a solid tool for future analyses.

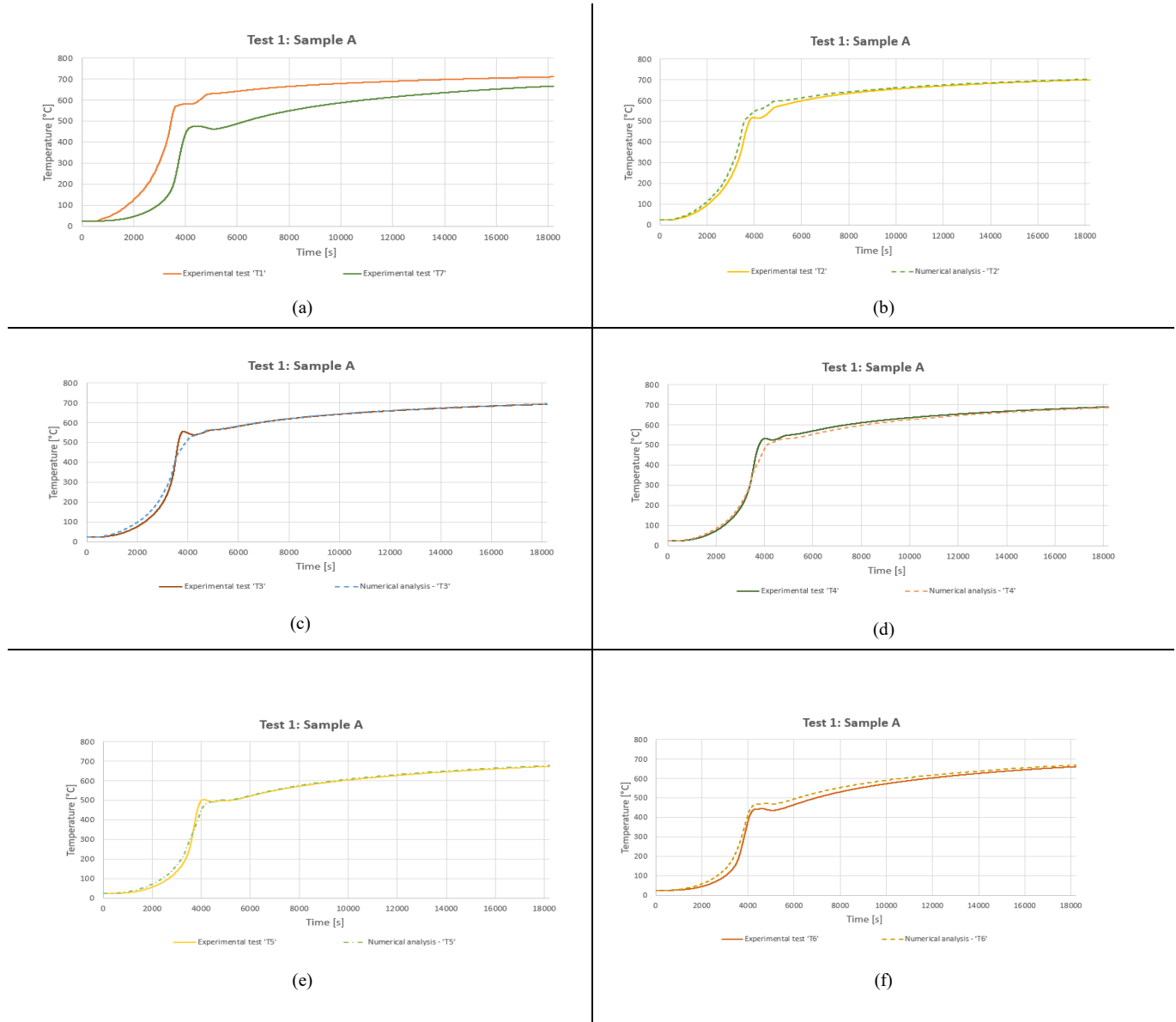
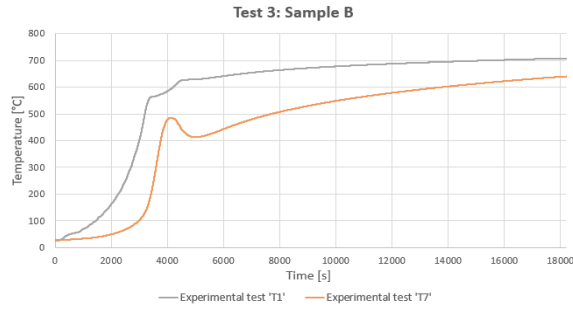
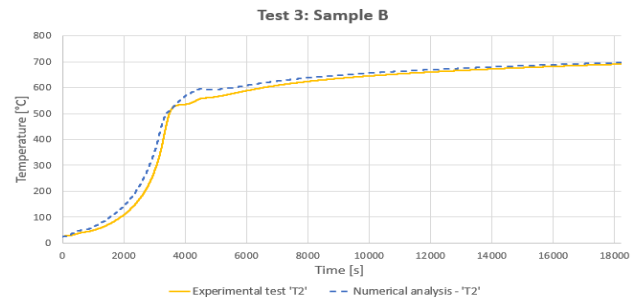


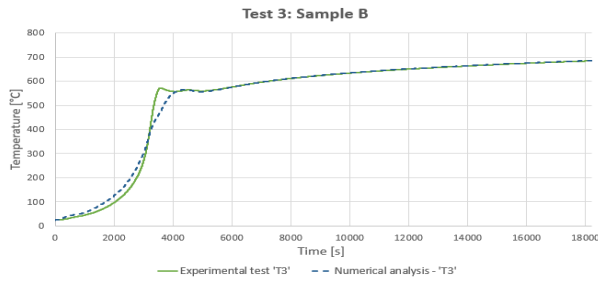
Figure 104. Comparison of the experimental and numerical results: (a) boundary conditions for the numerical problem—temperatures at nodes T1 and T7; (b) time-temperature relationship at node T2; (c) time-temperature relationship at node T3; (d) time-temperature relationship at node T4; (e) time-temperature relationship at node T5 and (f) time-temperature relationship at node T6 – Test 1, Sample A (first heating cycle).



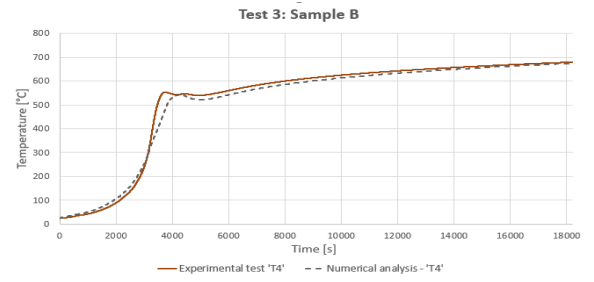
(a)



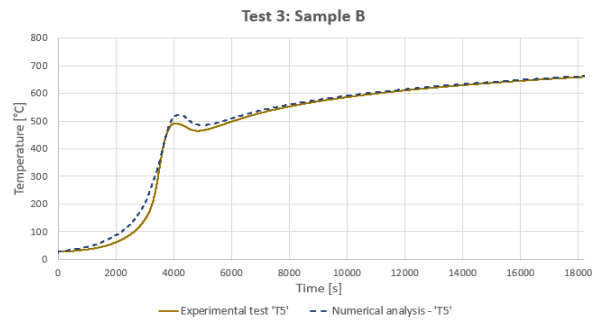
(b)



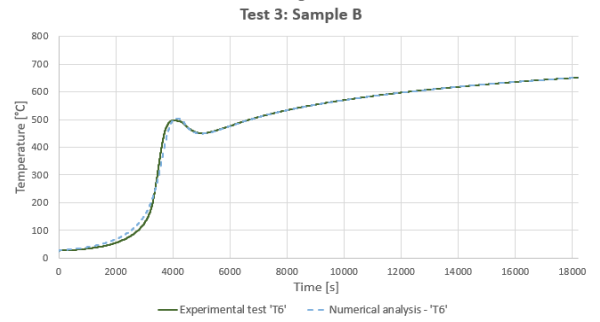
(c)



(d)

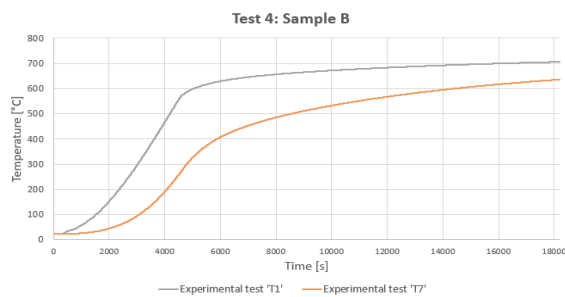


(e)

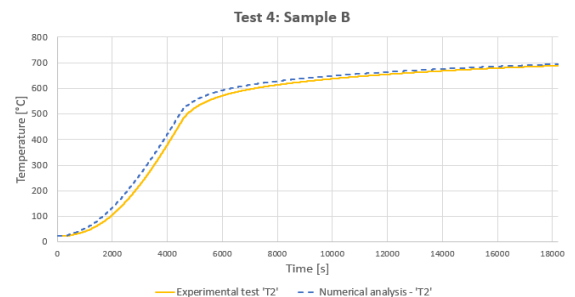


(f)

Figure 105. Comparison of the experimental and numerical results: (a) boundary conditions for the numerical problem—temperatures at nodes T1 and T7; (b) time–temperature relationship at node T2; (c) time–temperature relationship at node T3; (d) Time–temperature relationship at node T4; (e) time–temperature relationship at node T5 and (f) time–temperature relationship at node T6 – Test 3, Sample B (first heating cycle).



(a)



(b)



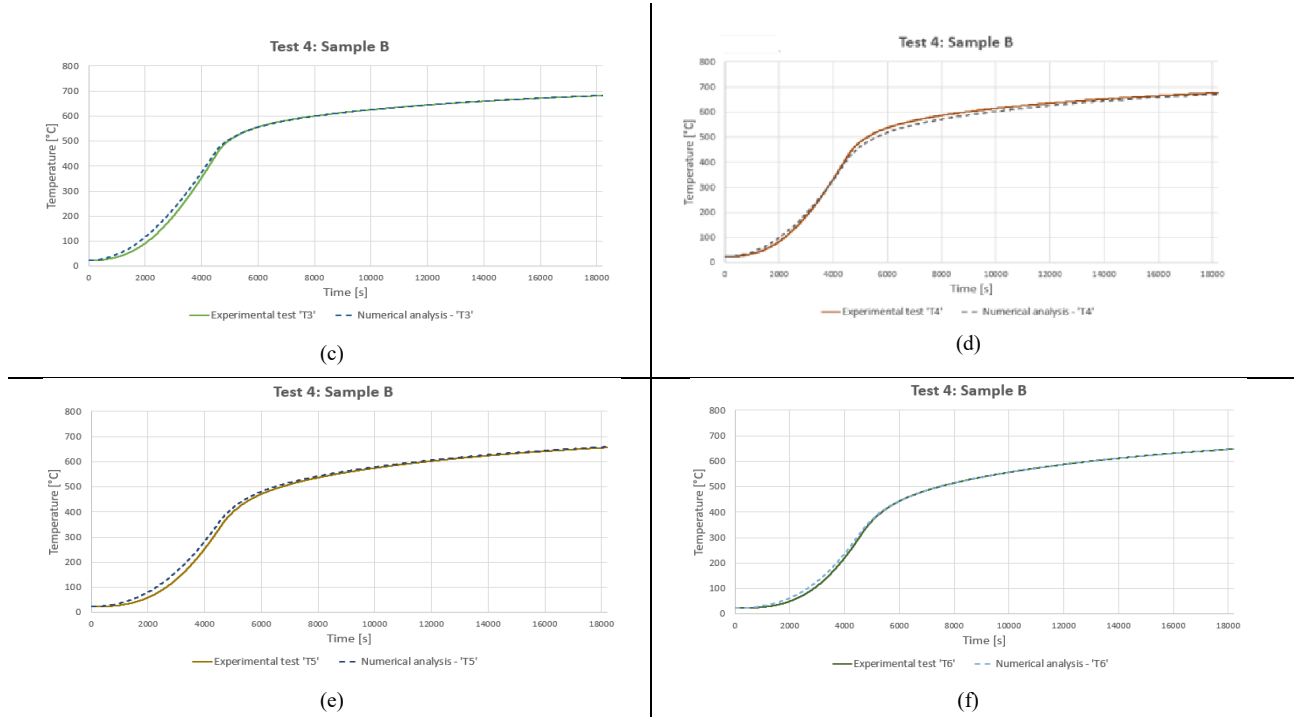
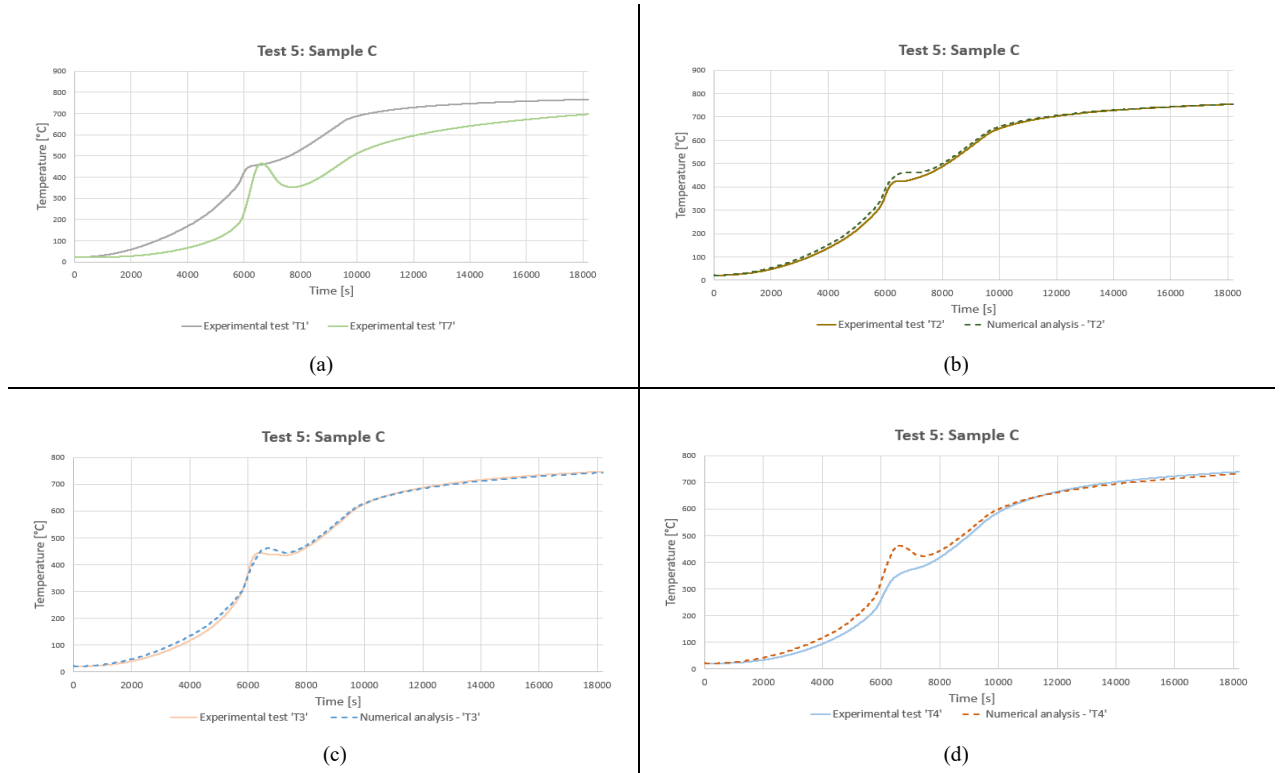


Figure 106. Comparison of the experimental and numerical results: (a) boundary conditions for the numerical problem—temperatures at nodes T1 and T7; (b) time–temperature relationship at node T2; (c) time–temperature relationship at node T3; (d) time–temperature relationship at node T4; (e) time–temperature relationship at node T5 and (f) time–temperature relationship at node T6 – Test 4, Sample B (second heating cycle).



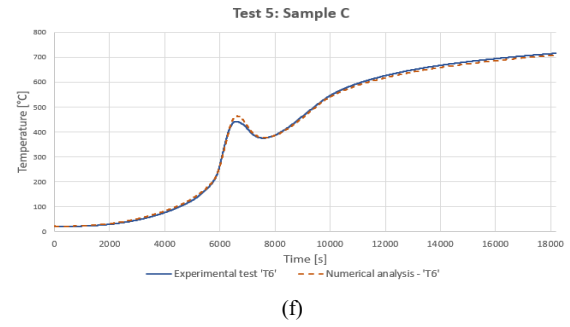
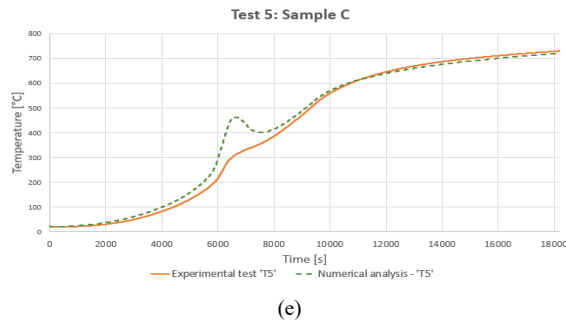


Figure 107. Comparison of the experimental and numerical results: (a) boundary conditions for the numerical problem—temperatures at nodes T1 and T7; (b) time–temperature relationship at node T2; (c) time–temperature relationship at node T3; (d) time–temperature relationship at node T4; (e) time–temperature relationship at node T5 and (f) time–temperature relationship at node T6 – Test 5, Sample C (first heating cycle).

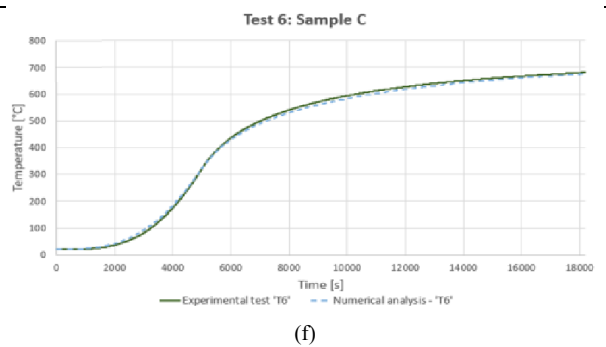
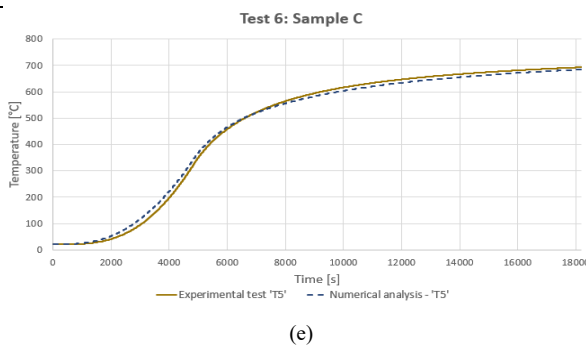
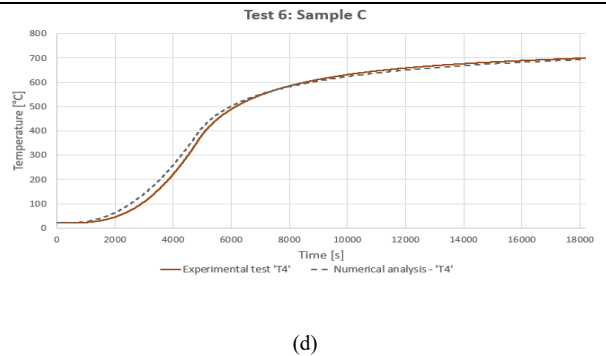
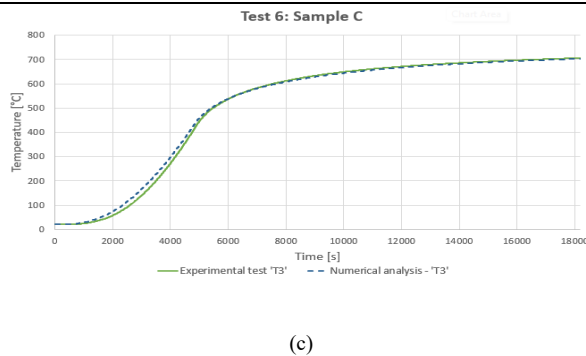
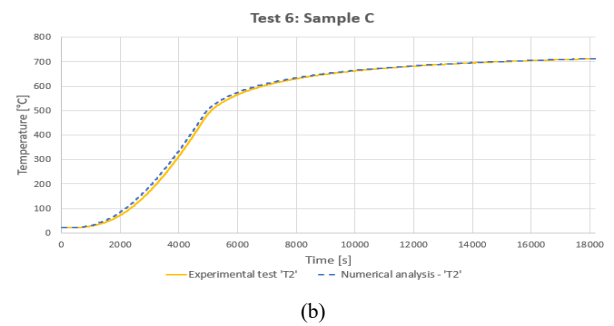
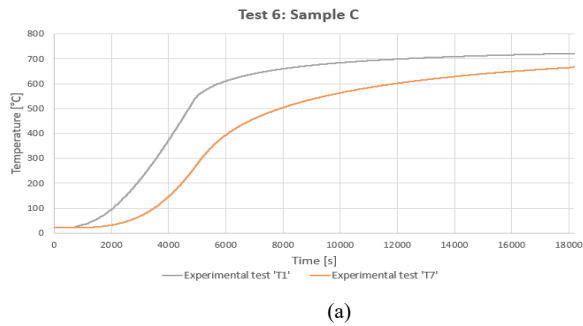


Figure 108. Comparison of the experimental and numerical results: (a) boundary conditions for the numerical problem—temperatures at nodes T1 and T7; (b) time–temperature relationship at node T2; (c) time–temperature relationship at node T3; (d) time–temperature relationship at node T4; (e) time–temperature relationship at node T5 and (f) time–temperature relationship at node T6 – Test 6, Sample C (first heating cycle).

## Appendix B. Thermal response of large-scale sandwich panels

This appendix presents in Figures 109-112 the detailed time–temperature data recorded from multiple thermocouples during fire exposure tests (cf. Figure 37 and 38). The results supplement the main analysis by illustrating thermal variations across panel surface.

▪ Time temperature results of tested sandwich panel assembly - Test 1'

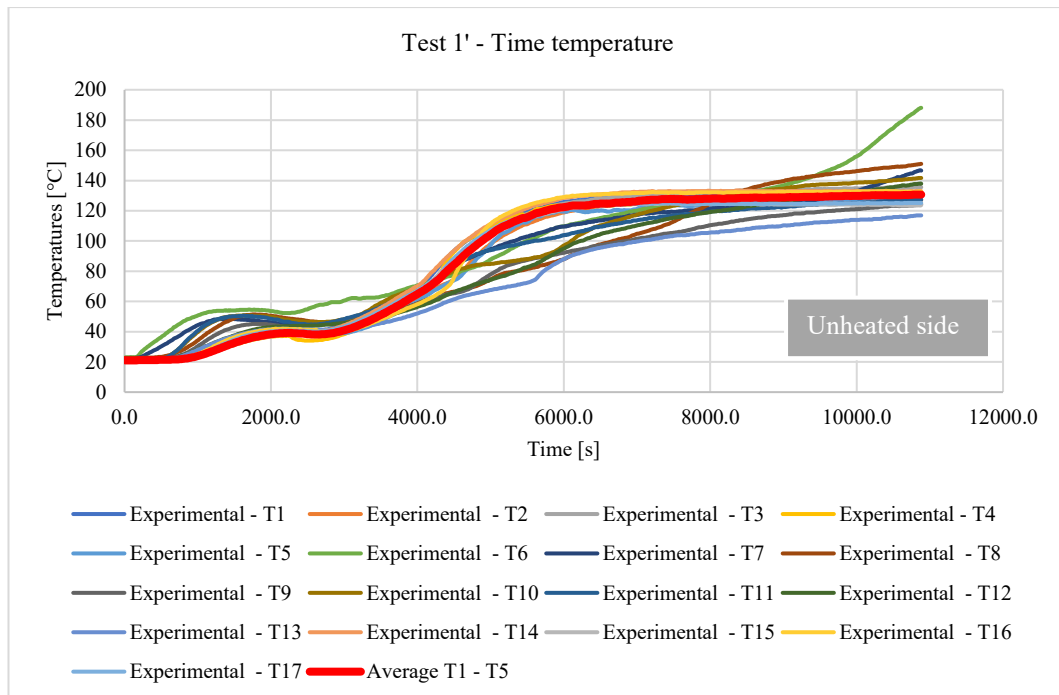


Figure 109. Time–temperature of all points – sample: (Test 1') — unheated face.

■ Time temperature results of tested sandwich panel assembly - Test 2'

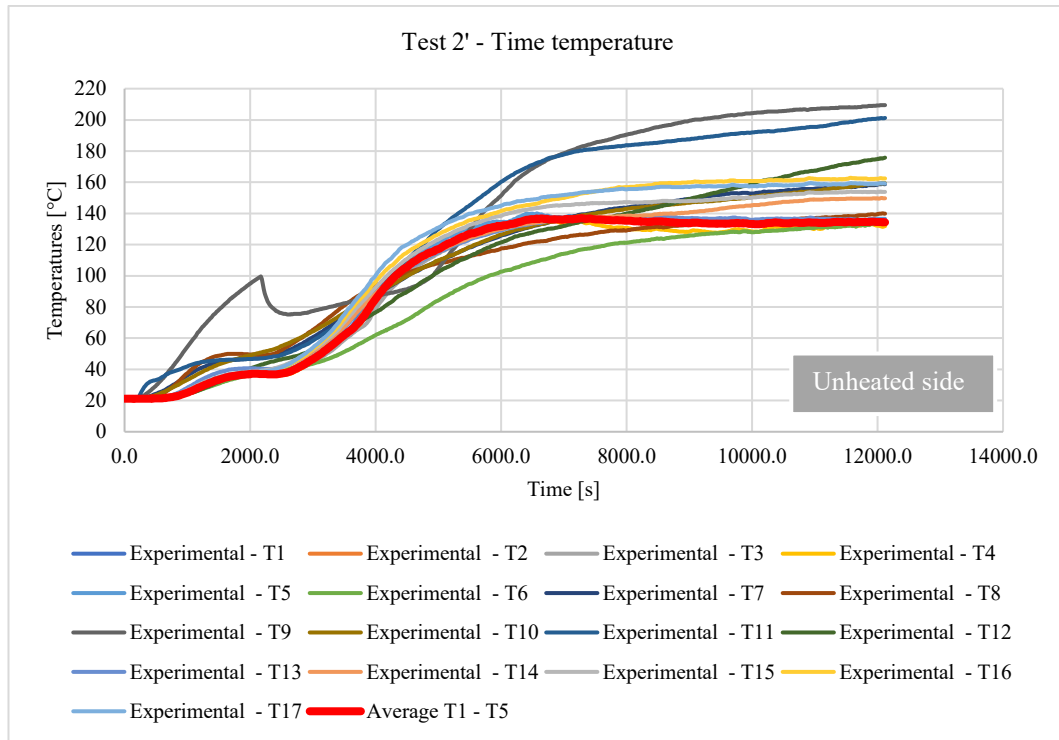


Figure 110. Time-temperature of all points – sample: (Test 2') — unheated face.

■ Time temperature results of tested sandwich panel assembly - Test 3'

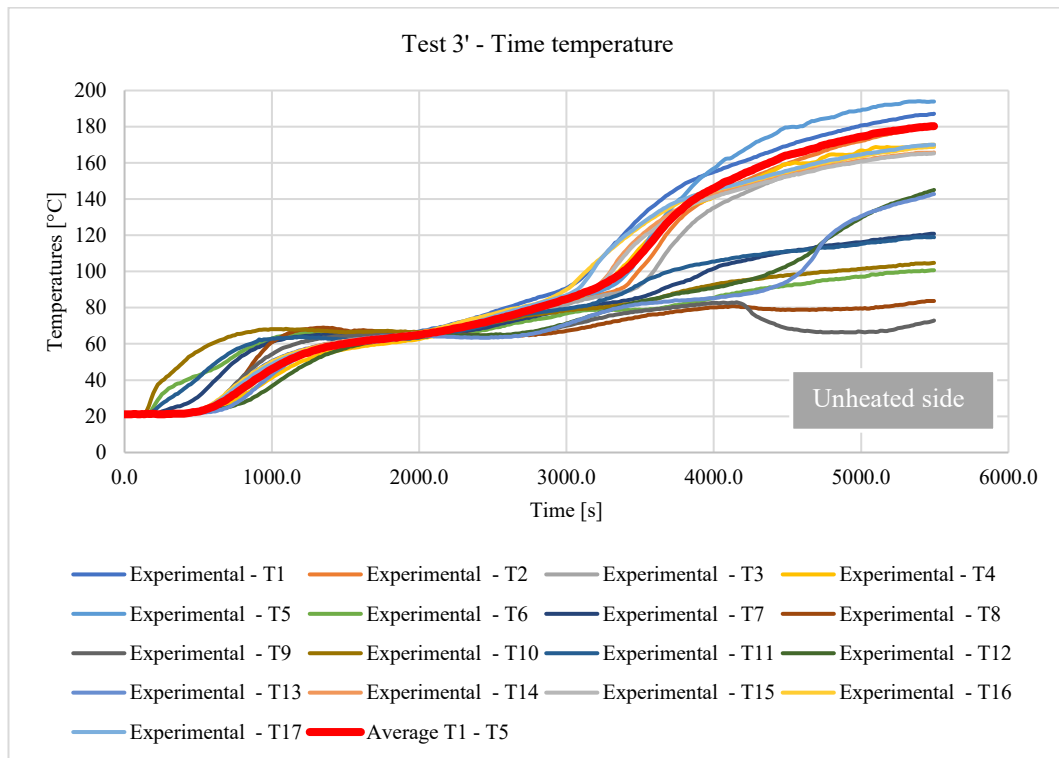


Figure 111. Time-temperature of all points – sample: (Test 3') — unheated face.

■ Time temperature results of tested sandwich panel assembly - Test 4'

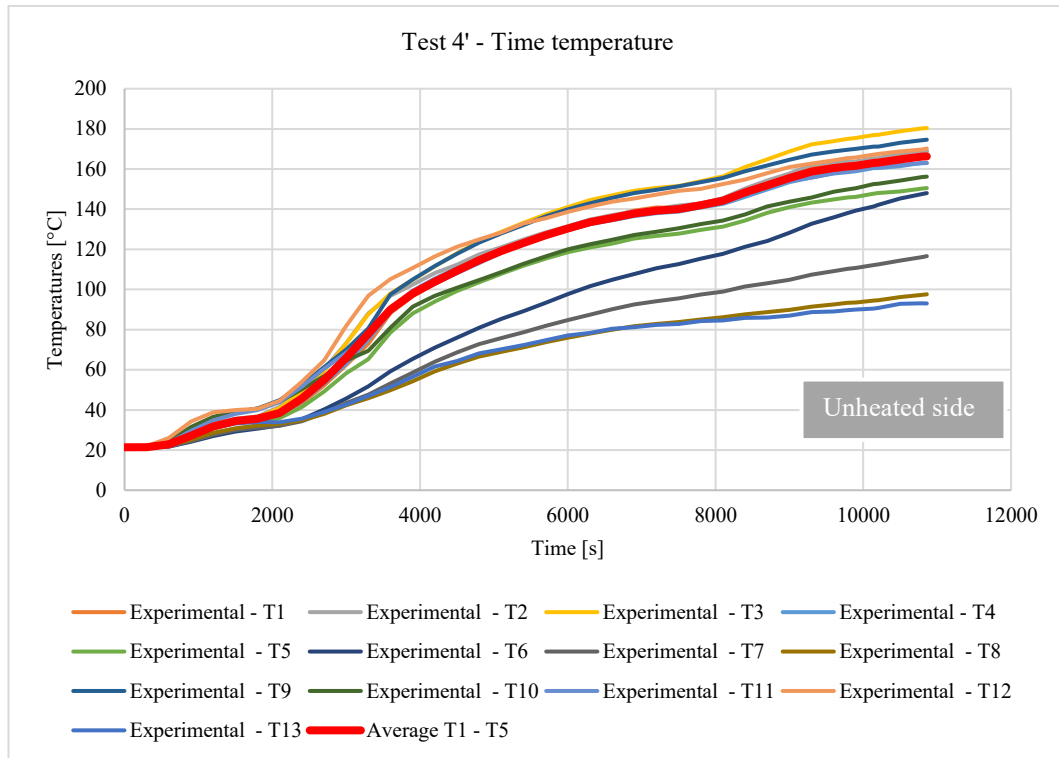


Figure 112. Time–temperature of all points – sample: (Test 4') — unheated face.

## Appendix C. Large-scale fire resistance experiments

This appendix presents the laboratory investigation of the thermal and structural response of a wall specimen subjected to fire exposure. Figures 113 – 120 illustrate the observed conditions from both the heated and unheated sides during the course of the experiment, including the final state at the conclusion of the test.

- Experimental test

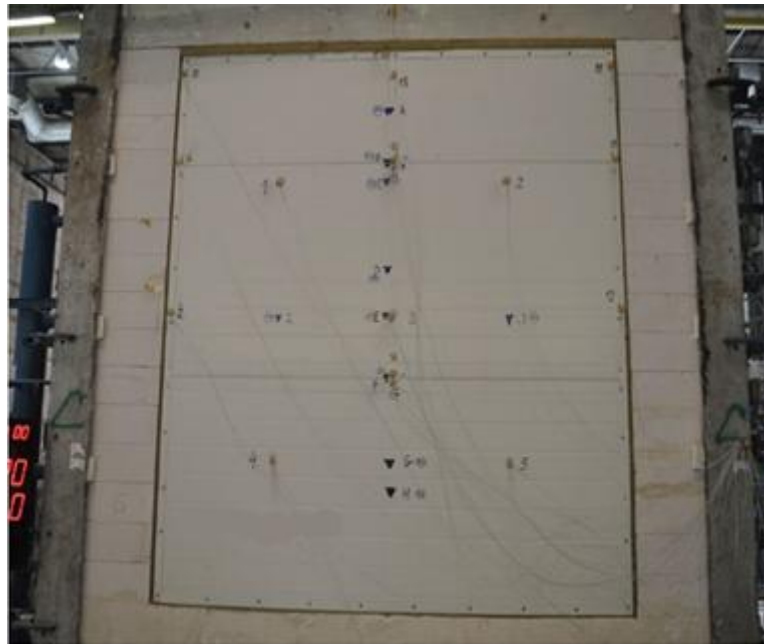


Figure 113. Initial setup of the tested wall specimen - unheated side of test 1'.



Figure 114. Condition of the tested wall specimen – unheated side of test 1' at 30 minutes.

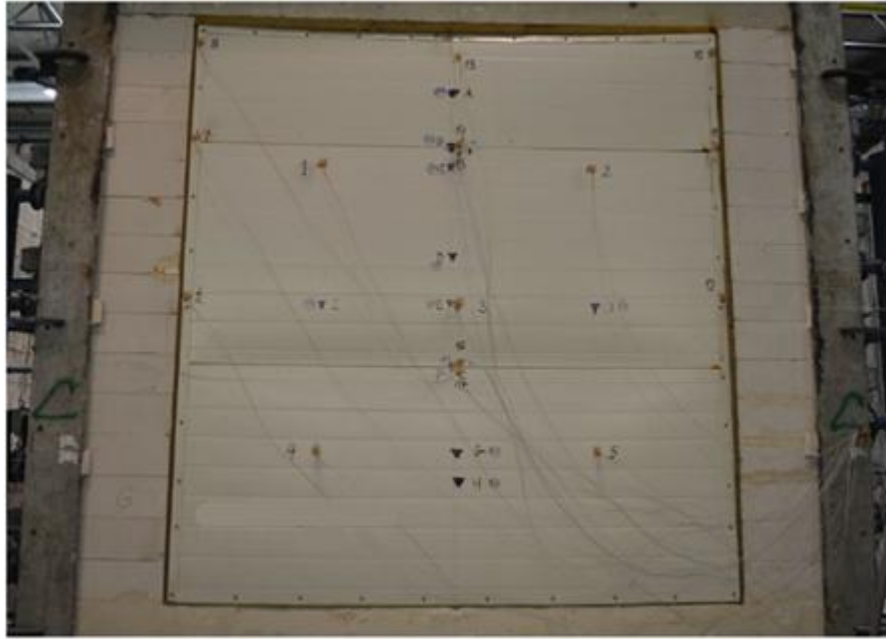


Figure 115. Condition of the tested wall specimen – unheated side of test 1' at the end of the test.



Figure 116. Condition of the tested wall specimen – heated side of test 1' at the end of the test.



Figure 117. Initial setup of the tested wall specimen - unheated side of test 4'.



Figure 118. Condition of the tested wall specimen – unheated side of test 2' at 95 minutes.





Figure 119. Condition of the tested wall specimen – unheated side of test 4' at 181 minutes.



Figure 120. Condition of the tested wall specimen – heated side of test 4' at the end of the test.